Inverse spin Hall effect in metallic heterostructures

Dissertation zur Erlangung des Doktorgrades der Naturwissenschaften
(Dr. rer. nat.) der Fakultät für Physik
der Universität Regensburg

vorgelegt von

Martin Obstbaum aus

Laupheim

im Jahr 2015

Promotionsgesuch eingereicht am: 15.12.2014
Die Arbeit wurde angeleitet von: Prof. Dr. Christian H. Back

Prüfungsausschuss:	Vorsitzender:	Prof. Dr. Jaroslav Fabian
	1. Gutachter:	Prof. Dr. Christian H. Back
	2. Gutachter:	Prof. Dr. Dieter Weiss
	weiterer Prüfer:	Prof. Dr. Christian Schüller

Termin Promotionskolloquium: 17.12.2015

Dedication:

To Eli and my parents

Contents

1 Introduction

Spintronics is a neologism describing the scientific and technological discipline of utilizing the spin degree of freedom in electronic circuitry. This endeavor might be rephrased as the "ever-evolving field of magnetic electronics" [1] at whose heart is the wish to effectively control and manipulate magnetization in terms of data storage. The great objective is a universal memory which offers high information densities, non-volatility, fast reading and writing cycles and low power consumption [1–3]. Magnetic multilayers, viz. metallic heterostructures have been the main building block ever since [2]. Based on the fact that there is an inequivalence of spin-up and spin-down electrons at the Fermi surface in a ferromagnetic material [4–6] the experimental findings of the charge-spin-coupling at ferromagnetic/normal metal (FM/NM) interfaces [7] and the giant magnetoresistance (GMR) in FM/NM/FM trilayers [8, 9] have emerged. Together with the seminal work in the field of spin diffusion in NM [10, 11] these findings have led to the technological development of the so-called spin valve [12, 13] which allows for effective electrical read-out of the magnetization configuration utilizing the GMR in a FM/NM/FM trilayer. Note that nowadays it is state of the art to use magnetic tunnel junctions (MTJ) where the NM layer is replaced by an insulator which enormously enhances the magnetoresistance [14–19].
Until recently one of the great problems has been the writing process, since it involved the need for magnetic fields [2]. The downscaling towards nanomagnets requires ever-greater magnetic anisotropies to sustain a defined magnetization direction [1]. In order to switch the magnetization, very high magnetic field pulses and therefore very intense current pulses are required. In terms of heat generation and power consumption this constitutes a vicious cycle. To this end, the direct transfer of spin angular momentum via spin-polarized currents which is enshrined in the theoretical concept of spin transfer torque (STT) [20–26] provides an alternative for the reorientation of a magnetization. Within the last ten years it has led to new possibly revolutionizing data storage concepts such as the race-track memory [27] which relies on the manipulation of domain walls via STT. In the past five years the topic has gained ever-more momentum when magnetization switching under the influence of STT from pure spin currents [28, 29] or induced by spin-orbit-fields [29–31] has experimentally been observed in FM/NM bilayers. These two effects can complement each other which further enhances the efficiency concerning magnetization switching [29]. Note that the idea of manipulating the magnetization by injecting pure spin currents has been characterized as "futuristic" [2, 32] not even ten years ago. Now it is already scientific state of the art and we are on the verge of technological applications using STT in magnetic random access memories [33].

In the experiments described in [28, 29, 33] the pure spin currents have been generated by the spin Hall effect (SHE) which converts a charge current into a transverse spin current [34]. In semiconductors and normal metals SHE emerges from the spin dependent scattering of electrons due to spin-orbit-coupling [35]. In a thorough theoretical work on the "spin Hall effect in the presence of spin diffusion" [36] it has been predicted to find spin accumulation of opposite polarization, which decreases on the scale of the spin diffusion length, on either side of a conductor slab. This led to the first experimental evidence of SHE in gallium arsenide (GaAs) semiconductor systems by optical means [37, 38]. The inverse spin Hall effect (ISHE) has been proposed and theoretically studied based on reciprocity arguments [34, 39]. ISHE summarizes the fact that a pure spin current is transformed into a transverse charge current due to spin-orbit coupling. Note that this bears the intriguing aspect of measuring and quantifying a spin current using standard charge based electronics [40]. To this end the so-called spin Hall angle α_{SH} is defined. Concerning ISHE it is the injected spin current divided by the generated charge current. Apart from understanding the types and origins of spin dependent scattering, the quest for material compounds which feature large spin Hall angles is one of the main triggers of studying ISHE.
In 2002 Tserkovnyak et al proposed that a precessing magnetization injects a pure spin current across FM/NM interfaces [41–43]. This so called spin pumping can be experimentally evidenced in ferromagnetic resonance (FMR) experiments [44–46]. Due to ISHE a spin current injected from spin pumping can be probed as a voltage signal and this constitutes a powerful experimental framework for quantifying spin Hall angles [47–53]. However, the published values for the spin Hall angles are still not fully in agreement considering the large number of experimental studies. The problem is twofold. On the one hand there is a large set of experimental parameters to be controlled for a reliable quantification of α_{SH}, for a discussion see [54]. On the other hand one has to be very careful as voltage signals due to ISHE can easily be confused with signals that stem from other origins. This is even more so setting up a spin pumping experiment, since one places the FM/NM bilayers in a microwave field. Under these circumstances the so-called spin rectification effect [55–59] which originates in anisotropic magnetoresistance (AMR) in FM and electromagnetic induction in the measurement circuit [60–62] are to be considered. A very interesting aspect of a spin current injected via spin pumping is the fact that it consists of both a time constant (dc) and an oscillating (ac) polarization component. This theoretically expected large ac-component [63] could recently be experimentally observed via the so-called ac-ISHE in a NiFe/Pt bilayer [62, 64]. This new field of ac-spintronics which encompasses spin currents in the GHz-regime has just emerged and it will be very interesting to see the future developments.
In this PhD-thesis one of the main aspects is the implementation of an experimental method to reliably quantify the ISHE from spin pumping in metal heterostructures [53]. This includes a thorough study of anisotropic magnetoresistance (AMR) in the presence of magnetization dynamics for a NiFe single layer, as well as NiFe/Pt, NiFe/Au and NiFe/Ta bilayers. Determination of the spin diffusion length for Pt

from thickness and temperature dependence of ISHE will be presented. Furthermore, towards the study of dynamic aspects of injected spin currents into NM [53, 64], the alternating current (ac) nature of the inverse spin Hall effect has been observed and uniquely confirmed for NiFe/Pt. In order to present a clear and comprehensive study on ISHE in metal heterostructures in the context of an experimental setup utilizing coplanar waveguide (CPW) structures for microwave purposes the thesis is organized as follows:

In Chapter 2 the underlying physical principles of spin Hall effects are in the focus. Its similarity to the anomalous Hall effect especially from a theoretical point of view shall be emphasized and the different nature and mechanisms of spin relaxation in conductors are presented. Then the nature of charge and spin currents and their phenomenological transformation into each other will be explained. This shall be the starting point for the subsequent explanation of the seminal experimental ideas and proofs of concept by Hirsch [34], Zhang [65], Valenzuela and Tinkham [40], Saitoh [47] and Ando et al. [66] in terms of observation and quantification of SHE and ISHE.

Chapter 3 starts with an explanation of magnetic moments and magnetization from both semi classical and quantum mechanical view points. Then the micromagnetic properties of ferromagnetic thin films are described. This is subsequently used as the basis for a theoretical description of FMR in ferromagnetic thin films and the spin pumping mechanism in ferromagnetic/ normal metal bilayers. Special emphasis is laid on the characterization of the magnetization dynamics and spin currents by deriving line shapes as a function of external magnetic field.

In Chapter 4 the extension of FMR principles and spin pumping towards the generation of voltages due to ISHE, AMR and electromagnetic induction are depicted. The first step is the introduction of the typical coplanar waveguide (CPW) structure which is used to excite magnetization dynamics by the generation of microwave magnetic fields. In order to determine the amplitude of the magnetic driving fields electromagnetic simulations are conducted using the specialized software provided by SONNET. Furthermore, the sample preparation and the used geometries of so-called in-plane and out-of-plane excitation are presented. Accounting for the geometrical subtleties, finally the characterization of voltage lines shapes which are produced by ISHE, AMR and electromagnetic induction as a function of external field takes place. It is the main objective to derive general expressions of voltage line shapes which can be applied to a broad spectrum of experimental configurations as well as material sets and which allows for quantification of physical parameters.

Chapter 5 marks the beginning of the presentation of experimental results. It is centered on FMR and spin pumping in NiFe/NM extended bilayer films as well as micro-structured samples. An explicit comparison of experimental results shall illustrate the similarity of microwave absorption (FMR) and voltage spectra in terms of extracting magnetic properties and spin pumping parameters. It furthermore provides results on the limits when transferring theoretical concepts from extended to micro-structured thin films.

Chapter 6 contains a general study of dc-voltages at ferromagnetic resonance. To

this end external field angle dependent measurements will provide insight into the origin of signals - AMR and ISHE. The symmetries of generated voltage signals are compared to the theoretical considerations given in chapter 4. Physical parameters are extracted using corresponding fits to angular dependencies for several NiFe/NM bilayer wires as well as for a single NiFe wire. Especially aspects of electromagnetic coupling between CPW and integrated NiFe/NM wires shall be discussed. It is one of the main objectives to show that it is possible to unambiguously study ISHE in NiFe/Pt and NiFe/Au bilayers with the spin pumping ISHE (SP-ISHE) method.
In Chapter 7 the study of SP-ISHE for NiFe/Pt and NiFe/Au will be elaborated towards the quantification of spin Hall angles α_{SH}. At first an explicit characterization of SP-ISHE with respect to its frequency dependence will be given. Furthermore, temperature dependent measurements of voltage signals at FMR and an unambiguous classification of both signals due to ISHE and AMR will be presented. Including an estimation of the spin diffusion length for Pt from a Pt-layer thickness dependence the spin Hall angle for Pt and Au shall be calculated from measured voltage amplitudes at FMR. Due to the significance of parameters entering the formula for α_{SH} a detailed discussion will take place. Finally α_{SH} will be plotted as a function of the most critical parameters. Furthermore, the temperature dependence of voltage signals due to ISHE for NiFe/Pt will be more closely analyzed and the spin diffusion length of Pt will be calculated as a function of temperature assuming a constant spin Hall angle.
In Chapter 8 bilayers of NiFe/$\mathrm{Au}_x\mathrm{Pt}_{1-x}$ are under investigation using the SP-ISHE method. The experimental study has emerged from theoretical considerations that the spin dependent scattering, viz. the spin Hall angle can be tuned as a function of Au in Pt [67]. To this end the SP-ISHE method shall be used for the quantification of spin Hall angles as a function of $\mathrm{Au}_x\mathrm{Pt}_{1-x}$-composition. In order to achieve maximal transparency for the experts of first-principles calculations of band structures and transport coefficients, the single steps towards the quantification of spin Hall angles from SP-ISHE results will be presented in a detailed manner. The chapter starts with a description of how to fabricate and reliably determine the composition of $\mathrm{Au}_x\mathrm{Pt}_{1-x}$-alloys. What follows are angle dependent measurements of several NiFe/$\mathrm{Au}_x\mathrm{Pt}_{1-x}$ bilayers as well as the characterization of spin pumping for different NiFe/$\mathrm{Au}_x\mathrm{Pt}_{1-x}$ interfaces. The normalization of voltage signal amplitudes in terms of alloy dependent parameters, among them the spin diffusion length, finally yields the spin Hall angle as a function of alloy composition. The chapter ends with a comparison of results from first principles calculations to the experimental study at hand.
In Chapter 9 the recent observation of the ac-ISHE in NiFe/Pt bilayers using the SP-ISHE method [64, 68] will be elaborated. Preliminary concepts concerning the detection of the expected sub-mV ac-signals in the GHz-regime will be explained. Then the experimentally observed line shapes will be compared to the theoretically expected voltage signals performing frequency, angle and power dependent measurements. In order to characterize and estimate the amount of parasitic voltage generating effects for NiFe/Pt studies of different NM capping layers of NiFe will be

presented. Finally the amplitude of ac- and dc-ISHE generated voltage signals will be compared.
In Chapter 10 a summary and conclusion of the main results of this thesis will be presented. This shall include final remarks on possible contact points of the present thesis in terms of future theoretical and experimental work.

2 Spin Hall effects

Fast electrons scattering off heavy atomic nuclei will be spin polarized after the collision [69]. This so-called Mott-scattering is due to spin-orbit-coupling between the relativistic electrons and the atom at which it scatters. It is a quantum mechanical consequence of the Dirac-equation [70]. If a spin-polarized electron beam is scattered from a heavy metal film and one measures the number of electrons arriving at detectors on two opposing sides of the scatterer perpendicular to the incoming beam, a number asymmetry proportional to the spin polarization of the incoming beam can be observed. This effect is commonly used to measure e.g. the spin polarization of photoelectrons extracted from materials in so-called Mott-detectors, see e.g. [71] and references therein.
In Mott-scattering free electrons are considered. What happens if spin-polarized electrons are moving in a conductor? Assume a metallic ferromagnet (FM) in which a charge current flows. Due to the imbalance of spin-up and spin-down electrons at the Fermi surface of FM [4], the charge is accompanied by a spin current. Following the idea of Mott-scattering this means that a charge current is measurable perpendicular to the direction of motion and the polarization of the spin current. This generalization of Mott-scattering to ferromagnetic metals is called anomalous Hall effect (AHE). It is a consequence of spin-orbit-interaction in FM [4, 72, 73]. The spin dependent transverse deflection of charge carriers is called anomalous scattering. The extension to non-magnetic conductors, also referred to as normal metals (NM), was first considered by Dyakonov and Perel in 1971 [35]. An unpolarized electric current flowing through a bulk conductor will generate a spin-current perpendicular to its direction. Since spin is not a conserved quantity in NM it is equilibrated by spin relaxation, viz. spin flip processes and integration over the whole conductor gives zero spin polarization. Only thin layers at the surface are polarized [74], in fact opposite sides of NM feature a spin polarization with equal absolute value, but antiparallel direction. The scale on which a non-vanishing spin polarization is present is given by the spin diffusion length [36]. Ever since Hirsch in [34] resurrected the ideas of spin current generation in NM by a flowing charge and named the topic spin Hall effect (SHE) in analogy to the ordinary Hall effect many theoretical and experimental investigations in this field have been conducted. Embedding SHE into the framework of spin diffusion [10, 11, 36] it was one of the major interests to identify the underlying principles of spin scattering mechanisms. It is of great interest whether extrinsic [37, 75, 76] or electron-band-structure intrinsic [38, 72, 77] mechanisms of spin-orbit-interaction are dominant or how large they can become. Especially the last point is vital for technical applications.
In the following section the mechanisms of spin dependent scattering are character-

ized. It shall be of major interest which types are dominating in certain cases, how distinct regimes can be identified, and how the magnitude of anomalous scattering might be tuned. Leaving open a detailed theoretical specification of the scattering processes, the second section contains a description of the SHE and its reverse the inverse spin Hall effect (ISHE). This shall take place on a phenomenological basis. Facts about charge and spin transport are discussed based on the drift-diffusion model [10, 11, 74, 78] and the experimentally close approaches described in [34] and [36] are considered. Especially the experimental challenges to observe SHE and ISHE shall be in the focus.

2.1 Mechanisms of spin dependent scattering

For fundamental considerations of electronic transport through a conductor one may start with the assumption of freely moving electrons [4] only confined by a box potential. The Hamilton operator correspondingly contains terms for kinetic and potential energy. The spin orbit coupling may now be added as a further term [76, 79]. Considering the principles of spin dependent scattering the electronic movement may be confined to two dimensions (x, y) and the spin quantization axis z perpendicular to the transport plane. The following Hamiltonian describes the assumed circumstances [75]:

$$H = H_0 + H_{\mathrm{SO}} \tag{2.1}$$

$$= \frac{\hbar}{2m}\nabla^2 + V(r) + \frac{1}{2m^2c^2}\frac{1}{r}\frac{\partial V}{\partial r}S_z L_z \tag{2.2}$$

Due to spin orbit coupling the electrons are scattered transversely relative to the transport direction. In general the origin of scattering can be divided up into extrinsic and intrinsic contributions. The first sums up scattering events at impurities, phonons, magnons, etc. (henceforth called impurities), the latter covers effects exclusively related to the electron band structure of the material.
The extrinsic anomalous scattering can be categorized into skew [76, 79] and side-jump type [75]. The first assumes free electrons approximated by plane waves in the presence of spin-orbit-interaction and can be explained with classical Boltzmann transport theory [75, 80]. This is illustrated in Fig. 2.1a). An electron is incident to a spherically symmetric spin-orbit-potential. In general, time reversal symmetry is not broken (e.g. by a magnetic field) and therefore the electrons at the Fermi surface are spin degenerate. Upon the scattering event electrons are deflected asymmetrically with respect to their spin degree of freedom. The linear trajectories of spin-up and -down electrons confine an angle δ.
The second extrinsic type results from theoretic considerations when assuming Gaussian electron wave packets [73, 75, 81]. The electron performs a side-way movement Δy inside the spin-orbit scattering potential of the impurity. The situation is shown schematically in Fig. 2.1b). After the scattering event the spin-split electron trajectories are parallel to the incident beam. Thus, viewing the scatterer as point-like the

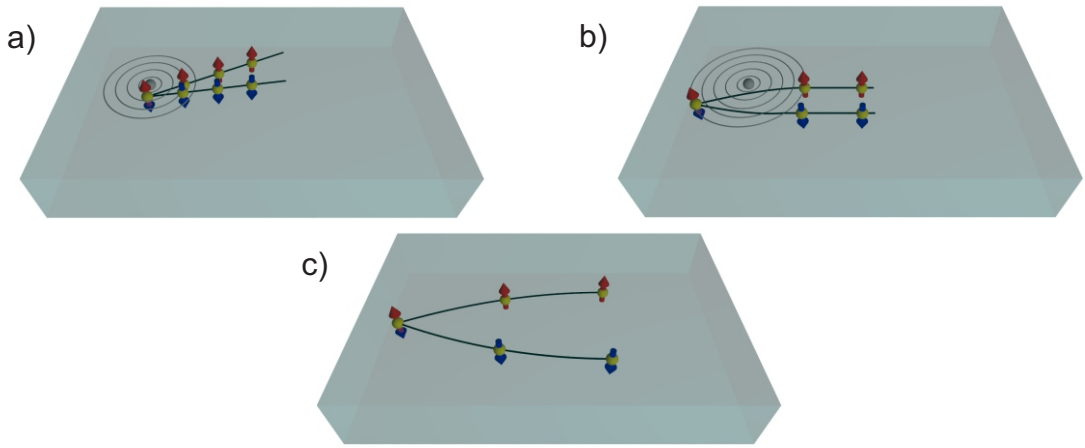

Figure 2.1: The different spin dependent scattering types are illustrated, in a) and b) skew and side-jump scattering, respectively, and in c) intrinsic type. In a) and b) the spin orbit coupling potentials are depicted as concentric circles around an impurity (grey). Electronic transport takes place from the left to the right in all pictures. Electrons and their spin degree of freedom are represented by yellow spheres and red and blue arrows respectively.

electron performs a side-jump. However, when assuming that the Gaussian electron wave packet is only scattered in the spin-orbit potential of an impurity but moves freely otherwise, side-jumps of only $\Delta y \approx 1 \times 10^{-16}\,\mathrm{m}$ are expected [75]. This is too small to have physical relevance. Yet, taking into account the effective spin-orbit Hamiltonian resulting from the band structure the side-jumps reach the order of $\Delta y \approx 1 \times 10^{-10}\,\mathrm{m}$ [75]. Hence side jump scattering can play a decisive role.
The last type of scattering considered here is exclusively due to the electronic band structure of a material. This intrinsic spin dependent scattering might dominate if the spin-orbit-coupling between bands is strong and hence a large interband conductivity is present [73]. In a semiclassical picture, the charge carriers acquire an anomalous velocity due to a nonzero Berry phase [73, 82, 83]. In Fig. 2.1c) this type of scattering is illustrated. The asymmetric scattering of spin-up and -down electrons is present if an electric field E is applied to a system with broken spatial inversion or time reversal symmetry. Note that for a ferromagnetic system the latter symmetry breaking is always present. Spin-orbit interaction couples spin and orbital part in spin-space and an anomalous Hall voltage is measurable [72, 83].
For intrinsic SHE the reasoning is analogous to the case of intrinsic AHE but one additionally has to account for the time-reversal symmetry breaking being present only on the scale of the system's spin diffusion length. The detailed mechanisms of spin-orbit-coupling in crystals shall not be discussed within the frame of this thesis. As a review consult e.g. [78]. It is noteworthy that the first calculation of intrinsic SHE assumed Rashba-spin-orbit-coupling [77] and was measured in a semiconductor

hole-gas system shortly after its prediction [38].
In the review article by Nagaosa et al. about AHE [73] different spin scattering regimes are empirically identified according to the conductivity of FM. Recent reviews about SHE [84, 85] pointed out that the regimes should be analogous for NM. Experimentally, the measured quantity to identify different regimes of extrinsic or intrinsic scattering is the transverse resistivity ρ_{xy} due to a longitudinal current I_{xx} through a conductor. This is summarized in the following formula, cf. [73, 86]:

$$\rho_{xy} = \mu_0(R_\mathrm{O}H_z + R_\mathrm{An}M_z) \tag{2.3}$$

The first term on the right hand side of Eq. (2.3) is the transverse resistivity caused by an external field H_z and the Lorentz force mediated ordinary Hall effect. The second term describes the anomalous Hall effect due to a nonzero magnetization M_z of the ferromagnetic material. R_O and R_An are the corresponding Hall coefficients. The investigation of ρ_{xy} with respect to the longitudinal resistivity ρ_{xx} and comparison to microscopically expected behavior of transport properties yields a classification of dominant scattering mechanism regimes [73]. From inversion of the system's conductivity tensor one can infer that

$$\rho_{xy} \approx \frac{\sigma_{xy}}{\sigma_{xx}^2 + \sigma_{xy}^2} \approx \frac{\sigma_{xy}}{\sigma_{xx}^2} \tag{2.4}$$

making the assumption that $\sigma_{xx} >> \sigma_{xy}$. The Bloch state transport lifetime τ and implications with respect to Eq. (2.4) can be compared to experimentally observed data. For skew scattering both σ_{xx} and $\sigma_{xy} \propto \tau \propto \frac{1}{\rho_{xx}}$ and therefore $\rho_\mathrm{xy} \propto \rho_{xx}$. For side-jump and intrinsic scattering only $\sigma_{xx} \propto \tau \propto \frac{1}{\rho_{xx}}$ and σ_{xy} is independent of τ so $\rho_{xy} \propto \rho_{xx}^2$. From experimental data three anomalous Hall regimes are identifiable [73]. The so-called high conductivity regime where $\sigma_{xx} > 1 \times 10^8\,\Omega^{-1}\,\mathrm{m}^{-1}$ is dominated by skew scattering. For values $1 \times 10^8\,\Omega^{-1}\,\mathrm{m}^{-1} > \sigma_{xx} > 1 \times 10^6\,\Omega^{-1}\,\mathrm{m}^{-1}$ a broad impurity density independent regime due to side-jump and intrinsic mechanism is recognizable. For conductivities lower than $1 \times 10^6\,\Omega^{-1}\,\mathrm{m}^{-1}$ the bad-metal-hopping regime prevails and ρ_{xy} decreases faster than linear for increasing ρ_{xy}. The microscopic origin of the bad-metal or low conductivity regime will not be discussed here, the interested reader might refer to [73] and references therein.
Bearing the different mechanism regimes of spin dependent scattering in mind the following sections are devoted to a phenomenological approach to spin Hall effects. As one will see, from an experimental point of view this change of paradigms helps a lot.

2.2 Phenomenology of SHE and ISHE

In order to understand experimental approaches, techniques and perspectives of spin Hall effects it is useful to understand the origin and nature of charge and spin currents [78, 87] and their phenomenological transformation into each other [74, 88]. The spin Hall angle α_{SH} is introduced as the parameter to define the magnitude of spin dependent scattering. Then experimental approaches will be discussed. Potentials and limits will be in the focus and spin pumping is established as one of the most versatile and promising methods to study spin dependent scattering of pure spin currents via ISHE in normal metals.

2.2.1 Charge and spin currents

According to [78, 87] the time-rate of change of a particle density can be defined with respect to a random walk and is given by [78]:

$$\frac{\partial n}{\partial t} = D\nabla^2 n + v_{\mathrm{d}}\nabla n \tag{2.5}$$

The first term on the right hand side describes diffusion of particles in terms of the diffusivity parameter $D = \frac{1}{2}v^2\tau$. Particles moving at the velocity v are being scattered after the momentum relaxation time τ. For metallic conductors v equals the Fermi velocity v_F, since only electrons at the Fermi-level participate in transport. The second term of Eq. (2.5) accounts for the fact that particles carrying charge like electrons might be biased with an electric field $\mathbf{E} = \frac{m\mathbf{v}_{\mathrm{d}}}{e\tau} = \frac{\mathbf{v}_{\mathrm{d}}}{\mu}$; $\mathbf{v}_{\mathrm{d}}$ is the drift velocity of the charged particles, e is the charge, and the mobility of the particles is defined by $\mu = \frac{e\tau}{m}$. The connection between a particle density's time-rate of change Eq. (2.5) and the corresponding particle current density (flux) $\mathbf{J}$ is given by the continuity equation:

$$\frac{\partial n}{\partial t} + \nabla(-\mu n\mathbf{E} - D\nabla n) = \frac{\partial n}{\partial t} + \nabla\mathbf{J} = 0 \tag{2.6}$$

It is equal to zero as both particle number and charge are conserved quantities of a closed system. For electrons the charge flux is defined as $\mathbf{j}_{\mathrm{c}} = -e\mathbf{J}$:

$$\mathbf{j}_{\mathrm{c}} = \sigma\mathbf{E} + D\nabla n \tag{2.7}$$

where $\sigma = en\mu$ is the conductivity.
Drift and diffusion of a spin density is more subtle. A spin flux has both a direction and independently of it a polarization. Examining general properties of spin currents a reduction to one-dimensional transport of particles with two spin eigenstates up ($|\uparrow\rangle$) and down ($|\downarrow\rangle$) is useful [78]. From a random walk perspective spin-up and -down electron densities obey the following time-rate of change:

$$\frac{\partial n_\uparrow}{\partial t} = D\frac{\partial^2 n_\uparrow}{\partial x^2} + v_{\mathrm{d}}\frac{\partial n_\uparrow}{\partial x} - \frac{w}{\tau}(n_\uparrow - n_\downarrow) \tag{2.8}$$

$$\frac{\partial n_\downarrow}{\partial t} = D\frac{\partial^2 n_\downarrow}{\partial x^2} + v_{\mathrm{d}}\frac{\partial n_\downarrow}{\partial x} + \frac{w}{\tau}(n_\uparrow - n_\downarrow) \tag{2.9}$$

The last terms on the right hand sides of Eqs. (2.8) and (2.9) account for the fact that for every momentum scattering event a spin-flip might occur. This is characterized by a certain transition probability w from up- to down-spin and vice versa. The total particle density is given by $n = n_\uparrow + n_\downarrow$ and its time evolution is given by Eqs. (2.5)-(2.7). The interesting quantity in terms of spin transport is $s = n_\uparrow - n_\downarrow$, this is the particle spin density. Combining Eqs. (2.8) and (2.9) the drift-diffusion equation for a spin density is as follows

$$\frac{\partial s}{\partial t} = v_\mathrm{d}\frac{\partial s}{\partial x} + D\frac{\partial^2 s}{\partial x^2} - \frac{s}{\tau_s} \tag{2.10}$$

and the corresponding continuity equation is given by:

$$\frac{\partial s}{\partial t} + \frac{\partial}{\partial x}(-\mu s E - D\frac{\partial s}{\partial x}) = \frac{\partial s}{\partial t} - \frac{\partial}{\partial x}J_\mathrm{s} = -\frac{s}{\tau_s} \tag{2.11}$$

J_s is the spin particle current density. Here the parameter $\tau_\mathrm{s} = \frac{\tau}{2w}$ has been introduced, the so-called spin relaxation time. The fact that spin is not a conserved quantity in the system manifests itself in Eq. (2.11) where the right hand side is nonzero but consists of a spin-sink term. The characteristic length scale on which spin conserved transport takes place is given by the spin diffusion length λ_sd [78]. Assuming $\frac{\partial s}{\partial t} = E = 0$, Eq. (2.11) reduces to:

$$D\frac{\partial^2 s}{\partial x^2} = \frac{s}{\tau_\mathrm{s}} \quad \Leftrightarrow \quad \frac{\partial^2 s}{\partial x^2} = \frac{s}{\lambda_\mathrm{sd}^2} \tag{2.12}$$

this defines the spin diffusion length as $\lambda_\mathrm{sd} = \sqrt{D\tau_\mathrm{s}}$. Suppose there is a given spin density s_0 at $x = 0$. It will evolve into a spatially dependent spin density $s(x)$ (also called spin accumulation) into positive x-direction according to the following formula:

$$s(x) = s_0 \exp\left(-\frac{x}{\lambda_\mathrm{sd}}\right) \tag{2.13}$$

If a steady state spin current $J_{\mathrm{s},0} = -D\partial s(x=0)/\partial x$ is incident at $x = 0$, $s(x)$ will be:

$$s(x) = J_{\mathrm{s},0}\frac{\lambda_\mathrm{sd}}{D}\exp\left(-\frac{x}{\lambda_\mathrm{sd}}\right) \tag{2.14}$$

and for $J_\mathrm{s}(x)$ the following relation holds:

$$J_\mathrm{s}(x) = J_{\mathrm{s},0}\exp\left(-\frac{x}{\lambda_\mathrm{sd}}\right) \tag{2.15}$$

Note that Eqs. (2.13) and (2.15) exhibit the same qualitative behavior as a function of x. It is a matter of choice of what one wants to keep track of - the spin accumulation or current densities. When it comes to spin Hall effects, it is the latter.

As the spin of electrons is quantized in units of $\hbar/2$ it is useful to define the electron spin flux or spin current density as follows:

$$j_\mathrm{s} = -\frac{\hbar}{2}\mu s E - \frac{\hbar}{2} D \frac{\partial s}{\partial x} \tag{2.16}$$

Accounting for three spatial dimensions it is essential to realize that the spin current density is a tensor quantity with the following components distinguishing transport direction (i) and spin quantization axis (j):

$$j_{\mathrm{s,ij}} = -\frac{\hbar}{2}\mu E_\mathrm{i} s_\mathrm{j} - \frac{\hbar}{2} D \frac{\partial s_\mathrm{j}}{\partial x_\mathrm{i}} \tag{2.17}$$

Eqs. (2.7) and (2.17) can effectively be used to draw a phenomenological picture about what happens if spin orbit coupling is included into the considerations, [74, 88]. Spin Hall and inverse spin Hall effect are the consequence.

2.2.2 SHE and ISHE

Including spin-orbit-coupling, anomalous current densities (i.e. transverse contributions) are to be included into Eqs. (2.7) and (2.17). Analogously to [74, 88] this can be done phenomenologically in component representation by the following two equations:

$$j_\mathrm{c,i} = j^{(0)}_\mathrm{c,i} + \frac{2e}{\hbar}\zeta \epsilon_\mathrm{ijk} j^{(0)}_\mathrm{s,jk} \tag{2.18}$$

$$j_\mathrm{s,ij} = j^{(0)}_\mathrm{s,ij} - \frac{\hbar}{2e}\zeta \epsilon_\mathrm{ijk} j^{(0)}_\mathrm{c,k} \tag{2.19}$$

here summation over repeated indices is assumed and ϵ_ijk is the unit antisymmetric tensor, the Levi-Civita symbol, cf. [89]. $j^{(0)}_\mathrm{c,i}$ and $j^{(0)}_\mathrm{s,ij}$ are given by Eq. (2.7) and (2.17), the longitudinal components of the respective current densities. The parameter ζ is a dimensionless constant proportional to the strength of spin-orbit coupling. The different sign for the additional terms in Eqs. (2.18) and (2.19) reflects the fact of different dependencies of charge and spin currents with respect to time reversal. Inserting Eqs. (2.17) and (2.7) into Eqs. (2.18) and (2.19) yields the two central phenomenological equations for charge and spin-charge-current densities in the presence of spin-orbit coupling, cf. [74, 88]:

$$j_\mathrm{c,i} = \sigma E_\mathrm{i} + eD\frac{\partial n}{\partial x_\mathrm{i}} - \frac{2e}{\hbar}\zeta\epsilon_\mathrm{ijk}\left(\frac{\hbar}{2}\mu E_\mathrm{j} s_\mathrm{k} + \frac{\hbar}{2} D \frac{\partial s_\mathrm{k}}{\partial x_\mathrm{j}}\right) \tag{2.20}$$

$$j_\mathrm{s,ij} = \frac{\hbar}{2}\mu E_\mathrm{i} s_\mathrm{j} + \frac{\hbar}{2} D \frac{\partial s_\mathrm{j}}{\partial x_\mathrm{i}} - \frac{\hbar}{2e}\zeta\epsilon_\mathrm{ijk}\left(\sigma E_\mathrm{k} + eD\frac{\partial n}{\partial x_\mathrm{k}}\right) \tag{2.21}$$

The first term proportional to ζ in Eq. (2.20) describes the fact that a transverse charge current is generated by a charge current carrying a net spin polarization.

This accounts for the AHE in ferromagnetic materials. The respective second term of Eq. (2.20) yields charge current generation by a spatially inhomogeneous spin density (ISHE). This situation is especially given when a pure spin current flows through a conductor. In this case the last term of Eq. (2.20) is usually written in the following equivalent form:

$$\mathbf{j}_\mathrm{c} = \frac{2e}{\hbar}\alpha_\mathrm{SH}\mathbf{j}_\mathrm{s} \times \mathbf{e}_\mathrm{s} \tag{2.22}$$

Here the so-called spin Hall angle $\alpha_\mathrm{SH} = \zeta$ is introduced. It is the dimensionless ratio of generated charge current to injected spin current density. $\mathbf{e}_\mathrm{s}$ is the unit vector of spin polarization.
In Eq. (2.21) the terms proportional to ζ describe the phenomenon that a pure charge current generates a spin current whose direction and polarization are perpendicular to the charge current. This is usually described by the following formula containing the spin Hall angle:

$$\mathbf{j}_\mathrm{s} = \frac{\hbar}{2e}\alpha_\mathrm{SH}\mathbf{e}_\mathrm{s} \times \mathbf{j}_\mathrm{c} \tag{2.23}$$

Note that in Eqs. (2.22) and (2.23) $\mathbf{j}_\mathrm{s}$ is defined as a vector entity pointing into the direction of the spin current densities. These formulae are a perfect basis for understanding experimental approaches and can be invoked for the quantification of spin Hall effects by the spin Hall angle.

2.2.3 Experimental approach to SHE and ISHE

In Fig. 2.2a) a schematic of SHE in a conductor slab is shown, cf. [34]. According to Eq. (2.23) a charge current density $\mathbf{j}_\mathrm{c}$ which flows along the x-direction generates a spin current density $\mathbf{j}_\mathrm{s}$ along the y-axis which has a polarization pointing along the z-direction. In steady state a spin accumulation with opposite polarization builds up at the y-edges of the conductor, see Fig. 2.2b). Note that this is analogous to the ordinary Hall effect where electrons flowing along x are deflected along y due to the Lorentz-force if a magnetic field which points along the z-direction is present. The fact that spin is not a conserved quantity manifests as the spin density falls off according to Eq. (2.13) on the characteristic length scale of λ_sd. In a first approach one might assume that the dimension of the sample along the y-axis is small compared to λ_sd. This implies that the spin information established at one asymmetric scattering event is maintained throughout the conductor. The spin accumulation is only zero in the very center region of the sample, as indicated in Fig. 2.2b). Upon these circumstances Hirsch suggested in [34] to measure the spin accumulation caused by SHE via the inverse spin Hall effect (ISHE). In Fig. 2.3a) the basic idea is presented. Due to SHE in NM there is a spin accumulation at the y-edges. Along with them comes a chemical potential difference between up- and down spins on either side. NM is covered with an insulating material layer, which has small squares cut out at the edges. On top a second NM is deposited and connects the two opposing y-edges

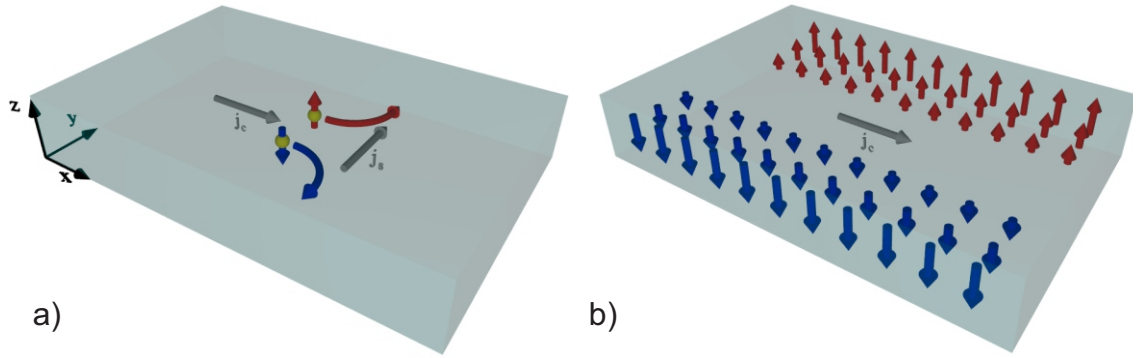

Figure 2.2: Phenomenological pictures of SHE in a conductor slab are shown. In a) the explicit transformation of a charge current $\mathbf{j}_c$ into a transverse spin current $\mathbf{j}_s$ is explained. b) shows the steady state condition. A constant $\mathbf{j}_c$ along the x-axis generates a spin accumulation (red, blue arrows) on the $\pm y$-edges of the conductor. The fact that the spin accumulation falls off exponentially from the edges to the center is also indicated.

of the NM underneath. The insulation layer forces the charge current exclusively through the lower NM. The chemical potential difference drives a pure spin current along the y-direction with its polarization along z in the upper NM. According to Eq. (2.22) a charge current density is generated along $-x$ and in steady state an electrical voltage drop is detectable in x-direction across the upper NM.
Though very elegant, detecting SHE and ISHE at the same time, as well as proving the Onsager reciprocity between the two effects [39, 90], the measurement technique proposed by Hirsch is difficult to be implemented for real samples. This has several fundamental reasons. The voltage detectable in a measurement scheme as presented in Fig. 2.3b) is proportional to the resistivity of the material involved and is naturally small for normal metals. Furthermore, the voltage is proportional to the magnitude of spin dependent scattering (α_{SH}) which builds up the spin accumulation. On the other hand a large α_{SH} entails a small λ_{sd}. As the preliminary basis for the measurement scheme of Fig. 2.3 is that the device's dimensions are smaller than λ_{sd}, one runs into problems for NM with possibly large spin Hall effect. Such materials, like Pt or Pd, usually have a λ_{sd} in the range of 1 to 20 nm, [91] and it is rather impossible to prepare such small samples. It took a decade to implement Hirsch's technique to measure SHE and ISHE. This was achieved changing the material compound from NM to a semiconductor two dimensional electron gas [92, 93].

Zhang suggested in [36] that SHE and "spin-relaxation should be studied on an equal footing". In [36] this is done using a Boltzmann approach to spin diffusion. Not going into detail about the theoretical technique, in the following its experimental implications shall be in the focus. As already mentioned above, the spin accumulation due to SHE at the edges of a conductor slab as shown in Fig. 2.2b) occurs on a length scale λ_{sd}. Therefore, in a macroscopically wide sample there

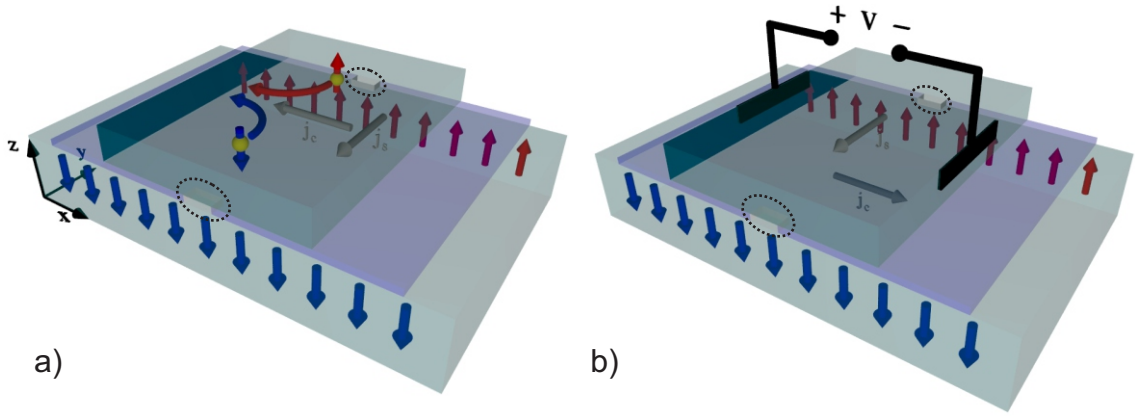

Figure 2.3: The measurement scheme as proposed in [34] is presented. In a) a method of how to probe a spin accumulation due to SHE by ISHE is described. The spin accumulation at $\pm y$-edges (red, blue arrows) in the lower NM drives a spin current $\mathbf{j}_s$ through the upper conductor. There $\mathbf{j}_s$ will be transformed into a charge current $\mathbf{j}_c$. Also indicated is that the two conductors (light and dark gray) are separated by an electrically insulating layer (purple). Contact between the two conductors only takes place at the $\pm y$-edges via two holes in the insulator (marked by the black ellipsis in the schematic). In b) the open-circuit condition is shown. $\mathbf{j}_s$ generates a voltage signal in the upper conductor due to ISHE which is proportional to the spin accumulation, established by $\mathbf{j}_c$ in the lower conductor.

is nonzero spin accumulation only at the very edges of the specimen. To this end one might think of spin layers [88]. The spin accumulation in these layers might be probed using Silsbee-Johnson spin-charge-coupling [7]. The idea is to directly attach a ferromagnetic probe to the spin accumulation [36]. For a schematic see Fig. 2.4a). A voltage difference dependent on the relative orientation of the ferromagnetic material's magnetization and the spin accumulation's polarization should be detectable [7, 10, 78]. Note that the spin accumulation's polarization could be simply reversed by reversing the charge current, see Eq. (2.23). In [36] it is estimated that one might be able to measure a voltage in the µV-range. Using the related method of nonlocal spin injection, which has been pioneered in [94] for an all-metallic mesoscopic system, finally led to the first electrical measurement of ISHE in the normal metal Al [40]. Spins are injected electrically from a ferromagnetic contact into an all-Al Hall bar structure. This leads to a spin accumulation in the Al near the FM interface. Next to the FM-contact, within the spin diffusion length of Al, the Al is shaped as a cross having two voltage probes attached to its arms. For a layout of the measurement scheme, see Fig. 2.4b). The charge current is forced to flow away from the Hall cross, but the spin density diffuses into both directions of the Hall bar and

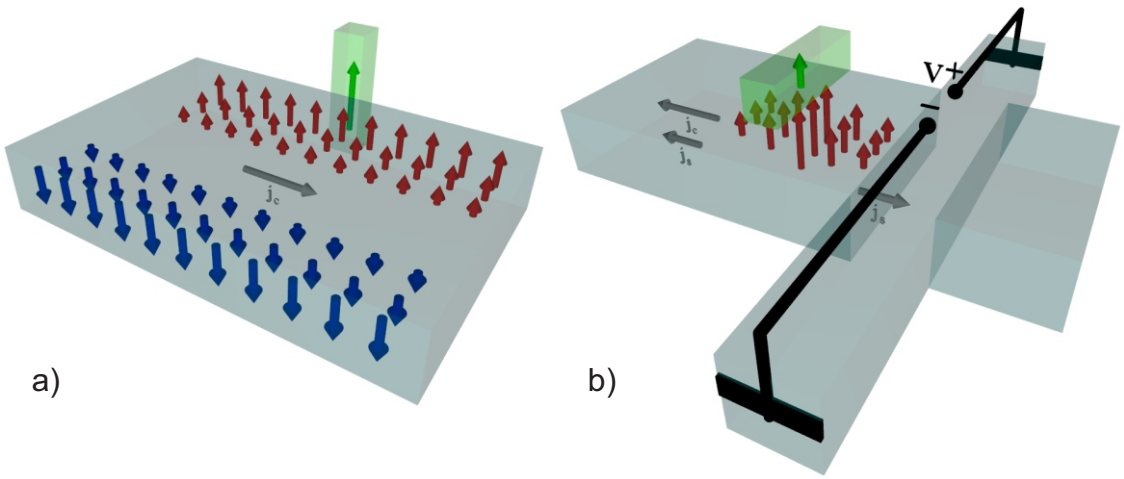

Figure 2.4: In a) the measurement scheme to study SHE proposed by Zhang in [36] is shown. A ferromagnetic probe (green) is brought into contact with the spin accumulation generated by SHE at the edges of a conductor. In b) the idea of the experiment which led to the first observation of ISHE in a NM layer, cf. [40], is shown. A spin polarized charge current is injected through a ferromagnetic contact into NM. In NM the charge current $\mathbf{j}_c$ is forced to the left in this picture. Due to its diffusive nature one is provided with a pure spin current $\mathbf{j}_s$ flowing to the left and to the right. As indicated $\mathbf{j}_s$ generates a voltage drop in the cross structure due to ISHE.

therefore a pure spin current flows towards the Al Hall cross. The magnetization of the FM points along the z-direction in this picture and the polarization of the spin current points parallel to it. The spin current's polarization, its direction and the path which connects the voltage probes build a right-handed trihedron. Hence in steady state a voltage is measurable according to Eq. (2.22) along the Al-cross. This is indicated by the voltage probes in Fig. 2.4b). Note that turning the magnetization of the FM contact into the x-y-plane results in zero voltage drop, in line with Eq. (2.22) [40]. From this measurement an α_{SH} of 0.4 - 1×10^{-4} has been extracted.

The promising results of [40] led to many electrical measurements of ISHE in materials with possibly larger α_{SH} [95–97]. Especially Pt and Au have been in the focus [96, 97]. For Pt the crux is that along with strong spin-orbit-coupling an enormously reduced spin diffusion length is expected. Actual measurements show values of $\lambda_{sd}(\mathrm{Pt}) = 1$ - 14 nm, [54, 91], for room to liquid helium temperature. Recalling the principle method introduced in [40], i.e. the Hall cross of the material to be examined has to have a distance to the spin injector smaller than λ_{sd}. Therefore, due to nanostructure fabrication limits a Hall bar consisting completely of Pt is no option. In [96] the solution for this problem has been to insert a conductor with small spin-orbit-coupling and consequential large λ_{sd}, in this case Cu was used [98],

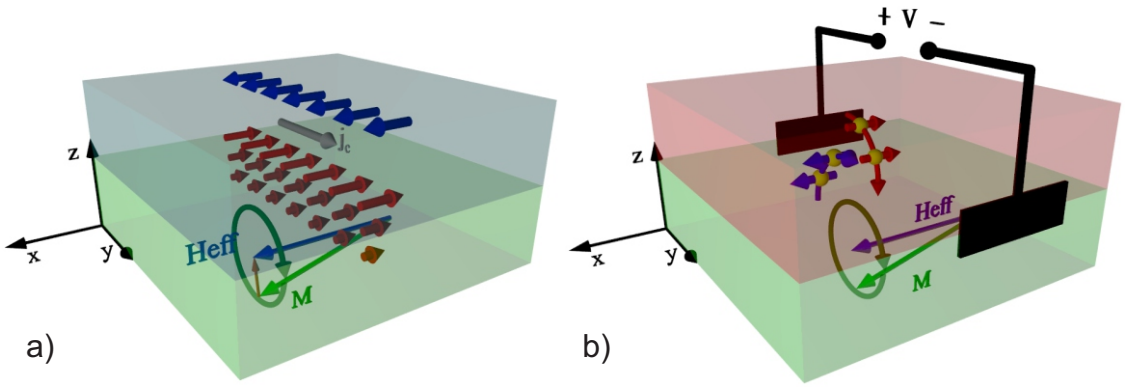

Figure 2.5: The fundamental experimental approaches for studying SHE and ISHE in FM/NM bilayers using magnetization dynamics are presented. In a) a spin accumulation is generated in the top NM layer (grey) due to SHE at the top layer's edges. This injects a spin current into the bottom FM layer (green) which exerts a spin transfer torque on the precessing magnetization and changes the damping. This experimental method is called modulation of damping (MOD) [66]. If the charge current in NM is oscillating the spin tranfer torque can drive the magnetization (ST-FMR) [100] In b) the SP-ISHE method is depicted. A precessing magnetization in the bottom FM-layer (green) injects a pure spin current into the top NM layer (red). There ISHE converts the spin current into a transverse charge current and in steady-state a voltage drop is measurable [47]

for the spin current to be transported into Pt. This led to a corresponding value of α_{SH} of 3.7×10^{-3}. As electrical shunting in Cu, which was directly attached to Pt, has been neglected in [96], $\alpha_{\mathrm{SH}}(\mathrm{Pt})$ is believed to be one to two orders of magnitude larger. A review by Liu et al [54] summarizes the debate about shunting effects that reduce the experimentally extracted spin Hall angles. In fact, a recalculation of the results of [96] yields $\alpha_{\mathrm{SH}}(\mathrm{Pt}) = 0.021 - 0.042$. This reconciles at least the order of magnitude for α_{SH} from [96] with values from alternative experimental approaches. Alternative methods involving a combination of magnetization dynamics and electrical detection guide a way out of this dilemma. To this end the basic concepts are utilization of spin transfer torque (STT) [20, 21] or spin pumping [42, 44, 99]. The latter is the one of interest for the present thesis. The first can be used to probe SHE and the second for ISHE. This offers the possibility to study the reciprocity of the two effects, an issue which still has to be proved experimentally on the very same sample.

Fig. 2.5 a) shows the principle idea of experimental techniques using STT. The basic material set is a bilayer of NM and FM. A charge current which flows along the y-axis in NM generates a spin accumulation along the z-direction which features a $\pm\mathbf{e}_x$-polarization, see Eq. (2.23). The spin accumulation at the FM/NM inter-

face diffuses into FM. Experimentally studied is the influence of the corresponding injected spin current on the magnetization's dynamics. Experimental techniques differ with respect to setting up a direct or an alternating charge current. In the first case there is a constant spin accumulation at the FM/NM interface and the transferred angular momentum, along with the spin current being injected into FM, alters the damping of a precessing magnetization due to STT. This technique has lately been called modulation of damping (MOD) [85]. MOD as a measure of SHE in Pt has been used in [66] and a value of $\alpha_{\mathrm{SH}} = 0.08$ has been determined. Setting up an alternating charge current modulates the spin accumulation at the NM/FM interface at the same frequency. If this is happening at the eigenfrequency of the magnetization, one may induce precession due to STT. Correspondingly this method is called ST-FMR. First established for magnetic tunnel junctions [101, 102], and nanomagnets [103], it has been pioneered as SHE generated ST-driving of magnetization dynamics in [100]. The concept always relies on measuring the related modulation of magnetoresistance. Specifically, in setups analogous to the one presented in [100], cf. Fig. 2.5a), it is a voltage signal measurable due to anisotropic magnetoresistance (AMR) [59]. The concept recently has been applied to Pt, Ta and W [28, 100, 104] and spin Hall angles $\alpha_{\mathrm{SH}}(\mathrm{Pt}) = 0.07$, $|\alpha_{\mathrm{SH}}(\beta\text{-Ta})| = 0.12$ to 0.15 and $|\alpha_{\mathrm{SH}}(\beta\text{-W}) = 0.30|$ have been determined. Yet, there are still unresolved issues using this technique. An elaborate discussion about microwave coupling into highly resistive materials like β-Ta and β-W is still missing. In fact, the alternative measurement technique of spin pumping connected with FMR yields $|\alpha_{\mathrm{SH}}(\beta\text{-Ta})| = 0.02$ [105] which is almost an order of magnitude smaller than the result from ST-FMR. Interestingly, [105] presents comparative results of α_{SH} of β-Ta to Pt, which shows that $\alpha_{\mathrm{SH}}(\mathrm{Pt}) > \alpha_{\mathrm{SH}}(\beta\text{-Ta})$ and the result for $\alpha_{\mathrm{SH}}(\mathrm{Pt})$ is in line with the one presented in [100]. To this end also questions about the quality and reproducibility of the examined β-Ta and β-W samples as well as of the corresponding FM/NM interfaces arise. The experimental method based on ST-FMR is of second order when probing SHE. In steady state a charge current in NM generates a spin accumulation; STT drives the magnetization; this mixes the magneto resistance with the rf-current in FM and therefore a dc-voltage is detectable.

In contrast, the technique based on spin pumping is of first order when measuring ISHE. It is the reciprocal experiment of MOD. A precessing magnetization in FM injects a pure spin current across the FM/NM interface. The generation of a charge current in NM according to Eq. (2.22) can be directly probed in an open circuit configuration as a voltage V_{ISHE}. This is schematically shown in Fig. 2.5b). The method shall be referenced as SP-ISHE in the present thesis. The idea of SP-ISHE has basically been introduced in [47] and qualitatively been refined in [48] and [106, 107]. SP-ISHE has turned out to be a powerful method to study the spin Hall angle especially for materials with large spin-orbit-coupling. Hence, in the past half decade many corresponding experiments have been conducted in order to yield quantitative results for α_{SH}. With this respect Pt is the prime example for showing the efforts, [49–53, 105, 108, 109]. However, the results for α_{SH} of Pt are varying in a range of 0.013 [50] to 0.16 [53]. In this respect two major issues are outstanding.

On the one hand spurious effects related to experimental setups are to be taken into account thoroughly as voltage generating effects like AMR can easily be confused with V_{ISHE}. On the other hand the spin diffusion length λ_{sd} of Pt plays a decisive role when calculating α_{SH} from the data. The assumption of the same λ_{sd} for Pt partly reconciles the published values for α_{SH} [54]. The remaining ambiguities might be successfully dissolved taking into account the spurious effects and a thorough study of λ_{sd}. The quest for materials featuring large spin Hall angles is therefore possible using SP-ISHE.
Moreover, spin pumping generates a spin current whose polarization oscillates at the magnetization's precession frequency. Such an ac-spin current can be uniquely probed by ISHE. The theoretical prediction is that the corresponding $V_{\mathrm{ISHE}}(t)$ is much larger than the ISHE-signal caused by the dc-component of the spin current [63, 110]. The ac-ISHE has recently been observed implementing SP-ISHE in NiFe/Pt [64, 68]. The work presented in this publication has been one of the major aspects of the present thesis, see Chapt. 9.

3 Ferromagnetic resonance and spin pumping

For the fundamental study of ISHE, see Eq. (2.22), in normal metals (NM) it is required to inject a pure spin current. A powerful method to do so is spin pumping (SP) in FM/NM bilayers [42, 44, 46]. The prerequisite for SP is to operate ferromagnetic resonance (FMR) in FM. In this chapter the needed basic principles of magnetization dynamics will be explained. We shall start off with fundamental aspects on magnetic moments and magnetization and then head on towards micromagnetism, cf. [111], and the characteristics of thin ferromagnetic films. It will always be kept track of the special properties of NiFe, the FM of choice throughout this work. Specifically, the magnetization dynamics of thin ferromagnetic films without in-plane anisotropies (NiFe) will be treated. The phenomenological Landau-Lifshitz-Gilbert (LLG) equation is introduced in order to describe the time-evolution of the magnetization, [112, 113]. Thence, the application of an oscillating external magnetic field will be incorporated into the considerations and ferromagnetic resonance (FMR) for thin magnetic films will be elaborated cf. [114–117]. At its heart this comprises the characterization of FMR via the Lorentzian-like line shapes of the involved dynamic susceptibilities [116]. Special attention is devoted to the extraction of parameters characterizing FM-films in terms of gyromagnetic ratio, effective magnetization, and dissipation of energy, viz. damping. These parameters are essential to quantify SP. Then, following the theoretical work of [41–43], SP is introduced as an analog of charge pumping through mesoscopic systems [118–121]. Spin currents transported across FM/NM interfaces are to be characterized by the spin mixing conductance. To this end the relevant concepts of circuit theory [122, 123] and non-collinear magnetoelectronics [124–126] will be reviewed. In the final part of this chapter the spin currents from SP will be characterized by their specific line shapes across FMR. This comprises both dc- and ac-components.

3.1 Magnetic moments and magnetization

The distinct feature of a ferromagnetic material is its nonzero magnetization $\mathbf{M}$, which is present even without an external magnetic field $\mathbf{H}_{\text{ext}}$ [111, 127]. $\mathbf{M}$ is the magnetic moment $\mathbf{m}$ divided by the volume V of the material. The archetype of $\mathbf{m}$ is a current loop. In this perception, which was brought forward by Ampère, the magnetic moment is defined as follows [111]:

$$\mathbf{m} = IA\mathbf{e}_{\text{n}} \tag{3.1}$$

I is the current around the circumference of an area A, whose orientation is parallel to the normal unit vector $\mathbf{e}_{\text{n}}$. Particularly, any charge whose movement is along a curved trajectory corresponds to a certain amount of magnetic moment. This is especially true for electrons orbiting an atom's nucleus. The link between magnetic moment $\mathbf{m}$ and angular momentum $\mathbf{l}$ is the so called gyromagnetic ratio γ:

$$\mathbf{m} = \gamma\mathbf{l} \tag{3.2}$$

Assume one electron orbiting an atomic nucleus. In a semiclassical approach to this problem it is used that $\mathbf{l} = \mathbf{r} \times \mathbf{p}$ and that the momentum $\mathbf{p}$ is quantized in units of $\hbar$. This yields the quantum for magnetic moments in atoms [127].

$$\mu_{\text{B}} = \frac{e\hbar}{2m_{\text{e}}} \tag{3.3}$$

μ_{B} is called Bohr magneton, e and m_{e} are the electron's charge and mass, respectively. Furthermore, the general equation

$$\mathbf{m} = -\frac{e}{2m_{\text{e}}}\mathbf{l} = \gamma\mathbf{l} \tag{3.4}$$

holds. This defines $\gamma = -\frac{e}{2m_{\text{e}}}$. The minus sign indicates that the magnetic moment and the respective angular momentum are antiparallel due to the electron's negative charge. The semiclassical viewpoint presented here provides an intuitive starting point for a correct quantum mechanical description of the magnetic moment. In quantum mechanics physical observables are represented by Hermitian operators which are defined analogously to their classical counterparts [128]. Experimentally it is the operators' eigenvalues which are measured. After one measurement process the system's state, which is described by a vector in Hilbert space, changes or collapses into an eigenstate corresponding to the measured physical observable. This implies that two physical entities can only be measured at the same time if they have joint eigenstates or equivalently if the corresponding Hermitian operators commute. As a matter of fact, the only information one can gather simultaneously from a measurement of angular momentum of an electron orbiting an atomic nucleus is its magnitude and its projection on one coordinate axis, which is usually referred to as the z-axis. The corresponding operators are $\hat{\mathbf{l}}^{\mathbf{2}}$ and $\hat{l}_z$ and their eigenstates are

denoted as $|lm\rangle$. The hat indicates that one deals with an operator and the eigenstate is represented in Dirac-notation. The eigenvalues are given by the following two equations, [127]:

$$\hat{\mathbf{l}}^{\mathbf{2}} = \hbar^2 l(l+1)\,|lm\rangle\,, \quad l = 0, 1, 2, ... \tag{3.5}$$

$$\hat{l}_z = \hbar m_\mathrm{l}\,|lm\rangle\,, \qquad m_\mathrm{l} = -l, ..., l \tag{3.6}$$

l is the angular momentum and m_l the so-called magnetic quantum number. m_l has $2l+1$ possible values ranging from $-l$ to $+l$ in steps of 1. Using Eq. (3.4), the eigenvalues of the magnetic moment operator $\hat{m}_z$ due to orbital electronic motion are given by:

$$m_z = \gamma\hbar m_\mathrm{l} = -\mu_\mathrm{B} m_\mathrm{l} \tag{3.7}$$

Yet, for the magnetic moment of electrons this is only half of the story. There is a second contribution for which there is no classical analog. It is of pure quantum mechanical nature; the electron's spin. With many respects, yet not with all, spin can be treated analogously to angular momentum. The corresponding operators are $\hat{\mathbf{s}}^{\mathbf{2}}$ and $\hat{s}_z$. For an electron the magnitude of spin is given by $s = \frac{1}{2}$ and therefore $m_\mathrm{s} = \pm\frac{1}{2}$. For the magnetic moment assigned with spin the following relation holds:

$$m_z = \gamma_\mathrm{s}\hbar m_\mathrm{s} = -g\mu_\mathrm{B} m_\mathrm{s} \tag{3.8}$$

It differs from Eq. (3.8) with respect to $\gamma_\mathrm{s} = g\gamma$. The so called g-factor accounts for the fact that spin has a different efficiency in creating magnetic moment as orbital angular momentum. Assuming $g = 2$, one realizes that both orbital motion and spin generated magnetic moment are quantized in units of μ_B.
Accounting for both orbital angular momentum and spin the magnetic moment operator $\hat{\mathbf{m}}$ for a single electron is given by:

$$\hat{\mathbf{m}} = \gamma(\hat{\mathbf{l}} + 2\hat{\mathbf{s}}) = g_\mathrm{j}\gamma\hat{\mathbf{j}} \tag{3.9}$$

$\hat{\mathbf{j}} = \hat{\mathbf{l}} + \hat{\mathbf{s}}$ is the overall angular momentum operator and $g_\mathrm{j}\gamma = \gamma_\mathrm{j}$ is the relevant proportionality factor linking magnetic moment and overall angular momentum.
So far only a single electron has been considered. A conceptual transfer to a multi-electron system may be performed by introducing overall operators $\hat{\mathbf{l}} \to \hat{\mathbf{L}}$, $\hat{\mathbf{s}} \to \hat{\mathbf{S}}$, $\hat{\mathbf{j}} \to \hat{\mathbf{J}}$. From this the so-called Landé g-factor g_J is given by [111]:

$$g_\mathrm{J} = \frac{3}{2} + \frac{S(S+1) - L(L+1)}{2J(J+1)} \tag{3.10}$$

S, L and $J = L + S$ can be estimated applying Hund's rules filling the elemental electron orbitals. Yet, being exact for single atoms and a good approximation for solid state materials with strongly localized valence electron orbitals viz. $4f$, these

rules ultimately fail for $3d$-transition-metals. This is especially true for the $3d$-ferromagnets Fe, Co and Ni. The orbital angular momentum is quenched in such materials due to the strong Coulomb interaction of d-orbitals with their environment and the total angular momentum per atom is well approximated by S plus taking into account electron transfer from the s- into the much narrower d-band at the Fermi surface. The corresponding large density of states $D(E_\mathrm{F})$ near the Fermi level results in an energy gain for the d-band when splitting into $d^\uparrow$- and $d^\downarrow$-band, [111]. E.g. for Fe crystallized in bcc-structure the valence electrons per atom are given by $3d^{7.4}4s^{0.6}$, the spin-split configuration is $3d^{\uparrow 4.8}3d^{\downarrow 2.6}$ and the magnetic moment per atom is given by $m_{\text{atom, Fe}} = 2.2\mu_\mathrm{B}$. For Co and Ni the atomic moments per atom are given by $m_{\text{atom, Co}} = 1.7\mu_\mathrm{B}$ and $m_{\text{atom, Ni}} = 0.6\mu_\mathrm{B}$ respectively, see [111]. These values can readily be used to determine the magnetic moment per atom for NiFe. Weighted averaging accounts for different compositions. The result for the most common composition $\mathrm{Ni_{80}Fe_{20}}$ is $m_{\text{atom, NiFe}} = 0.92\mu_\mathrm{B}$. The expected values for the saturation magnetization M_S of a material can be calculated by multiplying the number of atoms per unit volume with the magnetic moment per atom. Thus, $\mu_0 M_{\mathrm{S,NiFe}} = 0.96\,\mathrm{T}$.
The interaction between a magnetic moment $\mathbf{m}$ and a magnetic flux density $\mathbf{B}$ is classically given by, cf. [111, 127]:

$$\boldsymbol{\Gamma} = \mathbf{m} \times \mathbf{B} \tag{3.11}$$

$$|\boldsymbol{\Gamma}| = |\mathbf{m} \times \mathbf{B}| = mB\sin(\Phi) \tag{3.12}$$

$$E = \int_0^\Phi \mathrm{d}\Phi' mB\sin(\Phi') = -\mathbf{mB} \tag{3.13}$$

Γ is the torque acting on $\mathbf{m}$. The stored energy is given by integrating Γ with respect to the angle Φ between $\mathbf{m}$ and $\mathbf{B}$, see Eq. (3.13). Quantum mechanically the interaction is described by the so called Zeeman-Hamiltonian:

$$\hat{H}_\mathrm{Zee} = -\gamma(\hat{\mathbf{l}} + 2\hat{\mathbf{s}})\mathbf{B} \tag{3.14}$$

The definition of the magnetic moment as a consequence of angular momentum, see Eq. (3.2) together with the fact $\Gamma = \mathrm{d}\mathbf{l}/\mathrm{d}t$ leads to the following equation of motion for $\mathbf{m}$:

$$\frac{\mathrm{d}\mathbf{m}}{\mathrm{d}t} = \gamma \mathbf{m} \times \mathbf{B} \tag{3.15}$$

In order to transfer this result to the dynamics of a magnetization $\mathbf{M}(\mathbf{r}, t)$ one has to think about the consequence of inserting magnetized media into $\mathbf{B}$. To this end the auxiliary field $\mathbf{H}$ is introduced [111, 127]. This leads to two fundamentally different equations describing $\mathbf{B}$ in free space and in a magnetized medium respectively:

$$\mathbf{B} = \mu_0 \mathbf{H} \tag{3.16}$$

$$\mathbf{B} = \mu_0(\mathbf{H} + \mathbf{M}) \tag{3.17}$$

$\mathbf{H}$ is also called magnetizing force [111]. Consequently the equation of motion of $\mathbf{M}$ is given by an appropriate reformulation of Eq. (3.15):

$$\frac{\mathrm{d}\mathbf{M}}{\mathrm{d}t} = \gamma\mu_0\mathbf{M} \times \mathbf{H}_{\text{eff}} \tag{3.18}$$

$\mathbf{H}_{\text{eff}}$ is the so called effective magnetic field. It summarizes all possible field terms interacting with $\mathbf{M}$ inside a material. In static equilibrium $\mathrm{d}\mathbf{M}/\mathrm{d}t = 0$ and $\mathbf{M}$ is parallel to $\mathbf{H}_{\text{eff}}$. The possible different origins of $\mathbf{H}_{\text{eff}}$ will be discussed in the following section. It is one of the main objects in micromagnetic considerations and is essential in terms of describing magnetization dynamics in specific materials.

3.2 Micromagnetism and thin ferromagnetic films

The spatial dependence of a material's magnetization $\mathbf{M}(\mathbf{r})$ is described by minimization of the Helmholtz or Gibbs free energy per unit volume. The corresponding total differentials at constant temperature are given by [111].

$$\mathrm{d}f = \mu_0\mathbf{H}_{\text{eff}}\mathrm{d}\mathbf{M} \tag{3.19}$$

$$\mathrm{d}g = -\mu_0\mathbf{M}\mathrm{d}\mathbf{H}_{\text{eff}} \tag{3.20}$$

In the following the focus will be on the Helmholtz free energy, Eq. (3.19). This results in $\mathbf{H}_{\text{eff}}$ to be given by, [129]:

$$-\frac{1}{\mu_0}\nabla_{\mathbf{M}} f = \mathbf{H}_{\text{eff}} \tag{3.21}$$

$\nabla_{\mathbf{M}} f$ is the gradient of the free energy with respect to the magnetization. In principle, energy terms and corresponding effective magnetic fields of different origin are distinguishable [111, 129].

$$f = f_{\text{xc}} + f_{\text{ani}} + f_{\text{stress}} + f_{\text{dem}} + f_{\text{ext}} \tag{3.22}$$

$$\mathbf{H}_{\text{eff}} = \mathbf{H}_{\text{xc}} + \mathbf{H}_{\text{ani}} + \mathbf{H}_{\text{stress}} + \mathbf{H}_{\text{dem}} + \mathbf{H}_{\text{ext}} \tag{3.23}$$

Note that this approach is commonly used to describe domain formation and hysteresis characteristics of ferromagnetic materials, [111, 127]. $\mathbf{H}_{\text{stress}}$, which would be an internal effective field appearing while FM is deformed, is inapplicable for any considerations presented in this thesis and is therefore neglected in the following. $\mathbf{H}_{\text{xc}}$ and $\mathbf{H}_{\text{ani}}$ are effective magnetic fields accounting for minimization of Coulomb energy due to exchange interaction and crystal field, respectively. The first one enshrines the physical origin of a stable ferromagnetic state and therefore it prefers a magnetization pointing homogeneously into one direction. Note that $\mathbf{H}_{\text{stress}}$, $\mathbf{H}_{\text{xc}}$ and $\mathbf{H}_{\text{ani}}$ are all of electrostatic nature. In contrast $\mathbf{H}_{\text{dem}}$ and $\mathbf{H}_{\text{ext}}$ are dipolar fields. There is a certain self energy of a ferromagnetic material in its own dipolar field due to its nonzero magnetization. This leads to the so-called demagnetizing field $\mathbf{H}_{\text{dem}}$

and the physical effect it entails is referenced to as shape anisotropy. $\mathbf{H}_{\text{ext}}$ sums up any external magnetic field.
In the present work, the discussion shall be restricted to a uniform magnetization. The theoretical basis of implementing effective magnetic fields with respect to ferromagnetic resonance has been elaborated in [129]. The following is devoted to an estimation and characterization of the relevant effective field terms under circumstances of magnetization dynamics, see Eq. (3.18), in thin ferromagnetic films. Note that within the frame of the present thesis only NiFe-films with a thickness of approximately 10 nm and lateral dimensions which are 3 to 4 orders of magnitude larger will be studied.
The free energy density due to exchange can be defined as [111]:

$$f_{\text{xc}} = \frac{A_{\text{xc}}}{M_{\text{s}}^2}\left((\nabla M_x)^2 + (\nabla M_y)^2 + (\nabla M_z)^2\right) \tag{3.24}$$

The constant A_{xc} is the amplitude factor of the free energy density associated with exchange. It is usually called exchange stiffness [111]. For a ferromagnetic material A_{xc} is positive and f_{xc} is minimized under the circumstances of a homogeneously parallel $\mathbf{M}(\mathbf{r})$. In fact, this defines a certain length scale λ_{xc} which is the shortest length scale over which the magnetization can be twisted in order to minimize the free energy associated with the demagnetizing field [111].
$\mathbf{H}_{\text{dem}}$ is a consequence of Maxwell's equation about the divergence of the magnetic flux density $\nabla \cdot \mathbf{B} = 0$. Due to the definition $\mathbf{B} = \mu_0(\mathbf{H} + \mathbf{M})$ inside a magnetic material the following equation holds, [111]:

$$\nabla \cdot \mathbf{H} = -\nabla \cdot \mathbf{M} \tag{3.25}$$

This illustrates that a nonzero divergence of the magnetization corresponds to magnetic charges at the boundary of the ferromagnetic material. These charges generate an internal magnetic field ($\mathbf{H}_{\text{dem}}$) which points into the antiparallel direction with respect to $\mathbf{M}$. The usual definition of the demagnetizing field is:

$$\mathbf{H}_{\text{dem}} = -N\mathbf{M} \tag{3.26}$$

N is the so called demagnetizing tensor whose entries are determined by the geometric shape of the magnetic body. For ferromagnetic materials with an ellipsoidal shape and a magnetization pointing along one of the principle axes (x, y, z), N has diagonal form:

$$N = \begin{pmatrix} N_x & 0 & 0 \\ 0 & N_y & 0 \\ 0 & 0 & N_z \end{pmatrix} \tag{3.27}$$

N_x, N_y, N_z are the so called demagnetizing factors which are interdependent due to the general property $N_x + N_y + N_z = 1$. They are commonly used to estimate the internal fields even for non-ellipsoidal magnetized media [111]. For a thin ferromagnetic film with infinite elongation in the x-y-plane $N_x = N_y = 0$ and $N_z = 1$.

The free energy density of a magnetized body in its self generated field is, as from Eq. (3.13), given by [111]:

$$f_{\mathrm{dem}} = -\frac{1}{2}\mu_0 \mathbf{H}_{\mathrm{dem}}\mathbf{M} \tag{3.28}$$

The factor $\frac{1}{2}$ avoids double counting. For a thin ferromagnetic film $N_z = 1$ and Eq. (3.28) transforms into:

$$f_{\mathrm{dem}} = \frac{1}{2}\mu_0 M_z^2 = \frac{1}{2}\mu_0 M_s^2 \tag{3.29}$$

The last step holds if the magnetization is pointing into z-direction, out-of-plane. f_{dem} is zero for a magnetization which features only in-plane components. Finally, one can define the exchange length as, [111]:

$$\lambda_{\mathrm{xc}} = \sqrt{\frac{A_{\mathrm{xc}}}{\mu_0 M_{\mathrm{S}}^2}} \tag{3.30}$$

For NiFe typical values for exchange stiffness A_{xc} and saturation magnetization $\mu_0 M_{\mathrm{S}}$ are $10\,\mathrm{pJ\,m^{-1}}$ and $0.96\,\mathrm{T}$, respectively, cf. [111]. This yields $\lambda_{\mathrm{xc}} = 3.7\,\mathrm{nm}$. Magnetic films with a thickness below λ_{xc} are referred to as ultrathin, [130, 131]. Films with a thickness larger but still of the order of the exchange length are called thin. A classification can be established by studying the dispersion relation of perpendicular standing spin waves (PSSW), [132, 133]. We shall come back to this point when characterizing thin films using FMR in the next section of this chapter.
$\mathbf{H}_{\mathrm{ani}}$ accounts for the fact that there might be certain crystallographic axes along which f_{ani} is minimized. Of course $\mathbf{H}_{\mathrm{ani}}$ only plays a decisive role if there are defined crystallographic axes throughout the volume of interest. Since NiFe-alloys are polycrystalline $\mathbf{H}_{\mathrm{ani}}$ can usually be neglected, especially for bulk volumes. Regarding thin films in general $\mathbf{H}_{\mathrm{ani}}$ for in-plane magnetizations can be disregarded for exactly these reasons. However, for out-of-plane magnetizations a certain uniaxial anisotropy might be present. This is especially true if the film thickness is comparable to the size of the NiFe-crystallites, which can easily have a diameter of 5 nm using sputtering techniques for growth [134]. To account for this effect the following energy density is defined [116, 131, 135]:

$$f_{\mathrm{ani}} = K_{\perp}\left(\frac{M_z}{M_{\mathrm{s}}}\right)^2 \tag{3.31}$$

the index z denotes the out-of-plane direction associated with the ferromagnetic film.
Finally there is the free energy density associated with $\mathbf{H}_{\mathrm{ext}}$. Due to its dipole nature it is analogously defined as from Eq. (3.28):

$$f_{\mathrm{ext}} = -\mu_0 \mathbf{H}_{\mathrm{ext}}\mathbf{M} \tag{3.32}$$

Summarizing the main results of this section, only very few free energy terms are needed in order to describe $\mathbf{M}(\mathbf{r})$ for a thin homogeneously magnetized NiFe film. Only Eqs. (3.29), (3.31), and (3.32) have to be taken into account, which yields

$$f = \frac{1}{2}\mu_0 M_z^2 - \mu_0 K_\perp \left(\frac{M_z}{M_S}\right)^2 - \mu_0 \mathbf{H}_{\text{ext}}\mathbf{M} \tag{3.33}$$

For adiabatic perturbations of the magnetization, micromagnetic energy terms are always valid and are commonly used in order to describe $\mathbf{M}(\mathbf{r}, t)$. This is especially true for an oscillating magnetic driving field $\mathbf{h}(t)$ in the GHz-regime which forces $\mathbf{M}(\mathbf{r})$ to precess about its static equilibrium axis as is done in an FMR-experiment.

3.3 Ferromagnetic resonance

Ferromagnetic resonance (FMR) is an essential method to determine the properties of ferromagnetic materials (FM). Ever since the method has been introduced by Griffiths in 1946 [136] and elaborated theoretically by Kittel shortly afterwards [137, 138], multiple sorts of materials, with different magnetic order, structural properties, etc. have been examined. Outstanding in this respect are the studies of ultrathin ferromagnetic Fe, Co and Ni films in terms of the development of magnetocrystalline anisotropies, exchange coupling in multilayers and magnetic moments [116, 130, 139–142]. However, in this work FMR is rather used as a tool to facilitate spin pumping. Therefore, the discussion here will be kept as fundamental as possible and specialized to thin films whose internal magnetic fields can be derived from Eq. (3.33). Notwithstanding, connecting points to more complicated situations will be indicated.
In every FMR-experiment the ferromagnetic material is located by some means in an oscillating excitation field $\mathbf{h}(t)$ which drives the magnetization. As frequencies are typically in the GHz-regime the first length scale to be important is the skin depth δ_s, which is in the range of several hundred nm, [116]. To this end, the magnetization of a ferromagnetic film below 100 nm is driven homogeneously and the so called macrospin approximation can be used. In this picture the dynamics of the magnetization can be viewed analogously to a moving classical vector. The exchange length λ_{xc} sets another essential length scale. As from the defining equation Eq. (3.30) a magnetization might still be unstable in terms of the generation of spin waves. However, studies of 40 nm thick NiFe layers using Brioullin-Light-Scattering (BLS) presented in [117, 133, 143] show that the PSSW-modes are well separated energetically from any in-plane mode. Furthermore, if there is no considerable confinement in the lateral direction an FMR-experiment will only probe the fundamental mode with the wave vector $k = 0$. The NiFe layers in this work have a thickness of approximately 10 nm and therefore classcial vector treatment of the magnetization $\mathbf{M}$ is always justified and will be used henceforth. Note that this approach is usually used to derive the main physical aspects of ferromagnetic

resonance, see e.g. [114–117].
The time evolution of $\mathbf{M}$ is described by the Landau-Lifshitz-Gilbert (LLG) equation, which in SI units is given by:

$$\frac{\mathrm{d}\mathbf{M}}{dt} = -\gamma\mu_0(\mathbf{M}\times\mathbf{H}_{\mathrm{eff}}) + \frac{\alpha}{M_{\mathrm{S}}}\left(\mathbf{M}\times d\mathbf{M}/dt\right) \tag{3.34}$$

If $\mathbf{M}$ and $\mathbf{H}_{\mathrm{eff}}$ only consist of static components $\mathbf{M}_{\mathrm{stat}}$ and $\mathbf{H}_{\mathrm{eff,stat}}$, and therefore $\mathrm{d}\mathbf{M}/dt = 0$, the following relation holds:

$$\mathbf{M}\times\mathbf{H}_{\mathrm{eff}} = 0 \tag{3.35}$$

This is the so called static equilibrium condition [115]. It states that no static torque is active upon $\mathbf{M}$ after inserting $\mathbf{H}_{\mathrm{eff}}$ [131]. When $\mathbf{M}$ acquires a vector component perpendicular to $\mathbf{H}_{\mathrm{eff}}$, e.g. by means of a magnetic field pulse $\mathbf{h}$, $\mathbf{M}$ starts to precess around $\mathbf{H}_{\mathrm{eff}}$. This is accounted for by the first term on the right hand side of Eq. (3.34), which is equal to Eq. (3.18) except that γ is now positive and the minus sign due to the negative charge of electrons is explicitly noted.

Due to interaction of the magnetization with the magnetic material such as eddy currents, magnon-phonon-coupling, spin-orbit-coupling, defects and two-magnon scattering $\mathbf{M}$ will relax back into its initial equilibrium position aligned with $\mathbf{H}_{\mathrm{eff}}$. For a detailed treatment of the scattering mechanisms contributing to damping of the magnetization, see [131] and [135] as well as references therein. The magnitude of $\mathbf{M}$ is assumed to be conserved and the relaxation trajectory is confined to a spiral on a sphere of radius $|\mathbf{M}|$. The strength of the involved relaxation processes is summed up in the Gilbert-damping parameter α. The precession frequency f_0 is the eigenfrequency of the magnetization. It is an inherent property of the magnetization and is determined by the effective internal magnetic fields $\mathbf{H}_{\mathrm{eff}}$. Associated with f_0 is a distinct time-scale on which $\mathbf{M}$ relaxes back into the equilibrium position aligned with $\mathbf{H}_{\mathrm{eff}}$, fulfilling Eq. (3.35).
The modus operandi for FMR experiments is to apply an external magnetic field $\mathbf{H}_{\mathrm{ext}}$, which is a sum of static $\mathbf{H}$ and oscillatory $\mathbf{h}(t)$ components. If $\mathbf{h}(t)$ has a component which is perpendicular to $\mathbf{M}$, precession at the frequency f of $\mathbf{h}(t)$ will be facilitated. One has two possibilities to fulfill the resonance condition for the precessing magnetization. The first is to apply a constant static external field $\mathbf{H}$ and to vary the frequency f of $\mathbf{h}(\mathbf{t})$. When f coincides with the eigenfrequency f_0 of the magnetization, the absorption $\mathscr{A}(f)$ of the microwave field has a maximum. Another way to operate FMR is to retain f and vary f_0 of $\mathbf{M}$. This is usually done by changing the static effective field $\mathbf{H}_{\mathrm{eff,s}}$ via sweeping $\mathbf{H}$. If $f = f_0$ or experimentally $H = H_0$, $\mathscr{A}$ will be maximized. The line shape $\mathscr{A}(H)$ can be analyzed with respect to resonance position and line width and magnetic properties can be extracted. For the following considerations it is assumed that $|\mathbf{h}(t)| << |\mathbf{H}|$ and that $|\mathbf{m}(t)| << |\mathbf{M}_{\mathrm{stat}}|$, where $\mathbf{M}_{\mathrm{stat}}$ denotes the static component of $\mathbf{M}(t)$.
For the theoretical treatment of magnetization dynamics in the circumstances of small cone angle precession, as assumed here, it is most effective to use the coordinate system (x', y', z'), see Fig. 3.1a), where x' points along $\mathbf{M}_{\mathrm{stat}} = M_{\mathrm{S}}\mathbf{e}_{x'}$. In this

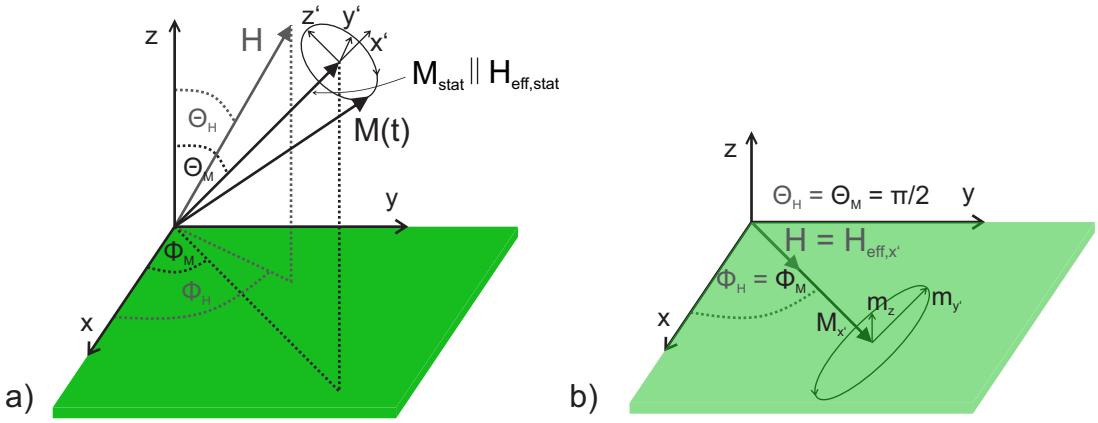

Figure 3.1: Static external magnetic field $\mathbf{H}$, static effective magnetic field $\mathbf{H}_{\text{eff,stat}}$ and precessing magnetization $\mathbf{M}(t)$ are depicted. In green a ferromagnetic film in the x-y-plane is shown, z is the respective out-of-plane direction. Polar angles ϕ_{H} and ϕ_{M} define the in-plane component of $\mathbf{H}$ and $\mathbf{H}_{\text{eff,stat}}$, respectively. The azimuthal angles Θ_{H} and Θ_{M} describe the respective out-of-plane components. The static component of $\mathbf{M}(t)$ is parallel to $\mathbf{H}_{\text{eff,stat}}$ and the first order dynamic components of $\mathbf{M}(t)$ are confined to the y'-z'-plane. Together with x', which points parallel to $\mathbf{H}_{\text{eff,stat}} = H_{\text{eff}}\mathbf{e}_{\text{x'}}$, y' and z' constitute a right-handed coordinate system. The transformation of (x, y, z) into (x', y', z') is explained in the text. In a) the general case of $\mathbf{H}$, $\mathbf{H}_{\text{eff}}\mathbf{e}_{\text{x'}}$ and $\mathbf{M}(t)$ having both in-plane and out-of-plane components is shown. In b) the special case of an in-plane static magnetization $M\mathbf{e}_{\text{x'}}$ due to an in-plane $\mathbf{H}$ is displayed, $\mathbf{e}_{\text{z'}} = \mathbf{e}_{\text{z}}$ and $\Theta_{\text{M}} = \Theta_{\text{H}} = \pi/2$. The circumstances are further simplified by $\mathbf{H}$ being parallel to $H_{\text{eff}}\mathbf{e}_{\text{x'}}$, no in-plane anisotropies, $\phi_{\text{H}} = \phi_{\text{M}}$. Furthermore the precession ellipsis with its dynamic magnetization components $m_{y'}$ and m_z is shown.

picture the dynamics is confined to the y'-z' plane and the following ansatz for the precessing magnetization can be made:

$$\begin{pmatrix} M_{x'} \\ m_{y'} \\ m_{z'} \end{pmatrix} = \frac{1}{2} \begin{pmatrix} 2M_{\text{S}} \\ m_{y'} \exp(i\omega t) + m_{y'}^{*} \exp(-i\omega t) \\ m_{z'} \exp(i\omega t) + m_{z'}^{*} \exp(-i\omega t) \end{pmatrix} = \begin{pmatrix} M_{\text{S}} \\ \Re(m_{y'} \exp(i\omega t)) \\ \Re(m_{z'} \exp(i\omega t)) \end{pmatrix} \tag{3.36}$$

The coordinate system (x, y, z) is the laboratory frame. It describes the absolute vector $\mathbf{M}(t)$ relative to the ferromagnetic film, which is displayed in green color in Fig. 3.1. The film lies in the x-y plane and z defines its out-of-plane direction. It is useful to parametrize $\mathbf{M}_{\text{stat}}$ with respect to it modulus $|\mathbf{M}_{\text{stat}}|$ as well as to the azimuthal and polar angles Θ_{M} and Φ_{M}, see Fig. 3.1a). This facilitates the transformation of (x, y, z) into (x', y', z') effectively by two successive rotations, established

by the two following rotation matrices, [89]:

$$\begin{pmatrix} \cos\phi_{\mathrm{M}} & \sin\phi_{\mathrm{M}} & 0 \\ -\sin\phi_{\mathrm{M}} & \cos\phi_{\mathrm{M}} & 0 \\ 0 & 0 & 1 \end{pmatrix}, \begin{pmatrix} \sin\Theta_{\mathrm{M}} & 0 & \cos\Theta_{\mathrm{M}} \\ 0 & 1 & 0 \\ -\cos\Theta_{\mathrm{M}} & 0 & \sin\Theta_{\mathrm{M}} \end{pmatrix} \tag{3.37}$$

Transposing the product of the two matrices yields the following relation connecting (M_x, M_y, M_z) to $(M_{x'}, m_{y'}, m_{z'})$:

$$\begin{pmatrix} M_x \\ M_y \\ M_z \end{pmatrix} = \begin{pmatrix} \sin\Theta_{\mathrm{M}}\cos\Phi_{\mathrm{M}} & -\sin\Phi_{\mathrm{M}} & -\cos\Theta_{\mathrm{M}}\cos\Phi_M \\ \sin\Theta_{\mathrm{M}}\sin\Phi_{\mathrm{M}} & \cos\Phi_{\mathrm{M}} & -\cos\Theta_{\mathrm{M}}\sin\Phi_{\mathrm{M}} \\ \cos\Theta_{\mathrm{M}} & 0 & \sin\Theta_{\mathrm{M}} \end{pmatrix} \begin{pmatrix} M_{x'} \\ m_{y'} \\ m_{z'} \end{pmatrix} \tag{3.38}$$

In order to solve the LLG, Eq. (3.34), in the coordinate system (x', y', z') the matrix displayed in Eq. (3.38) has to be applied to all relevant quantities entering $\mathbf{H}_{\mathrm{eff}}$. For a thin NiFe film $\mathbf{H}_{\mathrm{eff}}$ is given by the gradient with respect to $\mathbf{M}$ of Eq. (3.33). Transformation of the quantities entering Eq. (3.33), which describes the free energy of a thin ferromagnetic film without in-plane anisotropies, from (x, y, z) into (x', y', z') yields:

$$\frac{f}{\mu_0} = (M_{x'}\cos\Theta_{\mathrm{M}} + M_{z'}\sin\Theta_{\mathrm{M}})^2 \left(\frac{1}{2} - \frac{K_\perp}{M_{\mathrm{S}}^2}\right) + \mathbf{H}_{\mathrm{ext}}\mathbf{M} \tag{3.39}$$

Furthermore, the representation of the applied external field $\mathbf{H}_{\mathrm{ext}} = \mathbf{H} + \mathbf{h}(t)$ in (x', y', z') has to be found. In Fig. 3.1a) the parametrization of the static external field component $\mathbf{H}$ with respect to spherical coordinates $(|\mathbf{H}|, \Theta_{\mathrm{H}}, \Phi_{\mathrm{H}})$ is shown. Application of the transposed of the transformation matrix (Eq. (3.38)) yields:

$$\begin{pmatrix} H_{x'} \\ H_{y'} \\ H_{z'} \end{pmatrix} = |\mathbf{H}| \begin{pmatrix} \sin\Theta_{\mathrm{M}}\sin\Theta_{\mathrm{H}}\cos(\Phi_{\mathrm{M}} - \Phi_{\mathrm{H}}) + \cos\Theta_{\mathrm{M}}\cos\Theta_{\mathrm{H}} \\ \sin\Theta_{\mathrm{H}}\sin(\Phi_{\mathrm{H}} - \Phi_{\mathrm{M}}) \\ \sin\Theta_{\mathrm{M}}\cos\Theta_{\mathrm{H}} - \cos\Theta_{\mathrm{M}}\sin\Theta_{\mathrm{H}}\cos(\Phi_{\mathrm{M}} - \Phi_{\mathrm{H}}) \end{pmatrix} \tag{3.40}$$

For the special case of an in-plane static field $\mathbf{H}$ and absence of any in-plane anisotropies, as is the case for the used NiFe, the condition $\Phi_{\mathrm{H}} = \Phi_{\mathrm{M}}$ holds. As depicted in Fig. 3.1b), in this situation the static component of $\mathbf{M}$ is parallel to $\mathbf{H}$ and $m_{y'}$ and m_z are the applicable dynamic magnetization components. The fact that $z' = z$ shall be assumed henceforth.
For the external field the following ansatz is made:

$$\mathbf{H}_{\mathrm{ext}} = \frac{1}{2}\begin{pmatrix} 2H \\ h_{y'}\exp(i\omega t) + h_{y'}^*\exp(-i\omega t) \\ h_z\exp(i\omega t) + h_z^*\exp(-i\omega t) \end{pmatrix} = \begin{pmatrix} H \\ \Re(h_{y'}\exp(i\omega t)) \\ \Re(h_z\exp(i\omega t)) \end{pmatrix} \tag{3.41}$$

Using this in addition to the application of the gradient with respect to $\mathbf{M}$ to Eq. (3.39) results in the following effective field for a thin film without any in-plane

anisotropies and an external field as well as a saturated magnetization in-plane:

$$H_{\text{eff},x'} = H \tag{3.42}$$

$$H_{\text{eff},y'} = \frac{1}{2}\left(h_{y'}\exp(i\omega t) + h_{y'}^{*}\exp(-i\omega t)\right) \tag{3.43}$$

$$\begin{aligned} H_{\text{eff},z} &= \left(\frac{2K_{\perp}}{M_S^2} - 1\right) m_z + \frac{1}{2}\left(h_z\exp(i\omega t) + h_z^{*}\exp(-i\omega t)\right) \\ &= -\frac{M_{\text{eff}}}{M_{\text{S}}} m_z + \frac{1}{2}\left(h_z\exp(i\omega t) + h_z^{*}\exp(-i\omega t)\right) \end{aligned} \tag{3.44}$$

The abbreviation $M_{\text{eff}} = M_{\text{S}} - \frac{2K_{\perp}}{M_S}$ sums up the two additive effective field terms proportional to m_z. Inserting Eq. (3.36) and Eqs. (3.42) to (3.44) into the LLG (Eq. (3.34)), keeping only terms linear in $h_{y'}$, h_z, $m_{y'}$, m_z and ω, yields a system of two linear equations which describes the magnetization dynamics:

$$m_{y'} = \frac{i\gamma\mu_0}{\omega}\left(\frac{B_{\text{eff}}}{\mu_0} m_z - M_{\text{S}} h_z\right) - \alpha m_z \tag{3.45}$$

$$m_z = -\frac{i\gamma\mu_0}{\omega}(H m_{y'} - M_{\text{S}} h_{y'}) + \alpha m_{y'} \tag{3.46}$$

Here $B_{\text{eff}} = \mu_0(H + M_{\text{eff}})$ has been introduced. Mutually inserting Eqs. (3.45) and (3.46) into one another leads to the following two relations dependent on the excitation field components $h_{y'}$ and h_z:

$$m_{y'} = \frac{-M_{\text{S}}\left(\frac{B_{\text{eff}}}{\mu_0} + \frac{i\alpha\omega}{\gamma\mu_0}\right) h_{y'} - \frac{i\omega}{\gamma\mu_0} M_{\text{S}} h_z}{D} \tag{3.47}$$

$$m_z = \frac{-M_{\text{S}}\left(H + \frac{i\alpha\omega}{\gamma\mu_0}\right) h_z + \frac{i\omega}{\gamma\mu_0} M_{\text{S}} h_{y'}}{D} \tag{3.48}$$

Here the denominator is abbreviated by $D = \left(\frac{\omega}{\gamma\mu_0}\right)^2 - \left(\frac{B_{\text{eff}}}{\mu_0} + \frac{i\alpha\omega}{\gamma\mu_0}\right)\left(H + \frac{i\alpha\omega}{\gamma\mu_0}\right)$. From Eqs. (3.47) and (3.48) one can read off the response of the magnetization components to the external driving field $\mathbf{h}(t)$. It is given by the entries of the corresponding

susceptibility tensor χ:

$$\begin{pmatrix} m_{y'} \\ m_z \end{pmatrix} = \begin{pmatrix} \chi_{y'y'} & \chi_{y'z} \\ \chi_{zy'} & \chi_{zz} \end{pmatrix} \begin{pmatrix} h_{y'} \\ h_z \end{pmatrix} \tag{3.49}$$

$$\chi_{y'y'} = \frac{-M_\mathrm{S}\left(\frac{B_\mathrm{eff}}{\mu_0} + \frac{i\alpha\omega}{\gamma\mu_0}\right)}{D} \tag{3.50}$$

$$-\chi_{y'z} = \chi_{zy'} = \frac{\frac{i\omega}{\gamma\mu_0} M_\mathrm{S}}{D} \tag{3.51}$$

$$\chi_{zz} = \frac{-M_\mathrm{S}\left(H + \frac{i\alpha\omega}{\gamma\mu_0}\right)}{D} \tag{3.52}$$

The susceptibilities and therefore the dynamic components of the magnetization $m_{y'}$ and m_z are maximized when D is minimal. Setting the damping factor α to zero leads to the following resonance condition:

$$\left(\frac{\omega}{\gamma\mu_0}\right)^2 = \frac{B_0}{\mu_0} H_0 \tag{3.53}$$

Here $B_0 = \mu_0(H_0 + M_\mathrm{eff})$ and H_0 is the resonance field. Using the definition $\Delta H = \frac{\alpha\omega}{\mu_0\gamma}$, D becomes $i\Delta H\left(\frac{B_0}{\mu_0} + H_0\right) + (\Delta H)^2$ fulfilling Eq. (3.53). Assuming $\frac{B_0}{\mu_0} + H_0 >> \Delta H$, the $(\Delta H)^2$- term can be neglected. Making D real valued the susceptibilities at resonance are given by:

$$\chi^\mathrm{res}_{y'y'} = M_\mathrm{S}\left(\frac{1}{\frac{B_0}{\mu_0} + H_0} - i\frac{\frac{B_0}{\mu_0}}{\left(\frac{B_0}{\mu_0} + H_0\right)\Delta H}\right) \tag{3.54}$$

$$\chi^\mathrm{res}_{y'z} = -\chi^\mathrm{res}_{zy'} = \frac{M_\mathrm{S}\sqrt{\frac{B_0}{\mu_0} H_0}}{\left(\frac{B_0}{\mu_0} + H_0\right)\Delta H} \tag{3.55}$$

$$\chi^\mathrm{res}_{zz} = M_\mathrm{S}\left(\frac{1}{\frac{B_0}{\mu_0} + H_0} - i\frac{H_0}{\left(\frac{B_0}{\mu_0} + H_0\right)\Delta H}\right) \tag{3.56}$$

The absorption line shape for FMR-experiments of thin ferromagnetic films is almost a perfect Lorentzian [116]. This becomes clear if one replaces H by $H_0 + \delta H$ in Eqs. (3.50)-(3.52), applies the resonance condition Eq. (3.53) to D and keeps only terms linear in $\delta H - \Delta H$ [116]. The linearization of the problem is justified as long as $\Delta H << H_0$, which is the case for the NiFe-films and frequencies used in this

thesis. The line shapes of the susceptibilities are as follows:

$$\chi_{\mathrm{y'y'}} = \Im(\chi^{\mathrm{res}}_{y'y'}) \times \left(\frac{\Delta H(H-H_0) - i(\Delta H)^2}{(H-H_0)^2 + (\Delta H)^2} + \frac{\mu_0 \Delta H}{B_0} \right) \tag{3.57}$$

$$\chi_{\mathrm{y'z}} = -\chi_{\mathrm{zy'}} = \chi^{\mathrm{res}}_{y'z} \times \left(\frac{i\Delta H(H-H_0) + (\Delta H)^2}{(H-H_0)^2 + (\Delta H)^2} \right) \tag{3.58}$$

$$\chi_{\mathrm{zz}} = \Im(\chi^{\mathrm{res}}_{zz}) \times \left(\frac{\Delta H(H-H_0) - i(\Delta H)^2}{(H-H_0)^2 + (\Delta H)^2} + \frac{\Delta H}{H_0} \right) \tag{3.59}$$

Here $\Im(\chi^{\mathrm{res}}_{y'y'})$ and $\Im(\chi^{\mathrm{res}}_{zz})$ signify the imaginary parts of Eqs. (3.54) and (3.56). The imaginary parts of $\chi_{y'y'}$ and χ_{zz} (Eqs. (3.57) and (3.59)) show the Lorentzian line shapes characteristic for the microwave absorption $\mathscr{A}(H)$ in an FMR experiment. ΔH is the half width at half maximum (HWHM) of the Lorentzian line shapes and H_0 is the resonance field. From Eqs. (3.57)-(3.59) one experimentally obtains the damping factor α due to its proportionality to the line width ΔH and the gyromagnetic ratio γ as well as the effective magnetization M_{eff} from H_0 using the resonance condition Eq. (3.53). Note that the terms proportional to $\Delta H(H - H_0)$ and $(\Delta H)^2$ are called antisymmetric and symmetric Lorentzian line shapes, respectively.
The results gathered in this section are essential for the characterization of line shapes due to SP-ISHE in NM, anisotropic magneto resistance (AMR) in FM [59] and induction in FM/NM measurement circuitries [60]. At first, in the following section the spin pumping mechanism will be explained.

3.4 Spin pumping

The spin pumping (SP) mechanism was theoretically introduced by Tserkovnyak et al. in 2002 [42]. It provided an explanation for the experimental observation of enhanced Gilbert damping for ferromagnetic films capped with certain metallic materials such as Pt and Pd [44, 99]. SP essentially describes the fact that a precessing magnetization sends a pure spin current across a FM/NM interface if certain conditions are met. In Fig. 3.2 a schematic cartoon of spin pumping in a FM/NM bilayer is shown. The spin current has a time invariant direction which is perpendicular to the FM/NM-interface and a polarization with both dc and ac components. If a spin current corresponds to a net transport of angular momentum from FM into NM the damping factor which appears in the LLG, Eq. (3.34), inevitably rises [144]. To be able to estimate the effect of spin pumping for different capping materials both interface and NM spin transport properties have to be considered. This has been the subject in several publications about spin dependent or non-collinear magnetic transport across FM/NM interfaces [124–126] and spin diffusion in normal metals in the presence of spin pumping [41, 43].

The interface between FM and NM is considered to be a mesoscopic conductor

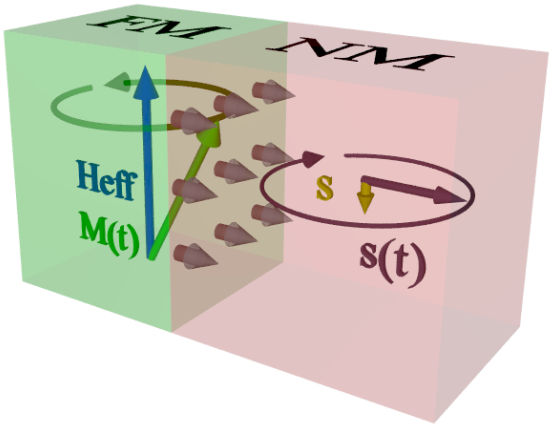

Figure 3.2: A schematic overview of spin pumping is shown. A precessing magnetization $\mathbf{M}(t)$ around $\mathbf{H}_{\text{eff}}$ in the green colored ferromagnetic layer (FM) injects a pure spin current into a normal metal (NM). The spin current is indicated by the small gray arrows directly at the FM/NM interface (direction vector) and its polarization vector, yellow for the dc component and purple for the ac component.

(or scattering region) linking two electron reservoirs A = FM and B = NM, this is illustrated in Fig. 3.3a). The boundaries of the interface are marked by dashed lines and letters a and b. Note that in reality the width of the interface goes to zero, which allows for its mesoscopic characterization. In [42] spin pumping is explained to be a conceptual analog of parametric charge pumping [121]. The latter has been implemented e.g. in quantum dots confining a region in a two-dimensional electron gas (2DEG) using gate electrodes [118–121]. Reservoirs A and B in this case would be the left and right region of the 2DEG with respect to the quantum dot. A mesoscopic conductor is defined by having at least one dimension on the order of the electrons mean free path λ_{el} or the phase conserving length λ_ϕ of an incident electron wave function, [80]. Electronic transport through mesoscopic regions, viz. the question how much current flows when a potential difference is applied across it, can effectively be treated using the so called Landauer-Büttiker formalism, [122, 123, 145, 146]. Following this concept, a mesoscopic zone is connected to electron reservoirs A and B by leads a and b, this is shown schematically in Fig. 3.3b). In this schematic the mesoscopic region is delimited by coordinates x_{a} and x_{b}. The leads should be perceived as a theoretical concept in order to summarize single transport channels which are characterized by the spin degenerate $\frac{2e^2}{h}$ or non-degenerate conductance quantum $\frac{e^2}{h}$. Only through these channels an electron can enter or leave the mesoscopic region and its transport properties are completely defined by the corresponding scattering matrix.

$$\hat{S} = \begin{pmatrix} \hat{r}_{\text{aa}} & \hat{t}_{\text{ab}} \\ \hat{t}_{\text{ba}} & \hat{r}_{\text{bb}} \end{pmatrix} \tag{3.60}$$

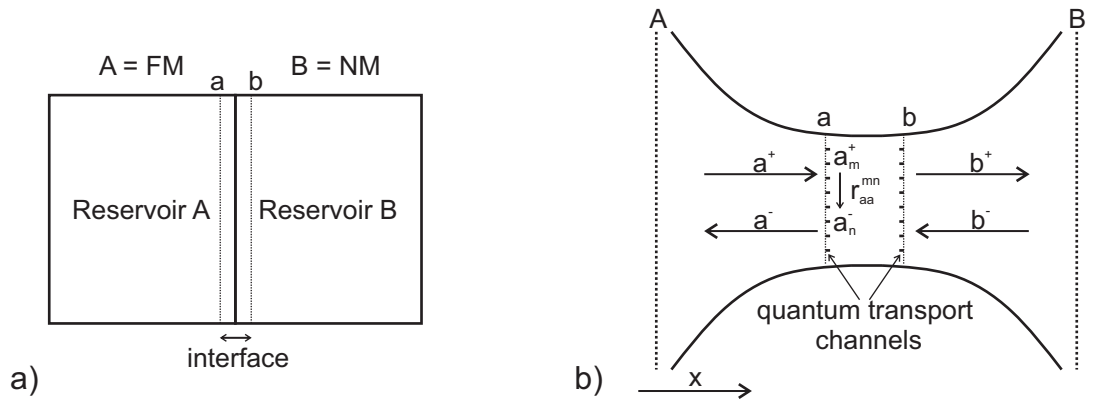

Figure 3.3: In a) the basic approach of dividing an FM/NM bilayer into reservoirs A = FM and B = NM as well as defining the interface between them as a mesoscopic zone, which delimited by the dashed lines a and b, is shown. In b) the full characterization of a general mesoscopic conductor as imagined in the framework of the Landauer-Büttiker formalism is shown. A and B denote the electron reservoirs left and right of the mesoscopic zone which has leads a and b. The leads delimit the mesoscopic zone and summarize the available single quantum channels through which electrons can enter and leave the scattering region. a^+, b^-, a^-, b^+ are the amplitudes of incoming and outgoing electron wave functions, respectively. $+$ and $-$ denote electrons traveling towards the $+x$- or $-x$-direction respectively. Also indicated is one exemplary case of an electron entering channel m at lead a with an amplitude a_{m}^{+} together with the probability $r_{\mathrm{aa}}^{\mathrm{mn}}$ to be reflected into channel n at lead a and amplitude a_{n}^{-}

The underlying quantum mechanical concept of the scattering matrix is that an incident electron wave function is transformed into an outgoing wave function by application of $\hat{S}$. This is also indicated in Fig. 3.3b) where a^+, b^-, a^-, b^+ are the amplitudes of incoming and outgoing electron wave functions, cf. [126]. Assuming that both a and b contain N quantum transport channels, the scattering matrix has $2N \times 2N$ entries. $\hat{r}_{\mathrm{aa}}$, $\hat{t}_{\mathrm{ab}}$, $\hat{t}_{\mathrm{ba}}$, $\hat{r}_{\mathrm{bb}}$ are the corresponding $N \times N$ reflection and transmission matrices. E.g. the entry $r_{\mathrm{aa}}^{\mathrm{nm}}$ is the probability of an electron arriving in channel m to be reflected into channel n in lead a, see Fig. 3.3b).

The chemical potentials of reservoirs A and B shall be μ_{A} and μ_{B}. The static equilibrium of the system is described by the condition $\mu_{\mathrm{A}} = \mu_{\mathrm{B}}$, see Fig. 3.4a). If the static equilibrium between A and B is disturbed, e.g. by application of a bias voltage, the assumption can be made that each reservoirs is still in static equilibrium with respect to itself. Reservoirs A and B inject charge carriers up to so-called quasi Fermi energies μ_{a} and μ_{b}, which are the chemical potentials in the leads a and b, i.e. directly at the boundary of the enclosed mesoscopic conductor [122]. This is

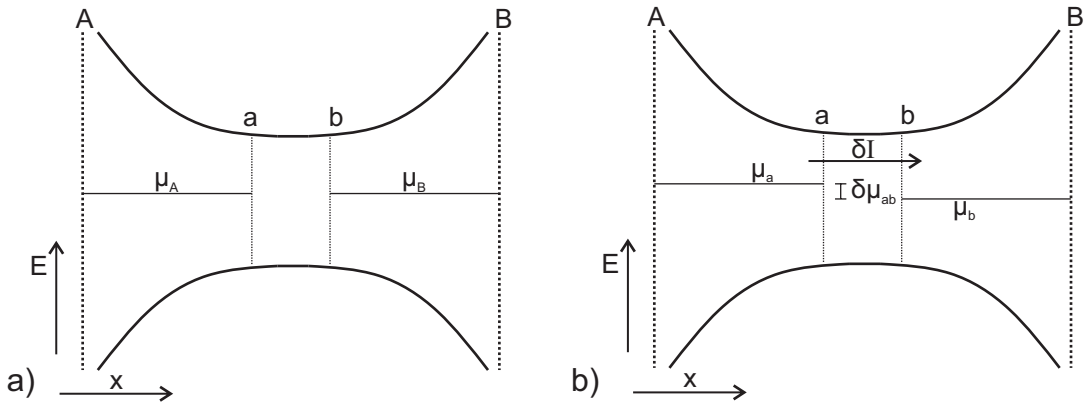

Figure 3.4: In a) the general case of an unbiased mesoscopic conductor delimited by a and b is shown. The system is in static equilibrium and the chemical potentials μ_{A} and μ_{B} of reservoirs A and B are equal. Note the relevant axis of the system (x) denotes the position relative to the mesoscopic region with delimiters x_{a} and x_{b}, and E signifies energy. In b) the situation of a bias voltage across the mesoscopic region is depicted. There is a difference $\delta\mu_{\mathrm{ab}} = \mu_{\mathrm{a}} - \mu_{\mathrm{b}}$ of quasi Fermi energies at the boundaries a and b, which drives a current δI.

schematically shown in Fig. 3.4b). Note that it is assumed that all quantum channels in lead a and b correspond to the same chemical potentials μ_{a} and μ_{b}. The difference in chemical potentials in lead a compared to lead b, $\delta\mu_{\mathrm{ab}} = \mu_{\mathrm{a}} - \mu_{\mathrm{b}} \neq 0$, drives a current given by [121, 122, 126]:

$$\delta I = G\delta\mu_{\mathrm{ab}} = \frac{2e^2}{h}\delta\mu_{\mathrm{ab}} \sum_{n\epsilon a}\sum_{m\epsilon b} |S_{\mathrm{nm}}|^2 = \frac{2e^2}{\hbar}\delta\mu_{\mathrm{ab}} \sum_{nm} |t_{\mathrm{nm}}|^2 \tag{3.61}$$

For an unbiased system, but oscillating chemical potentials μ_{a} and μ_{b} the situation is more subtle. Experimentally time dependent chemical potentials at contacts a and b can be set up by variation of tunnel barriers [118] or changing the internal energy levels of a quantum dot in the coulomb blockade regime [119]. Another possibility is to vary the charge density inside an open quantum dot [120], which is the electrostatic analog of a peristaltic pump. The essential observation is that two independent internal parameters and corresponding chemical potentials μ_{a} and μ_{b} oscillating coherently at the frequency f cause a net transport of charge if their mutual phase difference is nonzero. This process is called parametric charge pumping. The theoretical basis for treating oscillating chemical potentials in the framework of the Landauer-Büttiker formalism using the scattering matrix (Eqs. (3.60) and (3.61)) was developed in [145, 146] and was refined towards parametric charge pumping in [121]. To this end, the scattering matrix is parametrized by external parameters X_1

and X_2 and the following relation holds for the system's response:

$$I_{\mathrm{net}}^{\mathrm{pump}} = \frac{\omega e \sin(\phi) X_1 X_2}{2\pi} \sum_{n\epsilon a} \sum_{m\epsilon b} \Im \left(\frac{\partial S_{\mathrm{nm}}^*}{\partial X_1} \frac{\partial S_{\mathrm{nm}}}{\partial X_2} \right) \tag{3.62}$$

The net charge current is proportional to the frequency $f = \omega/2\pi$ and amplitudes X_1 and X_2 of the oscillating parameters. Furthermore, for $\phi = 0$ and integer multiples of π, hence X_1 and X_2 varying in- or out-of-phase, there is no net charge current $I_{\mathrm{net}}^{\mathrm{pump}}$ pumped. For a phase difference $\phi = \frac{\pi}{2}$, $I_{\mathrm{net}}^{\mathrm{pump}}$ is maximized and the flow direction is reversed for $\phi + \pi$. Eq. (3.62) only holds if the response of the system is bilinear in X_1 and X_2 and both parameters are coupled phase coherently. Note that it is worthwhile to keep track of both chemical potentials to be changed and the mathematically elegant scattering matrix approach when considering spin dependent transport through an FM/NM interface. Transferring the results of parametric charge pumping [121] to spin pumping the first step is to define the spin current in terms of an applicable scattering matrix [124–126].

$$I_{\mathrm{S}} = \frac{e^2}{h} \delta\mu_{\mathrm{S}} \sum_{nl,ml'} |t_{\mathrm{nlml'}}|^2 \tag{3.63}$$

$t_{\mathrm{nlml'}}$ is the transmission probability from quantum channel m with spin state l' into channel n with spin state l. $\delta\mu_{\mathrm{s}} = \mu_{\mathrm{s,a}} - \mu_{\mathrm{s,b}}$ is the spin chemical potential difference at the FM/NM interface. In Fig. 3.5a) $\mu_{\mathrm{s,a}} = \mu_{\mathrm{s,b}}$. Such a situation is fulfilled if there is no electrostatic voltage drop across the interface and all internal potentials are in static equilibrium. In the top panel of Fig. 3.5b) the effect of a bias voltage is depicted, $\delta\mu_{\mathrm{s}} \neq 0$. Hence, a spin current will flow from FM into NM [78].
If one is able to change $\mu_{\mathrm{s,a}}$ and $\mu_{\mathrm{s,b}}$ periodically with a fixed, but nonzero mutual phase difference ϕ, there should, in analogy to charge pumping, be a spin current flowing from FM to NM. This situation is schematically shown in the bottom panel of Fig. 3.5b). As a matter of fact, a precessing magnetization periodically changes the spin-resolved chemical potentials $\mu_\uparrow$ and $\mu_\downarrow$ at the interface. $\uparrow$ and $\downarrow$ correspond to the opposing directions of the ferromagnets spin quantization axis, which always lies parallel to the momentary magnetization unit vector $\mathbf{e}_{\mathrm{M}}$, [126]. This assumption is justified as for 3d-ferromagnets spin flip relaxation rates τ_{sf}^{-1} are on the order of 10^3 larger than typical precession frequencies [41]. The adiabatic change of $\mu_\uparrow$ and $\mu_\downarrow$ and viz. $\delta\mu_{\mathrm{S}}$ takes place towards perpendicular direction with respect to the momentary spin quantization axis. The applicable scattering matrix is parametrized by the azimuthal angle of the precession cone's basal plane $\phi(t)$, or equivalently by the magnetization's dynamic part $\mathbf{m}(t)$, [41–43]. It is very important to realize that two phase coherent parameters with a phase difference of $\frac{\pi}{2}$ are hidden behind $\mathbf{m}(t)$. As illustrated in Fig 3.6a), where a magnetization's precession cone is displayed from top view. $\mathbf{m}(t)$ can be decomposed in linearly independent vectors $m_{y'}(t)$ and $m_z(t)$. For adiabatic magnetization precession in FM, application of the scattering matrix theory led Tserkovnyak et al. to the following expression for the pumped

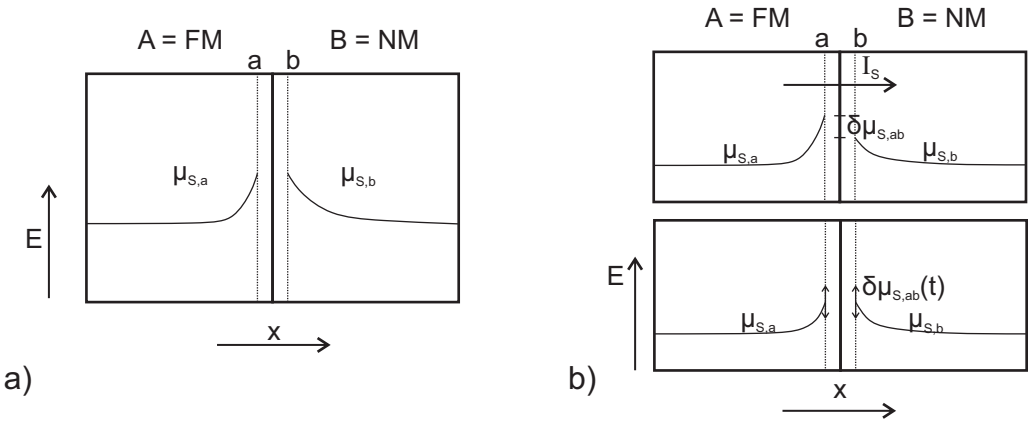

Figure 3.5: In a) reservoirs A = FM and B = NM are in equilibrium with respect to each other. The spin quasi chemical potentials at the interface $\mu_{\mathrm{S,a}}$ and $\mu_{\mathrm{S,b}}$ are equal and no spin current I_{S} is flowing. In b) the situation of a bias voltage across the interface a-b is depicted. There is a spin quasi chemical potential difference $\delta\mu_{\mathrm{S,ab}}$ and a spin current I_{S} will flow. In c) $\mu_{\mathrm{S,a}}$ and $\mu_{\mathrm{S,b}}$ are equal at the interface on time-average, but are varied in an oscillatory manner. This facilitates a time-dependent spin quasi chemical potential difference at the interface $\delta\mu_{\mathrm{S,ab}}(t)$.

spin current from FM into NM [42]:

$$\mathbf{I}_{\mathrm{s}}^{\mathrm{pump}} = \frac{\hbar}{4\pi}\left(A_{\mathrm{r}}\mathbf{e}_{\mathrm{M}} \times \frac{\mathrm{d}\mathbf{e}_{\mathrm{M}}}{\mathrm{d}t} - A_{\mathrm{i}}\frac{\mathrm{d}\mathbf{e}_{\mathrm{M}}}{\mathrm{d}t}\right) \tag{3.64}$$

A complete theoretical deduction of this formula, using applicable scattering matrices in spin space, can be found in the appendices of [41] and [131]. From the considerations above it is phenomenologically clear that $\mathbf{I}_{\mathrm{S}}^{\mathrm{pump}}$ is generally composed of two vector entities which are perpendicular to $\mathbf{e}_{\mathrm{M}}$ and to each other. The amplitude of the two terms is determined by the factors A_{r} and A_{i}, respectively. The vectorial nature of $\mathbf{I}_{\mathrm{s}}^{\mathrm{pump}}$ is given by its polarization $\hat{\mathbf{s}}(t)$. The flow direction corresponding to $\mathbf{I}_{\mathrm{s}}^{\mathrm{pump}}$ is always perpendicular to the FM/NM interface. Note that for Eq. (3.64) it is assumed that the pumped spin current is completely absorbed by NM [42].
In comparison with the LLG (Eq. (3.34)) the term proportional to A_{r} in Eq. (3.64) can be identified to change the damping α of the precessing magnetization whereas the term proportional to A_{i} influences the torque term and changes the gyromagnetic ratio γ [42]. Hence, experimentally A_{r} is accessible by measuring the change in line width of FMR spectra of a FM/NM hybrid in comparison to a single FM layer and A_{i} is reflected in the shift of the resonance field, cf. Sec. 3.3. The parameters A_{r} and A_{i} contain the applicable spin dependent reflection and transmission probabilities for spin currents incident from spin pumping [42]. They are defined as

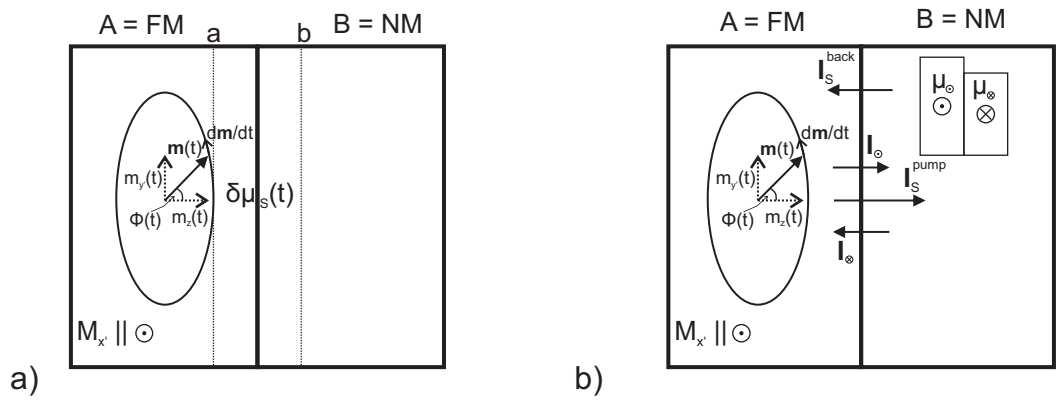

Figure 3.6: In a) the situation of setting up $\delta\mu_{\mathrm{S}}(t)$ at an FM/NM interface by magnetization precession is shown. The precession takes place in the y'-z-plane. $\mathrm{d}\mathbf{m}/\mathrm{d}t$ is parametrized by the components $m_{y'}(t)$ and $m_{\mathrm{z}}(t)$ as well as by the angle $\phi(t)$. The magnetization is saturated along the x'-direction. In b) it is illustrated that spin pumping might lead to spin accumulation in NM which drives a spin current $I_{\mathrm{S}}^{\mathrm{back}}$ back into FM.

follows:

$$A_{\mathrm{r}} + iA_{\mathrm{i}} = g^{\uparrow\downarrow} = \Re(g^{\uparrow\downarrow}) + i\Im(g^{\uparrow\downarrow}) \tag{3.65}$$

$g^{\uparrow\downarrow}$ is the dimensionless spin mixing conductance. It is specified in the field of non-collinear magnetoelectronics [124–126].
In spin dependent transport theory the scattering probabilities between the two possible eigenstates in spin space $|\uparrow\rangle$, $|\downarrow\rangle$, viz. the basis in which the spin quantization axis is parallel to the momentary magnetization direction $\mathbf{e}_{\mathrm{M}}$, are in the focus [126]. The applicable conductances for spin currents through an NM/FM-interface depending on the scattering matrix in the spin space basis can be defined as follows [125]:

$$G^{\uparrow} = \frac{e^2}{h}\left[M - \sum_{nm}|r_{\uparrow}^{\mathrm{nm}}|^2\right] = \frac{e^2}{h}\sum_{nm}|t_{\uparrow}^{\mathrm{nm}}|^2 \tag{3.66}$$

$$G^{\downarrow} = \frac{e^2}{h}\left[M - \sum_{nm}|r_{\downarrow}^{\mathrm{nm}}|^2\right] = \frac{e^2}{h}\sum_{nm}|t_{\downarrow}^{\mathrm{nm}}|^2 \tag{3.67}$$

$$G^{\uparrow\downarrow} = \frac{e^2}{h}\left[M - \sum_{nm}(r_{\uparrow}^{\mathrm{nm}})(t_{\downarrow}^{\mathrm{nm}})^*\right] = \Re(G^{\uparrow\downarrow}) + \Im(G^{\uparrow\downarrow}) \tag{3.68}$$

Four conductance parameters can be identified. $G^{\uparrow}$ and $G^{\downarrow}$ describe spin conserving transport across the interface. The real and imaginary parts of $G^{\uparrow\downarrow}$ determine the amount of angular momentum being transferred between FM and NM. $\mathbf{I}_{\mathrm{S}}^{\mathrm{pump}}$ is nothing else but transport of angular momentum per time. Its polarization is always

perpendicular to $\mathbf{e}_{\mathrm{M}}$ and therefore it only depends on $g^{\uparrow\downarrow} = \frac{h}{e^2} G^{\uparrow\downarrow}$.
For a general treatment of FM/NM hybrids one has to drop the preliminary assumption that NM is an ideal spin sink, [41]. If a spin current flows from FM into NM there might be a spin accumulation and a corresponding spin chemical potential difference in NM. Its magnitude is determined by spin relaxation processes and is characterized by a specific spin diffusion length λ_{sd}. Hence, the accumulation in NM drives a spin current $\mathbf{I}_{\mathrm{S}}^{\mathrm{back}}$ back into FM. This is illustrated in Fig. 3.6b). In this schematic the restriction with respect to the dc part of the spin current polarization is made. The net transport of angular momentum is given by the following formula [41]:

$$\mathbf{I}_{\mathrm{S}}^{\mathrm{net}} = \mathbf{I}_{\mathrm{S}}^{\mathrm{pump}} - \mathbf{I}_{\mathrm{S}}^{\mathrm{back}} \tag{3.69}$$

A general classification of materials as spin sinks, $I_{\mathrm{S}}^{\mathrm{back}} \approx 0$, and "spin leads" $I_{\mathrm{S}}^{\mathrm{back}} \approx I_S^{\mathrm{pump}}$ is possible on the basis of spin flip scattering properties in the presence of spin diffusion [41]. In this framework the parameter to be considered is $\epsilon = \tau_{\mathrm{el}}/\tau_{\mathrm{sf}}$, which divides the elastic by the spin flip scattering rate. A material is said to be a good spin sink if $\epsilon \geq 10^{-2}$ and causes a sizable increase of the Gilbert damping parameter α for $\epsilon \geq 10^{-1}$, [41].
The ϵ-value increases as a function of spin orbit coupling, which is proportional to Z^4 [147]. Z is the atomic number of the considered material. The general statement that heavier materials are more effective spin sinks can be made. However, Z is not the only parameter determining the effectiveness of a material in terms of being a good spin sink. In transport, be it spin or charge dependent only electrons near the Fermi surface participate. It is of eminent importance to consider the spin-orbit-coupling of these electrons caused by the interplay of bands of different nature. s-electrons which are hybridized with p- or d-electrons feature large spin-orbit-coupling and therefore small $\tau_{\mathrm{sf}} = \tau_{\mathrm{soc}}$ [41, 147].
Pt and Pd feature an $\epsilon > 10^{-1}$, whereas e.g. for Ag, Ta and Au $\epsilon \leq 10^{-2}$ [41]. The fact that ϵ(Pd) > ϵ(Ag, Ta, Au), which might be counter-intuitive due to the smaller Z of Pd with respect to the other materials, can be explained by the strong s-d-hybridization of electrons at the Fermi surface for Pd, cf. [148, 149]. Due to similar band structures with respect to s-d-hybridization at the Fermi energy of Pd and Pt, but a higher Z for the latter, Pt is a more effective spin sink than Pd [41, 44].
Note that from the aforementioned considerations it might be possible to tune the ϵ-value by doping light materials e.g. Cu with heavy materials such as Bi [150] or low ϵ-materials like Au with small amounts of Pt [151]. Furthermore, it is promising to study transition metal alloys with respect to effective spin sink properties. As from a large body of theoretical work in the field of first-principles calculations of band structures and transport properties, spin-orbit-coupling in such material compounds is suggested to be sizable. For an overview of the topic of "electronic and transport properties of disordered transition metal alloys" see [67].
The back flow into FM in spin pumping experiments can be incorporated into Eq. (3.64) by exchanging $g^{\uparrow\downarrow}$ with an effective spin mixing conductance $\tilde{g}^{\uparrow\downarrow}$, [41].

Hence, the net spin current transferred from FM into NM is given by:

$$\mathbf{I}_{\text{s, net}}^{\text{pump}} = \frac{\hbar}{4\pi}\left(\Re(\tilde{g}^{\uparrow\downarrow})\mathbf{e}_{\text{M}} \times \frac{d\mathbf{e}_{\text{M}}}{dt} - \Im(\tilde{g}^{\uparrow\downarrow})\frac{d\mathbf{e}_{\text{M}}}{dt}\right) \tag{3.70}$$

According to first principles calculations of NM/FM hybrids $\Re(g^{\uparrow\downarrow}) >> \Im(g^{\uparrow\downarrow})$, [144], and the following formula describes the net pumped spin current.

$$\mathbf{I}_{\text{s, net}}^{\text{pump}} = \frac{\hbar}{4\pi}\Re(\tilde{g}^{\uparrow\downarrow})\left(\mathbf{e}_{\text{M}} \times \frac{d\mathbf{e}_{\text{M}}}{dt}\right) \tag{3.71}$$

For spin sinks $g^{\uparrow\downarrow} \approx \tilde{g}^{\uparrow\downarrow}$ (e.g. for Pt and Pd). In such systems the examination of line width enhancement in FMR spectra allows a direct measurement of $g^{\uparrow\downarrow}$ which is linked to the increased Gilbert damping constant [42].

$$\alpha' = \alpha_{\text{FM/NM}} - \alpha_{\text{FM}} = g_{\text{J}}\frac{\Re(g^{\uparrow\downarrow})}{4\pi M} \tag{3.72}$$

where M is the total magnetic moment in units of μ_{B} and g_{J} is the Landé g-factor. It is more subtle to determine the spin mixing conductance of a spin lead like Cu, Ag or Au due to considerable back flow of pumped spin currents. Experimental approaches involve thickness dependent studies of ultrathin FM layers and FM/NM/FM trilayers, [46, 131, 152–154].
The result about the net spin current displayed in Eq. (3.71) is used in the following section to determine corresponding line shapes across FMR. Note that for this the assumption $\Re(\tilde{g}^{\uparrow\downarrow}) = \tilde{g}^{\uparrow\downarrow}$ will be used.

3.5 Line shapes and relative amplitudes of dc and ac spin currents from spin pumping

In order to quantify both the time constant and the oscillating pumped spin current from a thin film bilayer FMR experiment, the ansatz for $\mathbf{M}(t)$ specified in Eq. (3.36) is inserted into Eq. (3.71).

$$\mathbf{I}_{\mathrm{s,\,net}}^{\mathrm{pump}} = \frac{\hbar}{4\pi}\frac{\tilde{g}^{\uparrow\downarrow}\omega}{M_{\mathrm{S}}^2}\begin{pmatrix} \Im(m_{y'}^* m_z) \\ -M_{\mathrm{S}}(\Re(m_z)\sin(\omega t) + \Im(m_z)\cos(\omega t)) \\ M_{\mathrm{S}}(\Re(m_{y'})\sin(\omega t) + \Im(m_{y'})\cos(\omega t)) \end{pmatrix} \tag{3.73}$$

The first component of the spin current vector has no time dependence. This so-called dc-part is always along the magnetization's precession axis, the x'-direction, see Fig. 3.1. In an external magnetic field the amplitude of the pumped spin current, $I_{\mathrm{s,\,net}}^{\mathrm{pump}}$, will follow a distinct line shape. This is evident from the corresponding susceptibility factors as defined in Eqs. (3.57)-(3.59).
Assuming a pure in-plane driving field $h_{y'}(t)$, the following relation holds:

$$\Im(m_{y'}^* m_z) = \Im(\chi_{y'y'}^* \chi_{zy'})|h_{y'}|^2 = (\Re(\chi_{y'y'})\Im(\chi_{zy'}) - \Im(\chi_{y'y'})\Re(\chi_{zy'}))|h_{y'}|^2 \tag{3.74}$$

and for a respective pure out-of-plane driving field $h_z(t)$ the following applies:

$$\Im(m_{y'}^* m_z) = \Im(\chi_{zz}^* \chi_{y'z})|h_z|^2 = (\Re(\chi_{zz})\Im(\chi_{y'z}) - \Im(\chi_{zz})\Re(\chi_{y'z}))|h_z|^2 \tag{3.75}$$

The external field dependence of the dc spin current from spin pumping for pure ip and oop cases, respectively, is consequently given by:

$$I_{\mathrm{s,\,dc}}^{\mathrm{pump}}(\mathrm{ip}) \approx \frac{\hbar}{4\pi}\frac{\tilde{g}^{\uparrow\downarrow}\omega}{M_{\mathrm{S}}^2}\Im(\chi_{y'y'}^{\mathrm{res}})\chi_{zy'}^{\mathrm{res}}|h_{y'}|^2\frac{(\Delta H)^2}{(H-H_0)^2+(\Delta H)^2} \tag{3.76}$$

$$I_{\mathrm{s,\,dc}}^{\mathrm{pump}}(\mathrm{oop}) \approx \frac{\hbar}{4\pi}\frac{\tilde{g}^{\uparrow\downarrow}\omega}{M_{\mathrm{S}}^2}\Im(\chi_{zz}^{\mathrm{res}})\chi_{y'z}^{\mathrm{res}}|h_z|^2\frac{(\Delta H)^2}{(H-H_0)^2+(\Delta H)^2} \tag{3.77}$$

$\Im(\chi_{y'y'}^{\mathrm{res}})$, $\chi_{zy'}^{\mathrm{res}}$, $\Im(\chi_{zz}^{\mathrm{res}})$ and $\chi_{y'z}^{\mathrm{res}}$ are the prefactors of Eqs. (3.54) - (3.56). In Eqs. (3.76) and (3.77) the approximation can be replaced by equality signs if the offset appearing in Eqs. (3.57) and (3.59), which are proportional to $\Delta H/B_0$ and $\Delta H/H_0$, respectively, are negligible. Whereas the first offset is always very small, the second has a distinct driving frequency dependence and is non-negligible for the very lowest accessible frequencies of the fundamental FMR mode spectrum. Note that along with this approximation of vanishing offset comes the simplification that for a mixture of in-plane and out-of-plane driving fields the pumped spin current is a sum of Eqs. (3.76) and (3.77). Summarizing these results, $I_{\mathrm{s,\,dc}}^{\mathrm{pump}}$ is proportional to a symmetric Lorentzian line shape centered at the resonance field H_0 with a line width of ΔH (HWHM). It is proportional to the power P ($|h_{y'}|^2$, $|h_z|^2 \propto P$) and the frequency $f = \omega/2\pi$ of the irradiated microwave field or the magnetization precession, respectively. Note that a non-negligible offset $\Delta H/H_0$ yields a part of the pumped

spin current which is proportional to an antisymmetric Lorentzian line shape.
The y'- and the z-components of Eq. (3.73) represent the dynamic part of $\mathbf{I}_{\mathrm{s,\,net}}^{\mathrm{pump}}$, henceforth referred to as ac-part. In order to find the corresponding line shape for these ac-components, a reformulation of Eq. (3.73) is practical. Assuming a pure in-plane driving field the following relation holds

$$\mathbf{I}_{\mathrm{s,\,net}}^{\mathrm{pump}} = \frac{\hbar}{4\pi}\frac{\tilde{g}^{\uparrow\downarrow}\omega}{M_{\mathrm{S}}^2}\begin{pmatrix}(\Re(\chi_{y'y'})\Im(\chi_{zy'}) - \Im(\chi_{y'y'})\Re(\chi_{zy'}))|h_{y'}|^2\\ -M_{\mathrm{S}}A_0\sin(\omega t+\alpha)\\ M_{\mathrm{S}}C_0\sin(\omega t+\beta)\end{pmatrix} \tag{3.78}$$

Constants A_0, B_0 and angles α, β are given by the following relations:

$$A_0 = h_{y'}\sqrt{(\Re(\chi_{zy'}))^2 + (\Im(\chi_{zy'}))^2} \tag{3.79}$$

$$C_0 = h_{y'}\sqrt{(\Re(\chi_{y'y'}))^2 + (\Im(\chi_{y'y'}))^2} \tag{3.80}$$

$$\cos(\alpha) = \frac{\Re(\chi_{zy'})h_{y'}}{A_0} \tag{3.81}$$

$$\sin(\alpha) = \frac{\Im(\chi_{zy'})h_{y'}}{A_0} \tag{3.82}$$

$$\cos(\beta) = \frac{\Re(\chi_{y'y'})h_{y'}}{C_0} \tag{3.83}$$

$$\sin(\beta) = \frac{\Im(\chi_{y'y'})h_{y'}}{C_0} \tag{3.84}$$

From evaluation of Eqs. (3.57) and (3.58) one finds that $\alpha = \beta - \frac{\pi}{2}$. This is the phase shift naturally expected for the two perpendicular dynamic magnetization components $m_{y'}$ and m_z. Using the line shapes of the applying susceptibility factors, Eqs. (3.57)-(3.59), plus neglecting the offset $\Delta H/B_0$, the ac-components of $\mathbf{I}_{\mathrm{s,\,net}}^{\mathrm{pump}}$ are given by:

$$I_{\mathrm{s,\,ac}\,,y'}^{\mathrm{pump}}(\mathrm{ip}) = -\frac{\hbar}{4\pi}\frac{\tilde{g}^{\uparrow\downarrow}\omega}{M_{\mathrm{S}}}\chi_{zy'}^{\mathrm{res}}h_{y'}\sqrt{\frac{(\Delta H)^2}{(H-H_0)^2+(\Delta H)^2}}\ \sin(\omega t+\alpha) \tag{3.85}$$

$$I_{\mathrm{s,\,ac}\,,z}^{\mathrm{pump}}(\mathrm{ip}) = \frac{\hbar}{4\pi}\frac{\tilde{g}^{\uparrow\downarrow}\omega}{M_{\mathrm{S}}}\Im(\chi_{y'y'}^{\mathrm{res}})h_{y'}\sqrt{\frac{(\Delta H)^2}{(H-H_0)^2+(\Delta H)^2}}\ \sin(\omega t+\beta) \tag{3.86}$$

For the case of an out-of-plane driving field Eq. (3.78) holds upon exchanging $\chi_{y'y'}$ with χ_{zz} and $h_{y'}$ with h_z. The applicable line shapes of the ac-components of the pumped spin current for out-of-plane excitation are consequently given by:

$$I_{\mathrm{s,\,ac}\,,y'}^{\mathrm{pump}}(\mathrm{oop}) = -\frac{\hbar}{4\pi}\frac{\tilde{g}^{\uparrow\downarrow}\omega}{M_{\mathrm{S}}}\Im(\chi_{zz}^{\mathrm{res}})h_z\sqrt{\frac{(\Delta H)^2}{(H-H_0)^2+(\Delta H)^2}}\ \sin(\omega t+\alpha) \tag{3.87}$$

$$I_{\mathrm{s,\,ac}\,,z}^{\mathrm{pump}}(\mathrm{oop}) = \frac{\hbar}{4\pi}\frac{\tilde{g}^{\uparrow\downarrow}\omega}{M_{\mathrm{S}}}\chi_{y'z}^{\mathrm{res}}h_z\sqrt{\frac{(\Delta H)^2}{(H-H_0)^2+(\Delta H)^2}}\ \sin(\omega t+\beta) \tag{3.88}$$

One major difference between the dc and the ac components of the pumped spin current is the proportionality to $\sqrt{P}$ for the latter one. Furthermore, it is striking that the expected line shape of the ac-component is proportional to the square root of a Lorentzian function. Leaving out the prefactors, line shapes of both dc and ac components are normalized to 1. Their relative amplitudes at FMR for pure ip and oop case are given by the following set of relations:

$$|I^{\text{pump}}_{\text{s, ac},y'}(\text{ip})/I^{\text{pump}}_{\text{s, dc}}(\text{ip})| = M_{\text{S}}/(\Im(\chi^{\text{res}}_{y'y'})h_{y'}) \tag{3.89}$$

$$|I^{\text{pump}}_{\text{s, ac},z}(\text{ip})/I^{\text{pump}}_{\text{s, dc}}(\text{ip})| = M_{\text{S}}/(\chi^{\text{res}}_{zy'}h_{y'}) \tag{3.90}$$

$$|I^{\text{pump}}_{\text{s, ac},y'}(\text{oop})/I^{\text{pump}}_{\text{s, dc}}(\text{oop})| = M_{\text{S}}/(\chi^{\text{res}}_{y'z}h_{z}) \tag{3.91}$$

$$|I^{\text{pump}}_{\text{s, ac},z}(\text{oop})/I^{\text{pump}}_{\text{s, dc}}(\text{oop})| = M_{\text{S}}/(\Im(\chi^{\text{res}}_{zz})h_{z}) \tag{3.92}$$

As from the susceptibility factors (Eqs. (3.54)-(3.56)) the general statement can be made that the relative amplitudes of spin currents is largest for an out-of-plane ac polarization in combination with an out-of-plane driving field. This situation is described by Eq. (3.92).

The theoretical results concerning spin currents from spin pumping in thin ferromagnetic/normal metal bilayers can be probed via the inverse spin Hall effect. Consequently, a voltage due to ISHE can be interpreted as a measure for the injected spin current both for dc- and ac-case. Of course it is also very appealing to have a source of pure spin currents using SP. It offers a means to study types of spin dependent scattering and comparison of experimental results to first principles calculations.

However, parasitic effects are always an issue when placing a specimen which is composed of both ferromagnetic and conductive materials inside a magnetic microwave field. In order not to assign voltage signals caused by other physical effects to ISHE, one has to examine carefully possible experimental setup related voltages.

4 Experimental setup and measurable voltage signals

The study of ISHE in metallic heterostructures using pure spin currents requires the operation of spin pumping and as a preliminary basis FMR. The eigenfrequencies of the saturated magnetization of a ferromagnetic material like NiFe are typically in the GHz-regime. Relevant frequencies for magnetic excitation fields $\mathbf{h}(t)$ start approximately at 2 GHz. Below, the expected resonance field H_0 is too close to zero and consequently the saturation of the magnetization along the external field might not be complete and FMR-theory as presented in Sec. 3.3 is not applicable. The range above 2 GHz is in principle unlimited, provided that large magnetic fields can be supplied and appropriate microwave transmission lines are available. Assume a gyromagnetic ratio of $\gamma = 181.20\,\mathrm{GHz\,T^{-1}}$ and a saturation magnetization corresponding to $\mu_0 M_\mathrm{s} = 0.9\,\mathrm{T}$. These are typical values for 12 nm thick NiFe films grown by magnetron sputtering, cf. experimental results presented in Sec. 5.1. Assume further that $M_\mathrm{S} = M_\mathrm{eff}$ which is also a very good approximation for the NiFe films under consideration, cf. Sec. 5.1. The expected resonance field from Eq. (3.53) for an in-plane saturated magnetization and a 10 GHz precession frequency corresponds to $\mu_0 H_0 \approx 0.12\,\mathrm{T}$ and for 20 GHz to $\mu_0 H_0 \approx 0.38\,\mathrm{T}$. These field values are easily accessible using solenoids winded around a soft iron yoke.
In order to control the excitation field $\mathbf{h}(t)$ for FMR one has to use electric circuitry which operates with alternating currents in the GHz-regime. One needs to perform microwave or radio-frequency (rf) engineering, a field of electrical engineering which focuses on circuit design suitable for voltages and currents in the range of 300 MHz to 300 GHz [155]. The basic point of interest is the propagation of electromagnetic waves through conductors, i.e. the solutions of Maxwell's curl-equations for time periodic electric and magnetic fields, [155]. With this respect it is important to have a maximum power transfer from one device into the next and make the excitation field of the wished frequency available at the specimen. To this end characteristic impedances of electromagnetic waves on transmission lines or waveguides have to be matched. Rf-devices, like signal generators, powermeters or other passive or active circuit elements are specified to operate in certain frequency ranges. They have source and input impedances of typically $50\,\Omega$ which matches the wave propagation impedance of coaxial cable connectors with polyethylene dielectric coating, cf. [156]. Several device concepts are available in order to apply excitation fields to specimens. The two major types are cavity waveguides and transmission lines, [155]. Their impedance matching with respect to $50\,\Omega$ circuitry depends on geometric issues as well as on properties of the used dielectric materials. In general,

cavity resonators are restricted to a narrow frequency band and only specific electromagnetic modes are available [155]. Yet, when using these devices high powers can be reached and they are a good choice when probing the nonlinearity of the LLG. Transmission lines like e.g. microstrips, striplines, slotlines and coplanar waveguides, [155], typically provide a large frequency band in which the $50\,\Omega$ impedance matching is fulfilled to a good degree. For studies of frequency dependent effects like FMR and spin pumping this property is valuable. Furthermore, transmission lines bring the advantage that they can be used for insertion of microstructured samples into the excitation field in a very accurate way. Thus, pure in-plane or out-of-plane fields as specified in Secs. 3.3 and 3.5 can be implemented. Furthermore, voltage probes can be accurately connected to specimens. For these reasons transmission lines have been used throughout this thesis. All studies that will be presented have been conducted structuring coplanar waveguides (CPW) on semi-insulating GaAs- or Si- substrates.
The first section of this chapter provides details about the appropriate conceptual design of CPWs for FMR and SP measurements in the 2 to 20 GHz regime. Peculiarities concerning dimensions of both CPW and integrated NiFe/NM-bilayers will be discussed and an appropriate laboratory frame will be introduced. Furthermore, simulations of current densities as a function of frequency will be presented. This allows for calculation of excitation field amplitudes using Ampere's law [111] in a numerical approach. The importance of these results estimating the cone angle of magnetization precession and the corresponding amplitude of spin currents will be pointed out. The section will end with detailed overview schematics of NiFe/NM bilayer wires connected to voltage probes all-integrated into a CPW. The two basic types with respect to excitation geometry, together with their geometrical limitations will be presented.
In the following sections of this chapter voltage signals measurable on grounds of geometric considerations will be discussed. The derived formulas set a powerful framework for assessing different voltage signals in terms of the underlying physical effects. Characterization of the ISHE in NM, AMR in FM and electromagnetic induction in the measurement circuitry will take place on the basis of expected line shapes as well as angular and frequency dependencies. This is essential when quantifying spin Hall angles α_{SH} from voltage signals in NiFe/NM bilayers.

4.1 Details about coplanar waveguides and sample design

A coplanar waveguide (CPW) consists of well-conducting signal and ground lines. Conducting material, typically Al, Cu, Ag or Au, can be readily deposited on semi-insulating substrates like GaAs or Si. The conceptual design of a CPW as used in this thesis is shown in Fig. 4.1a). As indicated by the name, the ground lines are to be on ground potential and the signal line has a certain voltage amplitude relative to it. It is also shown how to possibly integrate a NiFe/NM bilayer into the CPW. The two displayed positions correspond to the two basic situations of almost pure in-plane and out-of-plane magnetic field generated by the CPW. A close-up of the CPW's central part which is shown in Fig. 4.1b) illustrates the respective magnetic field lines. A current I_{rf} of certain amplitude and frequency through the CPW along the y-direction generates a magnetic field according to Ampere's law which has x and z components [111]. For specification of directions see the coordinate system of the laboratory frame which is displayed in Fig. 4.1. On top of the signal line the magnetic field is parallel to the NiFe-film along the x-direction. In the gap between signal and ground line the field is perpendicular to it along z-direction.
In order to find the optimal electro-magnetic wave impedance of 50 Ω for the CPW in the desired range of 300 MHz-20 GHz the freely available software TX-LINE has been used. It is provided by NATIONAL INSTRUMENTS and it allows for optimization of impedance characteristics of distinct transmission line geometries. Parameters to be entered are the relative dielectric constant ϵ_{r} of the substrate and the conductivity σ of the transmission line material. The impedance is then defined by geometric means. The thickness of the substrate $t_{\mathrm{substrate}}$ and the transmission lines t_{TL} as well as the width of the signal line w_{SL} and the gap between signal and ground lines w_{gap} are the determining factors. These parameters are explained in Fig. 4.1b). GaAs has a dielectric constant of $\epsilon_{\mathrm{r}} = 12.9$. The thickness of the substrate usually was $t_{\mathrm{substrate}} = 460\,\mu\mathrm{m}$. For the transmission line's conductive material Au has been chosen, viz. $\sigma = 4.1 \times 10^7\,\Omega^{-1}\,\mathrm{m}^{-1}$ and $t_{\mathrm{TL}} = 140\,\mathrm{nm}$. For the remaining adjustable parameters the 50 Ω impedance condition in the low GHz-regime results in $w_{\mathrm{SL}} = 50\,\mu\mathrm{m}$ and $w_{\mathrm{gap}} = 30\,\mu\mathrm{m}$. This parameter set was used for the fabrication of most CPWs in this thesis. Note that the mutual relationship of w_{SL} and w_{gap} principally allows several different value sets. In the present case the 30 µm wide gap has been estimated to be optimal for integrating NiFe/NM specimens which are structured in the shape of $L = 400\,\mu\mathrm{m}$ long and $w = 5\,\mu\mathrm{m}$ wide wires. NiFe and NM layers of typically $t_{\mathrm{NiFe}} = t_{\mathrm{NM}} = 10\,\mathrm{nm}$ each (the exact number will be annotated when discussing the measurements) have been fabricated. These dimensional conditions allow for a magnetic excitation field which complies with both homogeneity across and suitable amplitude inside the NiFe/NM bilayer. The used geometrical parameters for NiFe/NM bilayers are specified in the close-up schematic Fig. 4.1c). The excitation field amplitude corresponds to the 0.1 mT-regime for microwave powers ranging from 10 to 500 mW. Corresponding results of numerical calculations can

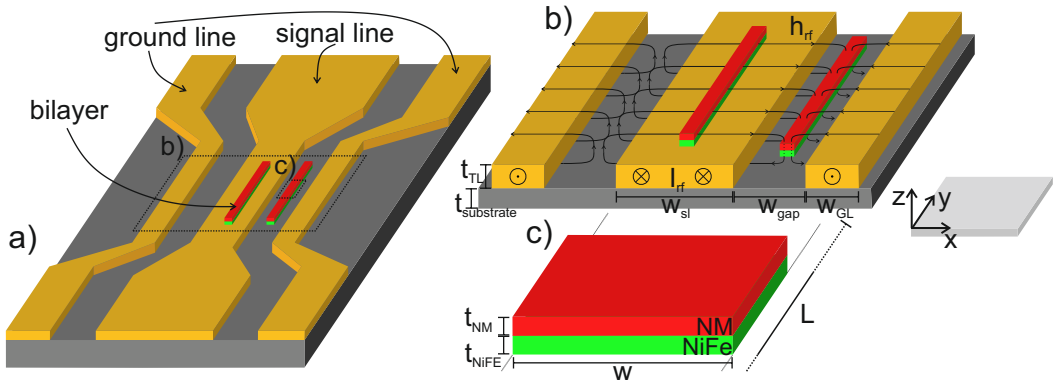

Figure 4.1: In a) a typical coplanar waveguide consisting of two so-called ground lines and one signal line is presented. Shown are the two basic cases of implementing an in-plane driving field, i.e. placing a FM/NM bilayer on top of the signal line and an out-of-plane excitation, i.e. location in the gap between signal and ground line. In b) the excitation geometries are depicted in detail in a close-up of the CPW's central part. Shown is a snap shot of magnetic field lines generated around signal and ground lines due to oppositely directed microwave currents flowing through them. c) focuses on the central region of a NiFe/NM bilayer wire. Furthermore for orientation a coordinate system (x, y, z) is displayed.

be found in Sec. 4.1.1.

The equations in Sec. 3.5 which are describing the injected spin currents from SP suggest that it is crucial to know the excitation field amplitudes in order to quantify these spin currents. It is not possible to measure the excitation field directly in the used experimental approach. From FMR-measurements only the susceptibilities, viz. the ratio of excitation field amplitude and corresponding dynamic magnetization component can be extracted. However, transmission lines are well-studied objects, see e.g. the detailed analyses of different geometries in [157], and excitation fields can be estimated by appropriate electromagnetic simulations. Two points of view are valuable. The lumped equivalent of transmission lines can be used to quickly estimate impedance and power transfer in rf-elements. It is the model of choice for conceptual design purposes and is for example used by the program TX-LINE, which refers to a corresponding parameter database. If one wants to know exactly the electric and magnetic fields present, one has to solve Maxwell's equations for the transmission line at hand [157]. For this purpose several software packages are available. For its specialization towards high frequent electromagnetic simulations with transmission lines the software provided by SONNET has been used. It not only allows for accurate estimation of transmission properties, but also simulates the current densities inside the transmission lines.

4.1.1 Calculation of magnetic excitation field amplitudes

The simple Ampereian picture which describes the magnetic field generated around a live conductor, see e.g. in [111], cannot be applied without precautions to currents in the GHz-regime. Assume that electromagnetic waves are propagating along the y-direction of the CPW which is displayed in Fig. 4.1a). In a CPW quasi transverse electro-magnetic (TEM) modes are supported, cf. [155]. The local electric **E**- and magnetic **H**-field are perpendicular to each other and to the direction of propagation, see Fig. 4.1b) for the **H**-field. This is described by applying Maxwell's equations to a general homogeneous, lossy medium, [155]:

$$\nabla \times \mathbf{E} = -i\omega\mu\mathbf{H} \tag{4.1}$$

$$\nabla \times \mathbf{H} = i\omega\epsilon\mathbf{E} + \sigma\mathbf{E} \tag{4.2}$$

Here complex number representation for the electric and magnetic field is used. Derivatives with respect to time are simply represented by scaling the fields with $i\omega$, $\mathscr{E}(x,y,z,t) = \Re(\mathbf{E}(x,y,z)\exp(i\omega t))$ and $\mathscr{H}(x,y,z,t) = \Re(\mathbf{H}(x,y,z)\exp(i\omega t))$. The frequency of the electro-magnetic wave is $\omega/2\pi$, $\mu = \mu' + i\mu''$ is the complex magnetic permeability, $\epsilon = \epsilon' - i\epsilon''$ is the complex electric permittivity and σ is the conductivity of the waveguide. For the electric field the following wave-equation holds, [155]:

$$\nabla^2\mathbf{E} + \omega^2\mu\epsilon\left(1 - i\frac{\sigma}{\omega\epsilon}\right)\mathbf{E} = 0 \tag{4.3}$$

It is common to define the complex propagation constant for the medium as follows, [155]:

$$\gamma = \alpha + i\beta = i\omega\sqrt{\mu\epsilon}\sqrt{1 - i\frac{\sigma}{\omega\epsilon}} \tag{4.4}$$

Assuming an electric field which has only a nonzero x-component and is uniform in x- and y-direction reduces Eq. (4.3) to:

$$\frac{\partial^2 E_x}{\partial z^2} - \gamma^2 E_x = 0 \tag{4.5}$$

The general solution of this differential equation is given by:

$$E_x(z) = E^+\exp(-\gamma z) + E^-\exp(\gamma z) \tag{4.6}$$

The first term on the right hand side describes a wave traveling into the positive z-direction and second term describes a wave traveling into the $-z$-direction. In the time domain the propagation factor of the positively traveling wave $\exp(-\gamma z)$ is given by the following equation:

$$\begin{aligned}\Re(\exp(-\gamma z)\exp(i\omega t)) &= \Re(\exp(-\alpha z)\exp(-i\beta z)\exp(i\omega t) \\ &= \exp(-\alpha z)\cos(\omega t - \beta z)\end{aligned} \tag{4.7}$$

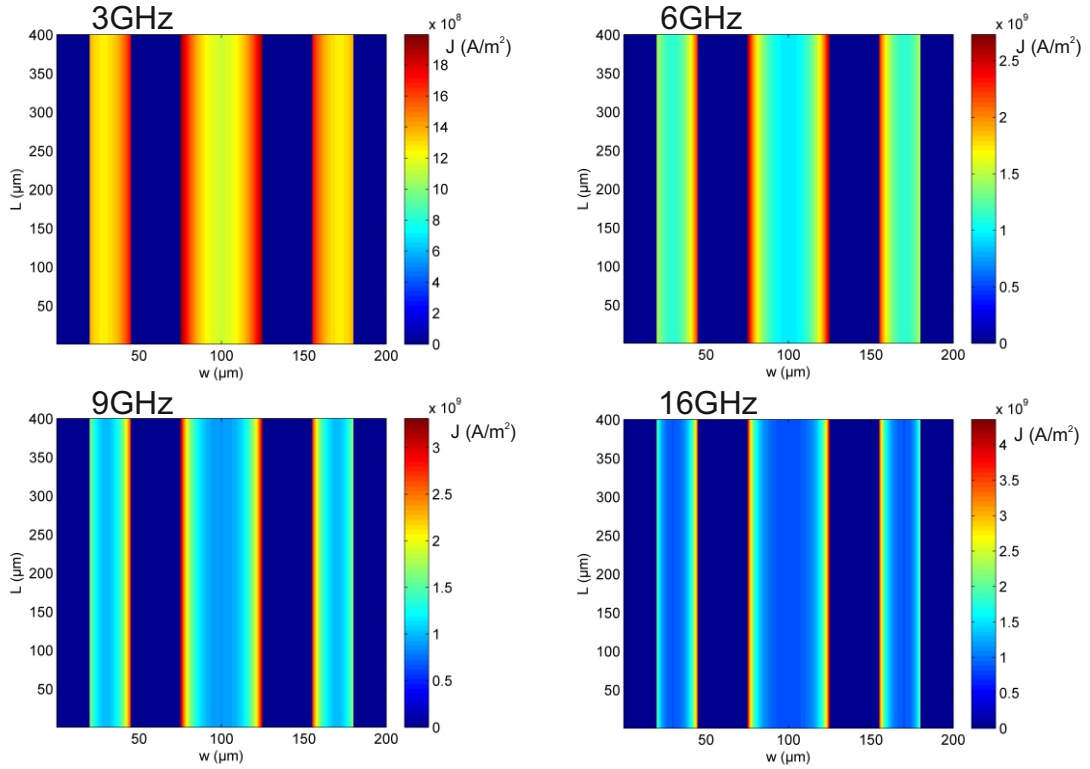

Figure 4.2: Displayed are current densities inside a CPW's signal and ground lines as simulated with the SONNET software feeding in an rf signal of 1 V amplitude and 10 mW dissipated power. Colors red to blue indicate high to low current densities. The results for four different frequencies in the range of 3 to 16 GHz are plotted.

Solutions for electromagnetic waves through media always adopt this general form of an exponentially damped harmonic wave, where the damping factor α describes real losses and β the phase shift of the wave. For good conductors $\omega\epsilon << \sigma$, which means that dielectric are small compared to conductivity losses. For a specification of different loss types the reader is referred to [157]. Under circumstances of dominant conductivity loss Eq. (4.4) reduces to:

$$\gamma = i\omega\sqrt{\mu\epsilon}\sqrt{\frac{\sigma}{j\omega\epsilon}} = (1+i)\sqrt{\frac{\omega\mu\sigma}{2}} \tag{4.8}$$

The real part of this equation corresponds to α and this defines the skin depth δ_s of the electric field into the material by:

$$\delta_s = \frac{1}{\alpha} = \sqrt{\frac{2}{\omega\mu\sigma}} \tag{4.9}$$

The amplitude of the current density decreases exponentially on the characteristic length scale δ_s inside conducting transmission lines [157]. For Au, assuming a

conductivity of $\sigma = 4.1 \times 10^7\,\Omega^{-1}\,\mathrm{m}^{-1}$ and a frequency of the propagating wave of 10 GHz, the skin depth is $\delta_s \approx 800\,\mathrm{nm}$, [155]. This result will now be interrelated to the geometric parameters, see Fig. 4.1b), of the CPW in use. As $t_{TL} << \delta_s$ one can assume a homogeneous current density distribution inside the CPW along z. However, along the x-direction of the CPW lines this statement cannot be made, w_{SL} and $w_{GL} >> \delta_s$. In order to extract the local amplitudes of in-plane and out-of-plane excitation fields it is necessary to know the distribution of current density layers as a function of frequency along the x-direction. To this end, electro-magnetic simulations have been carried out using the software provided by SONNET. Fig. 4.2 shows results of a simulation in the frequency band of 3 to 16 GHz of the current densities inside a CPW which has dimensions $w_{SL} = 50\,\mu\mathrm{m}$, $w_{gap} = 30\,\mu\mathrm{m}$ and $w_{GL} = 25\,\mu\mathrm{m}$. The numerical simulations of SONNET assume a grid of 5 nm along the x-direction. For each grid node the simulations yield one distinct value for the current density. As expected from the skin depth considerations the shift of increased current densities towards the boundaries of the transmission lines is proportional to the frequency. The frequency dependent magnetic field inside the CPW can now be calculated by adding up the contributions of all current density paths using Biot-Savart's law. The basic formula for this is, [111]:

$$\mathbf{B}(r) = \frac{\mu_0}{2\pi r} I \mathbf{e}_y \times \frac{\mathbf{r}}{r} \tag{4.10}$$

r is the distance between one current path, with the current I, and the location where the magnetic flux density is calculated. Adding up Eq. (4.10) the magnetic field both around and inside the CPW can be calculated at every point. As the magnetic specimen is usually located 50 nm above or below the CPW in the present experiments, the following results correspond to $\mathbf{B}(x,z) = \mathbf{B}(x, 50\,\mathrm{nm})$. Fig. 4.3a) shows the calculated amplitudes of the excitation field. The data correspond to a line scan along the x-direction at a fixed y-position. As already explained in the considerations about the conceptual design of the CPW the driving field $\mathbf{h}$ contains x- (in-plane) and z- (out-of-plane) components. These correspond to the black and red lines in Fig. 4.3a), respectively. It is evident that on top of the signal line an almost pure in-plane field is present. The exact numbers show that the out-of-plane field is at least three orders of magnitude smaller above the signal line's center position. The opposite reasoning holds for the in-plane field at the center of the gap between signal and ground line, which obviously is the position of a pure out-of-plane field. The magnetic specimens and respective bilayers have always been positioned at the center of signal line or gap respectively. Fig. 4.3b) shows the results for corresponding in-plane $h_{ip} = h_x$ and out-of-plane $h_{oop} = h_z$ excitation field components as a function of frequency. From these data it is clear, that h_{ip} at the center of the signal line depends strongly on the frequency. It varies as much as 30% in the range of 3 to 16 GHz. For h_{oop} this effect is much less pronounced and the data suggest that the field value above 6 GHz is constant to a good extent. The results for h_{ip} and h_{oop} correspond to current densities when a voltage of 1 V amplitude is put across the CPW. For the present 50 Ω system this is

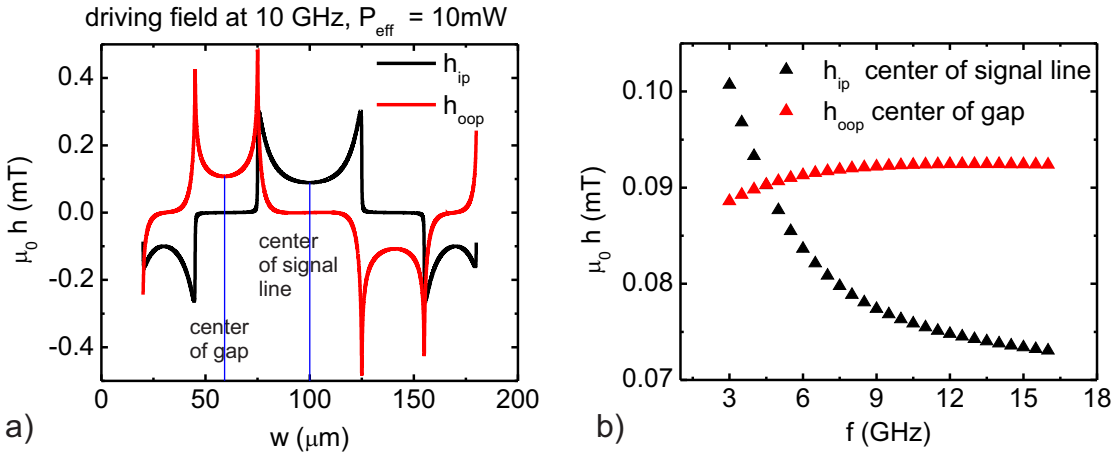

Figure 4.3: In a) in-plane and out-of-plane driving fields, $h_{\mathrm{ip}} = h_x$ and $h_{\mathrm{oop}} = h_z$ respectively, generated by a CPW ($w_{\mathrm{SL}} = 50\,\mu\mathrm{m}$, $w_{\mathrm{gap}} = 30\,\mu\mathrm{m}$ and $w_{\mathrm{GL}} = 25\,\mu\mathrm{m}$) are shown. The results correspond to a 10 GHz rf-current and a dissipated power of $P_{\mathrm{eff}} = 10\,\mathrm{mW}$. Both the center of the gap and the signal line are marked with blue solid lines. In b) h_{ip} above the center of the signal line and h_{oop} at the center of the gap are plotted as a function of rf-current frequency.

associated with a total electric power of 20 mW. However, this includes both ohmic and reactive contributions. In order to draw conclusions about the effective driving field, in subsequent considerations it will be essential to relate a measured loss in the transmission line with the simulated excitation field and therefore it is only the ohmic power that matters.

4.1.2 Integration of ferromagnetic / normal metal bilayers into coplanar waveguide structures

Bilayers of NiFe and various NM, such as Pt, Au, Ta, Cu, Al, and alloys of $\mathrm{Au}_x\mathrm{Pt}_{1-x}$ have been integrated into CPWs, in order to measure SP-ISHE. In Fig. 4.4 the single preparation steps 1 to 4, starting from substrate and ending with an out-of-plane excitation geometry sample for measuring the ISHE, are shown. The preparation steps for an in-plane excitation geometry are analogous. The NiFe/NM specimens have been structured in the shape of 400 µm long and 5 µm wide wires using electron beam lithography (EBL). NiFe and NM layers of typically 10 nm each, were deposited successively using magnetron sputtering or thermal evaporation onto a semi-insulating GaAs(001)-substrate. In order to get a clean NiFe/NM interface, the layers were deposited successively inside a UHV-chamber. In individual cases it was started off with extended bilayer films. Correspondingly, the first preparation step includes an ion-beam etching procedure to define wires. In order to study voltages due to ISHE the bilayer wires were connected to well-conducting probes.

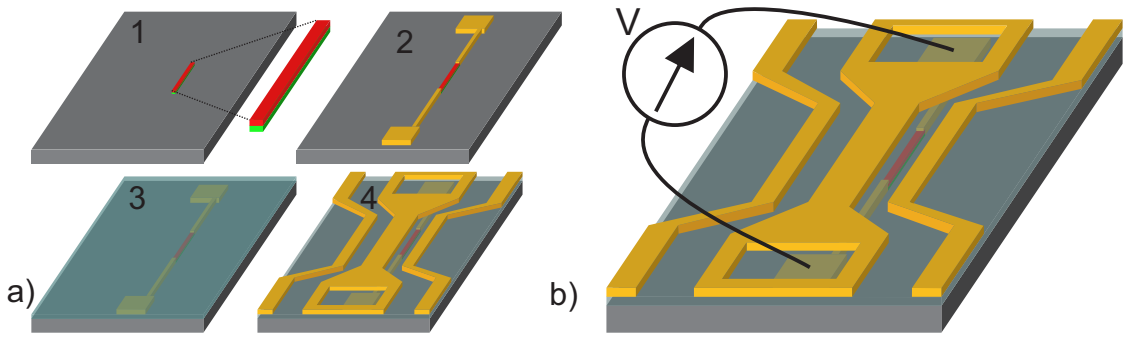

Figure 4.4: In a) the four fabrication steps integrating a FM/NM-bilayer wire into a CPW-structure, in order to measure SP-ISHE, are shown. In the first step FM and NM bilayers are deposited on a substrate (usually GaAs(001)). In the second step the bilayer wires are connected to voltage probes. The third step consists of covering the existing structure with Al_2O_3. In the final, fourth step the CPW is deposited. It is functionalized in terms of accessibility of voltage probes via wire bonding. In b) the final sample including a voltmeter is shown. Note that the preparation of an out-of-plane excitation geometry sample is depicted.

They consist of adhesive Ti (typically 10 nm) and conductive Au layer (90 to 100 nm thick). The electrical connections have been chosen as wide as the bilayer wires. This is instrumental with respect to measuring rf-voltage signals generated by ac-ISHE. This will be further specified in the corresponding chapter 9. To allow for Al-wire bonding the voltage probes end as 250 µm wide squares. After covering the bilayer and its connections with an insulating 50 nm thick layer of Al_2O_3 by atomic layer deposition, a CPW consisting of 10 nm thick Ti and 140 nm thick Au was structured on top of the NiFe/NM-electrical-connection-set. Squares at the ends of the signal line were left free of conducting material. This makes the voltage probes accessible for bonding. Note that it is in principle also possible to start with the CPW on the semi-insulating substrate and put the bilayer and the connections on top. However, this stacking order has proved to be less reliable with respect to working electrical connections and therefore has been dismissed.
Fig. 4.5 shows the final samples of pure in-plane and pure out-of-plane excitation geometry. Note that in 4.5b) the bilayer is shown on top of the CPW. This is only for the purpose of easier viewing. In reality as stated above the CPW-bilayer stacking order is reversed. The fixed position of the voltage probes, along the y-axis, plus the available driving field components h_x and h_z introduce certain geometric limitations when probing physical effects connected with FMR. The precessing magnetization has components $(M_{x'}, m_{y'}(t), m_z(t))$. The relative orientation of the magnetization with respect to voltage probes and excitation fields is determined by the angle ϕ_H as specified in the coordinate system shown in Fig. 4.5. In the following section this coordinate system will be used together with the results about pumped spin

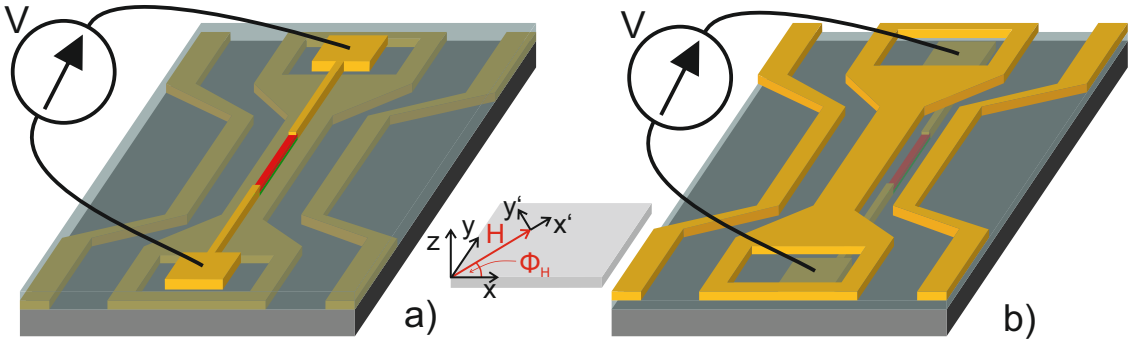

Figure 4.5: The bilayer together with its connections is integrated either on top of the signal line a) or in the gap between signal and ground line b). a) is the in-plane and b) the out-of-plane excitation field configuration. Also shown is the coordinate system which defines the orientation of the voltage probes and the in-plane driving field relative to the external field $\mathbf{H}$ via the angle ϕ_{H}.

currents at FMR, as derived in Sec. 3.4, to characterize voltages due to ISHE. This will be done explicitly for both geometries presented in Fig. 4.5a) and b).

4.2 Voltage signals due to inverse spin Hall effect

A spin current created by spin pumping at the FM/NM interface as specified in Eq. (3.73) is injected into NM. Fig. 4.6 gives an overview of the different types of generated voltages due to ISHE. In this picture the static component of $\mathbf{M}(t)$ points along $\mathbf{e}_x$ and the dynamics is confined to the y-z-plane. This leads to a dc spin current density into NM with its direction $\mathbf{e}_{j_\mathrm{s}}$ parallel to $\mathbf{e}_z$ and its polarization $\mathbf{s}$ parallel to $\mathbf{e}_x$. Therefore, according to Eq. (2.22), which shall be reprinted here for easier viewing,

$$\mathbf{j}_\mathrm{c} = \frac{2e}{\hbar}\alpha_\mathrm{SH}\mathbf{j}_\mathrm{s} \times \mathbf{e}_\mathrm{s}$$

a dc-voltage along $\mathbf{e}_y = \mathbf{e}_z \times \mathbf{e}_x$ is detectable. In Fig. 4.6 this is indicated by the yellow colored voltage probes. The ac spin current is defined by the oscillating part of the polarization $\mathbf{s}(t)$ which is confined to the y-z-plane. Using the fact that its direction $\mathbf{e}_{j_\mathrm{s}}$ is along $\mathbf{e}_z$ and not time-dependent, Eq.(2.22) leads to a voltage oscillating at the frequency of the precessing magnetization vector and an ac voltage is detectable along $\mathbf{e}_x = \mathbf{e}_z \times (-\mathbf{e}_y)$. In Fig. 4.6 this is indicated by the red-black colored voltage probe set.
In order to get a comprehensive and quantitative feeling for the voltages due to SP-ISHE for the experimental configuration at hand, what follows is a detailed description based on the geometries shown in Fig. 4.5. To this end, the schematics

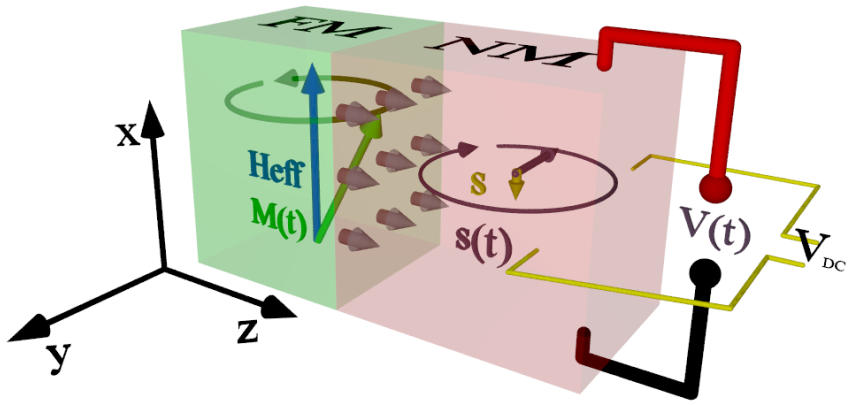

Figure 4.6: The schematic overview of spin pumping in an FM/NM bilayer is complemented with an appropriate coordinate system. The displayed voltage probes correspond to the expected ac and dc charge currents generated due to ISHE, see Eq. 2.22.

shown in Fig. 4.7 are used. Figs. 4.7a) and b) depict the situation of dc- and ac-**E**-field generation due to ISHE in a FM/NM bilayer, respectively. In general the static component of $\mathbf{M}(t)$ is confined to the x-y plane and points along $\mathbf{e}_{x'}$ at an angle ϕ_{H} relative to $\mathbf{e}_x$. The dynamics of $\mathbf{M}(t)$ takes place in the y'-z-plane. Since the spin current density always flows into NM along the z-direction, the dc-**E**-field due to ISHE builds up along $\mathbf{e}_{y'}$ and the corresponding ac-**E**-field is parallel to $\mathbf{e}_{x'}$. The experimental setup is conceptually designed such that the measurable quantity is a voltage V along the $\mathbf{e}_y$ direction. In this respect the first task is to correctly describe the transformation of $j_{\mathrm{s}}(z)$ into $j_{\mathrm{c}}(z)$ and subsequently into V.
The starting point is to normalize $\mathbf{I}^{\mathrm{pump}}_{\mathrm{s,\,net}}$ (Eq. (3.73)) with respect to the interface area F. This yields the spin current density injected into NM:

$$\mathbf{j}^{\mathrm{pump}}_{\mathrm{s,\,net}} = \frac{\hbar}{4\pi}\frac{\tilde{g}^{\uparrow\downarrow}_{\mathrm{F}}\omega}{M_{\mathrm{S}}^2}\begin{pmatrix} \Im(m^*_{y'}m_z) \\ -M_{\mathrm{S}}(\Re(m_z)\sin(\omega t) + \Im(m_z)\cos(\omega t)) \\ M_{\mathrm{S}}(\Re(m_{y'})\sin(\omega t) + \Im(m_{y'})\cos(\omega t)) \end{pmatrix} \tag{4.11}$$

In this equation the normalization with respect to F is implicit in the factor $\tilde{g}^{\uparrow\downarrow}_{\mathrm{F}} = \frac{\tilde{g}^{\uparrow\downarrow}}{F}$, the spin mixing conductivity. Note that $\mathbf{j}^{\mathrm{pump}}_{\mathrm{s,\,net}}$ is represented in the coordinate system (x', y', z) and so will be the charge current $\mathbf{j}_{\mathrm{c}}$ generated due to ISHE. At first the measurable dc voltage shall be under consideration. The time average of the pumped spin current density is given by integration over the precession period T.

$$\mathbf{j}^{\mathrm{pump}}_{\mathrm{s,\,dc,\,net}} = \frac{1}{T}\int_0^T \mathbf{j}^{\mathrm{pump}}_{\mathrm{s,\,net}} = \frac{\hbar}{4\pi}\frac{g^{\uparrow\downarrow}_{\mathrm{F}}\omega}{M_{\mathrm{S}}^2}\begin{pmatrix} \Im(m^*_{y'}m_z) \\ 0 \\ 0 \end{pmatrix} \tag{4.12}$$

This equation is to be inserted into Eq. (2.22) realizing that $\mathbf{j}_{\mathrm{s}} = |\mathbf{j}^{\mathrm{pump}}_{\mathrm{s,\,dc,\,net}}|\mathbf{e}_z$ and $\mathbf{e}_{\mathrm{s}} = -\mathbf{e}_{x'}$. Accounting for spin relaxation in the diffusive regime the z-dependence

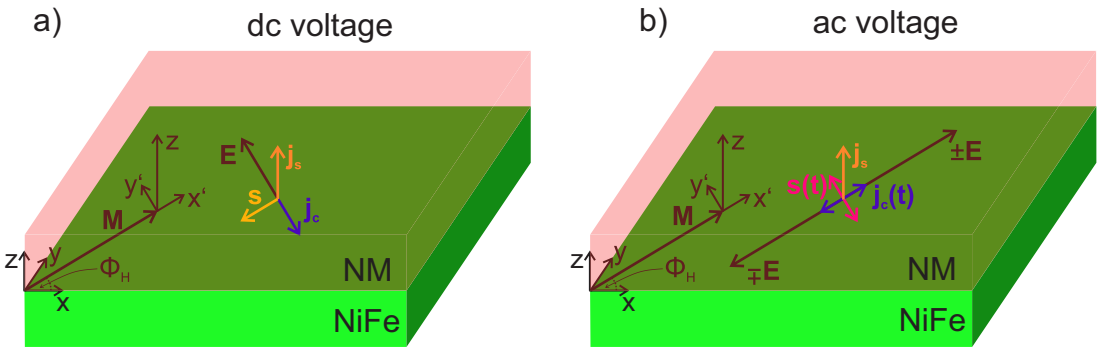

Figure 4.7: The schematics depict the general geometric circumstances of electric fields generated due to ISHE when a spin current density $j_s\mathbf{e}_z$ is pumped into NM and the static component of $\mathbf{M}(t)$ in FM is located at an angle ϕ_H in the x-y-plane. In a) the dc-electric-field generated along $\mathbf{e}_{y'}$ and in b) the ac-electric field generated parallel to $\mathbf{e}_{x'}$ is shown.

of the spin current density's absolute value in NM is given by [49, 51, 63]:

$$j_s(z) = j_s(0)\frac{\sinh\left(\frac{t_{NM}-z}{\lambda_{sd}}\right)}{\sinh\left(\frac{t_{NM}}{\lambda_{sd}}\right)} \tag{4.13}$$

$j_s(0)$ is the spin current density's absolute value at the FM/NM interface and λ_{sd} is the spin diffusion length of NM. Note that Eq. (4.13) is the solution of spin drift diffusion equation for steady state and zero electric field (Eq. (2.12)), for the boundary condition of vanishing spin current at $z = t_{NM}$ ($j_s(t_{NM}) = 0$).
The connection between the amplitude of the charge current and the spin current density as a function of z is given analogously to Eq. (2.22) by:

$$j_c(z)\mathbf{e}_{y'} = \frac{2e}{\hbar}\alpha_{SH} j_s(z)\mathbf{e}_z \times \mathbf{e}_{x'} \tag{4.14}$$

The average charge current density through the whole FM/NM bilayer is given by integration of the spin current density over the bilayer along the z-axis and devision by $t_{NM} + t_{FM}$:

$$\begin{aligned} j_c =< j_c(z) > &= \frac{2e}{\hbar}\alpha_{SH}\frac{1}{t_{NM}+t_{FM}}\int_0^{t_{NM}} dz j_s(z) \\ &= \frac{2e}{\hbar}\alpha_{SH} j_s(0)\frac{\lambda_{sd}}{t_{NM}+t_{FM}}\tanh\left(\frac{t_{NM}}{2\lambda_{sd}}\right) \end{aligned} \tag{4.15}$$

Note that there is no spin current density present inside FM and therefore the integration of j_c from $-t_{FM}$ to 0 is omitted in Eq. (4.15). The last equal sign results from the explicit integration.

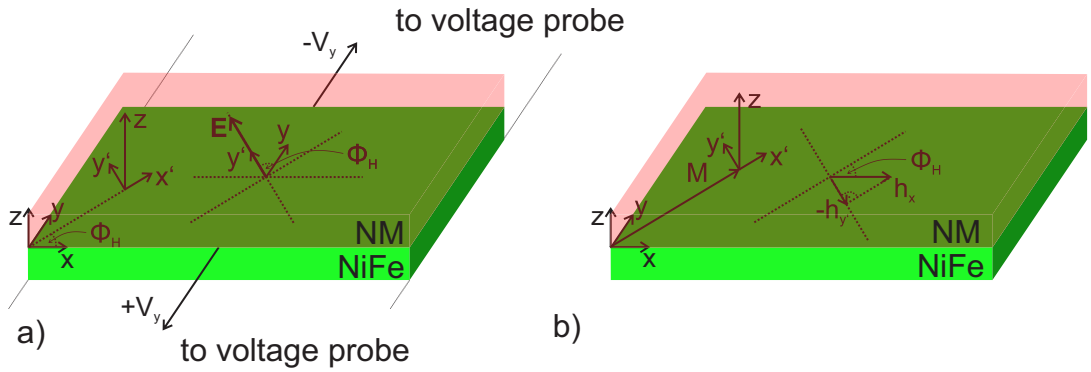

Figure 4.8: In a) the projection of the **E**-field due to dc-ISHE, which is along $\mathbf{e}_{y'}$, onto the voltage probe path along $\mathbf{e}_y$ using the angle ϕ_{H} is shown. In b) the projection of the in-plane driving field, which results from the CPW geometry given by $h_x\mathbf{e}_x$, onto $h_{y'}\mathbf{e}_{y'}$ using ϕ_{H} is explained.

The voltage along $\mathbf{e}_y$ is given by $V_y = \int_0^L \mathbf{E}\cdot\mathbf{dy}$. Using now Ohm's law $j_{\mathrm{c}}\mathbf{e}_{y'} = \sigma E\mathbf{e}_{y'}$ and the fact that the voltage probes are fixed along $\mathbf{e}_y$ the voltage measurable due to ISHE is given by:

$$\begin{aligned} V_{\mathrm{ISHE}} &= \frac{j_{\mathrm{c}}L}{\sigma}\mathbf{e}_{y'}\mathbf{e}_y = \frac{j_{\mathrm{c}}L}{\sigma}\cos(\phi_{\mathrm{H}}) \\ &= \frac{2e}{\hbar\sigma}\alpha_{\mathrm{SH}}\frac{\lambda_{\mathrm{sd}}}{t_{\mathrm{NM}}+t_{\mathrm{FM}}}\tanh\left(\frac{t_{\mathrm{NM}}}{2\lambda_{\mathrm{sd}}}\right)j_{\mathrm{s}}(0)L\cos(\phi_{\mathrm{H}}) \end{aligned} \tag{4.16}$$

Here it is used that $\phi_{\mathrm{H}} = \sphericalangle(\mathbf{e}_{y'}, \mathbf{e}_y)$ (for a schematic of the projection of $V_{y'}$ onto V_y see Fig. 4.8a)).
Replacing $j_{\mathrm{s}}(0)$ in Eq. (4.16) by the x'-component of Eq. (4.12) yields the general equation for a dc voltage due to SP-ISHE:

$$V_{\mathrm{ISHE}} = \alpha_{\mathrm{SH}}\frac{e}{\sigma}\frac{g_{\mathrm{F}}^{\uparrow\downarrow}\omega}{2\pi M_{\mathrm{S}}^2}\frac{\lambda_{\mathrm{sd}}}{t_{\mathrm{NM}}+t_{\mathrm{FM}}}\Im(m_{y'}^* m_z)\tanh\left(\frac{t_{\mathrm{NM}}}{2\lambda_{\mathrm{sd}}}\right)L\cos(\phi_{\mathrm{H}}) \tag{4.17}$$

The line shape is given by the representation of $\Im(m_{y'}^* m_z)$ in terms of the driving field and the applicable components of the susceptibility tensor. The appropriate line shapes for pure in-plane and pure out-of-plane driving fields have been delineated in Sec. 3.5.
For the pure in-plane driving field case a further parametrization of V_{ISHE} in terms of the angle ϕ_{H} is needed. The representation of $\mathbf{h} = (h_x, 0, 0)$ in terms of $h_{y'}$ has to be found. As from the schematic presented in Fig. 4.8b) the following relationship holds:

$$h_{y'} = -h_x\sin(\phi_{\mathrm{H}}) \tag{4.18}$$

Hence, the voltage due to ISHE under circumstances of an in-plane driving field as a function of external static field H is described by the following function:

$$\begin{aligned} V_{\mathrm{ISHE}}^{\mathrm{ip}} &= \alpha_{\mathrm{SH}} \frac{e}{\sigma} \frac{g_{\mathrm{F}}^{\uparrow\downarrow} \omega}{2\pi M_{\mathrm{S}}^2} \frac{\lambda_{\mathrm{sd}}}{t_{\mathrm{NM}} + t_{\mathrm{FM}}} \\ &\times \Im(\chi_{y'y'}^{\mathrm{res}}) \chi_{zy'}^{\mathrm{res}} h_x^2 \tanh\left(\frac{t_{\mathrm{NM}}}{2\lambda_{\mathrm{sd}}}\right) L \\ &\times \frac{(\Delta H)^2}{(H - H_0)^2 + (\Delta H)^2} \cos(\phi_{\mathrm{H}}) \sin^2(\phi_{\mathrm{H}}) \end{aligned} \tag{4.19}$$

For the out-of-plane driving field case the factor $\sin^2(\phi_{\mathrm{H}})$ does not occur since $\mathbf{e}_{z'} = \mathbf{e}_z$ and the following relation holds:

$$\begin{aligned} V_{\mathrm{ISHE}}^{\mathrm{oop}} &= \alpha_{\mathrm{SH}} \frac{e}{\sigma} \frac{g_{\mathrm{F}}^{\uparrow\downarrow} \omega}{2\pi M_{\mathrm{S}}^2} \frac{\lambda_{\mathrm{sd}}}{t_{\mathrm{NM}}} \\ &\times \Im(\chi_{zz}^{\mathrm{res}}) \chi_{y'z}^{\mathrm{res}} h_z^2 \tanh\left(\frac{t_{\mathrm{NM}} + t_{\mathrm{FM}}}{2\lambda_{\mathrm{sd}}}\right) L \\ &\times \frac{(\Delta H)^2}{(H - H_0)^2 + (\Delta H)^2} \cos(\phi_{\mathrm{H}}) \end{aligned} \tag{4.20}$$

In the presence of both driving field types the voltage measurable due to ISHE is a sum of Eqs. (4.19) and (4.20).
These two equations are the basis for quantifying spin Hall angles of NM using the SP-ISHE method. Solving Eqs. (4.19) and (4.20) for α_{SH} leads to the following formulae for in-plane and out-of-plane driving field cases respectively:

$$\alpha_{\mathrm{SH}} = \frac{V_{\mathrm{ISHE}}^{\mathrm{ip}} \sigma (t_{\mathrm{NM}} + t_{\mathrm{FM}}) M_{\mathrm{S}}^2}{e f g_{\mathrm{F}}^{\uparrow\downarrow} \Im(\chi_{y'y'}^{\mathrm{res}}) \chi_{zy'}^{\mathrm{res}} |h_x|^2 l \lambda_{\mathrm{sd}} \tanh\left(\frac{t_{\mathrm{NM}}}{2\lambda_{\mathrm{sd}}}\right) \cos(\phi_{\mathrm{H}}) \sin^2(\phi_{\mathrm{H}})} \tag{4.21}$$

$$\alpha_{\mathrm{SH}} = \frac{V_{\mathrm{ISHE}}^{\mathrm{oop}} \sigma (t_{\mathrm{NM}} + t_{\mathrm{FM}}) M_{\mathrm{S}}^2}{e f g_{\mathrm{F}}^{\uparrow\downarrow} \Im(\chi_{zz}^{\mathrm{res}}) \chi_{y'z}^{\mathrm{res}} |h_z|^2 l \lambda_{\mathrm{sd}} \tanh\left(\frac{t_{\mathrm{NM}}}{2\lambda_{\mathrm{sd}}}\right) \cos(\phi_{\mathrm{H}})} \tag{4.22}$$

Note that Eqs. (4.21) and (4.22) are evaluated at FMR, viz. $H = H_0$. $V_{\mathrm{ISHE}}^{\mathrm{ip}}$ and $V_{\mathrm{ISHE}}^{\mathrm{oop}}$ are the amplitudes of the symmetric line shapes of Eqs. 4.19 and 4.20, respectively. α_{SH} depends on many parameters but in principle all of them, though with distinct material specific challenges, can be measured for a given FM/NM hybrid. Note that the conductivity σ to be taken in the evaluation of α_{SH} is dependent on the definition of V_{ISHE}. If one is defining V_{ISHE} as the voltage which is picked off across the whole bilayer including a possibly conducting FM like NiFe, σ must also include this layer. If one would like to define V_{ISHE} as the exclusive voltage drop across NM the conductivity of NM has to be used in Eqs. (4.21) and (4.22). This might be indicated by replacing σ by σ_{NM}.
Concentrating on the ac-components of the spin current density, Eq. (4.11), the following formula holds:

$$\mathbf{j}_{\mathrm{s,\,ac,\,net}}^{\mathrm{pump}} = \frac{\hbar}{4\pi} \frac{g_{\mathrm{F}}^{\uparrow\downarrow} \omega}{M_{\mathrm{S}}^2} \begin{pmatrix} 0 \\ -M_{\mathrm{S}}(\Re(m_z)\sin(\omega t) + \Im(m_z)\cos(\omega t)) \\ M_{\mathrm{S}}(\Re(m_{y'})\sin(\omega t) + \Im(m_{y'})\cos(\omega t)) \end{pmatrix} \tag{4.23}$$

As for the dc-case the absolute value of the ac-component along the $\mathbf{e}_z$-direction is governed by Eq. (4.13) and application of Eq. (2.22) yields:

$$\mathbf{j}_\mathrm{c}(t) = \frac{2e}{\hbar}\alpha_\mathrm{SH}\frac{\lambda_\mathrm{sd}}{t_\mathrm{NM}+t_\mathrm{FM}}\tanh\left(\frac{t_\mathrm{NM}}{2\lambda_\mathrm{sd}}\right)|\mathbf{j}^\mathrm{pump}_{\mathrm{s,\,ac,\,net}}(0)|\mathbf{e}_z \times \frac{\mathbf{j}^\mathrm{pump}_{\mathrm{s,\,ac,\,net}}(0)}{|\mathbf{j}^\mathrm{pump}_{\mathrm{s,\,ac,\,net}}(0)|} \tag{4.24}$$

The nonzero components of $\mathbf{j}^\mathrm{pump}_{\mathrm{s,\,ac,\,net}}(0)$ are y' and z. The z-component has no relevance due to the cross product. Thus the generated ac charge current points along the $\mathbf{e}_{x'}$-direction and the time-dependent voltage using Ohm's law and the parametrization with respect to ϕ_H is given by:

$$\begin{aligned} V_\mathrm{ISHE}(t) = \alpha_\mathrm{SH}\frac{e}{\sigma}\frac{g_\mathrm{F}^{\uparrow\downarrow}\omega}{2\pi M_\mathrm{S}}\frac{\lambda_\mathrm{sd}}{t_\mathrm{NM}+t_\mathrm{FM}}(\Re(m_z)\sin(\omega t)+\Im(m_z)\cos(\omega t)) \\ \times\tanh\left(\frac{t_\mathrm{NM}}{2\lambda_\mathrm{sd}}\right)L\sin(\phi_\mathrm{H}) \end{aligned} \tag{4.25}$$

Expressing the dynamic magnetization components appearing in this equation by applicable susceptibilities, see Eqs. 3.85 and 3.87, for the in-plane driving field case the following relation holds:

$$\begin{aligned} V^\mathrm{ip}_\mathrm{ISHE}(t) = -\alpha_\mathrm{SH}\frac{e}{\sigma}\frac{g_\mathrm{F}^{\uparrow\downarrow}\omega}{2\pi M_\mathrm{S}}\frac{\lambda_\mathrm{sd}}{t_\mathrm{NM}+t_\mathrm{FM}} \\ \times\chi^\mathrm{res}_{zy'}h_x\tanh\left(\frac{t_\mathrm{NM}}{2\lambda_\mathrm{sd}}\right)L \\ \times\sqrt{\left(\frac{(\Delta H)^2}{(H-H_0)^2+(\Delta H)^2}\right)}\sin^2(\phi_\mathrm{H})\sin(\omega t) \end{aligned} \tag{4.26}$$

The $\sin^2(\phi_\mathrm{H})$-dependence results from the projection of $\mathbf{e}_{x'}$ onto $\mathbf{e}_{y'}$ due to the fixed direction of the voltage probes and from the representation of $h_{y'}$ as h_x, see Eq. (4.18). The minus sign in Eq. (4.26) is due to the fact that $h_{\mathrm{y'}}$ appears linearly. For the geometric conventions see Figs. 4.8b) and 4.9a).
For an out-of-plane driving field the following relation holds for the ac voltage due to ISHE:

$$\begin{aligned} V^\mathrm{oop}_\mathrm{ISHE}(t) = \alpha_\mathrm{SH}\frac{e}{\sigma}\frac{g_\mathrm{F}^{\uparrow\downarrow}\omega}{2\pi M_\mathrm{S}}\frac{\lambda_\mathrm{sd}}{t_\mathrm{NM}+t_\mathrm{FM}} \\ \times\chi^\mathrm{res}_{zz}h_z\tanh\left(\frac{t_\mathrm{NM}}{2\lambda_\mathrm{sd}}\right)L \\ \times\sqrt{\left(\frac{(\Delta H)^2}{(H-H_0)^2+(\Delta H)^2}\right)}\sin(\phi_\mathrm{H})\sin(\omega t) \end{aligned} \tag{4.27}$$

Comparing the expected dc- (Eqs. (4.19) and (4.20)) to the ac-voltages (Eqs. (4.26) and (4.27)), the peculiarities in the line shapes are striking. The dc-voltages caused by ISHE follow a symmetric Lorentzian line whereas the ac-signal is proportional

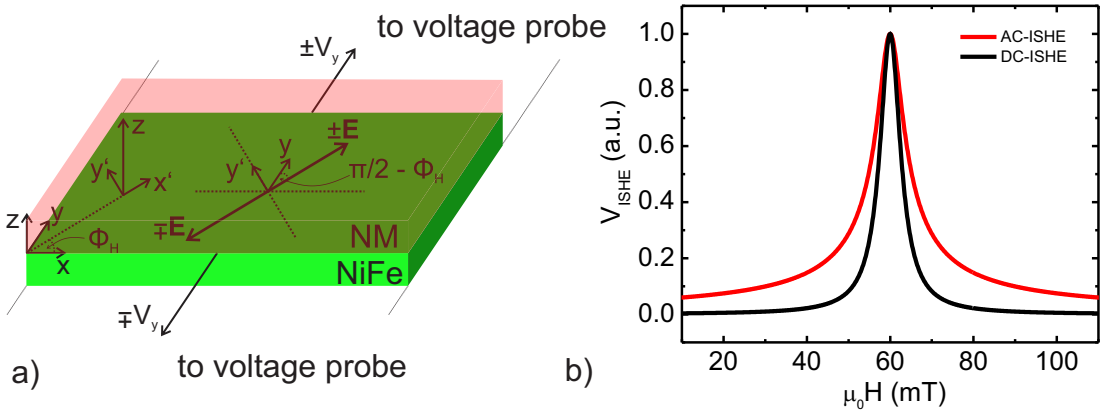

Figure 4.9: In a) the projection of the **E**-field due to ac-ISHE, which is parallel to $\mathbf{e}_{x'}$, onto the voltage probes along $\mathbf{e}_y$ using the angle $\pi/2 - \phi_\mathrm{H}$ is shown. In b) the expected voltage signal line shapes due to dc- and ac-ISHE are compared. The calculation of the plots assumes $\mu_0 H_0 = 60\,\mathrm{mT}$ and $\mu_0 \Delta H = 3\,\mathrm{mT}$

to its square root. The expected curves are explicitly plotted in Fig. 4.9b). The line shapes are plotted assuming a resonance field of $\mu_0 H_0 = 60\,\mathrm{mT}$ and a HWHM of $\mu_0 \Delta H = 3\,\mathrm{mT}$, values typical for NiFe/Pt under circumstances of a driving field frequency of 7 GHz, see Chapter 5.
As mentioned above one can ultimately fail concerning qualitative and especially quantitative studies of voltages due to ISHE, if disregarding possible parasitic effects. Therefore before presenting the experimental results the next two sections are used to discuss voltages due to AMR in FM and electromagnetic induction in the measurement circuit. The first is important for the understanding of the detected dc-voltages and the latter one might create signals to be confused with ac-ISHE.

4.3 Voltage signals due to anisotropic magnetoresistance AMR

In metallic FM like NiFe the AMR describes the dependence of resistance on the angle enclosed by a longitudinal current and the magnetization. Its microscopic origin is spin-orbit-coupling [79, 81, 111]. The total resistance of FM is described by the following formula [59]:

$$R(t) = R_0 + R_\mathrm{A} \cos^2(\theta(t)) \tag{4.28}$$

R_0 is the ordinary longitudinal resistance and $R_\mathrm{A} = R_\parallel - R_\perp$ is the additional contribution due to AMR. It is the difference between the resistance of FM when its magnetization **M** is parallel to when it is perpendicular to the current density

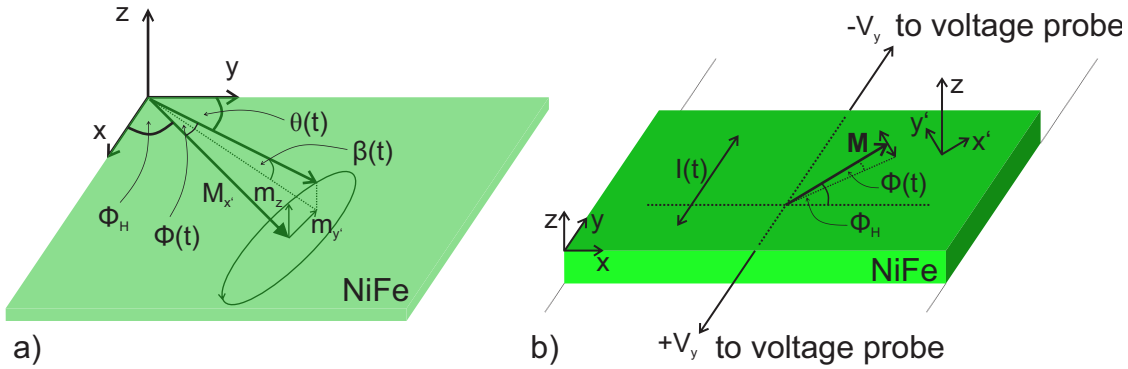

Figure 4.10: a) explains the angles describing the momentary position of the magnetization. $\Theta(t)$ is the angle of $\mathbf{M}(t)$ relative to the y-axis, $\phi(t)$ and $\beta(t)$ are its in-plane and out-of-plane components with respect to the NiFe film. In b) the projection of the magnetization precession onto the $x-y$-plane, viz. parallel to $\mathbf{e}_{y'}$ is shown. $m_{y'}$ is indicated by the double arrow and its direction is parametrized by $\phi_\mathrm{H}+\phi(t)$.

vector $\mathbf{j}_\mathrm{c}$. In general $\theta(t)$, the angle between $\mathbf{M}$ and $\mathbf{j}_\mathrm{c}$, and therefore the resistance $R(t)$ is time-dependent. Hence a the voltage detectable in a live FM is given by [59]:

$$V(t) = R(t)I(t) = R_0(I_0 + I(t)) + R_\mathrm{A}\cos^2(\theta(t))(I_0 + I(t)) \tag{4.29}$$

For an unbiased FM ($I_0 = 0$) integrated into a CPW such as presented in Fig. 4.5 the current consists purely of the time dependent component $I(t)$. Due to capacitive and inductive coupling a charge current flows along the y-direction through the NiFe/FM bilayer. When considering dc-voltages, the second term of Eq. (4.29) is the object of interest. Only this term gives rise to a dc-signal as it mixes two time-dependent quantities, $R(t)$ and $I(t)$.
As $I(t)$ is always along $\mathbf{e}_y$, $\theta(t)$ is the angle between the y-axis and the magnetization direction. Since the static component of $\mathbf{M}$ is always in-plane the static component of $\theta(t)$ is also in-plane. For the considerations of voltages due to ISHE it is convenient to use the parametrization with respect to ϕ_H, viz. $\theta(t) = \pi/2 - \phi_\mathrm{H}$. The cone angle of precession is a two-component object. The dynamic in-plane angle is denoted $\phi(t)$ and the out-of-plane component $\beta(t)$. All these angles are specified in Fig. 4.10a). The following trigonometric relation holds between the absolute angle $\theta(t)$ and the corresponding in-plane and out-of-plane angles:

$$\cos\theta(t) = \sin(\phi_\mathrm{H} + \phi(t))\cos(\beta(t)) \tag{4.30}$$

For small magnetization precession angles, which is the case for all measurements presented in this thesis, it is a good approximation to expand $\cos^2(\theta(t))$ in a Taylor series up to first order [59]. This yields (for the factor proportional to R_A in

Eq. (4.29)) the first non-vanishing dc component of the voltage:

$$< V(t) >= R_{\mathrm{A}} < \phi(t) I(t) > \sin(2\phi_{\mathrm{H}}) \tag{4.31}$$

where <> signifies time average. Only factors proportional to the in-plane cone angle $\phi(t)$ appear to first order. Note, that this is a very good approximation for thin FM-films as $\phi(t) >> \beta(t)$ leading to the simplified schematic displayed in Fig. 4.10b) where only in-plane angles are under consideration. Note that a conducting capping layer reduces the current through the FM and therefore leads to a smaller R_{A}.
Expressing Eq. (4.31) in terms of the dynamic susceptibilities characterizes the distinct line shape of the voltage associated with FMR. As $\phi(t)$ is small the following trigonometric relation holds:

$$\phi(t) = \frac{m_{y'}(t)}{M_{\mathrm{S}}} \tag{4.32}$$

Using the susceptibility tensor entries $< V(t) >$ can generally be written in the following way:

$$< V(t) >= \frac{R_{\mathrm{A}}}{M_{\mathrm{S}}} < (\chi_{y'y'} h_{y'}(t) + \chi_{y'z} h_z(t)) I(t) > \sin(2\phi_{\mathrm{H}}) \tag{4.33}$$

Both the driving fields $h_{y'}$, h_z and the current $I(t)$ are generated by the same source, i.e. the microwave current flowing through the CPW. Hence, they are oscillating at ω which is the precession frequency of the magnetization. Their relative phase cannot be determined a priori and has to be included as a parameter in the considerations. In order to evaluate the time averaged part of the right hand side of Eq. (4.33) the ansatz presented in Eq. (3.41) is used for $h_{y'}$ and h_z and similar for the current, viz.:

$$I(t) = I \exp(i\omega t) \tag{4.34}$$

This leads to the following term to be evaluated:

$$< V(t) >= \frac{R_{\mathrm{A}}}{M_{\mathrm{S}}} < [\Re\{\chi_{y'y'} h_{y'}(t)\} + \Re\{\chi_{y'z} h_z(t)\}] \Re\{I(t)\} > \sin(2\phi_{\mathrm{H}}) \tag{4.35}$$

Generally driving fields originating from different sources are involved. One is proportional to the current flowing in the CPW $I^{\mathrm{CPW}}(t)$, henceforth called h^{CPW}, and the second is generated by the current $I(t)$ in the NiFe/NM bilayer itself. The field caused by $I(t)$ at the location of FM, from now on called h^{NM}, is proportional to the conductance of the capping NM layer. Particularly, it is zero if no conductive layer is present since the current through FM generates no net driving field at the site of FM. Accounting for the different types of driving field Eq. (4.35) is modified the following way.

$$\begin{aligned} < V(t) > = \frac{R_{\mathrm{A}}}{M_{\mathrm{S}}} < [&\Re\{\chi_{y'y'}(h_{y'}^{\mathrm{NM}}(t) + h_{y'}^{\mathrm{CPW}}(t))\} \\ &+ \Re\{\chi_{y'z}(h_z^{\mathrm{NM}}(t) + h_z^{\mathrm{CPW}}(t))\}] \Re\{I(t)\} > \sin(2\phi_{\mathrm{H}}) \end{aligned} \tag{4.36}$$

This equation is analyzed with respect to line shape and ϕ_{H}-dependence in the following for the two special cases, presented in Fig. 4.5. For these geometries it is evident that $h_z^{\mathrm{NM}}(t)$ is zero as the NM layer is directly on top of the NiFe. At first the in-plane driving field case shall be examined. Here, additionally $h_z^{\mathrm{CPW}}(t) = 0$ and Eq. (4.36) reduces to:

$$< V(t) >= \frac{R_{\mathrm{A}}}{M_{\mathrm{S}}} < \Re\{\chi_{y'y'}(h_{y'}^{\mathrm{NM}}(t) + h_{y'}^{\mathrm{CPW}}(t))\}\Re\{I(t)\} > \sin(2\phi_{\mathrm{H}}) \tag{4.37}$$

Assume $h_{y'}^{\mathrm{NM}}(t) = h_{y'}^{\mathrm{NM}} \exp(i\omega t)$ and $h_{y'}^{\mathrm{CPW}}(t) = h_{y'}^{\mathrm{CPW}} \exp(i\omega t + \xi)$, where ξ is the phase angle between $I^{\mathrm{CPW}}(t)$ and $I(t)$. Time-averaging over one precession period yields the following result for the dc-voltage due to AMR:

$$\begin{aligned} V_{\mathrm{AMR}}^{\mathrm{ip}} = &-\frac{1}{2}\frac{IR_{\mathrm{A}}}{M_{\mathrm{S}}}\Im\{\chi_{y'y'}^{\mathrm{res}}\}\sin(2\phi_{\mathrm{H}})\sin(\phi_{\mathrm{H}}) \\ &\times \left\{ \left(h_x^{\mathrm{NM}} + h_x^{\mathrm{CPW}}\cos(\xi)\right)\left(\frac{\Delta H(H-H_0)}{(H-H_0)^2+(\Delta H)^2}\right)\right. \\ &\left. + h_x^{\mathrm{CPW}}\sin(\xi)\left(\frac{(\Delta H)^2}{(H-H_0)^2+(\Delta H)^2}\right)\right\} \end{aligned} \tag{4.38}$$

Note that the additional factor $\sin(\phi_{\mathrm{H}})$ has to be introduced for parametrization of $h_{y'}$ with respect to h_x, see Eq. (4.18) and Fig. 4.8b).
For the out-of-plane excitation geometry $h_{y'}^{\mathrm{CPW}}(t) = 0$ and Eq. (4.36) reads

$$< V(t) >= \frac{R_{\mathrm{A}}}{M_{\mathrm{S}}} < [\Re\{\chi_{y'y'}h_{y'}^{\mathrm{NM}}(t)\} + \Re\{\chi_{y'z}h_z^{\mathrm{NM}}(t)\}]\Re\{I(t)\} > \sin(2\phi_{\mathrm{H}}) \tag{4.39}$$

Using $h_z^{\mathrm{CPW}}(t) = h_z^{\mathrm{CPW}} \exp(i\omega t + \xi)$ the following line shape describes the voltage due to AMR:

$$\begin{aligned} V_{\mathrm{AMR}}^{\mathrm{oop}} = &\frac{1}{2}\frac{IR_{\mathrm{A}}}{M_{\mathrm{S}}}\sin(2\phi_{\mathrm{H}}) \\ &\times \left\{ \left(-\Im\{\chi_{y'y'}^{\mathrm{res}}\}h_x^{\mathrm{NM}}\sin(\phi_{\mathrm{H}}) + \chi_{y'z}^{\mathrm{res}}h_z^{\mathrm{CPW}}\sin(\xi)\right)\left(\frac{\Delta H(H-H_0)}{(H-H_0)^2+(\Delta H)^2}\right)\right. \\ &\left. + \chi_{y'z}^{\mathrm{res}}h_z^{\mathrm{CPW}}\cos(\xi)\left(\frac{(\Delta H)^2}{(H-H_0)^2+(\Delta H)^2}\right)\right\} \end{aligned} \tag{4.40}$$

From Eq. (4.38) and (4.40) it is clear, that the voltage due to AMR is generally described by an asymmetric line shape as a function of the external field.
Comparison of Eqs. (4.19) and (4.38) suggests that the ϕ_{H}-dependence of voltages due to dc-ISHE and AMR under circumstances of in-plane driving field (see Fig. 4.5a)) are equal except an amplitude factor. Thus, in general one can only distinguish both effects based on the measured voltage at FMR if the phase factor $\xi = 0$ and consequently $V_{\mathrm{AMR}}^{\mathrm{ip}}$ is purely antisymmetric. For the case of $\xi = 0$ one would extract the amplitude of $V_{\mathrm{ISHE}}^{\mathrm{ip}}$ by fitting the voltage curve (i.e. $V_{\mathrm{AMR}}^{\mathrm{ip}} + V_{\mathrm{ISHE}}^{\mathrm{ip}}$)

with a Lorentzian line shape that contains both symmetric and antisymmetric parts. Subsequently the symmetric part exclusively assigned to ISHE. As the phase-factor for real samples can hardly be known it is quite unsure whether this method as used in [49, 50] is reliable enough to determine α_{SH}. Such problems are not to be expected for out-of-plane driving fields and a unique separation of ISHE and AMR is possible.

4.4 Voltage signals due to electromagnetic induction

If the magnetic flux $\mathbf{B} = \mu_0\mathbf{H}$ through a conducting loop changes, an electric field $\mathbf{E}$ will be generated around the loop's circumference. This behavior is enshrined in Maxwell's law about the rotation of an $\mathbf{E}$-field.

$$\nabla \times \mathbf{E} = -\frac{\partial \mathbf{B}}{\partial t} \tag{4.41}$$

An analogous approach to this situation is to consider the induced voltage V_{ind} given by the rate of change of magnetic flux Φ through a loop of area a. This is described by Faraday's law of induction, cf. [111]:

$$\oint \mathbf{E}\mathrm{d}\mathbf{s} = V_{\mathrm{ind}} = -\iint \frac{\partial \mathbf{B}}{\partial t}\mathrm{d}\mathbf{a} = -\frac{\partial \mathbf{\Phi}}{\partial t} \tag{4.42}$$

$$\Phi = \iint \mathbf{B}\mathrm{d}\mathbf{a} = \mu_0 \iint \mathbf{H}\mathrm{d}\mathbf{a} \tag{4.43}$$

Every kind of electric circuitry will somehow feature conducting loops and it is not always possible to cancel the net magnetic flux through it completely.
A precessing magnetization in a FM/NM bilayer wire periodically changes the flux Φ through the area of the measurement circuitry and thus induces an oscillatory voltage at the same frequency. To understand this it is illustrative to start with the reciprocity theorem which describes the mutual interaction of two current loops. The magnetic flux Φ enclosed in a loop is connected to the current by the inductance, $\Phi = \mathscr{L} I$, cf. [111]. Regarding only the mutual inductance $\mathscr{L}_{12} = \mathscr{L}_{21} = \mathscr{L}$ of the two loops the reciprocity theorem states:

$$\Phi_1 = \frac{\Phi_2 I_2}{I_1} \tag{4.44}$$

From the definition of Φ, see Eq. (4.43), Φ_1 is given by:

$$\Phi_1 = \frac{\mu_0}{I_1} \iint \mathbf{H_2} I_2 \mathrm{d}\mathbf{a_2} = \frac{\mu_0}{I_1} \iint \mathbf{H_2}\mathrm{d}\mathbf{m_2} = \frac{\mu_0}{I_1} \iiint \mathbf{H_2}\mathbf{M}\mathrm{d}V \tag{4.45}$$

$\mathrm{d}\mathbf{m_2}$ is the differential magnetic moment of current loop 2. In the last step loop 2 is replaced by a magnetic material with magnetization $\mathbf{M}$. Φ_1 is to be identified with the magnetic flux through the measurement circuitry Φ_{circ} and I_1 with the current flowing in it. I_1 generates a field $\mathbf{H_2}$ inside the magnetic material and

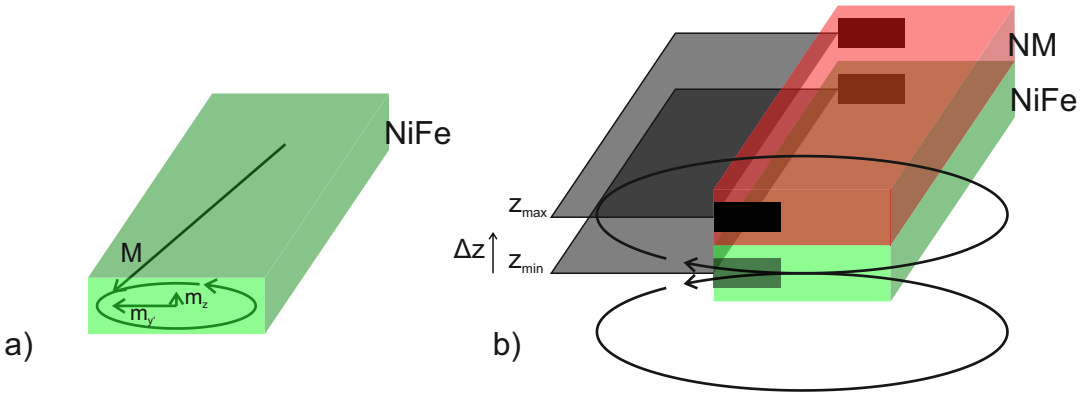

Figure 4.11: a) illustrates that the main contribution of magnetic flux Φ_{circ} through the measurement circuitry originates from the in-plane dynamic magnetization component $m_{y'}$. In b) the extremal positions z_{min} and z_{max} of the measurement circuit loop with respect to the NiFe/NM bilayer are shown. The sketched magnetic field lines indicate how the measurement circuit loop is more and more asymmetrically penetrated by magnetic flux for a change from z_{min} towards z_{max}.

corresponds to a field $\mathbf{H_1}(\mathbf{I_1})$ around it. $\mathbf{H_1}(\mathbf{I_1})$ can be evaluated for a rectangular shaped magnetic medium using the Karlqvist equations [60, 61, 158]. Assuming a time-dependent magnetization, as it is the case for precession, a voltage described by the following equation will be induced [68, 158]:

$$V_{\mathrm{ind}} = -\frac{1}{2}\,\mu_0\; t\; L\; \eta\; \frac{\partial m_{\mathrm{y'}}}{\partial t}\,\frac{Z_0}{Z_0 + \frac{1}{2}R_0} \tag{4.46}$$

For a thin film ferromagnetic material the in-plane component of the precessing magnetization $m_{y'}$ is the dominant source of Φ_{circ}. This is illustrated in Fig. 4.11a). Z_0 is the impedance of the measurement circuit, R_0 is the dc resistance of the FM/NM bilayer and t and L are the thickness and the length of FM. η is a number between 0 and 1 and accounts for the fact that the average current loop position z_{circ} of the measurement circuit which contains a FM/NM bilayer depends on the relative conductivities of FM and NM. To this end η is defined as:

$$\eta = \frac{\sigma_{\mathrm{NM}}}{\sigma_{\mathrm{FM}} + \sigma_{\mathrm{NM}}} \tag{4.47}$$

The two extreme cases of $\eta = 0$ and $\eta = 1$ are illustrated in Fig. 4.11b). The $\eta = 0$-case corresponds to a single FM-layer where the current loop lies exactly in the middle of the FM-layer. In this special case $\Phi_{\mathrm{circ}} = 0$ as $m_{\mathrm{y'}}$ generates a field $\mathbf{H_1}$ through the measurement circuit whose z-component cancels out completely. For $\eta = 1$ the z-component of $\mathbf{H_1}$ is maximized due to shifting the measurement circuit

loop into the middle of NM, this is indicated by the vertical displacement Δz in Fig. 4.11b). This situation is given for an electrically insulating FM like e.g. YIG [158, 159].
For the experimental setups presented in Fig. 4.5 the ac-voltage due to ISHE is proportional to m_z, which is the out-of-plane dynamic component of the precessing magnetization (Eqs. (4.26) and (4.27)). The ac-voltage due to electromagnetic induction (Eq. (4.46)) is dependent on $\partial m_{\mathrm{y'}}/\partial t$, the time derivative of the in-plane dynamic magnetization component. For a precessing magnetization $\partial m_{\mathrm{y'}}/\partial t \propto m_{\mathrm{y'}}$ and therefore both voltages the one due to ISHE and the one due to electromagnetic induction feature the same angular dependence with respect to ϕ_{H} as well as the same line shape as a function of external field. To this end it is very critical to separate the two effects. One elegant possibility is to study not only the amplitude of ac-voltages, but also its phase using a vector network analyzer [62].

5 Experimental results concerning ferromagnetic resonance and spin pumping

This chapter is devoted to the characterization of magnetic properties of NiFe single and NiFe/NM bilayers using ferromagnetic resonance (FMR). In the first section the common experimental approach to FMR, which is to study the absorption of a microwave magnetic field, will be explained and applied to a NiFe-film. This so-called absorption-FMR method is subsequently used to study different NiFe/NM layers with respect to spin pumping. By comparison of magnetic damping measured for NiFe and NiFe/NM samples the effective spin mixing conductivities of different NiFe/NM-interfaces are estimated. In the second section of this chapter FMR-experiments on micro-structured NiFe/Pt-bilayers are presented. The typically 5 µm wide, 400 µm long and 10 nm thick wires are integrated into CPW-structures implementing an in-plane magnetic excitation field. It will be pointed out that besides microwave absorption also voltage signals generated by ISHE and AMR can be used to extract magnetic properties. Application of both FMR-techniques at the same NiFe/Pt bilayer wire underpins their equivalence for the samples at hand. Furthermore, geometric limitations when extracting magnetic properties for the micro-structured specimens will be discussed.

5.1 Non-micro-structured NiFe thin films and NiFe/NM bilayers

In Fig. 5.1a) the FMR spectrum of a 12 nm thick NiFe film sputtered onto a GaAs(001) substrate driven at a frequency of 8 GHz is displayed. The plot shows the derivative of the absorption from a microwave field while increasing an external magnetic field $\mathbf{H}$, which saturates the magnetization of the NiFe-film in-plane. The experimental approach is depicted in Fig. 5.1b). The NiFe-film is put directly on top of the transmission lines of a CPW. Microwaves in the GHz-regime are fed into one end of the CPW by an appropriate signal generator. At the other end of the CPW the microwaves are rectified using a Schottky diode which shows a voltage offset proportional to the transmitted microwave's amplitude. When the magnetization is driven resonantly the absorption from the magnetic microwave field $\mathbf{h}(t)$ is maximized and proportionally the voltage across the Schottky diode changes. The small

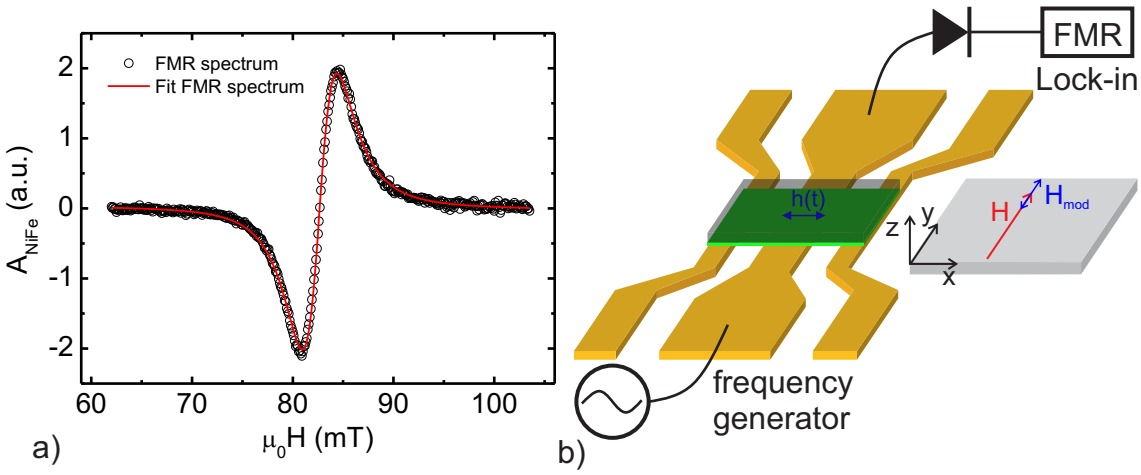

Figure 5.1: In a) a FMR spectrum of a 12 nm thick NiFe film is shown. The magnetization is saturated in-plane and its precession frequency for the shown case is $f = 8\,\mathrm{GHz}$. The black circles are averaged raw data and the red solid line is a fit according to Eq. (5.3). In b) the measurement setup is schematically shown. FM (green layer) is located on a substrate (transparent grey layer) and the whole stack is put face-down on a CPW. The absorption from the microwave field $h(t)$, which is generated by a radio frequency current through the CPW, is recorded using a Schottky diode and a lock-in amplifier. Added to the external static field H is a small additional field H_{mod} whose frequency is typically in the 1 to 100 Hz-regime. In the schematic the optimal condition for FMR is displayed, which is the perpendicular configuration between $h(t)$ and H.

voltage change is usually on top of a large offset. Therefore the external static field $\mathbf{H}$ is modulated with a small oscillatory component $\mathbf{H}_{\mathrm{mod}}$, see the coordinate system of Fig. 5.1b). The frequency of $\mathbf{H}_{\mathrm{mod}}$ in the present case is 86 Hz and its amplitude corresponds to a range of 0.1 to 1 mT. The modulated signal at the Schottky diode is then recorded by a lock-in amplifier which subtracts the large background by cross-correlation of the measured signal with a reference and subsequent integration via a low-pass filter. The result from the lock-in amplifier is

$$S_{\text{lock-in}} = V_{\text{Schottky}}(H + H_{\mathrm{mod}}) - V_{\text{Schottky}}(H) \tag{5.1}$$

If H_{mod} is small compared to the expected line width of the FMR-spectrum, the following approximation can be made:

$$S_{\text{lock-in}} = \frac{\mathrm{d}V_{\text{Schottky}}}{\mathrm{d}H} H_{\mathrm{mod}} \propto \frac{\mathrm{d}\mathscr{A}}{\mathrm{d}H} \tag{5.2}$$

viz. field modulation in combination with a lock-in amplifier yields a quantity which is proportional to the derivative of microwave absorption.

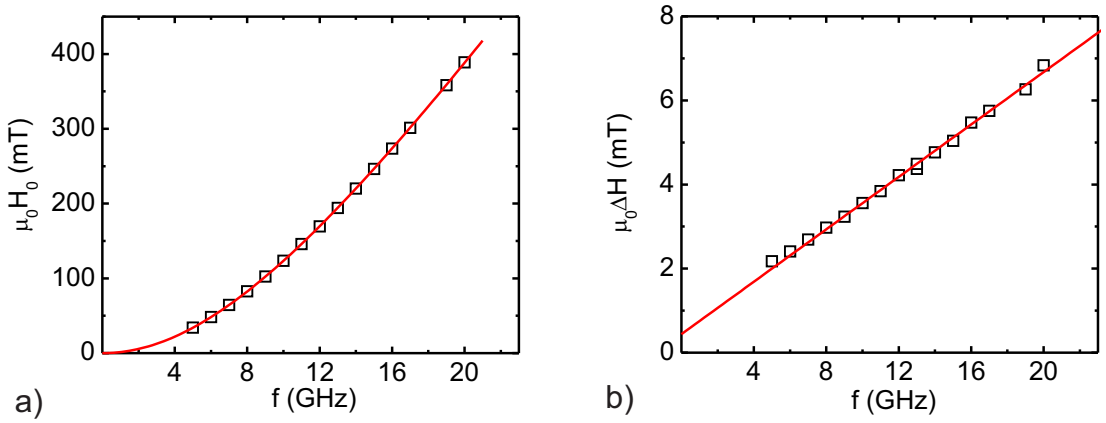

Figure 5.2: The resonance field H_0, a) and the HWHM ΔH, b) of FMR-spectra for a 12 nm thick NiFe are plotted as a function of frequency. The red solid lines are fits to data corresponding to Eq. (5.4), a) and Eq. (5.5), b). As best fit parameters $\gamma = 181.20 \pm 0.45\,\mathrm{GHz\,T^{-1}}$, $\mu_0 M_{\mathrm{eff}} = 0.850 \pm 0.005\,\mathrm{T}$ and $\alpha = 0.0088 \pm 0.0001$ are determined.

In order to extract the magnetic properties such as gyromagnetic ratio γ, effective magnetization M_{eff}, Gilbert damping coefficient α and magnetic susceptibilities at FMR $\chi^{\mathrm{Res}}_{y'y'}$, $\chi^{\mathrm{Res}}_{y'z}$, χ^{Res}_{zz}, absorption-FMR spectra are fitted with the following function (i.e. the solid red line in Fig. 5.1a)):

$$A = \frac{\mathrm{d}}{\mathrm{d}H}\left(\frac{a_1 \cos(\epsilon)\Delta H}{(H-H_0)^2+(\Delta H)^2} + \frac{a_1 \sin(\epsilon)(H-H_0)}{(H-H_0)^2+(\Delta H)^2}\right) + a_2 \tag{5.3}$$

All factors which do not depend on H are summarized in the amplitude factor a_1. The parameter a_2 accounts for a possible offset of the spectrum and ϵ is the phase angle between imaginary and real parts of the susceptibilities. The first summand on the right hand side of Eq. (5.3) is proportional to the derivative of a symmetric Lorentzian line shape. This is a logical choice as the microwave absorption $\mathscr{A}$ for FMR is proportional to $\Im(\chi_{y'y'})$ or $\Im(\chi_{zz})$ (for the line shapes of susceptibilities see Eqs. (3.57) and (3.59)). Theoretically, the microwave absorption across FMR should only depend on $\Im(\chi_{y'y'})$ or $\Im(\chi_{zz})$ and the first term on the right hand side of Eq. (5.3) should suffice. However, this is an idealization and in reality one has to consider that at resonance the coupling between CPW and magnetic sample might vary due to the present microwave absorption. As a consequence one has to account for both real and imaginary parts of the susceptibility in the fit function or respectively for a nonzero phase factor ϵ.

In Fig. 5.2 the extracted $\mu_0 H_0$ and $\mu_0 \Delta H$ are plotted as a function of frequency. From $\mu_0 H_0(f)$ both $\mu_0 M_{\mathrm{eff}}$ and γ can be inferred from a fit with the following

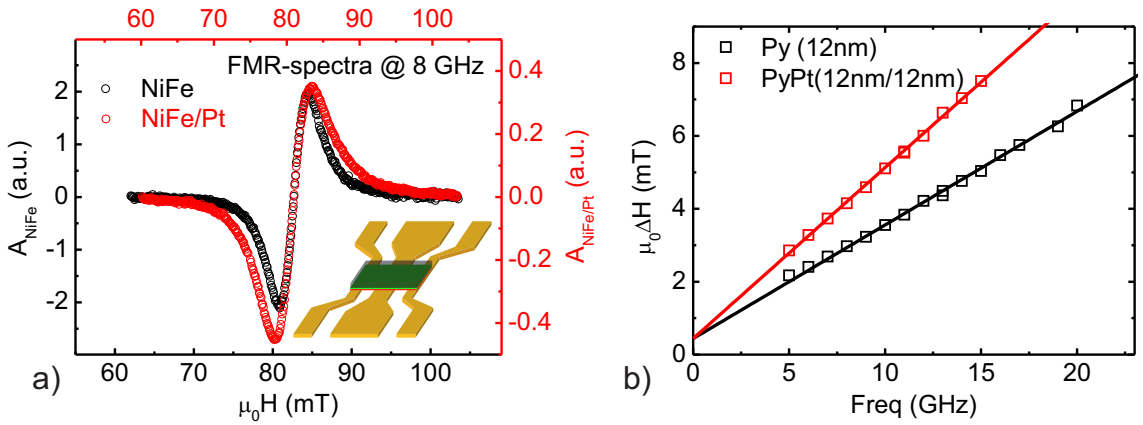

Figure 5.3: In a) FMR spectra of a single 12 nm thick NiFe film (black curve and corresponding black coordinate axes) and a 12 nm thick NiFe film capped with a 12 nm thick Pt layer, are shown. The experimental method of placing a NiFe/Pt-bilayer face down on a CPW is indicated. In b) the increased slope of the linear fit to $\mu_0 \Delta H(f)$-values for NiFe/Pt and a corresponding damping factor of $\alpha = 0.0135 \pm 0.0002$ suggest spin pumping.

function which solves the resonance condition Eq. (3.53) for $\mu_0 H_0$.

$$\mu_0 H_0 = \frac{1}{2}\left(-\mu_0 M_{\text{eff}} + \sqrt{(\mu_0 M_{\text{eff}})^2 + 4\left(\frac{2\pi f}{\gamma}\right)^2}\right) \tag{5.4}$$

The fit displayed in Fig. 5.2a) for $\mu_0 H_0$ yields an effective magnetization corresponding to $\mu_0 M_{\text{eff}} = 0.850 \pm 0.005$ T and a gyromagnetic ratio $\gamma = 181.20 \pm 0.45\,\text{GHz T}^{-1}$. A linear fit of $\mu_0 \Delta H(f)$ which is represented by the red solid line in Fig. 5.2b) allows for determination of the intrinsic damping factor α. For this the following relation is used:

$$\alpha = \frac{\gamma \mu_0}{2\pi} \frac{\mathrm{d}\Delta H}{\mathrm{d}f} \tag{5.5}$$

Inserting the inferred γ-value from the $\mu_0 H_0(f)$-fit into this equation yields $\alpha = 0.0088 \pm 0.0001$. Furthermore, a nonzero offset $\mu_0 \Delta H(0) = 0.53 \pm 0.6\,\text{mT}$ can be observed in Fig. 5.2b). This indicates that there is a certain extrinsic contribution to magnetization damping. However, this shall not be examined more closely in this work as it is generally not essential for SP-ISHE. The presented FMR method of putting a magnetic film on top of a CPW has then been conducted for different bilayers of NiFe/NM.
Normal metals under consideration are in particular platinum (Pt), gold (Au), tantalum (Ta), and tungsten (W). In Fig. 5.3a) an explicit comparison of FMR-spectra recorded at 8 GHz of a single 12 nm thick NiFe film and a bilayer of NiFe/Pt

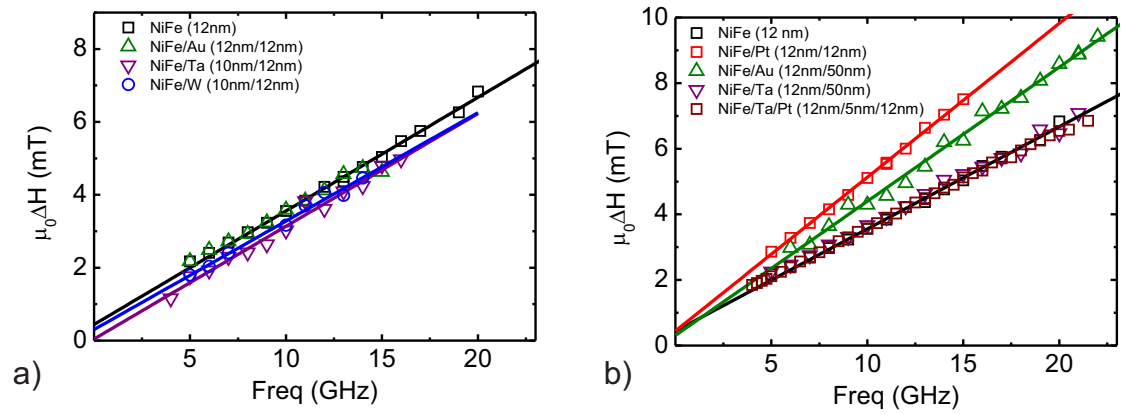

Figure 5.4: In a) $\mu_0 \Delta H(f)$ is plotted for NiFe(12 nm), NiFe/Au(12 nm12 nm), NiFe/Ta(10 nm12 nm) and NiFe/W(10 nm12 nm). The numbers are the corresponding thicknesses in nm. The solid lines are fits to data according to Eq. 5.5. In b) $\mu_0 \Delta H(f)$ is plotted for NiFe(12 nm), NiFe/Pt(12 nm12 nm), NiFe/Au(12 nm50 nm), NiFe/Ta(12 nm50 nm) and NiFe/Ta/Pt(12 nm5 nm12 nm). The solid lines are again linear fits to data.

($t_{\mathrm{NiFe}} = t_{\mathrm{Pt}} = 12\,\mathrm{nm}$) is presented. One can observe that the FMR-spectrum for the NiFe/Pt bilayer features a larger line width as the spectrum for the single NiFe film. In Fig. 5.3b) $\mu_0 \Delta H$ is plotted as a function of frequency. From the linear increase in line width for NiFe/Pt assuming the same γ-value as was determined before for the single NiFe layer, a damping parameter $\alpha = 0.0135 \pm 0.0002$ is calculated. Following the argumentation as given in Chapt. 3 this is expected as Pt is an effective spin sink and spin pumping increases the damping.
This information is used to estimate the spin mixing conductivity $g_{\mathrm{F}}^{\uparrow\downarrow}$ rewriting Eq. (3.72) in terms of saturation magnetization M_{S} and measured γ-value.

$$g_{\mathrm{F}}^{\uparrow\downarrow} = \frac{\mu_0 M_{\mathrm{S}} t_{\mathrm{FM}} \Delta\alpha}{\frac{\mu_0}{4\pi}\gamma\hbar} \tag{5.6}$$

Independent measurements using SQUID magnetometry yield $\mu_0 M_{\mathrm{S}} = 0.9\,\mathrm{T}$ for the sputtered NiFe film, $\Delta\alpha = \alpha_{\mathrm{NiFe/Pt}} - \alpha_{\mathrm{NiFe}} = 0.0047 \pm 0.0003$ and consequently $g_{\mathrm{F}}^{\uparrow\downarrow} = (2.67 \pm 0.2) \times 10^{19}\,\mathrm{m}^{-1}$. This value of $g_{\mathrm{F}}^{\uparrow\downarrow}$ for NiFe/Pt compares well to theoretical predictions presented in [41] and measurements in [44]. The method of deducing spin mixing conductivities from line width changes of FMR-spectra has been conducted for a set of normal metals. Plots of $\mu_0 \Delta H(f)$ and corresponding linear fits to the data for NiFe/Au, NiFe/Ta and NiFe/W are displayed along with the single NiFe film results in Fig. 5.4 a). The individual layer thicknesses of all films is 12 nm. It is noticeable that in this case the slopes of all $\mu_0 \Delta H(f)$-curves are equal within a small error range.

In principle two possibilities for the absence of a change in α for capped NiFe films with respect to uncapped NiFe films are conceivable. The first is that there is no spin pumping due to a very small spin mixing conductivity of the NiFe/NM interface. The second possible reason might be the large spin diffusion length λ_{sd} of the respective NM compared to its thickness. The consequential spin accumulation in NM leads to a back flow of spin current into the NiFe in this case [41]. In order to estimate which effect is applicable in the case at hand the thickness of the examined NM has been varied. Corresponding results of $\mu_0\Delta H(f)$ are plotted in Fig. 5.4b). Special emphasis is put on the examination of Pt and Au with respect to Ta capping. The $\mu_0\Delta H$ dependence for the case of 50 nm Au on top of 12 nm NiFe corresponds to an increased damping factor of $\alpha = 0.0118 \pm 0.0002$ and with $\Delta\alpha = 0.0030 \pm 0.0003$ this results in a spin mixing conductivity $g_{\mathrm{F}}^{\uparrow\downarrow} = (1.7 \pm 0.2) \times 10^{19}\,\mathrm{m}^{-1}$ for Au. It is slightly higher as reported value from FMR studies of Fe/Au which yield $g_{\mathrm{F}}^{\uparrow\downarrow} = 1.2 \times 10^{19}\,\mathrm{m}^{-1}$ [46, 160]. This difference might be explained by a variation in the pure NiFe damping factor slightly varying from sample to sample. The increase in damping factor for the 50 nm Au capping is consistent with the fact that $\lambda_{\mathrm{sd}} = 34\,\mathrm{nm}$ as inferred from Au-thickness dependent FMR measurements reported in [160] and is a unique indication that spin pumping from NiFe into Au generally takes place for the samples at hand. Also presented in Fig. 5.4b) are $\mu_0\Delta H(f)$-data for NiFe/Ta with $t_{\mathrm{Ta}} = 50\,\mathrm{nm}$ and for a trilayer of NiFe/Ta/Pt with $t_{\mathrm{Ta}} = 5\,\mathrm{nm}$ and $t_{\mathrm{Pt}} = 12\,\mathrm{nm}$. The first layer stack is examined in order to rule out that a similar effect as for the Au (back flow of spin current into NiFe due to large λ_{sd}) might lead to no increase in damping parameter. The second layer stack featuring another layer of Pt on top of Ta would lead to an increase in measured damping due to spin pumping if the NiFe/Ta interface would be transparent for a finite portion of spin current, viz. the spin mixing conductivity would be comparable at least to NiFe/Au. Within the error range of the extracted α for NiFe and NiFe/Ta, which yields a maximum $\Delta\alpha = 0.0002$, the spin mixing conductivity of Ta can be estimated to be not higher than $g_{\mathrm{F}}^{\uparrow\downarrow} = 1.1 \times 10^{18}\,\mathrm{m}^{-1}$. This is more than one order of magnitude smaller compared to Pt and Au. A possible reason for this enormous reduction of spin mixing conductivity for Ta might be a so called "dead-layer" meaning that Ta destroys the ferromagnetism at the NiFe/Ta interface. Though the results for spin pumping in Ta are not very promising setting up an experiment measuring ISHE it has been nevertheless included into studies of voltages at FMR in order to compare with Pt- and Au-cases for which fundamental differences should be observed.

So far FMR-experiments of NiFe and NiFe/NM samples have been restricted to extended films of about $1\,\mathrm{mm}^2$. However, the relevant samples for picking off voltage signals due to spin pumping and ISHE are shaped into wires of lateral dimensions in the µm-range. This introduces certain subtleties when extracting magnetic properties from FMR-spectra. The following section is devoted to this subject where FMR is extensively studied for a micro-structured NiFe/Pt bilayer.

5.2 Micro-structured NiFe/Pt bilayers

The advantage of a micro-structured film is that the type of excitation field can be selected by placing the wire either on top of the signal line or in the gap between signal and ground line, see Fig. 4.5. For in-plane excitation the microwave absorption inside the NiFe/NM-bilayer is solely proportional to $\Im(\chi_{y'y'})$ whereas for out-of-plane excitation the applicable susceptibility component is $\Im(\chi_{zz})$. Due to the thin film geometry (large demagnetizing field in z-direction) $\Im(\chi_{y'y'}) >> \Im(\chi_{zz})$. Therefore the absorption of an in-plane magnetic driving field by the precessing magnetization is expected to be much larger and so is the signal in an absorption-FMR experiment. Yet, as out-of-plane-excitation offers less geometrical restrictions of magnetization excitation for in-plane magnetized films and therefore is the relevant excitation scheme for measuring ISHE in NiFe/NM bilayers (see Eq. (4.20)), one would like to have a robust method for measuring the relevant magnetization precession properties also in this excitation geometry. Here the distinct line shapes across FMR of voltages which are detectable due to ISHE, AMR or inductive effects are essential. Especially voltages due to AMR and ISHE are appealing as it is a dc voltage which can directly be measured at the ends of the used wires. Of course ISHE only works in combination with spin pumping into a spin sink such as Pt or with limitations into Au as was reasoned in the previous section. Yet, the AMR-effect is always present in both single NiFe and NiFe/NM samples. In the following it shall be demonstrated using a NiFe/Pt-bilayer wire that the extraction of magnetic properties from absorption-FMR and voltage spectra is equivalent for the studied specimens in this work. It will also be discussed that samples shaped into wires must possibly be treated differently when it comes to effective fields entering the LLG. Especially the demagnetizing factor for the width direction N_x might be crucial.

In Fig. 5.5a) two different types of FMR-spectra of a 5 µm wide and 400 µm long NiFe/Pt bilayer wire with an individual layer thickness of 12 nm are shown. The data are recorded by implementing the measurement scheme presented in Fig. 5.5b). As the bilayer wire is located on top of the signal line a pure in-plane driving field is present. The external field angle is $\phi_{\mathrm{H}} = 45°$ and the magnetization's precession frequency is 8 GHz. The black curve in Fig. 5.5a) is recorded via field modulation and lock-in-detection and as such it represents the derivative of microwave absorption across FMR. The red curve in Fig. 5.5a) is the dc voltage measured across FMR. The characteristic line shape is described by

$$V = a_1 \left(\frac{\cos(\psi)(\Delta H)^2}{(H - H_0)^2 + (\Delta H)^2} + \frac{\sin(\psi)(H - H_0)\Delta H}{(H - H_0)^2 + (\Delta H)^2} \right) + a_2 \tag{5.7}$$

where $a_1 \cos(\psi) = A_{\mathrm{S}}$ and $a_1 \sin(\psi) = A_{\mathrm{A}}$ are the amplitudes of the appearing symmetric and antisymmetric Lorentzian line shapes and ψ is their relative phase angle. The line shape might have a constant offset which is accounted for by the parameter a_2. Note that Eq. (5.7) is a phenomenological sum of contributions from ISHE, cf. Eq. (4.19) and AMR, cf. Eq. (4.38).

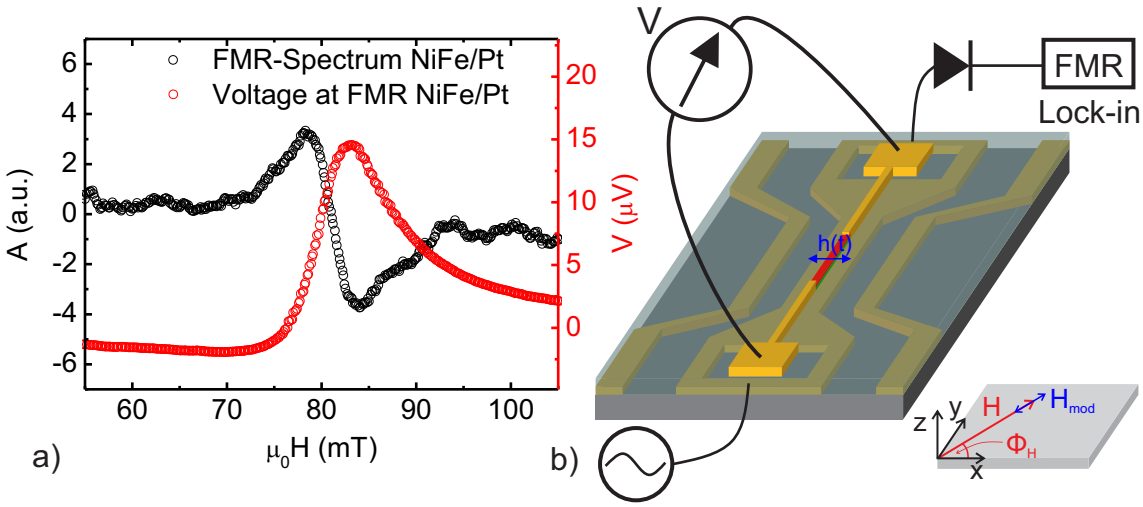

Figure 5.5: In a) both an absorption FMR (black curve) and a voltage spectrum (red curve) measured for a NiFe/Pt bilayer across FMR are shown. The driving frequency is $f = 8\,\mathrm{GHz}$ and the magnetic field angle is $\phi_\mathrm{H} = 45°$. In b) the experimental setup is displayed. The wire is integrated underneath the signal line of a CPW which corresponds to a pure in-plane excitation field $h(t)$ at the site of the bilayer. Both absorption FMR using external field modulation and lock-in-detection and measurement of the voltage signal across the bilayer is conducted at the same time. The coordinate system illustrates the direction of the external fields, viz. H and H_mod.

In Fig. 5.6 direct comparisons of $\mu_0 H_0(f)$ and $\mu_0 \Delta H(f)$ from both microwave absorption and voltage signal FMR spectra are presented. The corresponding γ-, $\mu_0 M_\mathrm{eff}$- and α-values are extracted from fits using Eqs. (5.4) and (5.5), respectively. From the microwave absorption technique the results are, $\gamma = 181.19 \pm 2.13\,\mathrm{GHz\,T^{-1}}$, $\mu_0 M_\mathrm{eff} = 0.862 \pm 0.024\,\mathrm{T}$ and $\alpha = 0.0157 \pm 0.0006$. From voltage spectra $\gamma = 181.06 \pm 2.45\,\mathrm{GHz\,T^{-1}}$, $\mu_0 M_\mathrm{eff} = 0.873 \pm 0.028\,\mathrm{T}$ and $\alpha = 0.0152 \pm 0.0005$. This suggests that within the error margin of the measurements both techniques can be used equivalently in order to characterize the magnetic properties of NiFe/NM bilayers. Considering the average value for both measurement techniques $\alpha = 0.0155 \pm 0.0006$. It is striking that this value is increased by an amount of 0.002 with respect to the extended film results presented in the previous section of this chapter.
A study of $\mu_0 H_0(\phi_\mathrm{H})$ and $\mu_0 \Delta H(\phi_\mathrm{H})$ at fixed frequency which is presented in Fig. 5.7 gives insight into the underlying physical difference between FMR on extended films compared to the studied wires. It allows for an estimation of how well the FMR theory for isotropic thin films can be applied to an inherently anisotropic thin film wire. Due to the better signal to noise ratio the voltage spectra across FMR are studied for this purpose. The data presented in Fig. 5.7 was recorded at a constant driving

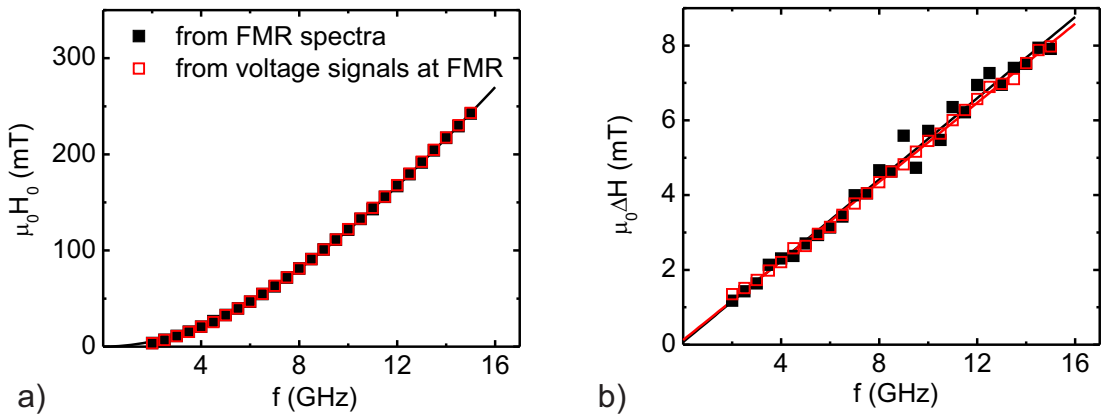

Figure 5.6: In a) $\mu_0 H_0(f)$ from absorption FMR (black squares) and from voltage spectra (red open squares) are displayed. A fit to the data using Eq. 5.4 yields $\gamma = 181.19 \pm 2.13\,\mathrm{GHz\,T^{-1}}$ and $\mu_0 M_{\mathrm{eff}} = 0.862 \pm 0.024\,\mathrm{T}$ and $\gamma = 181.06 \pm 2.45\,\mathrm{GHz\,T^{-1}}$, $\mu_0 M_{\mathrm{eff}} = 0.873 \pm 0.028\,\mathrm{T}$, respectively. In b) $\mu_0 \Delta H(f)$ from both methods is plotted. Fit to data using Eq. 5.5 yields $\alpha = 0.0157 \pm 0.0006$ and $\alpha = 0.0152 \pm 0.0005$, respectively.

frequency of 7.5 GHz varying the angle ϕ_{H} from 0 to 360° in 10°-steps. It is obvious that the $\mu_0 \Delta H$ values are larger for magnetizations with an increased component along the x-axis, for orientation see the coordinate system in Fig. 5.5b). In a first step this can be estimated by using a $A\cos^2(\phi_{\mathrm{H}})$-fit to the data, see Fig. 5.7a). The amplitude A of this fit corresponds approximately to a change in α of 0.002. This is exactly the difference observed for the extended NiFe/Pt films compared to NiFe/Pt wires. The reason is that magnetic edge modes appearing at higher and lower values of the swept static H-field are excited. They merge with the central voltage line shape around H_0 and result in an increased line width broadening. This explanation fits nicely with studies of spin wave excitations in transversely magnetized long stripes, which is presented and analytically discussed in [161]. For ϕ_{H}-multiples of 90° the edge modes are insignificant due to the elongation of the wire towards 400 µm and FMR results consistent with extended film measurements are observed. Summarizing the $\mu_0 \Delta H(\phi_{\mathrm{H}})$ dependence, one should either interpret the results of FMR measurements of extended films or for wires in which the magnetization points along the y-axis to quantify spin pumping from the measured change in damping factor α using Eq. (3.72). This is even more important, as the spread of $\mu_0 \Delta H$-values around $\phi_{\mathrm{H}} = 180° \pm 45°$-multiples is very large and comparisons of NiFe to NiFe/NM samples entail a large uncertainty.

Another interesting feature is the $\mu_0 H_0(\phi_H)$ dependence which is presented in Fig 5.7b). The $\cos^2(\phi_{\mathrm{H}})$-dependence which is represented by a fit to the data cannot be caused by edge modes, as they do not change the resonance position of the central mode. The reason for the change of $\mu_0 H_0$ as a function of ϕ_{H} indicates that there is a nonzero demagnetizing factor N_x along the 5 µm width dimension. However, the

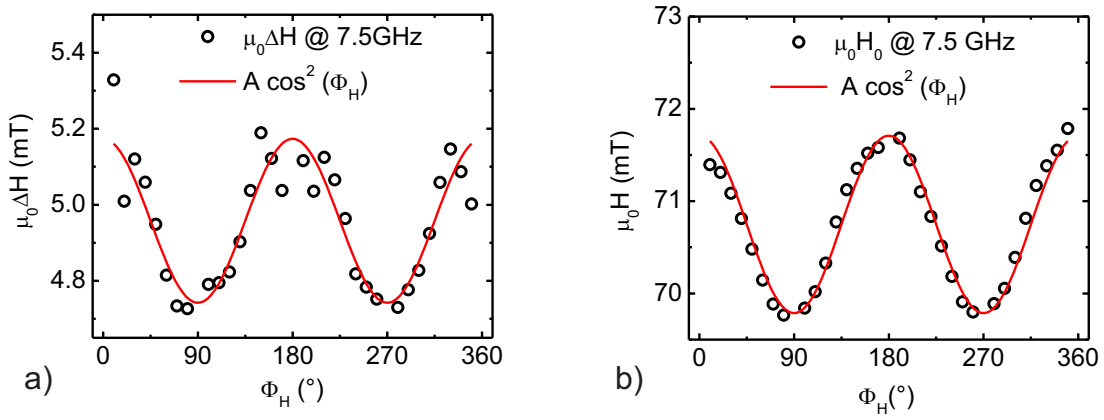

Figure 5.7: In a) $\mu_0 \Delta H$ extracted from a voltage spectrum across FMR of a 400 µm long, 5 µm wide and 12 nm/ 12 nm thick NiFe/Pt bilayer wire is plotted as a function of angle ϕ_H. The red solid line is a fit to the data corresponding to the function $A \cos^2(\phi_H)$. In b) $\mu_0 H_0$ is plotted as a function of ϕ_H. The red solid line is a fit to the data corresponding to $A \cos^2(\phi_H)$.

condition $N_z >> N_x$ is still valid as can be seen from the small amplitude of the fit in Fig. 5.7b), $A \approx 2\,\mathrm{mT}$. This means, that the shape anisotropy of the wires is still negligible for the 5 µm wide wires and the FMR theory for laterally extended thin films is still valid in case one accounts for a slight modification of M_{eff} dependent on ϕ_H in the calculations of the susceptibilities.

6 Study of dc-voltages due to AMR and ISHE

For NiFe/Pt and NiFe/Au spin pumping is a source of pure spin currents as was evidenced by line width broadening in FMR-measurements in the previous chapter. Hence, voltage signals at FMR are, dependent on the magnitude of respective spin Hall angle, proportional to the ISHE in Pt or Au. At the same time experimental setup related parasitic effects like the AMR have to be considered and, as far as possible, be excluded for the quantification of ISHE.
By analyzing the line shapes of voltage spectra for different in-plane static field configurations, which are specified by the angle ϕ_{H}, one gets essential insight into the symmetries of underlying voltage generating effects. It is one of the main issues of this chapter to present results which suggest that only the out-of-plane excitation allows for a geometric separation between AMR and ISHE. Moreover, a detailed study of angular dependencies of symmetric and antisymmetric voltage spectra for out-of-plane excitation is carried out. The quantification of additional parasitic in-plane driving fields due to rf-currents flowing through the conductive layer of NiFe/NM shall be in the focus. To this end the examination of the phase angle between the out-of-plane excitation field generated by the CPW and the in-plane parasitic field due to the rf-current through the bilayer is essential.

6.1 Angle dependent measurements of voltage signals at FMR for in-plane excitation with a CPW

In Fig. 6.1a) the voltage measured across FMR (green line) using in-plane excitation for a NiFe/Pt bilayer is shown. The individual layer thickness is 12 nm. Additionally, symmetric and antisymmetric line shape parts L_{S} (red line) and L_{A} (blue line) are displayed. They are extracted from fit with respect to the measured data using Eq. (5.7). The external field angle for the presented data is $\phi_{\mathrm{H}} = 45°$. For a schematic of the used angle see Fig. 4.5a) or Fig. 5.5b) and the corresponding coordinate systems. Spectra are recorded for different ϕ_{H}-values and the amplitudes A_{S} and A_{A} are extracted from the fits. $A_{\mathrm{S}}(\phi_{\mathrm{H}})$ and $A_{\mathrm{A}}(\phi_{\mathrm{H}})$ are plotted in Fig. 6.1b). Both show qualitatively the same angular dependence. In general the dc-voltage generating effects in NiFe/Pt are ISHE in the Pt and AMR in the NiFe layer. Hence, the adequate formulas to describe the dc-voltage signals are Eqs. (4.19) (for ISHE) and (4.38) (for AMR). To this end A_{A} is expected to be proportional

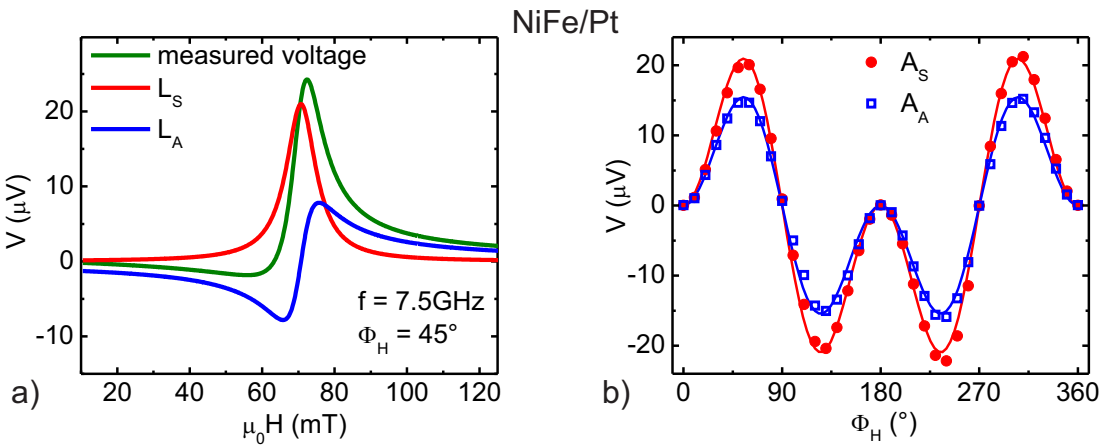

Figure 6.1: In a) the characteristic line shape of a voltage signal across FMR is plotted against external magnetic field for in-plane excitation. The green curve is the measured voltage line shape, the red L_S and the blue L_A curve are symmetric and antisymmetric line shape contributions from fit of the green curve with the function defined by Eq. (5.7). The data are acquired at an external field angle of $\phi_H = 45°$ and at a precession frequency of the magnetization of 7.5 GHz. In b) amplitudes of L_S and L_A, A_S red dots and A_A blue open squares respectively, are plotted as a function of external field angle ϕ_H. Both $A_S(\phi_H)$ and $A_A(\phi_H)$ are fitted with the function defined by Eq. 6.1.

to $(1 - \cos(\xi))\sin(\phi_H)\sin(2\phi_H)$ (it is only due to AMR in NiFe). Whereas A_S is proportional to $\sin(\xi)\sin(\phi_H)\sin(2\phi_H) + \cos^2(\phi_H)\sin(\phi_H)$ (both AMR in NiFe and ISHE in Pt contribute). Using the relation $\cos^2(\phi_H)\sin(\phi_H) = \frac{1}{2}\sin(\phi_H)\sin(2\phi_H)$, $A_S(\phi_H)$ and $A_A(\phi_H)$ can be fitted with the same function of ϕ_H, which is given by:

$$A = a\sin(\phi_H)\sin(2\phi_H) \tag{6.1}$$

Fits to the data, which are represented by the red and blue solid lines in Fig. 6.1b) show very good agreement.

Furthermore, it is not possible to purely assign L_S to ISHE as has been reasoned in [49, 50]. In addition to ISHE, AMR might contribute significantly to L_S depending on the phase difference ξ between the current through the CPW and the current which flows in the NiFe/Pt bilayer. This is a matter of electromagnetic coupling between the two current carrying systems. L_S purely caused by ISHE is only given if $\xi = 0$. Such a statement can hardly be made as physical circumstances in real samples cannot be simulated completely and already small variations from idealizations might lead to $\xi \neq 0$ and a large symmetric line shape contribution due to AMR relative to ISHE.

Due to the impossibility to make sure that A_S is only due to ISHE using in-plane excitation one should establish a reliable method, i.e. a method which separates

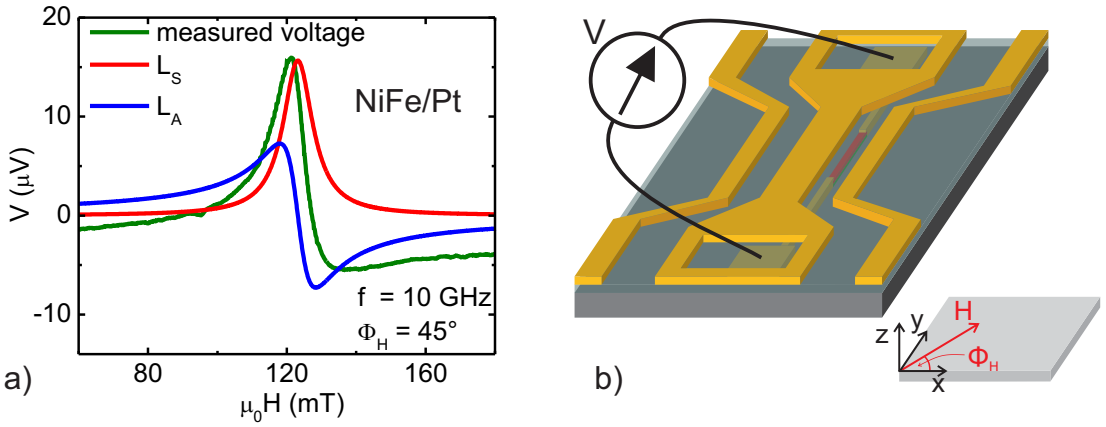

Figure 6.2: In a) the characteristic line shape of a voltage signal across FMR is plotted against external magnetic field for out-of-plane excitation. The green curve is the measured voltage line shape, the red L_S and the blue L_A curve are symmetric and antisymmetric line shape contributions from fit of the green curve with the function defined by Eq. (5.7). The data are acquired at an external field angle of $\phi_H = 45°$ and at a precession frequency of the magnetization $f = 10\,\text{GHz}$. In b) the voltage spectra measurement scheme for out-of-plane excitation and the specification of the external field angle ϕ_H are shown.

ISHE from AMR on the basis of their different general symmetries. To this end a conceptual transfer from in-plane to out-of-plane excitation of an in-plane magnetization using a CPW is necessary. Corresponding experimental results will be discussed in the following section.

6.2 Angle dependent measurements of voltage signals at FMR for out-of-plane excitation with a CPW

The out-of-plane excitation measurement scheme and the specification of the external field angle ϕ_H is shown in Fig. 6.1b). In Fig. 6.1a) the measured voltage spectrum of a NiFe/Pt bilayer across FMR is shown. The external field angle is $\phi_H = 45°$ and the excitation frequency is 10 GHz. The NiFe layer thickness is nominally the same as for the case of in-plane excitation treated before, viz. 12 nm and the Pt layer is slightly thicker, $t_{Pt} = 15\,\text{nm}$. The voltage spectrum is similar to the one in Fig. 6.1a). It is a sum of symmetric and antisymmetric line shapes L_S and L_A, whose relative amplitudes A_S and A_A can be extracted by a fit using Eq. (5.7). However, $A_S(\phi_H)$ and $A_A(\phi_H)$ for out-of-plane excitation, which are presented in Fig 6.3a), are different compared to the plots shown in Fig. 6.1b) for in-plane excitation. What catches the eye first is the distinct asymmetry with respect to $\phi_H = 180°$. The

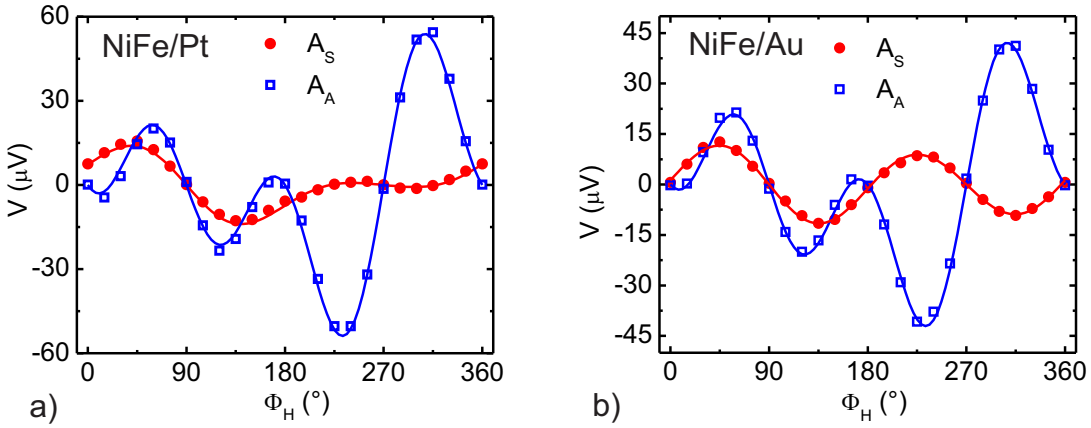

Figure 6.3: The amplitudes of L_S and L_A, A_S red dots and A_A blue open squares respectively, are plotted as a function of external field angle ϕ_H. The angular dependence of the respective voltage spectra was recorded at 10 GHz. $A_\mathrm{S}(\phi_\mathrm{H})$ is fitted with the function defined in Eq. (6.3) and $A_\mathrm{A}(\phi_\mathrm{H})$ using Eq. (6.2). Red and blue solid lines represent the respective fits. a) shows data for NiFe/Pt and b) for NiFe/Au

action of both out-of-plane driving field caused by the CPW and in-plane driving field due to the capacitively and inductively coupled current that flows through the Pt breaks the reciprocity of magnetization reversal in the NiFe layer. Dc-voltage line shapes at FMR are described by Eq. (4.20) (ISHE) and Eq. (4.40) (AMR) and the corresponding two functions are adequate to fit $A_\mathrm{A}(\phi_\mathrm{H})$ and $A_\mathrm{S}(\phi_\mathrm{H})$:

$$A_\mathrm{A} = (a\sin(\phi_\mathrm{H}) + b)\sin(2\phi_\mathrm{H}) \tag{6.2}$$
$$A_\mathrm{S} = (c\sin(\phi_\mathrm{H}) + d)\sin(2\phi_\mathrm{H}) + e\cos(\phi_\mathrm{H}) \tag{6.3}$$

The fit to the data is presented as respective blue (A_A) and red (A_S) solid lines in Fig. 6.3a). The fit parameters determine the physical quantities of AMR and ISHE. In analogy to Eqs. (4.20) and (4.40) the following relations hold:

$$a = A_\mathrm{AMR}\Im(\chi^\mathrm{res}_{y'y'})h_x \tag{6.4}$$
$$b = A_\mathrm{AMR}\chi^\mathrm{res}_{y'z}h_z\sin\xi \tag{6.5}$$
$$c = A_{\mathrm{ISHE,\ ip}}/2 \tag{6.6}$$
$$d = A_\mathrm{AMR}\chi^\mathrm{res}_{y'z}h_z\cos\xi \tag{6.7}$$
$$e = A_{\mathrm{ISHE,\ oop}} \tag{6.8}$$

A_AMR, $A_{\mathrm{ISHE,\ ip}}$ and $A_{\mathrm{ISHE,\ oop}}$ summarize the remaining parameters appearing in Eqs. (4.40), (4.19) and (4.20), respectively. Parameters b and d can be used to estimate the phase angle ξ between the rf current flowing in the CPW and the

embedded NiFe/NM bilayer wires,

$$\xi = \arctan\left(\frac{b}{d}\right) \tag{6.9}$$

The fits to the data presented in Fig. 6.3a) yield $b = -17.3$, $d = 7.0$ and $|\xi| \approx 68°$. The knowledge of ξ allows for the estimation of the ratio of the out-of-plane field h_z which is generated by the CPW to the in-plane-field h_x which is caused by the current flowing in the Pt layer. Both drive the magnetization precession. For h_x/h_z the following relation holds using Eqs. (6.4) and (6.5):

$$\frac{h_x}{h_z} = \frac{a}{b}\frac{\chi^{\mathrm{res}}_{y'z}}{\Im(\chi^{\mathrm{res}}_{y'y'})}\sin(\xi) \tag{6.10}$$

From the fit to data of $A_{\mathrm{A}}(\phi_{\mathrm{H}})$ the parameter values $a = 48.4$ and $b = -17.3$ are extracted. The susceptibility factors $\Im(\chi^{\mathrm{res}}_{zz})$ and $\chi^{\mathrm{res}}_{y'z}$ are determined using Eqs. (3.56) and (3.55) taking for the very same NiFe/Pt wire the extracted line width and resonance field from a fit to the data of the spectrum presented in Fig. 6.2a). The applicable susceptibility factor $\Im(\chi^{\mathrm{res}}_{y'y'})$ is calculated from the relation,

$$\frac{\chi^{\mathrm{res}}_{y'z}}{\Im(\chi^{\mathrm{res}}_{y'y'})} = \frac{\Im(\chi^{\mathrm{res}}_{zz})}{\chi^{\mathrm{res}}_{y'z}} \tag{6.11}$$

This can be concluded from Eqs. (3.54) - (3.56). The results are $\Im(\chi^{\mathrm{res}}_{zz}) = 20.76$ and $\chi^{\mathrm{res}}_{y'z} = 55.89$. Inserting them together with the parameters a and b into Eq. (6.10) yields $h_x/h_z = 0.96$. Hence, for the NiFe/Pt bilayer at hand the in-plane field due to the current through Pt is comparable to the out-of-plane field generated by the CPW. Analogously to the voltage due to AMR, one might call the in-plane driving field parasitic. Its relative amplitude to the out-of-plane driving field signifies that it is not negligible for conductive capping layers of NiFe.

The role of the parasitic in-plane field is further studied using angle dependent measurements of voltage amplitudes A_{S} and A_{A} for NiFe/Au. The individual layer thickness in this case is 12 nm. Corresponding data, including fits according to Eqs. (6.2) and (6.3), are plotted in Fig. 6.3b). Again the symmetry with respect to $\phi_{\mathrm{H}} = 180°$ is broken. The corresponding fit parameters needed to calculate the phase ξ via Eq. (6.9) and subsequently the parasitic field ratio h_x/h_z are $a = 40.7$, $b = -11.3$ and $d = 10.2$. The phase angle for the case of NiFe/Au is given by $|\xi| = 48°$. It substantially differs from the result for NiFe/Pt. This indicates that the phase ξ is extremely sensitive to changes concerning the conductivity of materials. Assuming the same ratio of the applicable susceptibilities in Eq. (6.10) as for NiFe/Pt, the parasitic field ratio for NiFe/Au is calculated as $h_x/h_z = 0.99$. The value for h_x/h_z is similar for the two bilayers which corroborates the statement that capping layers which have conductivities much higher than the NiFe-layer underneath, generate substantial parasitic magnetic excitation fields.

Furthermore, the contribution of ISHE to the voltage amplitude A_{S} can be studied

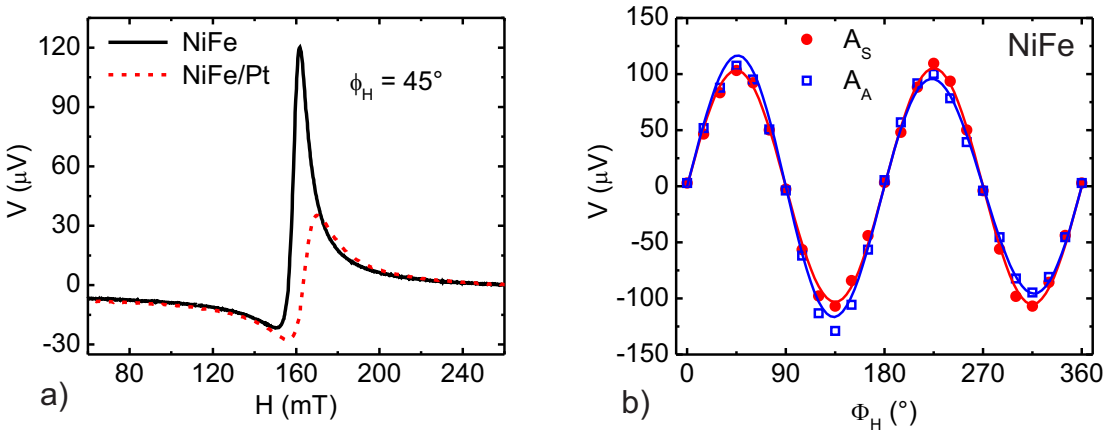

Figure 6.4: In a) a direct comparison of voltage spectra at 12 GHz and $\phi_H = 45°$ for NiFe and NiFe/Pt is displayed. In b), A_S (red dots) and A_A (blue open squares) are plotted as a function of external field angle ϕ_H for NiFe. The angular dependence of the respective voltage spectra was recorded at 10 GHz. $A_S(\phi_H)$ is fitted with the function defined in Eq. (6.3) and $A_A(\phi_H)$ using Eq. (6.2). Red and blue solid lines represent the respective fits.

for NiFe/Pt and NiFe/Au via parameters c (Eq. (6.6)) and e (Eq. (6.8)). The values from the fit for NiFe/Pt are $c = 2.23 \pm 0.52$ and $e = 7.35 \pm 0.35$. Comparison with the parameter $d = 7.0 \pm 0.27$ suggests that voltage signals due to AMR and ISHE contribute to the symmetric line shape. This is especially the case for $\phi_H = 45°$, where symmetry arguments allow for both contributions. For NiFe/Au $c = 0.66 \pm 0.30$ and $e = 1.25 \pm 0.20$. Though distinguishable via fit, these parameters are one order of magnitude smaller than the pure AMR connected amplitude $d = 10.2 \pm 0.15$. This means that the largest part contributing to A_S for NiFe/Au is generally due to AMR. One additional very important fact can be deduced from the A_S-plots in Fig. 6.3. I.e. the sign change of the voltage with respect to external field reversal, viz. opposite sign for $\phi_H = 180°$ and $\phi_H = 0°$.
In order to set the statements about the parasitic fields and the appearance of signals caused by both ISHE and AMR on a solid basis, material dependent studies are carried out. As hitherto, all studied layers are shaped as 400 µm long and 5 µm wide wires. First of all, a NiFe single layer wire with a thickness of 12 nm is examined. In Fig. 6.4a) a comparison of voltage spectra for NiFe and NiFe/Pt is presented. It is obvious, that the two line shapes show the same qualitative behavior for the chosen angle $\phi_H = 45°$. Both consist of large L_S- and L_A-contributions. The picture changes when one considers the angular dependence of voltage signals. A_S and A_A are plotted as a function of ϕ_H for NiFe in Fig. 6.4b). Fits to the data according to Eqs. (6.2) and (6.3) suggest that only parameters $b = 106.02$ and $d = 104.21$ are substantial. Both b and d are the parameters which correspond to the symmetric and antisymmetric

line shape amplitudes of voltages due to AMR under the circumstances of an out-of-plane driving field. In this case from Eq. 6.9 a phase angle $\xi = 45.50°$ is calculated from b and d. Due to the absence of the conductive capping layer for the single NiFe film one does neither expect a parasitic in-plane field h_x nor any voltage signal due to ISHE. Information about the parasitic in-plane field can be extracted from the fit parameter a. The fact that it is nonzero can be observed in $A_A(\phi_H)$ in Fig. 6.4b), since it is the reason for the slight asymmetry of the data points with respect to $\phi_H = 180°$. It corresponds to $a = 14.76$ from the fit to the data using Eq. 6.2. This suggests that also in the single NiFe layer an additional in-plane field h_x drives the magnetization. Its quantification using Eq. (6.10) yields $h_x/h_z = 0.04$. The most plausible explanation is that due to oxidation of the NiFe surface (the film was not capped in situ) the rf-current does not flow homogeneously through the ferromagnetic material and contributes to a very small additional parasitic in-plane field. Considering the expected absence of ISHE it is important to compare the relative magnitude of the parameter d to the parameters c and e which are extracted from the fit to $A_S(\phi_H)$ using Eq. 6.3. In fact, the parameters c and e are within the error margin of d and this suggests that within the measurement limits no ISHE is present. This proves that the recording of the angular dependence of voltage magnitudes of line shapes is a very effective method to check whether ISHE does generate a voltage in a NiFe/NM bilayer through parameters c and d in Eq. 6.3. To this end also bilayers are studied for which spin pumping is not detectable. Two samples one denoted NiFe/Ta 1 and the other NiFe/Ta 2 are examined with respect to angular dependencies of voltage signals at FMR. For NiFe/Ta 1 the individual layer thickness is 12 nm for NiFe and 14 nm for Ta. It was grown by magnetron sputtering in the same UHV-chamber as the already examined NiFe, NiFe/Pt, and NiFe/Au bilayers at the University of Regensburg. NiFe/Ta 2 was fabricated at the IBM research center in Almaden USA by See-Hun Yang in the research group of Stuart Parkin. Concerning NiFe/Ta 2 the layers are grown on an oxidized silicon substrate. The thickness of NiFe is 12 nm and the Ta capping has a thickness of 10 nm. In order to prevent oxidation the Ta-layer is capped by 0.3 nm of Al and 1.2 nm of Al_2O_3. The two NiFe/Ta bilayers differ with respect to two major aspects. First, the conductivity of the NiFe layer of NiFe/Ta 2 is twice as high as for the other bilayer. Second, the Ta layer of NiFe/Ta 1 is not capped and an oxidation of the first two nanometers of Ta and therefore a thickness of 12 nm is assumed. Voltage spectra for both NiFe/Ta bilayers are recorded as a function of ϕ_H. The results for $A_A(\phi_H)$ and $A_S(\phi_H)$ are presented in Figs. 6.5a) and b). The fits according to Eqs. (6.2) and (6.3) are again represented by the solid lines. The characteristic $\sin(2\phi_H)$-dependence of $A_S(\phi_H)$ for both NiFe/Ta 1 and NiFe/Ta 2 which is observable in Figs. 6.5a) and b) suggests the absence of a voltage signal due to ISHE. The parameters c and e when fitting with Eq. (6.3) are indeed zero within the error margin of parameter d which proves the statement. Note that this is consistent with the absence of spin pumping for NiFe/Ta, which has been found in chapter 5. Furthermore, the effect of the parasitic in-plane field h_x from the rf-current flowing through the Ta-layer is clearly distinguishable in Figs. 6.5a) and b).

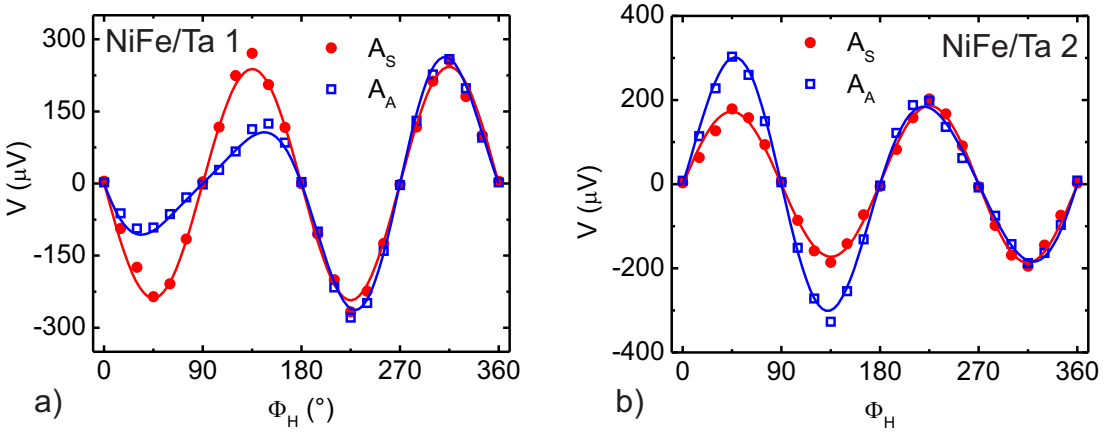

Figure 6.5: The voltage amplitudes A_S (red dots) and A_A (blue open squares) are plotted as a function of external field angle ϕ_H for NiFe/Ta. The angular dependence of the respective voltage spectra was recorded at 10 GHz. $A_\mathrm{S}(\phi_\mathrm{H})$ is fitted with the function defined in Eq. (6.3) and $A_\mathrm{A}(\phi_\mathrm{H})$ using Eq. (6.2). Red and blue solid lines represent the respective fits. In a) data of a bilayer grown in a UHV-chamber at the University of Regensburg denoted NiFe/Ta 1 is shown. In b) data a bilayer fabricated at the IBM research center in Almaden, denoted NiFe/Ta 2 is displayed.

One observes an enhanced asymmetry for $A_\mathrm{A}(\phi_\mathrm{H})$ with respect to $\phi_\mathrm{H} = 180°$ when comparing the results to data for the NiFe single layer. Yet, with respect to Pt or Au capping layers the effect is rather small which results in the general observation that b is larger than a for both NiFe/Ta samples. Specifically $a = 114.8$ and $b = -179.15$ for NiFe/Ta 1 and $a = 83.67$ and $b = 240.91$ for NiFe/Ta 2. This yields a phase angle $\xi = 36.68°$ for the first and $\xi = 53.32°$ for the latter sample. The observed difference in the phase angle is most likely due to the different conductivities of both bilayers. Using the respective results for ξ and the parameter $d = 240.54$ for NiFe/Ta 1 and $d = 179.43$ for NiFe/Ta 2 yields a parasitic field ratio (Eq. (6.10)) of 0.15 and 0.11, respectively.
Furthermore, what catches the eye is the large amplitudes of fits for the two tantalum bilayers. If the conventional AMR were the only voltage generating effect, A_S and A_A should be smaller than for a NiFe-single layer of same thickness. This is even more so as the tantalum bilayers have a lower resistance than the studied NiFe-layer. However, this is clearly not observed in the data of Fig. 6.4b) and Fig. 6.5. It is very likely that another effect similar to ISHE is active in NiFe/Ta. A Rashba-type electric field within the NiFe film due to the asymmetry of the upper with respect to the lower interface might generate a non-negligible voltage contribution. However, this shall not be discussed in detail within the frame of this phd-thesis, though it might be relevant for future experimental studies of NiFe/Ta.
Given the angular dependence presented in Fig. 6.3 for NiFe/Pt and NiFe/Au it is

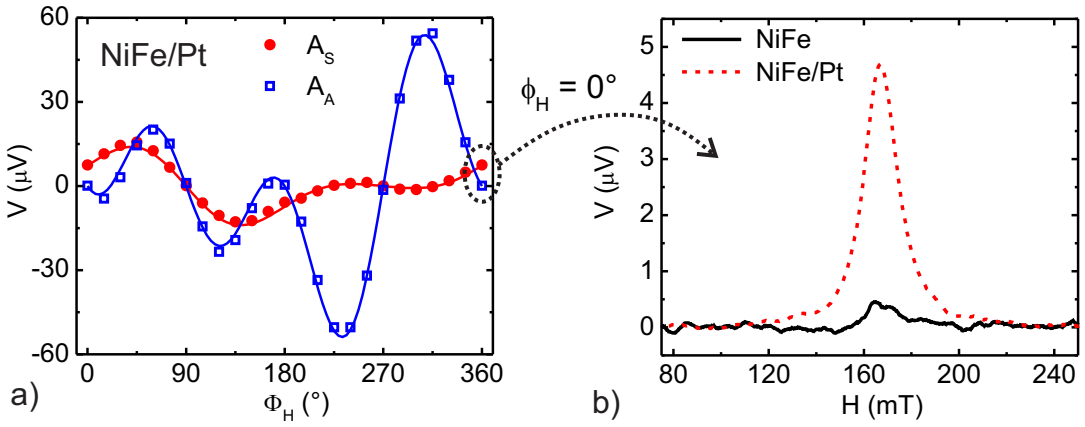

Figure 6.6: In a) $A_{\mathrm{S}}(\phi_{\mathrm{H}})$ and $A_{\mathrm{A}}(\phi_{\mathrm{H}})$ for NiFe/Pt are plotted. The data points for the external field angle $\phi_{\mathrm{H}} = 360° = 0°$ are marked with the black colored ellipse. In b) corresponding voltage spectra for pure NiFe and NiFe/Pt under circumstances of a driving frequency of 12 GHz at $\phi_{\mathrm{H}} = 0°$ are shown.

promising to further study ISHE for these material sets. The following section will deal with the quantification of spin Hall angles α_{SH} from voltages due to ISHE at the angular position $\phi_{\mathrm{H}} = 0°$. At this specific angle the signal is only caused by ISHE, see the angular position marked in Fig. 6.6a) by the black ellipse. Furthermore, the parasitic in-plane field, which is always present and non-negligible for conductive capping layers like Pt and Au, is parallel to the static magnetization component for $\phi_{\mathrm{H}} = 0°$ and conclusively has no effect on the magnetization dynamics and spin pumping. The comparison of voltage spectra for NiFe and NiFe/Pt for $\phi_{\mathrm{H}} = 0°$ in Fig. 6.6b), shows the significant difference between voltages due to AMR and ISHE. As the AMR does not generate voltages for $\phi_{\mathrm{H}} = 0°$, the signal vanishes for pure NiFe. The voltage measured for NiFe/Pt in this configuration is caused only by ISHE and the line shape is purely symmetric. Yet, one can still distinguish a small contribution due to AMR for pure NiFe in Fig. 6.6b). To this end, it will be one of the major issues to exactly find the $\phi_{\mathrm{H}} = 0°$-position.

7 Experimental results concerning the dc inverse spin Hall effect for NiFe/Pt and NiFe/Au bilayers

This chapter is devoted to a unique determination of spin Hall angles for Pt and Au using SP-ISHE under the assumption that the spin-diffusion model is valid in the normal metals. According to the argumentations on symmetries of voltages due to AMR and ISHE in the previous chapter, out-of-plane excitation of the magnetization is used, see Fig. 6.1b). At an external field angle of $\phi_H = 180°$-multiples the voltage signals are only caused by ISHE. The importance of small angle variation across the desired angular position will be pointed out and temperature dependent measurements of voltage signals corroborate the physical difference between $\phi_H = 0°$ and $\phi_H = 45°$. Being sure that AMR is excluded geometrically, a quantification of spin Hall angles for Pt and Au is performed. This includes a detailed discussion about parameters and measurement errors entering the quantification process. For Au it will be essential to incorporate the back flow from the spin pumping process into an effective spin mixing conductivity $\tilde{g}_F^{\uparrow\downarrow}$ [131, 153]. Concerning Pt it is the reported short spin diffusion length in the 1 nm range which is the most critical parameter [54]. In order to obtain an estimation for the so-called effective spin diffusion length of the studied Pt the voltage amplitudes due to ISHE will be studied as a function of Pt thickness. Temperature dependent measurements offer further insight into the behavior of the spin diffusion length of Pt. The results reconcile the used magnitude range for extracting the spin Hall angle from low temperature NLSV and the spin Hall angle quantification from SP-ISHE at room temperature.

7.1 Characterization of voltages due to SP-ISHE

In the following without loss of generality $\phi_H = 0°$ is chosen for analyzing voltage line shapes with respect to ISHE and α_{SH}. In order to find $\phi_H = 0°$ voltage spectra for small steps around this respective angular position are recorded. In Fig. 7.1 a material specific overview of this process is presented. Studies for NiFe/Pt and NiFe/Au as well as for NiFe single and NiFe/Ta bilayers are shown. The individual layer thicknesses are 12 nm in this section. All data correspond to a driving field frequency of 12 GHz. The angular steps for NiFe/Pt and NiFe/Au, panels a) and b) of Fig. 7.1, are chosen as 1°. The line shapes, which are intentionally offset for easier viewing, are becoming more and more symmetric towards $\phi_H = 0°$. Upon crossing

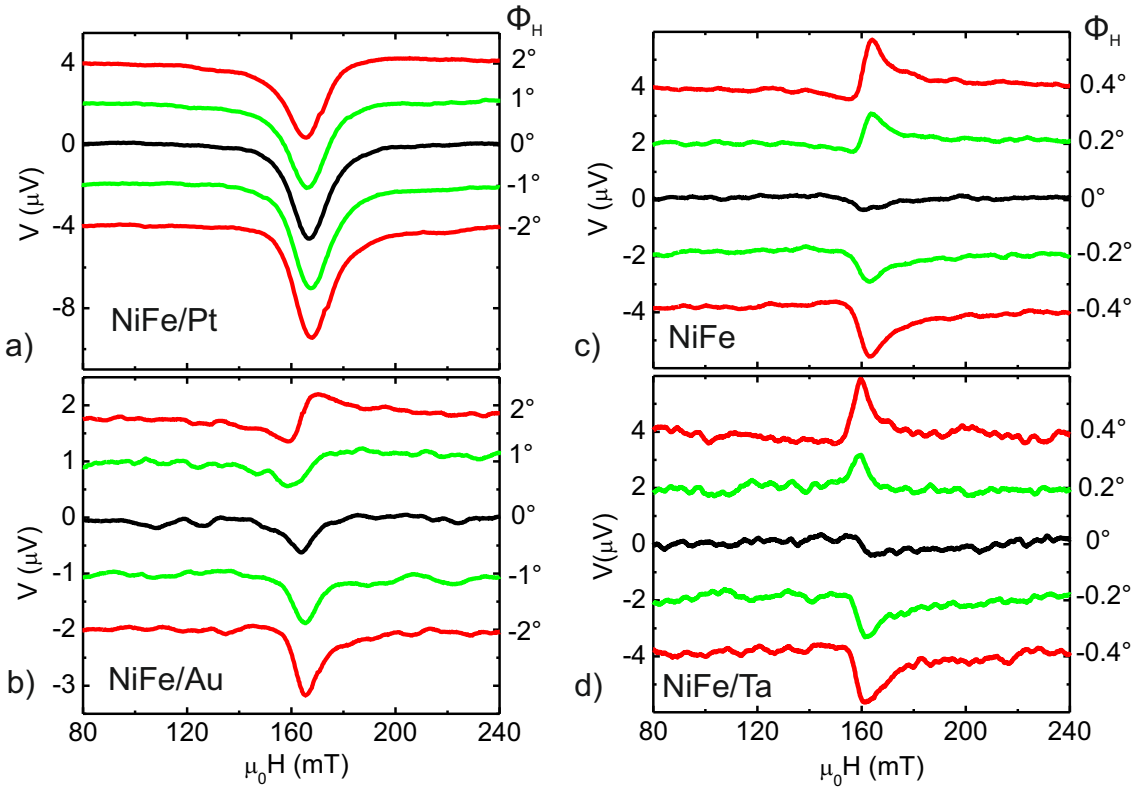

Figure 7.1: Voltage spectra for different NiFe/NM bi- as well as for a single NiFe layer are displayed. Equally colored plots are curves correspond to equal $\pm\phi_{\mathrm{H}}$-values. The black curves are the voltage spectra at exactly $\phi_{\mathrm{H}} = 0°$. In a) to d) results for different materials, NiFe/Pt, NiFe/Au, NiFe, NiFe/Ta are plotted. The curves are artificially offset with respect to each other for easier viewing.

the $\phi_{\mathrm{H}} = 0°$-position the antisymmetric amplitude A_{A} of the line shape first vanishes and subsequently changes sign. This is expected for the dc-voltage due to AMR, since in proximity of $\phi_{\mathrm{H}} = 0°$ the terms proportional to $h_{\mathrm{z}}^{\mathrm{CPW}} \sin(2\phi_{\mathrm{H}})$ dominate (see Eq. (4.40)). For comparison of the physical difference of NiFe/Pt and NiFe/Au with respect to uncapped NiFe and NiFe/Ta (where no spin pumping occurs and therefore no voltage due to ISHE is expected) panels c) and d) of Fig. 7.1 contain respective line shape sets. In this case ϕ_{H} is varied in steps of 0.2° in order to get an insight what happens exactly at $\phi_{\mathrm{H}} = 0°$ for these bilayers. At the supposed $\phi_{\mathrm{H}} = 0°$-configuration there are still very small signals distinguishable for both NiFe and NiFe/Ta. However, the are predominantly antisymmetric and can therefore not be caused by ISHE. The case of NiFe and NiFe/Ta illustrates that it might be very crucial to find the exact magnetization configuration where a voltage due to AMR completely vanishes and one should be very accurate in this process.
Having found $\phi_{\mathrm{H}} = 0°$ for NiFe/Pt and NiFe/Au a frequency dependence of voltage signals gives further insight into whether the signal is indeed generated by spin

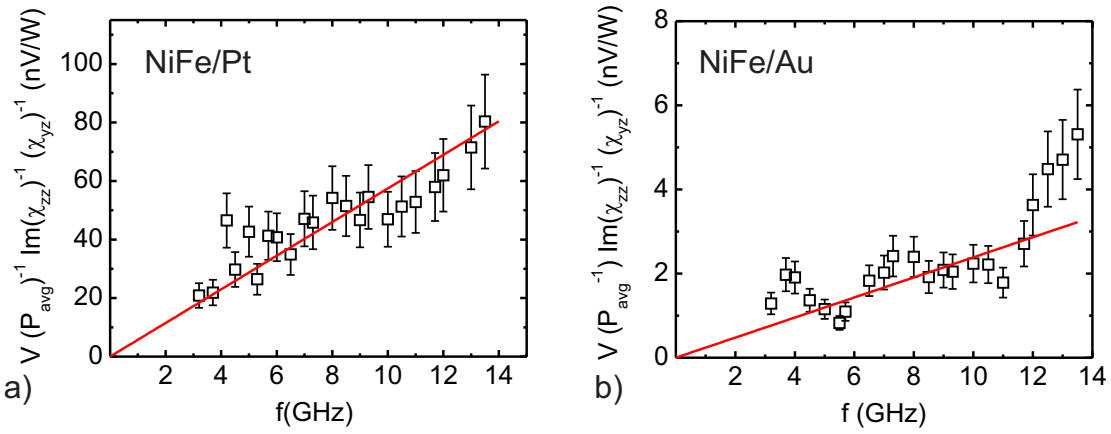

Figure 7.2: The frequency dependence of the ISHE caused voltage amplitude of a) NiFe/Pt and b) NiFe/Au is displayed. The data points are the voltage amplitudes A_S normalized by average microwave power and applicable susceptibility factors. A relative error of 20% is assumed for each data point due to uncertainties in the average microwave power (vertical error bars). The red lines are linear fits to data assuming a fixed intercept at (0,0).

pumping in combination with ISHE. In fact this is a very important test, but only two publications have presented corresponding results [52, 53]. The pumped spin current at FMR and correspondingly the amplitude of the voltage due to ISHE is expected to increase linearly with the precession frequency, cf. Eqs. (3.77) and (4.20). In order to observe this linear increase of voltage it is important to normalize the line shape amplitude A_S by all parameters which themselves depend on frequency. The first parameter to be considered is the square of the external out-of-plane driving field h_z^2 which is directly proportional to the microwave power at the site of the bilayer wire. The relevant power can be best approximated by taking the average of input and output power measured in units of dBm using a rf-powermeter. This approach is chosen as the FM/NM bilayer is located at the center longitudinal position of the CPW, symmetrically to it the microwave input and output terminals. The average power P_{avg} is a critical parameter in the sense that it is very difficult to estimate where the power consumption in the device really takes place. To this end P_{avg} is only a measure of h_z^2 if the microwave power falls off as a continuous exponential function along the CPW. A measure for how well the average power can be used for normalization is the difference between input and output power, which should be minimal and constant as a function of frequency. In order to do uncertainties full justice a relative error of 20% is assumed.
Two further parameters which have to be considered due to their frequency dependence in the normalization process are the susceptibilities of the magnetization at resonance $\Im(\chi_{zz}^{\mathrm{Res}})$ and $\chi_{y'z}^{\mathrm{Res}}$, cf. Eqs (3.56) and (3.55). The frequency dependence

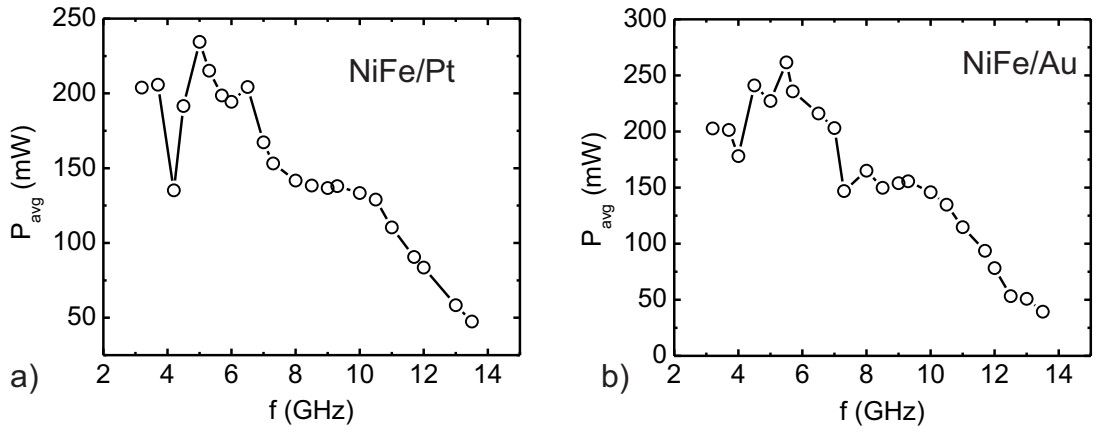

Figure 7.3: The average power P_{avg} dissipated in the CPW for a) the NiFe/Pt and b) the NiFe/Au sample.

manifests itself in the factors $H_0(f)$ and $\Delta H(f)$. However, as $\Delta H(f)$ is constantly overestimated for the 5 µm wide bilayer wires when analyzing voltage line shapes at $\phi_{\mathrm{H}} = 0°$, i.e. due to edge modes (see Sec. 5.2), the susceptibility factors at resonance are rewritten in the following way:

$$\Im(\chi_{zz}^{\mathrm{res}}) = \frac{\mu_0 M_{\mathrm{S}} \mu_0 H_0}{(2\mu_0 H_0 + \mu_0 M_{\mathrm{eff}}) \alpha 2\pi f/\gamma} \tag{7.1}$$

$$\chi_{y'z}^{\mathrm{res}} = \frac{\mu_0 M_{\mathrm{S}} \sqrt{(\mu_0 H_0)^2 + \mu_0 H_0 \mu_0 M_{\mathrm{eff}}}}{(2\mu_0 H_0 + \mu_0 M_{\mathrm{eff}}) \alpha 2\pi f/\gamma} \tag{7.2}$$

In these formulas $\Delta H(f)$ is substituted by $\alpha 2\pi f/\gamma$. For NiFe/Pt $\alpha = 0.0135$, for NiFe/Au $\alpha = 0.009$, and $\gamma = 181.20 \pm 0.45\,\mathrm{GHz\,T^{-1}}$ for both films. These results stem from the extended film FMR measurements with corresponding respective layer thicknesses of 12 nm, see Sec. 5.1. The results for the normalization process together with a linear fit which has a fixed intercept at $(0, 0)$ are displayed in Fig. 7.2a) for NiFe/Pt and in Fig. 7.2b) for NiFe/Au. In the case of NiFe/Pt almost all shown data points are in agreement with the linear fit assuming an error margin of 20%. Yet, some outliers are recognizable, especially in the frequency range of 4 to 6 GHz. The plot presented in Fig. 7.3a) suggests that this correlates with a large scatter of P_{avg} in this region. A similar reasoning applies for the case of NiFe/Au where especially with increasing frequency more and more outliers relative to the linear fit appear. The corresponding $P_{\mathrm{avg}}(f)$ dependence is plotted in Fig. 7.3b). Nevertheless, the results plotted in Fig. 7.2a) and b) suggest that the generated voltage signals in NiFe/Pt and NiFe/Au at $\phi_{\mathrm{H}} = 0°$ are caused by SP-ISHE.

Temperature dependent measurements of voltages at FMR provide further insight into the nature of signals at different angles ϕ_{H}. The sample under consideration is a bilayer of NiFe/Pt with individual layer thicknesses of 12 nm. At a fixed driving frequency of 18 GHz and under circumstances of out-of-plane excitation, voltage

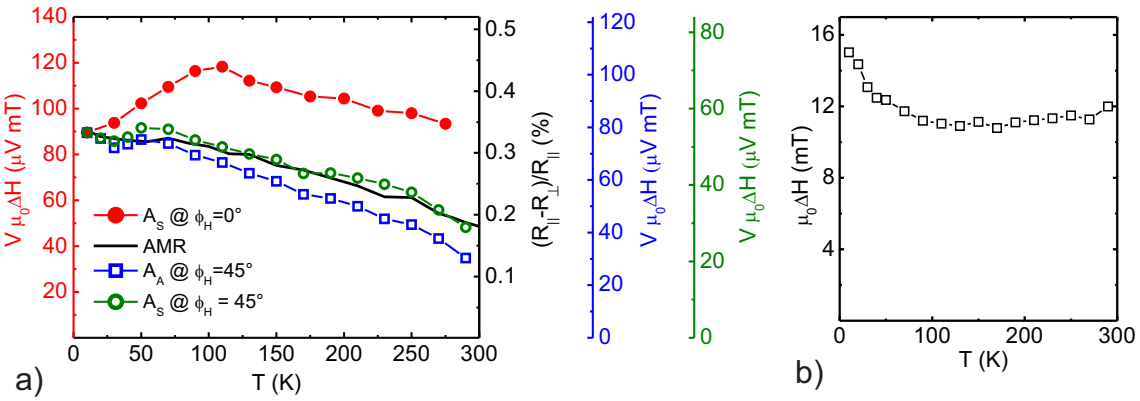

Figure 7.4: In a) voltage amplitudes at FMR in NiFe/Pt multiplied with the corresponding line width of spectra for a precession frequency of 18 GHz at $\phi_H = 0°$ and $\phi_H = 45°$ are displayed. The red curve corresponds to A_S (amplitude of symmetric line shape) at $\phi_H = 0°$. The green and the blue curves correspond to A_S and A_A (amplitude of antisymmetric line shape) at $\phi_H = 45°$. The black line are results for static AMR in the same sample. In b) the line width from fit to FMR measurements, Eq. 5.3, is shown as a function of temperature.

spectra across FMR are recorded for both $\phi_H = 0°$ and $\phi_H = 45°$. The amplitudes A_S and A_A are extracted from fits according to Eq. (5.7). The temperature is varied from 10 to 150 K in steps of 20 K and from 150 to 300 K in steps of 25 K. In order to gather comparative results on the origin of voltages at $\phi_H = 0°$ and $\phi_H = 45°$, $A_S(T)$ and $A_A(T)$ are treated as if they were only caused by AMR. Corresponding plots are displayed in Fig. 7.4a). To see the pure AMR caused temperature dependence all amplitudes are multiplied by $\mu_0\Delta H(T)$. This is done as voltage signals due to AMR are proportional to the susceptibility $\chi_{y'z}$ which contains the temperature dependent factor $1/\Delta H(T)$ (see Eq. (7.2)). For an explicit plot of $\mu_0\Delta H(T)$ see Fig. 7.4b).

Together with the scaled voltage amplitudes in Fig. 7.4a) data points from static AMR-measurements are presented. The static AMR is measured by setting up a dc-current through the NiFe/Pt bilayer along the y-direction (see coordinate system in Fig. 6.2b)). Shown is the temperature dependence of the relative resistance change when switching the magnetization from parallel $R_\parallel$ to perpendicular $R_\perp$ with respect to the dc current direction. In this case $R_\parallel - R_\perp = R_A$ is divided by $R_\parallel$. The corresponding axes of the curves presented in Fig. 7.4a) are scaled such that the four displayed plots coincide at a temperature of 10 K. The curves corresponding to A_S and A_A at $\phi_H = 45°$ are strikingly similar to the data points measured for the normalized statically measured R_A, which indicates that both symmetric and antisymmetric voltage line shapes for this angular position are mainly due to AMR. In contrast the curve representing $A_S(T)$ at $\phi_H = 0°$ shows a different temperature dependence. The voltage is interpreted to be due to ISHE. In fact, the temperature

Properties	NiFe/Pt-a	NiFe/Pt-b	NiFe/Pt-c	NiFe/Au
t_{NiFe}(nm)	12	14	12	12
t_{Pt}(nm)	12	11.5	15	12
$\sigma(10^6\,\Omega^{-1}\,\mathrm{m}^{-1})$	2.4	2.39	3.4	5.4

Table 7.1: Parameters for NiFe/Pt-a to -c as well as for NiFe/Au are listed.

dependence of ISHE differs from that of AMR. As both $\Im(\chi_{zz}^{\mathrm{Res}})$ and $\chi_{y'z}^{\mathrm{Res}}$ determine the amplitude of a voltage signal due to ISHE it is proportional to $1/(\Delta H)^2$. This also leads to its pronounced dependence at low temperatures where $\mu_0\Delta H$ varies strongly as can be seen in Fig. 7.4b).
Summarizing this section, the results of frequency and temperature dependent measurements of voltage signals at $\phi_{\mathrm{H}} = 0°$ corroborate that a unique study of ISHE is possible with the presented experimental technique. On this basis spin Hall angles for Pt and Au are determined in the following section.

7.2 Quantifying spin Hall angles for Pt and Au

The calculation of spin Hall angles is conducted using Eq. (4.22) for the special case of $\phi_{\mathrm{H}} = 0°$ and out-of-plane excitation. The formula shall be displayed in the following for easier viewing:

$$\alpha_{\mathrm{SH}} = \frac{V_{\mathrm{ISHE}}^{\mathrm{oop}}\sigma(t_{\mathrm{NM}} + t_{\mathrm{FM}})M_{\mathrm{S}}^2}{ef\tilde{g}_{\mathrm{F}}^{\uparrow\downarrow}\Im(\chi_{zz}^{\mathrm{res}})\chi_{y'z}^{\mathrm{res}}|h_z|^2 l\lambda_{\mathrm{sd}}\tanh\left(\frac{t_{\mathrm{NM}}}{2\lambda_{\mathrm{sd}}}\right)} \tag{7.3}$$

Prior to the explicit calculation of α_{SH} for Pt and Au the experimental accessibility, significance and possible uncertainties of the appearing parameters will be discussed. $V_{\mathrm{ISHE}}^{\mathrm{oop}}$ is the amplitude of the measured voltage line shape. At $\phi_{\mathrm{H}} = 0°$ it is equal to A_{S}. σ is the conductivity of the NiFe/NM bilayers and is given by the following formula:

$$\sigma = \rho^{-1} = \left(R\frac{A}{l}\right)^{-1} \tag{7.4}$$

A is the cross-sectional area of the NiFe/NM wire and is given by the characteristic width of 5 µm times the specific thickness of the bilayer stack $t_{\mathrm{FM}} + t_{\mathrm{NM}}$. The individual layer thicknesses of studied NiFe/Pt and NiFe/Au wires and the corresponding conductivities of the bilayers are summarized in Tab. 7.1. In order to keep the uncertainty on the thickness low, a calibration via atomic force microscopy is conducted in advance of sample growth. For the calculation of α_{SH} it is assumed that $l = 350\,\mu\mathrm{m}$, which is the separation of the voltage probes along the y-direction of the bilayer. e is the electron charge, f is the magnetization's precession frequency. M_{S} is the saturation magnetization of the respective NiFe-layer. Using SQUID magnetometry it is determined to correspond to an approximate value of $\mu_0 M_{\mathrm{S}} = 0.9\,\mathrm{T}$.

However, as each susceptibility factor is proportional to M_S, α_{SH} is independent of the magnitude of M_S since it appears to the same order in both the denominator and the nominator of Eq. (7.3). The susceptibility factors which enter Eq. (7.3) are evaluated at FMR. As discussed in the previous section they are given by Eqs. (7.1) and (7.2). The values of parameters entering the calculation of α_{SH} via these two equations shall be shortly reviewed. For γ the value obtained from extended film measurements is used, $\gamma = 181.20 \pm 0.45\,\mathrm{GHz\,T^{-1}}$. The effective magnetization $\mu_0 M_{\mathrm{eff}}$ is obtained by a fit of $\mu_0 H_0(f)$ using Eq. (5.4) and the needed resonance field values result from the line shape analysis of voltage spectra. Similarly, $\mu_0 \Delta H$ is extracted from voltage spectra. However, the assumption $\mu_0 \Delta H = \alpha 2\pi f/\gamma$ might not be valid for the $\phi_H = 0°$ configuration and a linear fit to $\mu_0 \Delta H$-data yields a constantly higher α compared to extended film FMR measurements (cf. Fig. 5.7a)). It can be reasoned that the amount of spin current to be pumped from NiFe into NM and therefore the voltage due to ISHE is proportional to the intrinsic damping of the NiFe plus the increased damping due to spin pumping and therefore the extended film results should enter Eqs. (7.1) and (7.2). Yet, since this reasoning is not yet footed on a profound theoretical basis, results for α_{SH} will be calculated for a range of damping factors with $\alpha_{\mathrm{min}} = \alpha_{\mathrm{extendedFilm}} = \alpha = 0.0135 \pm 0.0002$ and $\alpha_{\mathrm{max}} = \alpha_{\phi_H = 0°} = 0.0175$ for NiFe/Pt and the respective values for NiFe/Au are $\alpha_{\mathrm{min}} = 0.009$ and $\alpha_{\mathrm{max}} = 0.013$. This proceeding might stimulate further theoretical considerations and computational simulations with respect to magnetization dynamics, and the spin pumping contribution of edge modes for FM/NM bilayer wires which have a width on the micron scale or below.
Furthermore, the amplitude squared of the driving field $|h_z|^2$ when calculating α_{SH} enter Eq. (7.3). As discussed in Sec. 4.1.1 simulations of h for a fixed power of 20 mW have been performed. The results for a CPW with respective ground and signal line as well gap widths of 25, 50 and 30 µm are presented in Fig. 4.3. In Eq. (7.3) enters a respectively scaled driving field accounting for the specifically measured P_{avg} at the distinct frequencies using the formula:

$$h_z = \sqrt{\frac{P_{\mathrm{avg}}(\mathrm{mW}))}{10\,\mathrm{mW}}} \times h_z(@10\,\mathrm{mW}) \tag{7.5}$$

As one extracts the P_{avg} from the ohmic loss inside the CPW the values for h_z are to be calculated relative to 10 mW, which is the effective value of 20 mW for a 50 Ω-system.

The last two parameters which appear in the calculation of α_{SH} from measured voltage amplitudes due to ISHE are the effective spin mixing conductivity $\tilde{g}_F^{\uparrow\downarrow}$ and the spin diffusion length λ_{sd}. Both parameters have to be characterized from the perspective of $\epsilon = \tau_{el}/\tau_{sf}$, the ratio of momentum relaxation and spin flip rate [41, 43, 154]. A small ϵ as for Pt corresponds to a small λ_{sd} and a large ϵ as for Au entails a large λ_{sd}. The consequences for $\tilde{g}_F^{\uparrow\downarrow}$ are as follows. For the approximately 10 nm thick Pt layers studied in the course of this work $\tilde{g}_F^{\uparrow\downarrow} = g_F^{\uparrow\downarrow} = (2.67 \pm 0.2) \times 10^{19}\,\mathrm{m^{-1}}$ which is the value obtained from the spin pumping measurements presented in Chapt. 5. For the 12 nm thick Au layer the value $g_F^{\uparrow\downarrow} = 1.2 \times 10^{19}\,\mathrm{m^{-1}}$ [46, 160]

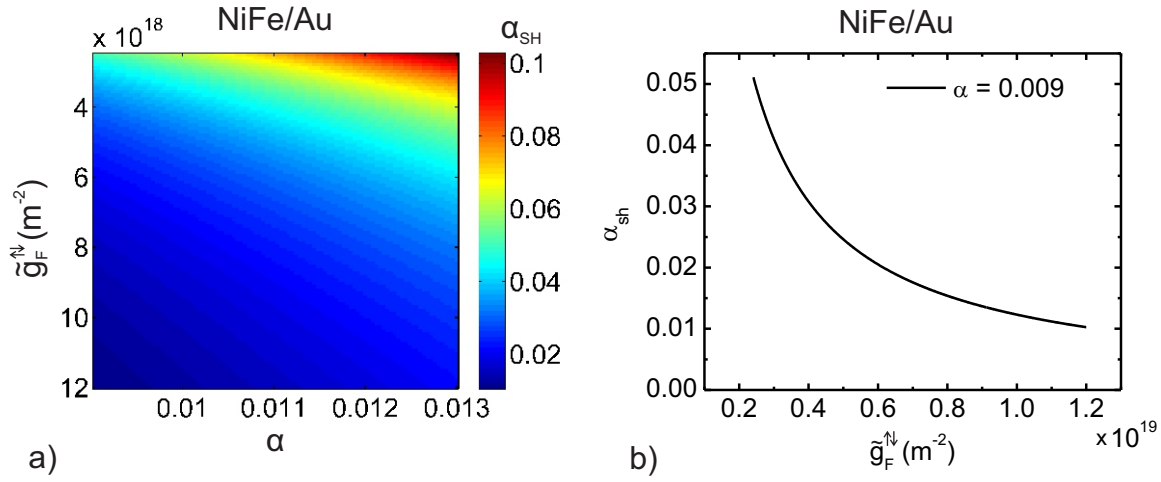

Figure 7.5: In a) α_{SH} is plotted as a function of damping α and effective spin mixing conductivity $\tilde{g}_{\mathrm{F}}^{\uparrow\downarrow}$. In b) a line scan of α_{SH} across the color plot for fixed $\alpha = 0.009$ is shown.

has to be used for the calculation of α_{SH}, since due to the large back flow of spin current $\tilde{g}_F^{\uparrow\downarrow}$ has not been detectable against the uncertainty of the extracted damping factor α of the single NiFe-film (see Fig. 5.4a)). However, the back flow in the spin pumping process has been carefully addressed experimentally in [46, 131, 153, 160]. Especially the results in [153] suggest that for a Au thickness of 12 nm and a value for the spin diffusion length of $\lambda_{\mathrm{sd}} = 34\,\mathrm{nm}$ only approximately one fifth of the spin current injected by spin pumping is effectively deposited in the Au layer. For the Au studied in this work λ_{sd} is several tens of nm, which is corroborated by the results of comparative spin pumping experiments of 12 nm and 50 nm thick Au capping layers of NiFe (see Fig. 5.2). For the calculation of α_{SH} a value of $\lambda_{\mathrm{sd}} = 34\,\mathrm{nm}$ shall be assumed.

Results of α_{SH} calculated for NiFe/Au from voltage amplitudes A_{S} at $\phi_{\mathrm{H}} = 0°$ are displayed as a color plot in Fig. 7.5a). Each point in the color plot corresponds to the average of 10 A_{S}-values for frequencies in the range of 7 to 11.5 GHz. This range is chosen due to the flat $P_{\mathrm{avg}}(f)$ dependence, see Fig. 7.3b). The x-axis of the color plot is given by the aforementioned magnetization damping factor α obtained for extended thin films (minimum value) and a bilayer wire including edge modes (maximum value). The y-axis consists of different values for the effective spin mixing conductivity $\tilde{g}_{\mathrm{F}}^{\uparrow\downarrow}$. The minimum and the maximum axis-values are given by $1.2 \times 10^{19}\,\mathrm{m}^{-2}$ divided by 5 which equals to $0.24 \times 10^{19}\,\mathrm{m}^{-2}$ and $1.2 \times 10^{19}\,\mathrm{m}^{-2}$, respectively. In Fig. 7.5a) it can be observed that the calculated value for α_{SH} of Au increases for increasing measured damping factor α and decreasing effective spin mixing conductivity $\tilde{g}_{\mathrm{F}}^{\uparrow\downarrow}$. The values for α_{SH} correspondingly vary as much as one order of magnitude. However, an the increased value of measured α corresponds to experimental estimation when including the effect of edge modes. Yet, these should

not significantly contribute to the spin pumping and therefore the most realistic estimates of α_{SH} for Au should be provided by fixing $\alpha = 0.009$ value. A consequent plot of α_{SH} as a function of $\tilde{g}_{\mathrm{F}}^{\uparrow\downarrow}$ is presented in Fig. 7.5b). The value of α_{SH} for Au equals 0.01 when disregarding back flow and 0.05 if fully accounting for back flow. The latter value is characterized as the most realistic value from the SP-ISHE experiment and therefore it will be used henceforth for comparative purposes.
Concerning Pt the most debatable and critical parameter is the spin diffusion length entering Eq. (7.3). Especially for Pt it is actually not justified to use the model of spin diffusion due to $\epsilon \approx 1$ [41, 147]. Nevertheless this has constantly been done when calculating spin Hall angles from experiment as well as from theoretical models [63, 110]. Therefore it will be proceeded in an analogous manner for the NiFe/Pt bilayers studied in this work. However, one might rephrase λ_{sd} for Pt as an effective spin diffusion length. The values of λ_{sd} which have entered respective calculations of α_{SH} in several experimental publications span one order of magnitude, 1.4 nm [54] to 10 nm [49, 50]. In order to do this parameter full justice and help towards resolving this issue, Pt thickness dependent measurements of voltage signals due to ISHE are performed. NiFe/Pt bilayers with a constant thickness of 12 nm for NiFe and thicknesses of 2, 5, 8 and 10 nm for Pt are studied using out-of-plane excitation at $\phi_{\mathrm{H}} = 0°$. Voltage spectra for a frequency range of 7 to 12 GHz are measured across FMR and A_{S} is interpreted to be solely due to ISHE. This frequency range is chosen for the fact that the transmitted power shows no strong dependence on frequency, see Fig. 7.3. According to theory for perfect spin sinks like Pt the thickness dependence of a voltage due to SP-ISHE should follow

$$V \propto V_0 \frac{\lambda_{\mathrm{sd}}}{t_{\mathrm{Pt}} + t_{\mathrm{NiFe}}} \tanh\left(\frac{t_{\mathrm{Pt}}}{2\lambda_{\mathrm{sd}}}\right) \tag{7.6}$$

This model assumes spin diffusion and no back flow of spin current. In order to be able to interpret the thickness dependence of the voltage signal due to ISHE correctly, one has to take into account that a measured voltage is also proportional to the resistance of the studied bilayer wires which naturally increases with decreasing t_{Pt}. The resistances of respective bilayer wires are displayed in Fig. 7.6b). The extracted voltage amplitudes from fits are further normalized to average power, susceptibilities and driving frequency. The resulting values are denoted $V_{\mathrm{norm}} R^{-1} f^{-1}$ and are plotted against frequency in Fig. 7.6c). In Fig. 7.6a) the values for constant thickness are averaged and plotted together with their standard deviation as a function of Pt thickness. The fit which uses the formula presented in Eq. (7.6) yields a spin diffusion length of $\lambda_{\mathrm{sd}} = 1.9 \pm 0.7$ nm. With respect to the order of magnitude this is in good agreement with the values of $\lambda_{\mathrm{sd}} = 1.4$ nm published in [54] and $\lambda_{\mathrm{sd}} = 3.4$ nm in [109]. Note that the discrepancy of the λ_{sd}-values presented in [54] and [109] would yield a calculated α_{SH} differing by a factor of 2.2. It is larger for $\lambda_{\mathrm{sd}} = 1.4$ nm. This fact makes the spin diffusion length a very critical parameter and to this end a thickness dependence of Pt on top of NiFe starting well below 2 nm is still missing and should be carried out in future experiments. Therefore and also against the background of the large spread of presented values [50, 54, 109], it

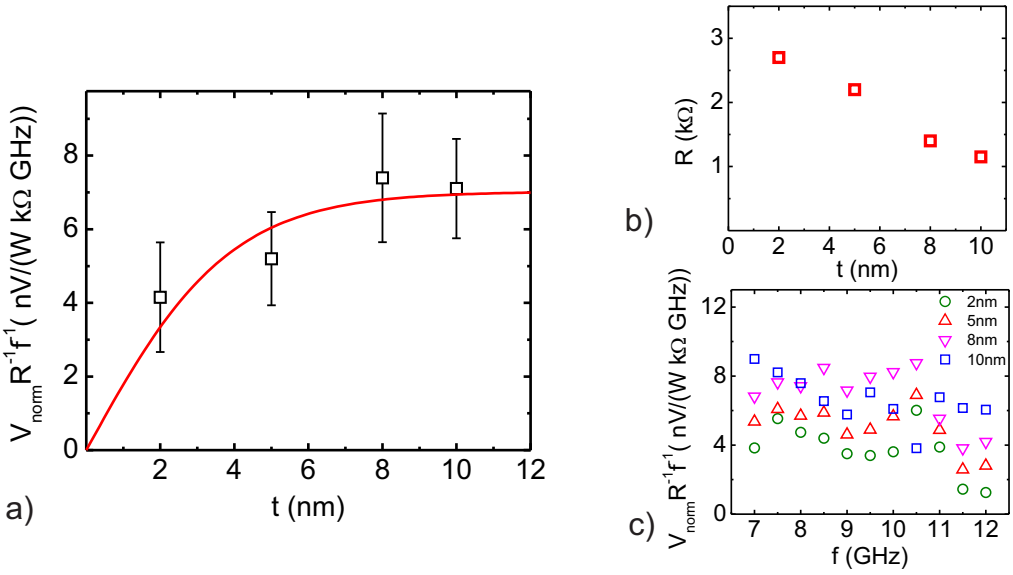

Figure 7.6: In a) the voltage amplitude in nV normalized by average microwave power in W, resistance in kΩ, and frequency in GHz of NiFe/Pt bilayers is plotted as a function of thickness of the Pt layer. The data are measured at $\phi_{\mathrm{H}} = 0°$ and out-of-plane excitation geometry. Every point in the graph is the arithmetic mean of 11 normalized amplitude values in the frequency range of 7 to 12 GHz, the step size is 0.5 GHz. The vertical error bars correspond to the standard deviation of the normalized amplitude values in the applicable frequency range. Also displayed is a fit to data corresponding to $A \tanh\left(\frac{t}{2\lambda_{\mathrm{sd}}}\right)$. The result of best fit to data yields $\lambda_{\mathrm{sd}} = 1.9 \pm 0.7$ nm. In b) the resistance of the NiFe/Pt bilayers is plotted as a function of the Pt thickness. In c) the normalized voltage amplitudes represented by single points in a) for the different Pt thicknesses are explicitly plotted as a function of frequency in the range of $f = 7$ to 12 GHz.

is most informative to compute α_{SH} as a function of λ_{sd}.
For Pt results of α_{SH} for three different samples will be discussed. The Pt of these samples is nominally the same, grown by magnetron sputtering in the same UHV chamber. The studied NiFe/Pt-bilayers differ slightly in terms of individual layer thicknesses. Exact information, also with respect to the determined bilayer conductivity is listed in Tab. 7.1. The bilayer wire denoted NiFe/Pt-a is integrated into a CPW which has dimensions $w_{\mathrm{gap}} = 35\,\mu\mathrm{m}$, $w_{\mathrm{SL}} = 50\,\mu\mathrm{m}$. The ground line has a width in the mm-range. Corresponding simulations with respect to the out-of-plane driving field amplitude h_z in the center of the gap for this CPW geometry yield analogous results as presented in Figs. 4.2 and 4.3. The bilayer wires NiFe/Pt-b and NiFe/Pt-c are located in a CPW with respective widths of gap, signal and ground line of 30, 50, 25 µm. The driving field amplitude in the center of the gap is higher

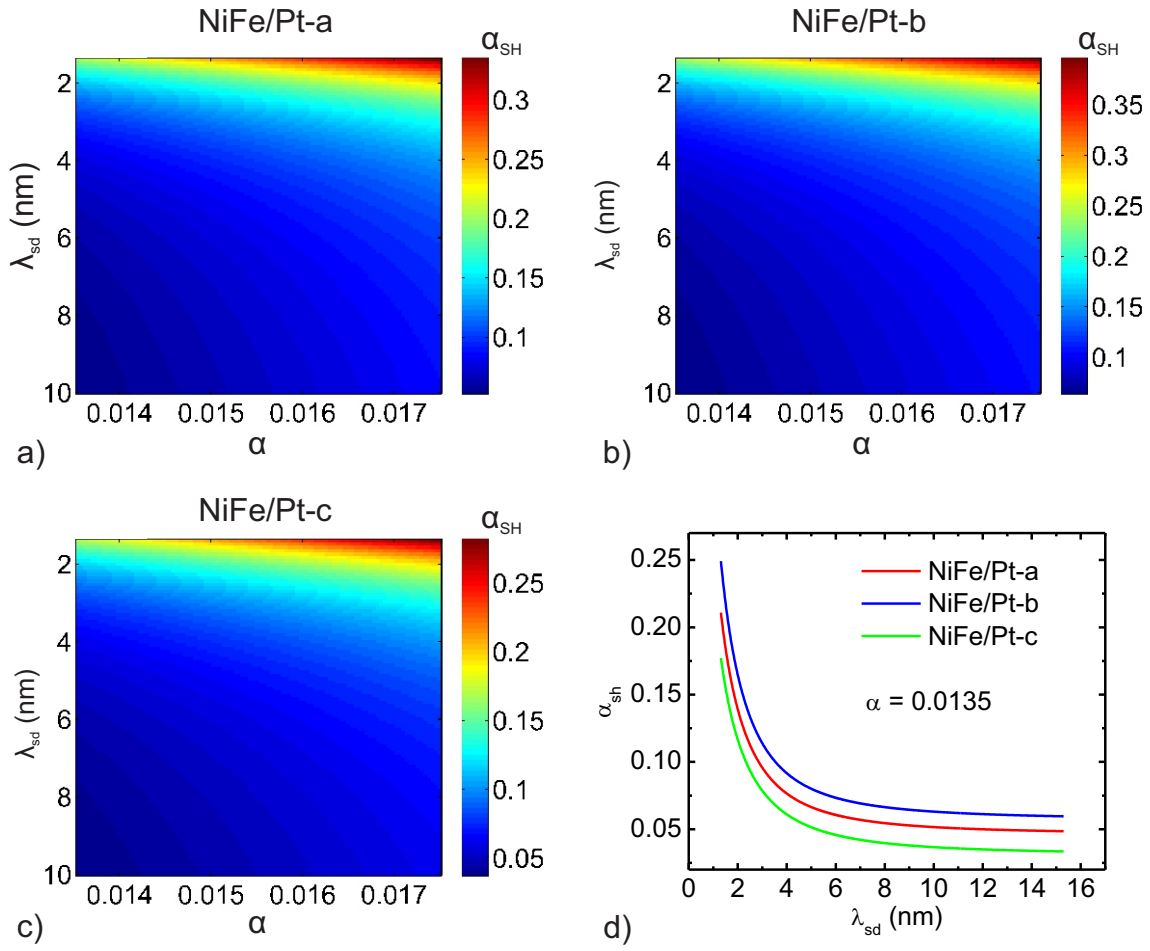

Figure 7.7: Color plots of the spin Hall angle α_{SH} as a function of Gilbert damping α_{Gd} and spin diffusion length λ_{sd} are presented. In a), b) and c) results for NiFe/Pt-a to -c are plotted, respectively. In d) α_{SH} is plotted as a function of λ_{sd} for fixed damping parameter $\alpha = 0.0135$.

for the latter CPW-type due to the smaller gap width. The results for α_{SH} are plotted in Fig. 7.7. The respective color plots are a function of spin diffusion length ranging from 1.3 to 10 nm and damping parameter α which ranges from 0.0135 to 0.0175. The minimum value of the λ_{sd}-axis corresponds to the lower limit of the obtained value for λ_{sd} from the thickness dependent measurements. The maximum value of λ_{sd} for the calculation of α_{SH} is given by 10 nm, which is the range of the value determined for a temperature of 4.2 K in GMR experiments, cf. [91, 162]. As for the case of NiFe/Au each point in the color plot corresponds to the average of 10 A_{S}-values from voltage spectra at $\phi_{\mathrm{H}} = 0°$ in a frequency range of 7 to 11.5 GHz. The graphs plotted in Fig. 7.7 show that the amplitudes of α_{SH} strongly depend on the spin diffusion length λ_{sd} used in Eq. (7.3) especially for low values. Assuming a damping factor $\alpha = 0.0135$ the spin Hall angle α_{SH} as a function of λ_{sd} is plotted for NiFe/Pt-a to -c are shown in Fig. 7.7d). One can see that the values for NiFe/Pt-a

to c are slightly different, which can equivalently be observed in the range of the corresponding color bars of the plots in Figs. 7.7a) to c). Yet, this can be accounted for by a slight deviation of individual thicknesses of the NiFe and Pt layers from the assumed values which are presented in Tab. 7.1. Taking into account the α_{SH} values obtained for the three different NiFe/Pt layers as presented in Fig. 7.7d) and assuming the measured spin diffusion length of $\lambda_{\mathrm{sd}} = 1.9\,\mathrm{nm}$ the spin Hall angle for Pt from the presented SP-ISHE method is given by $\alpha_{\mathrm{SH}} = 0.14 \pm 0.04$.

7.3 Temperature dependence of the spin diffusion length for Pt from the spin Hall angle

If one takes a closer look to the problem of different spin Hall angles due to different assumptions, for Pt it is the spin diffusion length which is the most critical parameter. The values $\lambda_{\mathrm{sd}} = 1.4\,\mathrm{nm}$ from [54] and $\lambda_{\mathrm{sd}} = 1.9\,\mathrm{nm}$ as determined in the course of the present work are measured at room temperature. The corresponding spin Hall angle is approximately 0.1. The spin diffusion length used in [49] and [50] for calculation of α_{SH} was assumed to be 10 nm and consequently $\alpha_{\mathrm{SH}} \approx 0.01$. However, the value of $\lambda_{\mathrm{sd}} = 10\,\mathrm{nm}$ is an assumption in [49, 50] and the corresponding measurements which are published in [91, 162] were conducted at a temperature of $T = 4.2\,\mathrm{K}$. To this end, temperature dependent measurements of dc-voltages using the SP-ISHE method give insight into the role of the spin diffusion length. Temperature dependent measurements have already been used to prove that the signal at $\phi_{\mathrm{H}} = 0°$ for out-of-plane excitation is uniquely generated by ISHE. One can go a step further and examine the temperature dependent parameters entering the formula for spin Hall angle quantification Eq. (7.3). These are, σ, M_{S}, $\Im(\chi_{zz}^{\mathrm{Res}})$, $\chi_{y'z}^{\mathrm{Res}}$, $g_{\mathrm{F}}^{\uparrow\downarrow}$, $V_{\mathrm{ISHE}}^{\mathrm{oop}}$ and finally λ_{sd}. In the present measurements all parameters can be determined from experiment, only the spin diffusion length and the spin Hall angle remain freely adjustable. In Fig. 7.8a) the conductivity σ of the NiFe/Pt bilayer and the spin mixing conductivity $g_{\mathrm{F}}^{\uparrow\downarrow}$ of the NiFe/Pt interface are plotted as a function of temperature. As expected for metallic systems σ increases proportional to $1/T$ when approaching lower temperatures. Also $g_{\mathrm{F}}^{\uparrow\downarrow}$ increases for decreasing temperature. This is expected as the spin mixing conductance of the NiFe/Pt interface is a function of the Pt conductivity [41, 124, 163]. In Fig. 7.8b) $\mu_0 M_{\mathrm{eff}}$ is plotted as a function of temperature. The value for $\mu_0 M_{\mathrm{eff}}$ at room temperature is obtained from absorption FMR-spectra extracting $\mu_0 H_0(f)$ by fitting with Eq. (5.4). Subsequently $\mu_0 M_{\mathrm{eff}}(\mathrm{T})$ is calculated using Bloch's $T^{3/2}$-law [127]. The $\mu_0 M_{\mathrm{eff}}(\mathrm{T})$ values together with the line widths of FMR-spectra for a frequency of 18 GHz (see Fig. 7.4b)) are used to calculate the susceptibilities (Eqs. (7.2) and (7.1)) as a function of temperature. If one now further assumes, that α_{SH} is constant over the whole measured temperature range of 10 to 300 K, $\lambda_{\mathrm{sd}}(T)$ can be extracted from $V_{\mathrm{ISHE}}^{\mathrm{oop}}$ using α_{SH} and λ_{sd} determined from the room temperature measurements, see Fig. 7.7. The conductivity of the NiFe/Pt-bilayer increases by less than a factor of two from 300 K

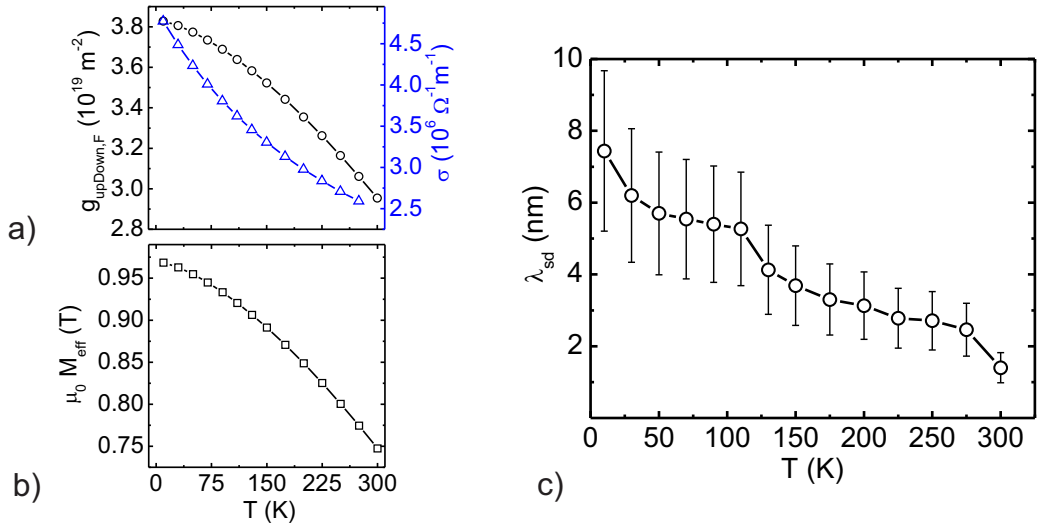

Figure 7.8: In a) and b) the temperature dependencies of $g_F^{\uparrow\downarrow}$, σ of the bilayer, and $\mu_0 M_{\text{eff}}$ are plotted. In c) the spin diffusion length is calculated as a function of temperature. For this $\alpha_{\text{SH}} = 0.12$, [53], is assumed to be constant for the whole studied temperature range. And the spin diffusion length is computed by solving Eq. (7.3) for λ_{sd}.

to 10 K, see Fig. 7.8a). Therefore, the-spin orbit-coupling of Pt should marginally change for this temperature range and consequently the assumption of a constant α_{SH} is justified. This is corroborated by results presented in [164]. In the following $\alpha_{\text{SH}} = 0.12$ [53] and $\lambda_{\text{sd}}(@300\,\text{K}) = 1.4\,\text{nm}$ [54] is assumed. In Fig. 7.8c) the spin diffusion length obtained from solving Eq. (7.3) for λ_{sd} is plotted as a function of temperature. It roughly increases by a factor of 4 from 300 to 10 K. Especially, one recognizes that the obtained value for λ_{sd} at 10 K agrees well with the value extracted using giant magnetoresistance measurements at 4.2 K in [91, 162].

8 Experimental results concerning SP-ISHE in NiFe/Au_xPt_{1-x} bilayers

Pt and Au are amongst the most studied materials in terms of quantification of spin Hall angles using spin pumping in combination with ISHE, [49, 50, 53]. However, both from the experimental as well as from the theoretical point of view there are still many open questions. One of the main issues is that comparison of first-principles calculations, assuming certain origins and types of spin dependent scattering, to experimental results for pure NM is rather impossible [165]. The main problem is connected with the definition of what is "pure" in terms of a material. Consider for example Pt. From the theoretical point of view pure means that there are no impurities incorporated into the Pt and its conductivity is uniquely determined by temperature or structural defects and electron-electron interactions at low temperatures. Yet, comparing theoretical predictions for the conductivity of Pt with experimental results there are discrepancies as large as two orders of magnitude. This suggests that the Pt fabricated in ultra high vacuum chambers by thermal or sputter deposition is in a state incorporating impurities of unknown origin. The material is in the so-called dilute limit and not within the applicability of first-principles calculations and both the magnitude and the underlying physical origin of measured spin Hall angles quantifying the spin dependent scattering cannot be described. It is favorable to depart the dilute limit regime and fabricate alloys of materials featuring constituents with strong spin orbit coupling and spin dependent scattering. To this end Au_xPt_{1-x}-alloys are a good choice. Both materials mix without any clustering as they are located next to each other in the periodic table of elements and both feature large atomic numbers Z which suggests large spin orbit coupling. Furthermore the dilute limit results for spin Hall angles of Pt and Au have already been studied in detail, see Chapt. 7, and can be directly compared to Au_xPt_{1-x}-alloys. What has been studied experimentally so far is only the effect of small amounts of Pt (1.4 atomic %) in Au [151, 166]. In this case a spin Hall angle $\alpha_{\mathrm{SH}} = 0.12$ which is attributed to surface assisted skew scattering is reported.
In this chapter results about SP-ISHE in NiFe/Au_xPt_{1-x} bilayers are presented for a wide range of alloy composition. This is done against the background of a well established theoretical framework to calculate the electronic and transport properties of disordered transition metal alloys in a first-principles approach [67]. Issues of preparation of both Pt- and Au-rich alloys will be discussed and an explanation of how

to determine the relative contents of materials by x-ray photo-electron spectroscopy (XPS) will be given. Spin pumping measurements of both extended bilayer films and wires are conducted in order to extract gyromagnetic ratio γ, effective magnetization M_{eff}, damping α and spin mixing conductivity $g_{\text{F}}^{\uparrow\downarrow}$. Furthermore, thickness dependent measurements for two different alloys, i.e. $Au_{0.72}Pt_{0.28}$ and $Au_{0.66}Pt_{0.34}$, are conducted in order to estimate how the spin diffusion length λ_{sd} evolves from the Pt-rich (λ_{sd} = 1.4 - 4 nm [54, 109] and present work) towards the Au-rich end (λ_{sd} = 34 nm [153]) of the alloy-scale. Calculated values of spin Hall angles α_{SH} from experimentally measured dc-voltages due to ISHE will be presented for a wide range of Au_xPt_{1-x}-alloys. This includes a discussion of critical parameters entering the computation of α_{SH}. In order to establish a well-suited basis for the comparison of experimental results to first principles calculations a detailed description of how the voltage data are normalized by Au_xPt_{1-x}-composition dependent parameters is presented. Finally an explicit comparison of experimental results to first-principles calculations will be presented. The transport coefficients, viz. longitudinal and transverse conductivities (σ_{xx} and σ_{xy}) are calculated for the whole composition range of Au_xPt_{1-x}-alloys using a Kubo-Bastin [167] form. The underlying electronic structure of Au_xPt_{1-x}-alloys is calculated using a relativistic KKR-Green function in combination with the coherent potential approximation [67, 168]. The theoretical data is provided by Kristina Chadova, Diemo Ködderitzsch and Hubert Ebert from the Department Chemie of the LMU in Munich.

8.1 Fabrication and characterization of NiFe/Au_xPt_{1-x} bilayers

Several different Au_xPt_{1-x}-alloys on NiFe are fabricated. In order to cover the whole range of relative Au to Pt contents a GaAs(001)-substrate is placed in the field of view of both sorts of material beams in a sputter deposition chamber. The Au and Pt targets are mounted in two neighboring magnetron sputter guns, which are located in a UHV-chamber. The thickness of NiFe is constantly kept at 12 nm and the Au_xPt_{1-x} layers are tuned towards a layer thickness of t_{AuPt} = 12 nm. In order to fabricate several different NiFe/Au_x Pt_{1-x} bilayer wires at a time, an e-beam resist mask featuring laterally offset wires is structured on a 1 cm^2 GaAs-substrate piece, see Fig. 8.1a). This automatically generates a Au to Pt gradient which, depending on the individual growth rates of the materials can cover a wide composition range of Au_xPt_{1-x}-alloys. Together with the characteristically 5 µm wide and 400 µm long wires an equal number of 1 mm^2 films is structured onto the GaAs-substrate. The center of each square is assigned the same lateral position as one respective wire. The concept is illustrated in Fig. 8.1a). The films are denoted as calibration squares and are used for thickness verification, XPS and spin pumping measurements. The other approach which is used to fabricate Au_xPt_{1-x}-alloys is to put the e-beam resist mask featuring wires and calibration squares on a smaller, 4 by 4 or 5 by 5 mm^2,

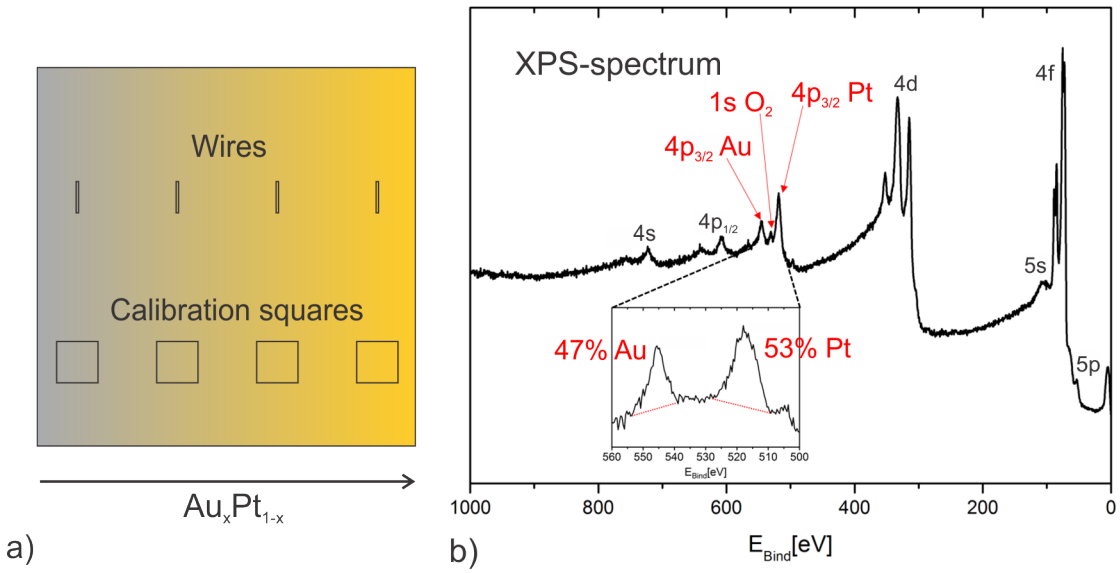

Figure 8.1: In a) a schematic of a GaAs film which features e-beam resist patterned wires and calibration squares is displayed. The color jet from grey to yellow (left to right) corresponds to the Au_xPt_{1-x}-gradient. In b) an x-ray photo-electron spectrum (XPS) for $Au_{0.47}Pt_{0.53}$ is shown. The energy core levels used for evaluation of the relative contents are indicated by red arrows. The inset shows a close-up of these $4p_{3/2}$ corresponding energy peaks. The height of the peaks is calculated relative to the delineated red base lines.

substrate piece and laterally offset the pieces with respect to each other on a sample holder. If markers on the sampler holder are defined, this method allows one for calibrated positions for specific alloy-composition. Nevertheless, the calibration squares are always present for verification.
In Fig. 8.1b) an exemplary XPS spectrum is shown. In this case relative contents of Au = 0.47 and Pt = 0.53 are determined by comparing energies of photo electrons from inner shell orbitals $4p_{3/2}$. This orbital is chosen for the fact that the corresponding energy levels are well separated for the two materials. In the inset a close-up of the $4p_{3/2}$-peaks together with respective base lines which are determined manually are shown. Measuring the height between peak and respective base line yields the relative Au to Pt contents. From such spectra Au_xPt_{1-x}-alloys of various compositions can be verified. The ones to be compared in terms of SP-ISHE, and subsequent α_{SH}-quantification, are listed together with the measured electrical conductivities σ_{AuPt} in the first two columns of Tab. 8.1. The studied Au_xPt_{1-x}-alloys cover a range of 20 to 72% of Au in Pt and together with the dilute limits of Pt and Au this is appropriate for a comprehensive study of SP-ISHE. In order to measure voltages due to ISHE the bilayer wires shown in the schematic of Fig. 8.1a) undergo further micro structuring processes involving deposition of Au-contacts, in-

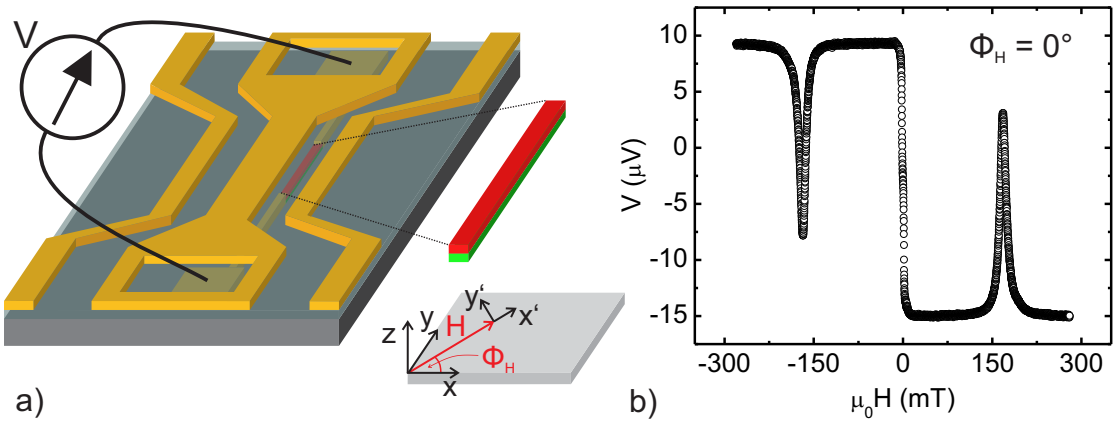

Figure 8.2: In a) the used out-of-plane excitation scheme operated by a CPW is shown. The coordinate system defines the angle ϕ_H of the external field **H** in the x-y-plane. In b) a measured voltage spectrum at $\phi_H = 0°$ for a precession frequency of 12 GHz in a NiFe/$Au_{0.27}Pt_{0.73}$ is displayed. Both the characteristic sign change of the voltage amplitude on reversing the external magnetic field and the purely symmetric line shape suggest that the signal is only caused by ISHE.

sulating Al_2O_3, and Au-signal- and -ground-lines, cf. Fig. 4.4. In order to be able to examine voltages due to ISHE without any parasitic signal caused by AMR the CPW is deposited such that the NiFe/Au_xPt_{1-x} bilayer wires are located in the gap between signal and ground line. The layout used for all NiFe/Au_xPt_{1-x} bilayers is presented in Fig. 8.2a). Furthermore, an external in-plane magnetic field H facilitates the magnetization to be saturated parallel to it, in fact at an angle ϕ_H. The corresponding coordinate system is also displayed in Fig. 8.2a). A voltage signal at $\phi_H = 0°$ is expected to be purely caused by ISHE. An exemplary measurement at $\phi_H = 0°$ for a precession frequency of 12 GHz using a NiFe/$Au_{0.22}Pt_{0.78}$ bilayer wire is displayed in Fig. 8.2b). The voltage signal is purely symmetric with respect to the resonance field H_0 and changes sign on magnetization reversal as expected for ISHE, see Eq. (2.22). Such voltage spectra are recorded for various frequencies for all compositions presented in Tab. 8.1.

However, in order to compare the voltage spectra recorded for the different NiFe/Au_xPt_{1-x}-bilayer wires data have to be normalized correctly.

8.2 Voltage due to ISHE and normalization with respect to Au_xPt_{1-x} dependent parameters

As a first step towards quantitative results of ISHE in Au_xPt_{1-x}-alloys angular dependent measurements of voltage line shapes across FMR are conducted. Analogously

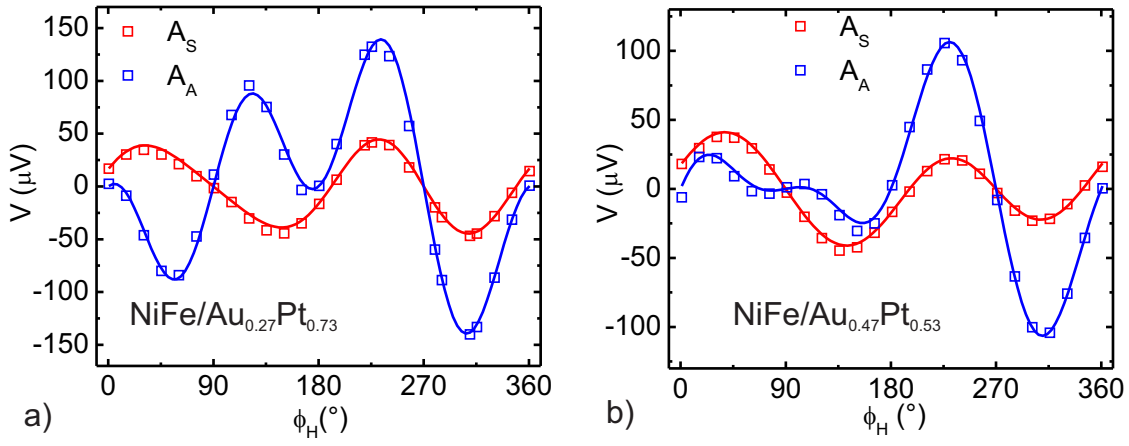

Figure 8.3: The symmetric and antisymmetric amplitudes, A_S red dots and A_A blue open squares respectively, are plotted as a function of external field angle ϕ_H. A_S and A_A are extracted from voltage spectra at FMR at 12 GHz. In a) and b) the results for $NiFe/Au_{0.27}Pt_{0.73}$ and $NiFe/Au_{0.47}Pt_{0.53}$ are displayed, respectively. The blue and red solid lines are fits to the data according to Eqs. (6.2) and (6.3).

to the procedures presented in chapter 6 voltage spectra are recorded for different external in-plane field angles ϕ_H. The amplitudes A_S and A_A of symmetric and antisymmetric Lorentzian line shape parts are extracted from fits, cf. Eq. (5.7), and plotted as a function of ϕ_H. This is carried out for all alloys listed in Tab. 8.1. Exemplarily, the angular dependencies of voltage amplitudes for $NiFe/Au_{0.27}Pt_{0.73}$ and $NiFe/Au_{0.47}Pt_{0.53}$ are displayed in Fig. 8.3. The red and blue solid lines are fits to A_A and A_S using Eqs. (6.2) and (6.3), respectively. For specification of the method and the used fit parameters (6.4)-(6.8) see Sec. 6. One can clearly distinguish the influence of the parasitic in-plane driving field in Figs. 8.3a) and b) from the symmetry breaking of voltage amplitudes A_A with respect to $\phi_H = 180°$. Yet, neither the parasitic in-plane field nor the information about electromagnetic coupling (phase angle ξ Eq. (6.9)), that one can gain from the AMR assigned fit parameters of the angular dependence, shall be under consideration here.
The fit-parameter as defined in Eq. (6.8), which corresponds to the voltage amplitude due to ISHE under the influence of the out-of-plane driving field generated by the CPW shall be in the focus. It represents the amplitude of the $\cos(\phi_H)$ contribution of the red solid lines fitting the A_S-amplitudes in Figs. 8.3a) and b) and is plotted as a function of Au_xPt_{1-x} in Fig. 8.4a). The data suggest that there is a considerable voltage amplitude due to ISHE for all studied $NiFe/Au_xPt_{1-x}$-bilayers. The plotted horizontal error bars correspond to an uncertainty from the alloy's composition determination, which is assumed to be ±5%, and the vertical error bars are the errors of the best fits to the data.
In order to gain a quantitative picture of ISHE as a function of Au_xPt_{1-x}-composition,

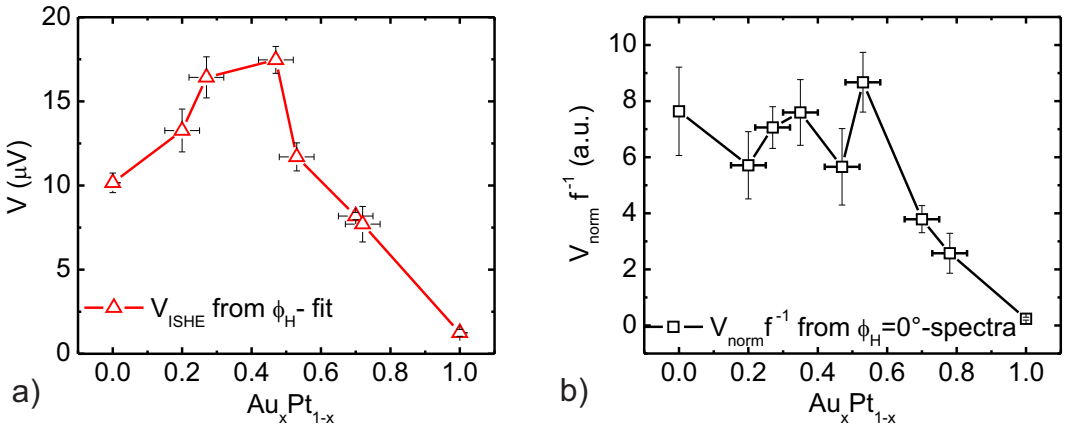

Figure 8.4: In a) the fit parameter e from fits to the ϕ_{H}-dependence of A_{S}, see Eqs. (6.3) and (6.8), is plotted as a function of Au_xPt_{1-x}-composition. The horizontal and the vertical error bars correspond to the assumed $\pm 5\%$ uncertainty in alloy composition determination and error from ϕ_{H}-fit to data, respectively. In b) the amplitudes $V_{\mathrm{ISHE}}^{\mathrm{oop}} = A_{\mathrm{S}}$ normalized with respect to magnetic susceptibilities, microwave power and frequency are plotted as a function of Au_xPt_{1-x}-composition. A_{S} is extracted from the fits using Eq. (5.7) for 10 different frequencies in the range of 7 to 11.5 GHz. The vertical error bars are the standard deviations from the respective A_{S}-average.

voltage spectra at $\phi_{\mathrm{H}} = 0°$, as presented in Fig. 8.2b) for NiFe- /$Au_{0.27}Pt_{0.73}$ at $f = 12\,\mathrm{GHz}$, are recorded for all alloys in a frequency range of 7 to 11.5 GHz. Each voltage spectrum is fitted with respect to Eq. 5.7 and $V_{\mathrm{ISHE}}^{\mathrm{OOP}}(f) = A_{\mathrm{S}}(f)$ is extracted. $V_{\mathrm{ISHE}}^{\mathrm{oop}}$ is then normalized with respect to frequency dependent parameters, i.e. susceptibilities $\Im(\chi_{zz}^{\mathrm{res}})$, $\chi_{y'z}^{\mathrm{res}}$ and the average microwave power P_{avg} consumed by the CPW. The susceptibilities are calculated using Eqs. (7.1) and (7.2). The magnetic properties that enter the analysis, viz. γ, $\mu_0 M_{\mathrm{eff}}$ and α are determined via microwave absorption FMR, using the experimental method as explained in Chapt. 5, on the $1\,\mathrm{mm}^2$ bilayer films of all NiFe/Au_xPt_{1-x}. The normalized values are denoted V_{norm}. Dividing V_{norm} by the respective frequency itself, yields frequency independent amplitudes of voltage spectra. Their spreading due to uncertainties in the microwave power defines the respective error bars. Finally, each data point as a function of Au_xPt_{1-x}-composition corresponds to the average of 10 A_{S}-values and an error bar which represents the respective standard deviation. The results are plotted in Fig. 8.4b). One can see the qualitative consistency of the results plotted in Figs. 8.4a) and b) with respect to the statement that a considerable voltage due to ISHE is present for all Au_xPt_{1-x}-alloys. For quantitative and comparative studies of ISHE, the results of Fig. 8.4b) are further processed.
Voltage signals are proportional to the resistance of the NiFe/Au_xPt_{1-x}-bilayer wires.

This is plotted in Fig. 8.5a). The results displayed in Fig. 8.4b) are respectively normalized and plotted in Fig. 8.5b). A linear decrease of the normalized signals due to ISHE is observed when going from the Pt- to the Au-rich end of the scale. Yet, a voltage due to ISHE is proportional to another very essential parameter - the effective spin mixing conductivity $\tilde{g}_{\mathrm{F}}^{\uparrow\downarrow}$, which determines the amplitude of the net pumped spin current across the NiFe/Au_xPt_{1-x}-interfaces. For this purpose the Gilbert damping parameters α of the 1 mm^2 calibration squares are compared to the α of an uncapped NiFe-film and $\tilde{g}_{\mathrm{F}}^{\uparrow\downarrow}$ is calculated using Eq. (5.6). The calculation is explicitly performed for three different NiFe/Au_x Pt_{1-x}-alloys. Only for NiFe/$Au_{0.20}Pt_{0.80}$,NiFe/$Au_{0.27}Pt_{0.73}$ and NiFe/$Au_{0.47}Pt_{0.53}$ the damping factor of the uncapped NiFe is known from FMR-measurements in the present study. Therefore only for these interfaces the value of $\tilde{g}_{\mathrm{F}}^{\uparrow\downarrow}$ can be determined experimentally. Corresponding results are plotted in Fig. 8.5c). One observes a decrease of $\tilde{g}_{\mathrm{F}}^{\uparrow\downarrow}$ for increasing Au content. In order to estimate the values for all NiFe/Au_xPt_{1-x}-interfaces listed in Tab. 8.1 $\tilde{g}_{\mathrm{F}}^{\uparrow\downarrow}$ is assumed to decrease linearly as a function of Au_xPt_{1-x}. This assumption is corroborated when adding the $\tilde{g}_{\mathrm{F}}^{\uparrow\downarrow}$-value for Pt, as determined in Chapt. 5, and $g_{\mathrm{F}}^{\uparrow\downarrow}$ for Au, as from [153]. Note the missing tilde for the Au case in this argumentation. It makes clear that another assumption for all studied NiFe/Au_xPt_{1-x}-bilayers is made here, namely $\tilde{g}_{\mathrm{F}}^{\uparrow\downarrow} = g_{\mathrm{F}}^{\uparrow\downarrow}$, viz. all studied alloys are assumed to be perfect spin sinks. In fact, this assumption seems to hold as can be seen from the results for the damping factor α as a function of $Au_{0.72}Pt_{0.28}$-alloy thickness. This is displayed in the inset of Fig. 8.5c). The damping factor is almost constant for a thickness of 6 and 12 nm which suggests that no spin current back flow is present and consequently $\tilde{g}_{\mathrm{F}}^{\uparrow\downarrow} = g_{\mathrm{F}}^{\uparrow\downarrow}$ for a $Au_{0.72}Pt_{0.28}$-alloy thickness larger than 6 nm. This argumentation especially holds for all of the studied 12 nm thick alloys. The red curve displayed in Fig. 8.5c) is a linear fit with respect to the presented data points. The results from the fits are listed in Tab. 8.1 as $g_{\mathrm{F}}^{\uparrow\downarrow}$. Towards comparative results of the signals caused by ISHE NiFe/Au_xPt_{1-x}-bilayers the normalization in terms of $g_{\mathrm{F}}^{\uparrow\downarrow}$ is essential. The explicitly normalized voltage amplitudes with respect to susceptibilities, average microwave power, frequency, bilayer resistance and effective spin mixing conductivity are plotted in Fig. 8.5d). Note that for the normalization of the Au data point $\tilde{g}_{\mathrm{F}}^{\uparrow\downarrow} = g_{\mathrm{F}}^{\uparrow\downarrow}/5$ is used [131, 153]. The increased vertical error bars for the data compared to results in Fig. 8.5b) correspond to the additional error due to the uncertainty in the linear fit of $g_{\mathrm{F}}^{\uparrow\downarrow}$. The data presented in Fig. 8.5c) suggest that ISHE is comparable in amplitude for the whole studied Au_xPt_{1-x} composition range. However, one parameter has been left out so far, the spin diffusion length as a function of Au_xPt_{1-x}.

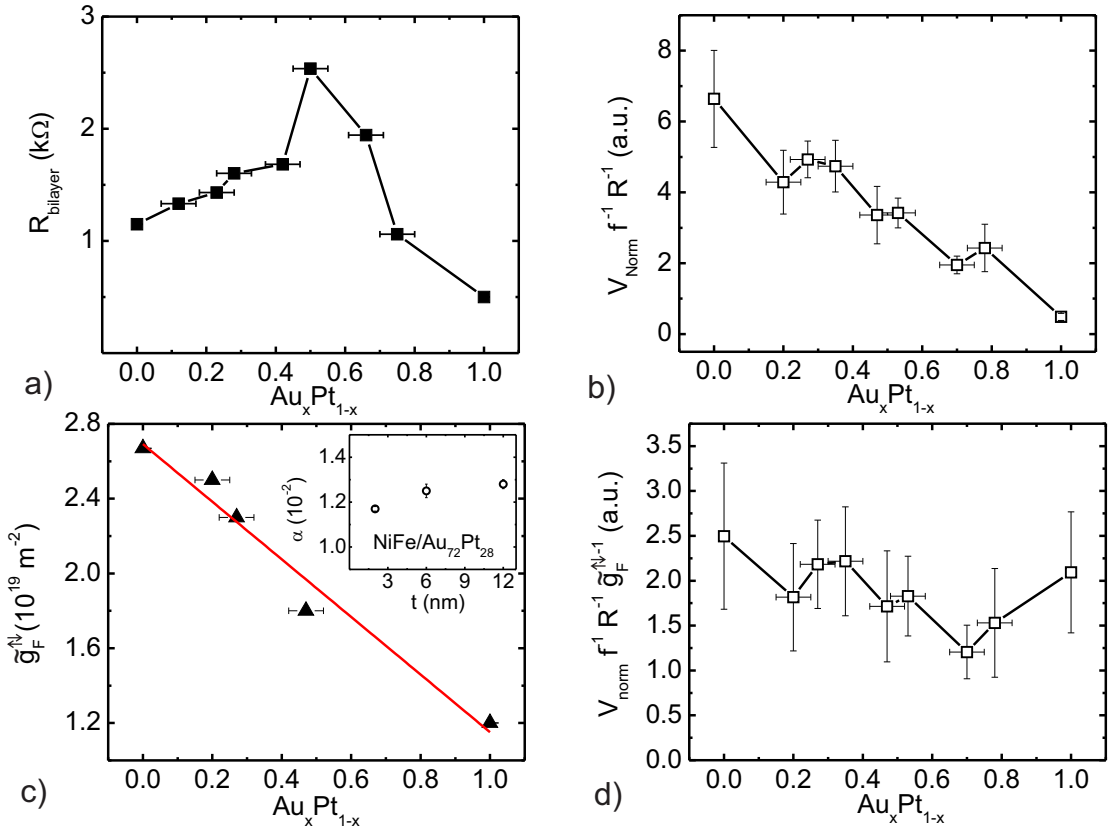

Figure 8.5: In a) the resistance of the 5 µm wide and 400 µm long NiFe/Au_xPt_{1-x} bilayer wires is plotted as a function of Au_xPt_{1-x}-composition. In b) the normalized ISHE voltage amplitudes presented in Fig. 8.4b) are divided by the bilayer wire resistance. In c) the spin mixing conductivity of NiFe/Au_xPt_{1-x} is plotted as a function of Au_xPt_{1-x}-composition. The black triangles correspond to calculated values using Eq. (5.6) and the change of the Gilbert damping constant α due to spin pumping. The red solid line is a linear fit to data. In the inset α is plotted as function of $Au_{0.72}Pt_{0.28}$ thickness for NiFe/$Au_{0.72}Pt_{0.28}$-bilayers. In d) the results of $V_{\mathrm{ISHE}}^{\mathrm{oop}}$ normalized to all Au_xPt_{1-x}-dependent parameters is plotted as a function Au_xPt_{1-x}-composition.

8.3 Experimental results concerning the spin diffusion length and spin Hall angles

The measured voltages at $\phi_{\mathrm{H}} = 0°$ which are caused by ISHE are directly proportional to the spin Hall angle α_{SH} which for out-of-plane excitation is described by Eq. (7.3). For easier viewing the formula shall be reprinted here:

$$\alpha_{\mathrm{SH}} = \frac{V_{\mathrm{ISHE}}^{\mathrm{oop}} \sigma (t_{\mathrm{NM}} + t_{\mathrm{FM}}) M_{\mathrm{S}}^2}{e f g_{\mathrm{F}}^{\uparrow\downarrow} \Im(\chi_{z'z'}^{\mathrm{res}}) \chi_{y'z'}^{\mathrm{res}} |h_z|^2 l \lambda_{\mathrm{sd}} \tanh\left(\frac{t_{\mathrm{NM}}}{2\lambda_{\mathrm{sd}}}\right)} \tag{8.1}$$

The results presented in Fig. 8.5d) describe in a first approach the relative behavior of the spin Hall angle as a function of Au_xPt_{1-x}-composition. However, the role of the spin diffusion length λ_{sd} which has been neglected so far shall be now incorporated.

In order to estimate λ_{sd} as a function of Au_xPt_{1-x}-composition, thickness dependencies of voltage signal amplitudes at $\phi_{\mathrm{H}} = 0°$ are studied. 2, 6 and 12 nm thick layers of the $Au_{0.72}Pt_{0.28}$-alloy have already been studied with respect to Gilbert damping of the NiFe-layer underneath, see inset of Fig. 8.5c). Now as displayed in Fig. 8.6a) the normalized voltage amplitudes are in the focus. Every data point is the aforementioned average of 10 normalized voltage values in the frequency range of 7 to 11.5 GHz and the error bars correspond to their standard deviation from the mean value. The red solid line is a fit to the data which corresponds to Eq. (7.6) which consists of the terms dependent on λ_{sd} appearing in Eq. (8.1). The best fit to the data yields $\lambda_{\mathrm{sd}} = 2.76$ nm. The voltage amplitudes for two NM-layer thicknesses of 4 and 12 nm of a NiFe/$Au_{0.66}Pt_{0.34}$-bilayer are studied analogously. The data and fit presented in Fig. 8.6b) suggest a spin diffusion length of $\lambda_{\mathrm{sd}} = 0.8$ nm. The obtained λ_{sd} for $Au_{0.72}Pt_{0.28}$ and $Au_{0.66}Pt_{0.34}$ are plotted in Fig. 8.7a). The value for Au, $\lambda_{\mathrm{sd}} = 34$ nm [153], and Pt, $\lambda_{\mathrm{sd}} = 1.9$ nm (see Sec 7.2) are also added. Comparison of the qualitative behavior of λ_{sd} and the measured conductivity σ_{AuPt} as a function of Au_xPt_{1-x} suggests a correlation between the two parameters. The conductivity is explicitly plotted in the inset of Fig. 8.7a). Though the exact correlation between λ_{sd} and σ_{AuPt} is not known the following approach is chosen to deduce the values for λ_{sd} for the whole Au_xPt_{1-x}-range. Values for λ_{sd} for $Au_{0.70}Pt_{0.30}$ and $Au_{0.53}Pt_{0.47}$ are calculated relative to the λ_{sd}-σ-pair for $Au_{0.72}Pt_{0.28}$ from the rule of proportion. For the alloys with major percentage of Pt λ_{sd} is analogously computed but this time relative to the λ_{sd}-σ-pair for pure Pt. Corresponding results for λ_{sd} are plotted in Fig. 8.7b). The inset shows a close-up of the range from dilute Pt to $Au_{0.72}Pt_{0.28}$. Furthermore, all calculated results for λ_{sd} are listed in Tab. 8.1. They are now used to calculate the spin Hall angle as a function of Au_xPt_{1-x}-composition using Eq. (8.1).

The obtained values for α_{SH} are represented by the black colored data points in Fig. 8.7c). One can observe that α_{SH} increases from 0.14 for the dilute Pt limit to values between 0.17 and 0.18 for the alloys of $Au_{0.27}Pt_{0.73}$ to $Au_{0.47}Pt_{0.53}$ and disregarding the outlier for $Au_{0.53}Pt_{0.47}$ there is a subsequent asymmetrical decrease

Au_xPt_{1-x}	σ_{AuPt} $(10^6\,\Omega^{-1}\,m^{-1})$	$g_F^{\uparrow\downarrow}(10^{19}\,m^{-2})$	λ_{sd}(nm)
Pt	3.20	2.66	1.90
$Au_{0.20}Pt_{0.80}$	2.8	2.36	1.66
$Au_{0.27}Pt_{0.73}$	2.5	2.26	1.48
$Au_{0.35}Pt_{0.65}$	2.0	2.14	1.21
$Au_{0.47}Pt_{0.53}$	1.9	1.96	1.13
$Au_{0.53}Pt_{0.47}$	0.70	1.87	0.50
$Au_{0.70}Pt_{0.30}$	1.40	1.62	0.99
$Au_{0.72}Pt_{0.28}$	3.90	1.59	2.76
Au	9.60	1.17	34.00
NiFe	1.60	-	-

Table 8.1: The experimentally studied Au_xPt_{1-x}-alloys together with distinct parameters are listed.

towards the back flow corrected value of 0.05 for the Au dilute limit. The spin Hall angle measured for $Au_{0.53}Pt_{0.47}$, which is in excess of 30%, could be called giant. It is in the range of the largest spin Hall angle reported, which is 30% measured for W [104]. Yet, the large spin Hall angle for $Au_{0.53}Pt_{0.47}$ is very likely to be due to an underestimation of λ_{sd}.
The blue colored curve displayed in Fig. 8.7c) corresponds to the results of α_{SH} from first-principles calculations. The corresponding theoretical framework for calculating the electronic band structure of the Au_xPt_{1-x}-alloys using a relativistic multiple scattering Korringa-Kohn-Rostocker (KKR) Green function is explained in [67, 168]. The method of coherent potential approximation (CPA) is used to include disorder and short-ranged order effects. The longitudinal and the transverse conductivities σ_{xx} and σ_{xy} respectively, are computed for the whole Au_xPt_{1-x}-composition range using a Kubo-Bastin form [167]. The values of α_{SH} from theory, which are represented by the blue colored data points in Fig. 8.7c), correspond to the ratio σ_{xy}/σ_{xx}. Note that the first-principles calculations are conducted at zero temperature. Comparison of experimental to theoretical data in Fig. 8.7c) reveal that there is a fundamental disagreement for the dilute Pt and Au limit values. Whereas the spin Hall angles from experiment adopt a constant nonzero value, the theoretical data go strictly to zero. In order to understand this the σ_{xx}-values from theory are plotted in the inset of Fig. 8.7c). There the dilute versus clean limit problem is evident. In a clean material (pure Au or pure Pt) the longitudinal conductivity diverges at zero temperature and therefore $\alpha_{SH} = \sigma_{xy}/\sigma_{xx}$ goes to zero. Yet, disregarding the dilute (experiment) and clean (theory) limits the spin Hall angles from experiment are in agreement with the theoretical model represented by the blue curve (again disregarding the experimental value for $Au_{0.53}Pt_{0.47}$). The justification of the theoretical model towards applicability to the experimental data in the alloy range of $Au_{0.20}Pt_{0.80}$ to $Au_{0.72}Pt_{0.28}$ is further corroborated by similar results for the

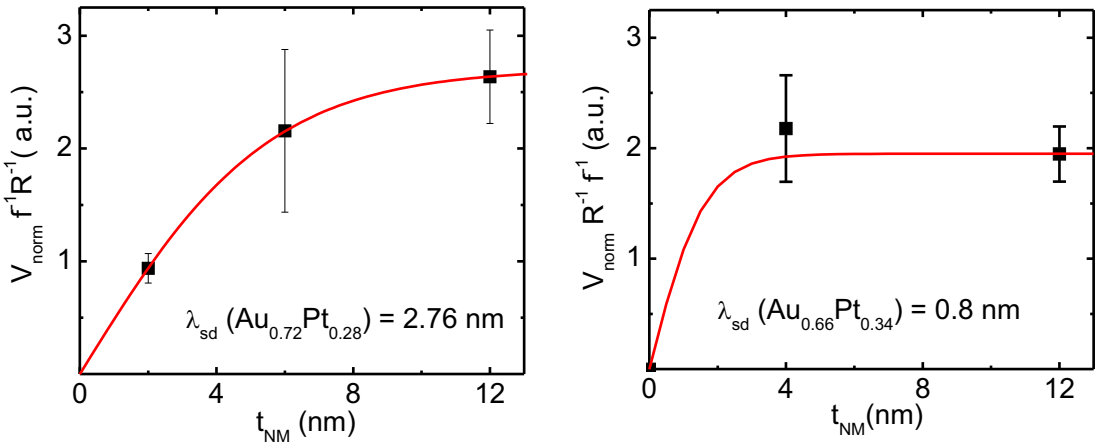

Figure 8.6: In a) normalized A_S-values corresponding to voltage spectra due to ISHE are plotted as a function of $Au_{0.72}Pt_{0.28}$ thickness in respective NiFe/$Au_{0.72}Pt_{0.28}$-bilayers. The red solid line is a fit to data according to Eq. (7.6). It yields $\lambda_{sd} = 2.76\,nm$. In b) analogous results are presented as in panel a), but with concerning NiFe/$Au_{0.66}Pt_{0.34}$-bilayers. The fit yields $\lambda_{sd} = 0.8\,nm$.

longitudinal conductivities from theory and experiment. Corresponding results are plotted in Fig. 8.7d). Note that for the experimental data points the following is true, $\sigma_{xx} = \sigma_{AuPt}$ (exact values see Tab. 8.1). In Fig. 8.7d) also the transverse conductivities σ_{xy} which are proportional to the spin-dependent scattering in the alloys are displayed as a function of Au_xPt_{1-x} for both theory and experiment. Concerning the experimental data σ_{xy} is recalculated from the obtained α_{SH}-values. Both the longitudinal and the transverse conductivities from experiment and theory are in agreement.

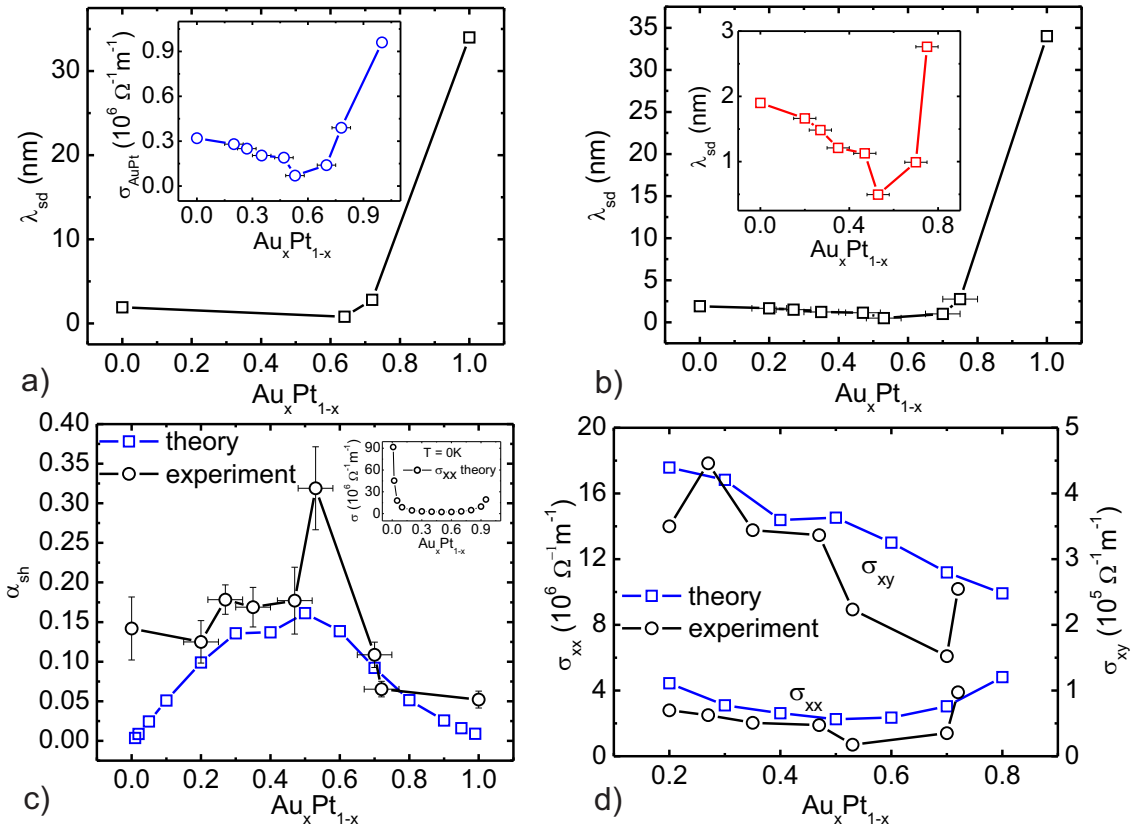

Figure 8.7: In a) the λ_{sd}-values obtained for $Au_{0.72}Pt_{0.28}$ and $Au_{0.66}Pt_{0.34}$ obtained from alloy thickness dependence are plotted together with the values for Pt (1.9 nm[54] and Sec. 7.2) and Au (34 nm [153]) as a function of Au_xPt_{1-x}-composition. In the inset the conductivity of Au_xPt_{1-x}-alloys is plotted as a function of Au_xPt_{1-x}-composition. In b) λ_{sd}, calculated under the assumption of proportionality of λ_{sd} and σ_{AuPt}, is plotted as a function of Au_xPt_{1-x}-composition. The plot in the inset focuses on spin diffusion lengths omitting the value for pure Au. In c) calculated α_{SH} from experimental data using Eq. (8.1) and from first principles calculations using KKR, CPA and a linear response Kubo formalism (the abbreviations are explained in the text) are plotted. The inset shows the longitudinal resistance calculated using the linear response Kubo formalism as a function of Au_xPt_{1-x}-composition. In d) the longitudinal and transverse conductivities σ_{xx} and σ_{xy} from theory and experiment are displayed in one graph.

9 Experimental detection of the ac-inverse spin Hall effect

From the theoretical point of view spin pumping from FM into NM creates spin currents with both direct (dc) and alternating (ac) polarization components [41, 42], see section 3.4. The dc-component of spin currents from spin pumping is well studied experimentally applying the SP-ISHE method, Eq. (2.22). However, the 2 to 3 orders of magnitude larger ac-component [63] escaped experimental detection until recently [62, 68] and has already gone through a profound discussion about the major role of parasitic effects and their potential of being confused with voltage signals due to ISHE, [62, 158, 159]. This chapter is dedicated to the observation and characterization of the ac-ISHE, i.e. to the detection of the time dependent component of a spin current from spin pumping in a NiFe/Pt bilayer system. Parts of this chapter have been published in "Spin Hall voltages from a.c. and d.c. spin currents" [68] and the corresponding supplementary material [64].
At first an exact explanation of the experimental setup allowing for the detection of ac-spin currents due to their transformation into ac-voltage signals in the GHz-regime will take place. The possibilities of how to detect and quantify such voltage signals will be in the focus. To this end the experimentally observed line shapes as a function of external magnetic field will be studied and a comparison to the theoretical results presented in Sec. 4.2 will be drawn. The presentation of power and angular dependent measurements suggests that the origin of the measured ac-voltages is ac-ISHE. However, it is very crucial to distinguish signals caused by electromagnetic induction from voltages due to ac-ISHE. Notwithstanding, comparative measurements for NiFe/Al,NiFe/Cu and NiFe/Au under the same experimental circumstances corroborate that parasitic effects play a minor role in NiFe/Pt. NiFe/Cu allows for an estimation of the magnitude of the signal purely generated by electromagnetic induction. Results concerning NiFe/Al suggest that AMR plays no significant role as a parasitic effect when dealing with ac-ISHE. Finally, an analysis of voltage amplitudes will take place incorporating considerations about the electromagnetic wave propagation properties of the used NiFe/Pt bilayer wires and a comparison of the magnitude of ac and dc ISHE for the very same device will be shown.

9.1 Experimental setup - measuring ac-voltages in the GHz-regime

NiFe/Pt bilayer wires are integrated into coplanar waveguides (CPW). Their location is either on top of the signal line or in the gap between signal and ground lines. The position on top of the signal line is equivalent to the so-called microstrip configuration and the position in the gap between signal and ground lines to the CPW geometry, [155, 157]. A close-up of the configurations is shown in Fig. 9.1a). The structuring of FM/NM bilayers as transmission lines facilitates propagation of microwaves along them and signals due to ac-ISHE can be fed into appropriate wave guides for detection. In general the coupling between two transmission lines is determined by the standing wave ratio, [68]:

$$T = 1 - \frac{Z_1 - Z_0}{Z_1 + Z_0} \tag{9.1}$$

Z_0 and Z_1 are the impedances of the two transmission lines. In the present case Z_0 corresponds to the FM/NM bilayer and Z_1 to the waveguide which detects the signal. In the present case Z_1 is $50\,\Omega$ for the used rf-measurement equipment and the value for Z_0 can be estimated using TX-LINE (for more information see Chapt. 4). If Z_0 equals Z_1 a signal can be transmitted without any loss. Exact values estimated for the systems under consideration will be discussed later in the results sections.
For the used 5 µm wide, 400 µm long and 20 nm thick NiFe/Pt bilayer wires the voltage due to dc-ISHE is around 10 µV. Calculations in [63, 110] suggest that the amplitude of a voltage due to ac-ISHE is 2 to 3 orders of magnitude larger. Hence, for the same experimental conditions one expects 1 mV signals in the GHz frequency range generated by ac-ISHE. The used measurement setup is schematically depicted in Fig. 9.1b). A frequency generator feeds a microwave signal into terminal 1 of the CPW. At terminal 2 the transmitted signal is rectified using a Schottky-diode. This allows for FMR measurements due to microwave absorption as has been described in Chapt. 5. Voltages due to ac-ISHE can be picked off at terminal 3 which connects the NiFe/Pt wire to a $50\,\Omega$ rf-cable. As suggested by measurements using a powermeter, the transmission of a signal fed into terminal 1 going through the bilayer wire into terminal 3 experiences only a relative loss of 20 dB, see Fig. 9.2a). Under circumstances of the implemented input power amplitude at terminal 1 of 20 dBm the background signal at terminal 3 is as large as 100 mV.

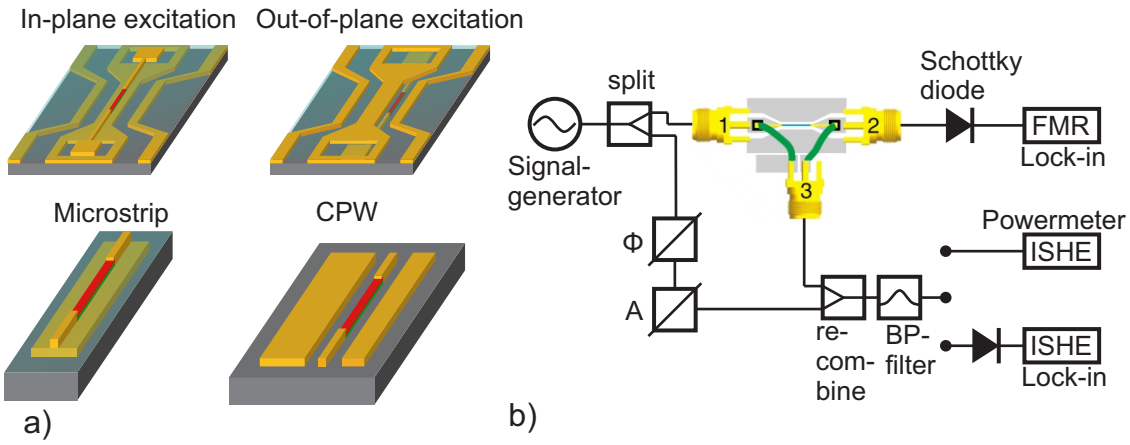

Figure 9.1: In a) the two considered types of integration of FM/NM bilayers into CPWs with respect to spin pumping and ac-ISHE are shown. For the in-plane excitation scheme the FM/NM wire and the signal line of the CPW underneath constitute a microstrip. For out-of-plane excitation the bilayer constitutes and the signal and ground line constitute a CPW. In b) the experimental setup in order to measure the voltages due to ac-ISHE is depicted. The sample features three terminals which consist of 50 Ω rf-connectors. The signal transmitted from terminal 1 to 2 is used to measure FMR with a Schottky diode and a lock-in detector. Terminal 3 is connected to the bond pads of the FM/NM bilayer and is used to measure voltages generated by ISHE in NM. A signal at terminal 3 can be either measured using a rf-powermeter or a Schottky diode and a lock-in detector. To separate the signal caused by ac-ISHE from the large background the input microwave signal is separated into two paths before terminal 1. One path is used in order to apply a phase and an amplitude shift and the other path is going from terminal 1 to terminal 3. The signals from the two paths are recombined after terminal 3. Subsequently a band pass filter is implemented two exclude higher harmonic effects.

In order to guarantee for an acceptable signal to noise ratio when studying voltage spectra caused by ac-ISHE one needs to experimentally compensate this large background. This is done by splitting the input signal into two identical copies using a so-called beam splitter. One signal path goes from terminal 1 to terminal 3 and the other goes through an arm where the signal can be manipulated with respect to phase and amplitude (phase and amplitude shifter respectively). Recombination of the signals from the two paths is then used to cancel out the background signal. Furthermore, a bandpass-filter centered around the precession frequency excludes any higher harmonic artifacts. The signal can then be measured either by an rf-powermeter or by a Schottky diode using respective signal rectification characteristics. The use of a Schottky diode holds certain advantages. It allows for eliminating of the background signal when using external field modulation and lock-in detection which even renders the signal splitting into two paths unnecessary. In Fig. 9.2b) voltage spectra for NiFe/Pt at a frequency of 8 GHz using both rf-powermeter and lock-in measurement technique are shown. The spectra are recorded for in-plane excitation at an external field angle of $\phi_{\mathrm{H}} = 90°$ (the respective microstrip transmission line is shown in Fig. 9.2a)). One can distinguish a step-like feature at the resonance field measuring with the rf-powermeter. The detected power is recalculated in terms of voltage amplitude using a dBm-V-conversion table for a 50 Ω-system. In order to recover the corresponding voltage signal at terminal 3 when using the Schottky-diode together with field-modulation and lock-in detection the following train of thoughts is needed. Under the circumstances of field-modulation the output of the Lock-in amplifier is given by:

$$S(H) = V_{\mathrm{Schottky}}(H + \Delta H) - V_{\mathrm{Schottky}}(H) \tag{9.2}$$

H is the external field, ΔH is the amplitude of the modulation field and V_{Schottky} is the voltage drop across the Schottky diode. If ΔH is small compared to the line width of the measured voltage spectrum, the following is true:

$$S(H) = \frac{\mathrm{d}V_{\mathrm{Schottky}}(H)}{\mathrm{d}H}\Delta H \tag{9.3}$$

Hence, the signal displayed by the Lock-in amplifier is proportional to the derivative of the voltage across the Schottky diode. Note that this is analogous to the microwave absorption measurement technique presented in Chapt. 5. Numerical integration according to the following formula yields the voltage drop across the Schottky diode:

$$V_{\mathrm{Schottky}}(H) = \int \mathrm{d}H \frac{S(H)}{\Delta H} \tag{9.4}$$

In order to draw conclusions with respect to the voltage signal at terminal 3 one has to implement the rectification characteristics of the used Schottky diode. In the present case a voltage drop of 1 µV across the Schottky diode corresponds to a signal of 1 nW power fed into it. Using the power to voltage conversion for a 50 Ω

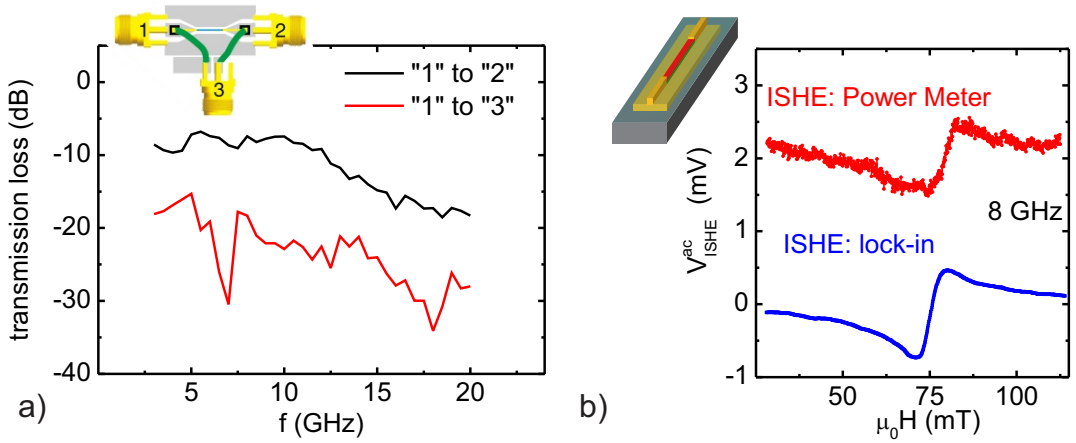

Figure 9.2: The black curve in a) is the transmission loss of a microwave signal when transmitted from terminal 1 to terminal 2. The red curve is the transmission loss from terminal 1 to terminal 3. It represents the background signal. In b) detected voltage spectra using a rf-powermeter (red curve) and a lock-in detector in combination with field modulation (blue curve). The blue curve is the numerically integrated signal, which was measured with the lock-in detector.

system yields the voltage amplitude caused by FMR-dependent effects in the sample at terminal 3, i.e. the blue curve in the graph of Fig. 9.1b).
Both spectra presented in Fig. 9.1 have comparable amplitudes in the sub-mV-range which proves that both measurement and evaluation techniques yield consistent results. However, the data presented in the following are all measured using the lock-in amplifier method due to both, easy handling and an order of magnitude better signal-to-noise ratio compared to the rf-powermeter. In the subsequent section a closer look to the line shapes of rectified ac-voltages at FMR is presented.

9.2 Line shape of voltage signals due to ac-ISHE

Voltage spectra for various precession frequencies are recorded using the in-plane excitation geometry. The first step is to measure the spectra at an angle $\phi_{\mathrm{H}} = 90°$ where one expects a signal caused by ac-ISHE which is maximized due to optimal geometric driving field conditions $h_{y'} = h_x \sin(\pi/2) = h_x$. Fig. 9.3a) shows the results for a bipolar external magnetic field sweep. The presented curves correspond to numerically integrated voltage spectra, which are recorded using field modulation and lock-in detection. It is evident, that characteristic line shapes appear for different frequencies and corresponding external magnetic field strengths. The resonant field positions $\mu_0 H_0$ as a function of frequency strongly suggests that one observes an effect that corresponds to resonant magnetization precession. As this is expected for ac-ISHE where spin currents are injected by spin pumping, it is the first indication to

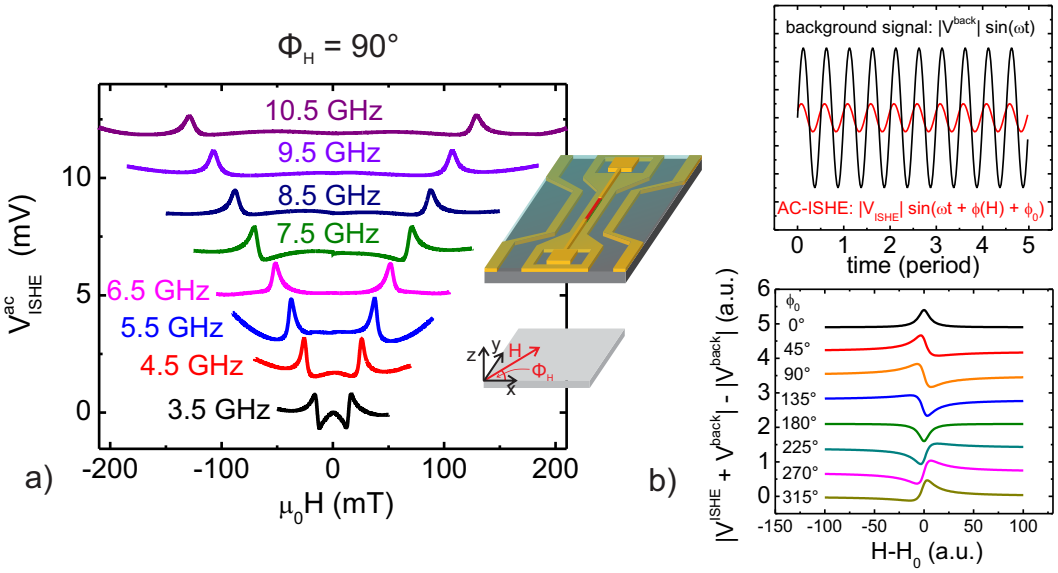

Figure 9.3: In a) numerically integrated voltage signals measured with a lock-in detector are plotted as a function of external field. The external field is swept in a bipolar manner for several driving frequencies from 3.5 to 10.5 GHz. For all spectra the external field angle is $\phi_H = 90°$ and the in-plane excitation field scheme is used. The upper panel in b) shows the sine wave representation of the background (black curve) and the ac-ISHE (red curve) signal. There is an offset phase angle of ϕ_0 and additionally a field dependent phase angle $\phi(H)$ between the background the ac-ISHE signal. In the lower panel of b) a simulation of line shapes is plotted for different offset phase angles ϕ_0.

really observe voltages due to ac-ISHE. Contrary to a voltage from dc-ISHE the line shape's amplitude does not change sign upon magnetization reversal, viz. voltage spectra at positive and negative field are symmetric with respect to external zero field. In Eq. (4.26), which is the formula describing voltages due to ac-ISHE for the in-plane excitation setup, the dependence on magnetization direction is contained in $\sin^2(\phi_H)$. This factor does not change sign under magnetization reversal, which is simply given by $\phi_H + \pi$, and therefore one indeed expects the voltage spectra to be symmetric with respect to external zero field. The expected line shape is given by the square root of a symmetric Lorentzian function, for a plot see Fig. 4.9b). This is clearly not what is observed from measurements presented in Fig. 9.3a). E.g. the voltage spectrum recorded for $f = 5.5$ GHz is largely antisymmetric whereas the signal for $f = 10.5$ GHz is almost purely symmetric with respect to the resonance field. The line shapes can be explained by considering the sum of voltage signals due to ac-ISHE and a large ac-background which accumulates to an arbitrary but fixed phase. To this end, one has to consider that the voltage signal due to ac-ISHE and the background from capacitive and inductive coupling generally have a nonzero

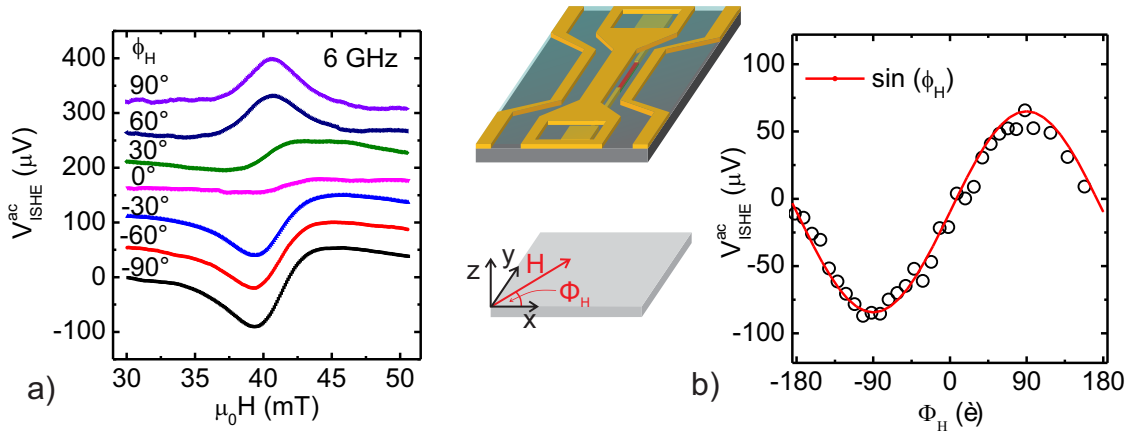

Figure 9.4: In a) voltage signals detected with a lock-in detector for a driving frequency of 6 GHz are plotted. Spectra for different field angles ϕ_H are shown. The out-of-plane excitation scheme is used. In b) the amplitudes of voltage spectra are plotted as a function of ϕ_H. The red solid line represents two piecewise fits from $-180°$ to $0°$ and from $0°$ to $180°$.

phase angle ϕ_0. The situation is depicted in the upper panel of Fig. 9.3b) where two corresponding sine waves are plotted. One has to recognize that the voltage due to ac-ISHE additionally features an external field dependent phase $\phi(H)$ between magnetization precession and driving field h_x. It performs a phase shift of π going through FMR, according to the formula $\phi(H) = \arctan((H - H_0)/\Delta H)$. For instance, if $\phi_0 = \pi$-multiples, the line shape is purely symmetric, whereas for $\phi_0 = \pi/2$-multiples the line is completely antisymmetric. If the phase angle adopts some intermediate angle the line shape can be anything from symmetric to antisymmetric. The results from corresponding simulations are presented in the lower panel of Fig. 9.3b).

9.3 Angular and power dependence of voltage signals

Further insight into whether voltage signals are due to ac-ISHE or due to other effects is provided by angle dependent measurements. A signal caused by ac-ISHE should be proportional to $\sin(\phi_H)$, see Eq. (2.22). This behavior is expected for the voltage amplitudes due to ac-ISHE when the driving field is out-of-plane, see Eq. (4.27). Therefore one needs to consider the out-of-plane excitation scheme with a CPW. Voltage spectra from $\phi_H = -90°$ to $90°$ are recorded, see Fig. 9.4a). At $\phi_H = \pm 90°$ the magnitude of the signal is maximal and at $\phi_H = 0°$ the signal vanishes. In Fig. 9.4b) the extracted amplitudes are plotted as a function of ϕ_H. A fit to the data using $A \sin(\phi_H)$ yields the expected result. Note that for the in-plane geometry such a statement is not reliable as both the magnetization precession amplitude and the voltage due to ac-ISHE are proportional to $\sin(\phi_H)$. The change of line shape

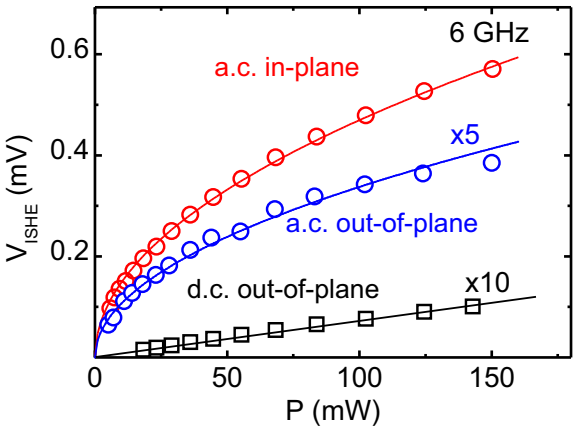

Figure 9.5: Amplitudes extracted from voltage spectra for a driving frequency of 6 GHz are plotted as a function of input power. The red and blue open circles correspond to ac-voltages under circumstances of in-plane and out-of-plane excitation field, respectively. The black open squares correspond to dc-ISHE and out-of-plane excitation geometry. For easier viewing the data represented by the blue and the black data points are scaled by factors 5 and 10, respectively. Blue and red solid lines are fits to data according to $\sqrt{P}$ and the black solid line is a linear fit to data.

which depends on ϕ_{H} might analogously be assigned to the phase angle ϕ_0 between voltage signal due to ISHE and background as explained in the preceding chapter. From Eqs. (4.26) and (4.27) it is expected that a voltage signal due to ac-ISHE is proportional to the driving field. In contrast to that a voltage signal due to dc-ISHE is proportional to the excitation field squared. In Fig. 9.5 voltage amplitudes at a fixed frequency of 6 GHz are plotted as a function of the microwave power P of the signal fed into terminal 1. For easier viewing the power dependent data points are scaled respectively. Voltage signals due to ac-ISHE for both in-plane and out-of-plane driving field depend on $\sqrt{P}$ whereas the dc-ISHE signal is a function of P. As the driving field is proportional to $\sqrt{P}$ the results are in-line with theoretical considerations concerning voltages due to ac-ISHE.

9.4 Estimation of parasitic effects when measuring voltages due to ac-ISHE

In principle ac-voltages due to other effects as ISHE are possible. The most prominent for the sample design at hand are AMR and electromagnetic induction which have been both theoretically considered in sections 4.3 and 4.4.
One cannot exclude a voltage signal due to electromagnetic induction on the ground of angle or power dependent measurements as a similar dependence on these parameters as for ac-ISHE voltages is expected. V_{ind} as specified in Eq. (4.46) is proportional to $\partial m_{y'}/\partial t$ and therefore scales with $\sqrt{P}$. Furthermore, $m_{y'} = \chi_{y'y'} h_x \sin(\phi_{\mathrm{H}})$ for in-plane and $m_{y'} = \chi_{y'z'} h_z$ for out-of-plane driving field. When including the projection onto the fixed voltage probes along y this accumulates to a $\sin^2(\phi_{\mathrm{H}})$- or $\sin(\phi_{\mathrm{H}})$-dependence for in-plane and out-of-plane driving field respectively.
In order to quantify the importance of inductive signals a series of different NiFe/NM bilayers is examined. The normal metal capping layers under consideration and in comparison to Pt are Al, Cu and Au. For Al and Cu one expects not to measure a voltage signal due to ac-ISHE as both the spin diffusion length is very long compared to their thickness of only 10 nm and their spin Hall angle is very small. Yet, due to the similar resistivity of the considered metal layers the signal due to induction should be comparable. In Fig. 9.6a) voltage spectra at 8 GHz and $\phi_{\mathrm{H}} = 90°$ across FMR of NiFe/Al, NiFe/Cu, NiFe/Au and NiFe/Pt with individual layer thicknesses of 10 nm (only for Cu the layer thickness is 20 nm) are presented. The graphs include both spectra for in-plane and out-of-plane excitation geometry. The measured relative amplitudes for both excitation schemes are consistent and the different magnitudes can be explained by the difference in magnitude of applicable susceptibilities and driving fields. The inductive signal is further studied for NiFe/Cu for Cu capping layers of 10 nm and 20 nm thickness. The result is displayed in Fig. 9.6 b). Doubling the Cu-capping layer thickness increases the signal due to induction substantially. This is due to the fact that the conduction loop of the voltage measurement circuit is shifted towards the Cu layer proportionally to the conductance, which in turn increases the net magnetic flux conduction loop and thus the induced voltage signal. In order to estimate the maximum percentage of induced voltage in NiFe/Pt a direct comparison to NiFe/Cu is conducted. The resistance of both devices is almost equal, i.e. 1.6 kΩ and 1.7 kΩ respectively. For the spectra corresponding to the out-of-plane excitation scheme in Fig 9.6a) the ratio of amplitudes is given by $V_{\mathrm{Cu}}^{\mathrm{ac}}/V_{\mathrm{Pt}}^{\mathrm{ac}} = 6\,\mu\mathrm{V}/108\,\mu\mathrm{V} \approx 0.06$. The conclusion is to have only about 6% of inductive signal making up for the completed voltage magnitude in NiFe/Pt. In the case of NiFe/Au a voltage due to dc-ISHE has clearly been distinguishable, see Chapts. 6 and 7. However the measured ac-voltage signal presented in Fig. 9.6 cannot be assigned to ac-ISHE. The slightly larger amplitude as compared to NiFe/Cu can be well explained by the higher conductance of the NiFe/Au bilayer and the corresponding electromagnetic induction voltage drop.
In order to estimate a possible contribution from AMR a comparison of voltage

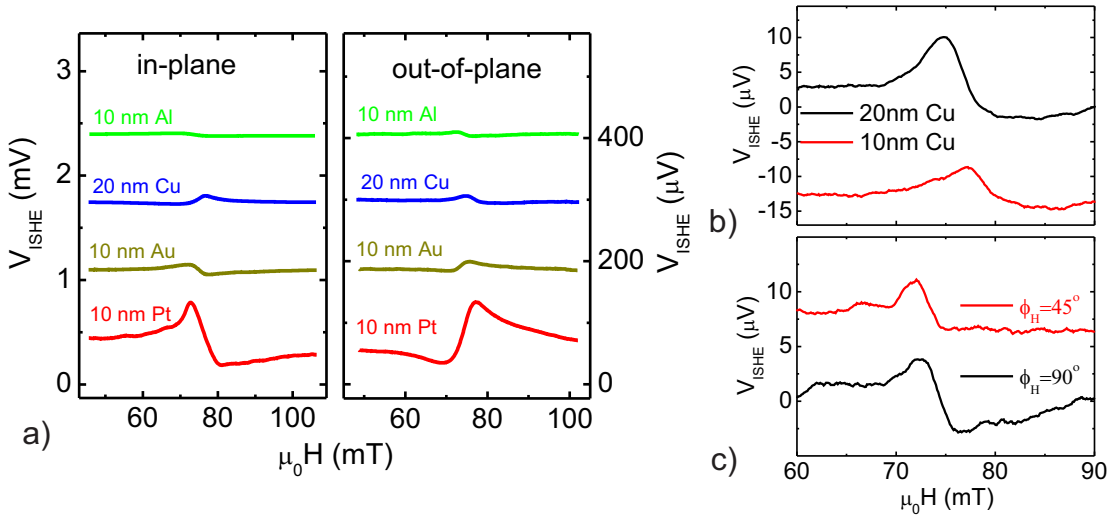

Figure 9.6: In a) ac-voltage spectra for in-plane and out-of-plane excitation for NiFe/Al, NiFe/Cu, NiFe/Au and NiFe/Pt are presented. The spectra correspond to a driving frequency of 8 GHz and an external field angle of $\phi_{\mathrm{H}} = 90°$. In b) ac-voltage spectra of NiFe/Cu which have a NM-thickness of 10 nm and 20 nm, respectively, are shown. In this case out-of-plane excitation is used. In c) ac-voltage spectra for NiFe/Al at two different external field angles $\phi_{\mathrm{H}} = 45°$ and $\phi_{\mathrm{H}} = 90°$ are shown.

signals for NiFe/Al at $\phi_{\mathrm{H}} = 90°$ and $\phi_{\mathrm{H}} = 45°$ is conducted, see Fig 9.6c). The first order contribution of AMR which is proportional to the precession frequency has an expected angular dependence of $\cos(2\phi_{\mathrm{H}})$, see [59]. Especially, a signal due to AMR is expected to vanish for $\phi_{\mathrm{H}} = 45°$. Corresponding data presented in Fig. 9.6c) suggest that the inductive signal dominates, viz. the expected $\sin(\phi_{\mathrm{H}})$-dependence of the voltage amplitude. Hence, voltage signals due to AMR are negligible for studies of ac-ISHE in NiFe/Pt.

9.5 Comparison of amplitudes of ac- and dc-ISHE

According to theoretical considerations presented in [63] the voltage amplitude due to ac-ISHE is expected to be one order of magnitude larger than the dc-ISHE caused voltage. In order to measure the dc-ISHE on the same NiFe/Pt bilayer wire as used for the measurement of ac-ISHE a nanovoltmeter is connected to terminal 3 (cf. Fig 9.1). In Fig. 9.7 voltage signals due to ac- (top red curve) and dc-ISHE (bottom black curve) are plotted. The voltage spectra are recorded implementing out-of-plane excitation and $\phi_{\mathrm{H}} = 0°$ (dc-) and $\phi_{\mathrm{H}} = 90°$ (ac-case). In order to extract the amplitude of voltages due to ac-ISHE it is best to fit the line shape, which is measured using the lock-in amplifier, with the derivative with respect to the external field H (Eq. 4.20). Subsequent renormalization of the extracted amplitude fit parameter with respect to Schottky-diode and 50 Ω-system power to voltage conversion yields the voltage amplitude due to ac-ISHE. The amplitude of the presented voltage spectra in Fig. 9.7 is 120 µV and 10 µV respectively.
From the theoretical point of view one has to compare Eq. (4.20) for the voltage due to dc- and Eq. (4.27) for the signal caused by ac-ISHE. Their relative amplitudes at FMR are given by:

$$\frac{V_{\mathrm{ISHE}}^{\mathrm{oop,\,ac}}}{V_{\mathrm{ISHE}}^{\mathrm{oop,\,dc}}} = \frac{V^{\mathrm{ac}}}{V^{\mathrm{dc}}} = \frac{M_{\mathrm{S}}}{\chi_{y'z}^{\mathrm{res}} h_z} \tag{9.5}$$

Note that this coincides with the relative amplitudes of dc and ac spin currents from spin pumping as theoretically deduced in Sec. 3.5 (Eq. (3.91)). The experimentally expected ratio is estimated by plugging in measured values for M_{S}, i.e. $\mu_0 M_{\mathrm{S}} = 0.9\,\mathrm{T}$, the extracted value from FMR-measurements for the susceptibility at 6 GHz, $\chi_{y'z}^{\mathrm{res}} = 61.5$, and the simulated driving field scaled with the respective average microwave power, $\mu_0 h_z = 0.3\,\mathrm{mT}$. From this the amplitude for voltages due to ac-ISHE is expected to be a factor of 50 larger than the signal caused by dc-ISHE. However, from the data presented in Fig. 9.7 $V^{\mathrm{ac}}/V^{\mathrm{dc}} = 12$, which is roughly a factor of 4 smaller than expected. To this end, one has to consider the transmission properties of microwaves along the studied NiFe/Pt bilayer wire which is rather far from having the ideal impedance for matching with the 50 Ω terminal where the voltage is picked off. The NiFe/Pt wire in the gap between signal and ground line of the 50 Ω-CPW is a CPW itself, see Fig. 9.1a). It corresponds to a characteristic impedance of 250 Ω, which is estimated using TX-LINE. From the standing wave ratio, Eq. (9.1), the expected transmission of microwaves from the NiFe/Pt wire into the measurement terminal is only about 33%. Therefore the experimentally feasible value $V^{\mathrm{ac}}/V^{\mathrm{dc}} = 12$ is only approximately a third of the true ratio. This is still a little smaller than the theoretically expected value of 50. But, considering the fact that the impedance estimation of the NiFe/Pt-CPW is only very rough using TX-LINE, the experimental ratio of ac- to dc-ISHE caused voltage amplitudes compares well to the expected one.
$V^{\mathrm{ac}}/V^{\mathrm{dc}}$ can also be estimated using the published values for $\alpha_{\mathrm{SH}} = 0.12$ [53] and $\lambda_{\mathrm{sd}} = 1.4\,\mathrm{nm}$ [54]. Inserting the published values into Eq. (4.27) yields $V^{\mathrm{ac}} = 0.4\,\mathrm{mV}$

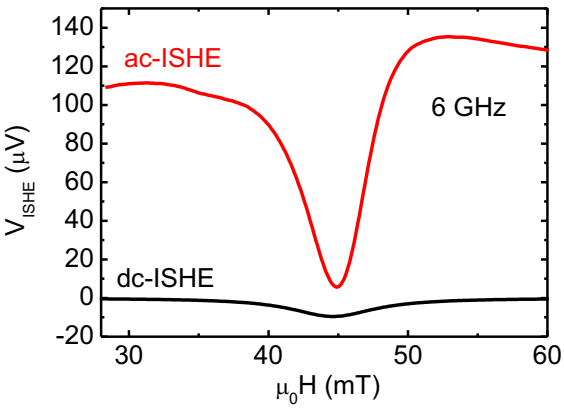

Figure 9.7: Voltages due to ac-ISHE measured in the same NiFe/Pt bilayer for a driving frequency of 6 GHz using out-of-plane excitation are presented. Under equal experimental circumstances with respect to driving field the signal due to ac-ISHE is 12 times larger than the signal due to dc-ISHE.

and $V^{\mathrm{ac}}/V^{\mathrm{dc}} = 40$, which also compares well to the value from the experiment.

For in-plane excitation only the voltage due to ac-ISHE can be uniquely measured. The estimation of voltage amplitudes due to ac-ISHE can be conducted for in-plane excitation using Eq. (4.26). For a frequency of $f = 10\,\mathrm{GHz}$ the applicable susceptibility $\chi^{\mathrm{res}}_{y'z'}$ adopts a value of 56.5. Using further $\mu_0 h_{\mathrm{x}} = 0.27\,\mathrm{mT}$ a peak-to-peak amplitude $V^{\mathrm{ac}}_{\mathrm{pp}} = 4.2\,\mathrm{mV}$ is expected for the voltage measured due to ac-ISHE. Comparing the result for the recorded 10 GHz-spectrum presented in Fig. 9.3a) to the theoretical estimation one has to account for the transmission properties of the NiFe/Pt-microstrip, see Fig. 9.1a). Using TX-LINE a characteristic impedance of $Z_1 = 480\,\Omega$ is calculated. Therefore only 18% of the theoretically predicted value $V^{\mathrm{ac}}_{\mathrm{pp}} = 4.2\,\mathrm{mV}$ is expected to be measured. For the 10 GHz-spectrum of Fig. 9.7a) $V^{\mathrm{ac}}_{\mathrm{pp}} = 0.70\,\mathrm{mV}$ which compares well to the transmission property corrected theoretical value of $V^{\mathrm{ac}}_{\mathrm{pp}} = 0.76\,\mathrm{mV}$.

It might be an interesting task to optimize the impedance matching in future sample preparations. This will further stimulate the emerging field of ac-spintronics where due to the large voltage signals technological applications are well imaginable. From a scientific point of view it might also be very interesting to further study the statement about a complex spin Hall angle for Pt [62].

10 Summary and conclusions

In the present PhD-thesis it has been the objective to establish an experimental technique which implements magnetization dynamics and spin pumping (SP) in NiFe/NM layers to study both time constant (dc) and oscillating (ac) components of spin currents via the inverse spin Hall effect (ISHE). Performing careful investigations towards exclusion of parasitic effects, SP-ISHE could be set on a robust experimental basis. To this end the key element has been to geometrically separate voltage signals generated by ISHE from signals due to parasitic effects like AMR by integrating NiFe/NM wires into the gap between signal and ground line of a CPW. The robustness of the approach has been proven by comparing the experimental findings for different excitation geometries and FM/NM bilayers to theoretically expected results. Hence, the quantification of spin Hall angles for Pt and Au has been performed while investigating at the same time important parameters such as the spin diffusion length of the normal metal and the spin mixing conductivity of the NiFe/NM interface. Furthermore, the comparison of experimental results of spin Hall angles from SP-ISHE for a broad spectrum of Au_xPt_{1-x}-alloys with first principles calculations shows consistent results. This brings us into a position where studies of spin dependent scattering can be established in close collaboration between experiment and theory. This might finally disclose issues concerning the nature of spin dependent scattering, whether being intrinsic or extrinsic for certain material systems as well as find technologically relevant materials which exhibit large spin Hall effects. The other subsequent topic originating from the established experimental method of SP-ISHE has been the first observation of the ac-ISHE in Pt.

In order to give a conclusive overview of the topics which have been studied in the present work, what follows is a chapter-wise summary of the most important results. This also comprises final remarks on points of contact for possible future experimental and theoretical efforts.

In chapter 3 the theoretical foundations of magnetization dynamics and FMR have been elaborated towards the specific case of thin ferromagnetic films. In section 3.3 the solutions of the Landau-Lifshitz-Gilbert equation have been represented by the susceptibility factors of the dynamic magnetization components. The susceptibilities have been specified by certain line shapes as a function of external field. Their connection to the microwave absorption has been essential for the determination of the magnetic properties of NiFe single layers and NiFe/NM bilayers. Note that the derived formulas can be supplemented by further effective field terms, which may for example arise in crystalline ferromagnetic materials like Fe or GaMnAs or ferromagnetic wires for which, compared to thin films, a second dimension is reduced

towards the 1 µm scale or below. In section 3.4 the spin pumping mechanism has been explained based on the concepts of non-collinear magnetoelectronics and in section 3.5 the derived susceptibility line shapes for thin ferromagnetic films have been incorporated into expressions for spin currents caused by spin pumping in FM/NM bilayers. To this end the generally different components of spin currents, viz. the time constant and the oscillating part of the polarization have been derived and formulas which allow for estimation of their relative amplitudes have been explicitly specified.
In chapter 4 the expected voltage signals due to both ISHE and experimental setup related parasitic effects, viz. AMR and electromagnetic induction, have been elaborated. In section 4.1 the used coplanar waveguide is characterized with respect to its microwave impedance. The simulations of rf-currents in the frequency range of 3 - 16 GHz show that due to the skin effect the current density decreases in the central part of the transmission lines of the CPW for increasing frequency. This has been accounted for in subsection 4.1.1 when the excitation field generated by the CPW has been calculated as a function of frequency. Such estimations are essential for both the determination of optimal CPW geometries and the correct quantification of excitation fields. In sections 4.2 to 4.4 the line shapes of voltages due to ISHE, AMR and electromagnetic induction have been elaborated. This has been done in the context of the two fundamentally different integration possibilities of NiFe/NM bilayer wires into the used CPW structure, viz. presence of pure in-plane or out-of-plane magnetic driving field. The fundamental symmetrical differences for the present effects in the context of the used CPW geometries have been discussed. The derived equations are formulated in a very general manner including information about electromagnetic coupling between CPW and FM/NM bilayer and additional driving fields due to conductive capping layers of FM. To this end the theoretical results are not limited to the experimental issues presented in this work, but can e.g. be used in terms of studying the dynamic aspects of AMR in the presence of spin-orbit-fields in ultrathin FM-layers [169] or dilute ferromagnetic semiconductors like GaMnAs [170–172].
In chapter 5 several NiFe/NM bilayers have been studied in terms of FMR and spin pumping. In section 5.1 the magnetic properties of NiFe and the spin mixing conductivities of NiFe/NM interfaces have been extracted from microwave absorption spectra in non-micro-structured thin films. The NM layers under consideration were Pt, Au, Ta and W. It has been confirmed that the used Pt is a very effective spin sink. Furthermore, for Au it has been evidenced that a spin current can be transferred via spin pumping from the NiFe-layer. However, as the spin diffusion length for Au adopts a value of approximately 30 nm the line width broadening of spectra has not appeared for 10 but only for 50 nm thick layers. For Ta and W no spin pumping effect has been detected. It has been concluded that there is a dead layer present at the NiFe interface for these materials. In section 5.2 FMR and spin pumping have been studied for micro-structured NiFe/NM wires integrated into CPW structures. The equivalence of extracting magnetic properties and spin mixing conductivities from both microwave absorption and voltage spectra has been

concluded. When the total magnetic moment is reduced, which naturally happens for micro-structured wires, voltage spectra are valuable due to the large signal to noise ratio. This is essential for NiFe/NM wires integrated into the gap between signal and ground line where furthermore the applicable out-of-plane susceptibility is very small due to the thin film geometry. Moreover, differences between non-micro-structured and micro-structured films have been elaborated. As suggested by studies of the line width as a function of angle ϕ_H it is essential to account for magnetic edge modes when extracting magnetic properties in the studied 5 µm wide wires. However, the resonance field of spectra as a function of ϕ_H suggests that the wires can still be treated as thin ferromagnetic films. To this end a future prospect might be to study spin pumping when scaling the width of the wires down to the 1 µm scale or below. In this respect the mutual application of micromagnetic simulations and measurements of voltage spectra across FMR might bring further insight into the role of edge modes in the spin pumping process.
In chapter 6 a general study of amplitudes of dc voltage spectra as a function of ϕ_H has proved that a geometrical separation of ISHE from parasitic effects is possible for in-plane magnetized NiFe/NM bilayers using out-of-plane excitation with a CPW. In section 6.2 the fit of angular dependencies of voltage spectra for out-of-plane excitation has been established as a powerful tool not only to unambiguously determine the presence of ISHE caused voltage signals, but also in terms of characterizing parameters of electromagnetic coupling and parasitic excitation fields. In line with the results of spin pumping measurements it has been shown that ISHE is detectable for NiFe/Pt, NiFe/Au, but not for a NiFe single and a NiFe/Ta bilayer. However, for Ta despite the fact that no ISHE is measurable one finds that the voltage amplitudes are too large as to be explained by a pure action of AMR. To this end further studies of NiFe/Ta might give insight whether in these circumstances spin-orbit-fields generate additional voltage signals in the NiFe layer.
In chapter 7 the experimental study of voltage signals exclusively caused by ISHE for NiFe/Pt and NiFe/Au has been elaborated. The results presented in section 7.1 corroborate that a unique study of ISHE for certain external field angles is possible. In order to find this exact angular position the method of recording voltage spectra for small steps around $\phi_H = 0°$ has proved to be essential. Furthermore, the comparison of the temperature dependence of voltage signals at $\phi_H = 0°$ and $\phi_H = 45°$ shows the expected different behavior. Including a study of static AMR the results strongly suggest that at $\phi_H = 0°$ a signal is purely caused by ISHE whereas for $\phi_H = 45°$ the voltage is dominated by AMR. Towards the quantification of α_{SH} at $\phi_H = 0°$ the most critical parameters have been identified in section 7.2. These are the microwave power which determines the amplitude of the magnetic excitation field, the spin mixing conductivity and the spin diffusion length. The problem of the microwave power has been accounted for by only taking voltage spectra into account for which the measured transmitted signal through the CPW shows weak frequency dependence. The spin diffusion length is a very critical parameter especially in the case of Pt. Pt-thickness dependent measurements of voltage signals due to ISHE have been conducted. The extracted value of $\lambda_{sd} = 1.9$ nm is consistent with pub-

lished values. However, two issues remain critical and should be further studied in future experimental and theoretical work. The first is an influence of a possible spin memory loss in NiFe/NM interfaces. However, there are no experimental indications in the present work which might corroborate the importance of this effect. The second issue is especially critical for NiFe/Pt. The spin drift-diffusion-model might not be correct for the measured short spin diffusion length. Here a valuable approach might be to alternatively use the reciprocity of spin pumping and spin transfer torque in order to quantify the spin Hall angle [173, 174]. Notwithstanding, spin Hall angles for Pt and Au have been quantified using the spin diffusion model. Three different NiFe/Pt-samples have been studied and taking into account all three of them a value of $\alpha_{\mathrm{SH}} = 0.14 \pm 0.04$ has been obtained. In the case of NiFe/Au one sample has been studied. Accounting for the back flow via an effective spin mixing conductivity value of $\tilde{g}_{\mathrm{F}}^{\uparrow\downarrow} = 0.24 \times 10^{19}\,\mathrm{m}^{-2}$ the spin Hall angle of Au has been determined to be $\alpha_{\mathrm{SH}} = 0.05 \pm 0.01$. In section 7.3 it has been presented that using the assumption of a fixed spin Hall angle for Pt in a temperature range of 10 to 300 K the spin diffusion length can be calculated consistently with published temperature dependent values for λ_{sd} at 4.2 K. This corroborates that the spin Hall angle for Pt might indeed have a weak temperature dependence.
In chapter 8 SP-ISHE has been studied for a wide composition range of $\mathrm{Au}_x\mathrm{Pt}_{1-x}$-alloys. Angle dependent measurements of voltage spectra for NiFe/$\mathrm{Au}_x\mathrm{Pt}_{1-x}$ bilayers suggest the presence of considerable ISHE for all studied alloys. The quantification of spin Hall angles as a function of Au-content in Pt has taken place using the spin diffusion model. Thickness dependent measurements of voltages due to ISHE for two different alloys have indicated that there is no considerable back flow of spin current into NiFe for the studied 12 nm thick $\mathrm{Au}_x\mathrm{Pt}_{1-x}$-alloy layers. In section 8.3 the spin diffusion lengths of $\mathrm{Au}_{0.72}\mathrm{Pt}_{0.28}$ and $\mathrm{Au}_{0.66}\mathrm{Pt}_{0.34}$ have been determined to be 2.76 nm and 0.8 nm respectively. In this respect the spin diffusion length for the whole alloy range has been estimated relative to the measured conductivities and spin Hall angles have been calculated. The experimental results are in agreement with first principles calculations and the observed deviations might be well explained accounting for the fact that the estimation of spin diffusion lengths from conductivities is only a rough estimation. Therefore the result of the spin Hall angle in excess of 0.3 for $\mathrm{Au}_{0.53}\mathrm{Pt}_{0.47}$ should be tried to be remeasured. Notwithstanding, spin Hall angles between 0.15 and 0.20 have been calculated for a composition range of $\mathrm{Au}_{0.73}\mathrm{Pt}_{0.27}$ to $\mathrm{Au}_{0.53}\mathrm{Pt}_{0.47}$. The type of spin dependent scattering as a function of $\mathrm{Au}_x\mathrm{Pt}_{1-x}$-composition could be further studied in future efforts in collaboration with experts concerning first-principles calculations.
In chapter 9 the observation of the time dependent component of a spin current from spin pumping via the ac-ISHE studying NiFe/Pt bilayers has been reviewed. The experimental results of line shapes as a function of precession frequency, as well as angular and power dependencies have provided strong indication that the observed large voltage signals in the GHz-regime are caused by ac-ISHE. Comparison of signals in NiFe/Pt with voltages measured in NiFe/Al and NiFe/Cu confirm the observation. For NiFe/Au the situation is a little more complicated and the observed

voltage signals could not be uniquely assigned to ISHE against the main parasitic effect of electromagnetic induction. For the case of Pt it could be confirmed that the voltage due to ac-ISHE is at least one order of magnitude larger as the signal due to dc-ISHE. The expected factor of 50 for the relative amplitude of voltages could be roughly confirmed assuming that the microwave transmission properties of the studied NiFe/Pt bilayers are far from matching with the impedance of $50\,\Omega$ of the measurement terminals. Considering the results concerning the dc-ISHE in Au_xPt_{1-x} it might be very interesting to study ac-ISHE for these alloys. This might also give further insight whether the spin Hall angle is indeed a complex quantity as argued in [62].

Bibliography

[1] S. D. Bader and S. S. P. Parkin. Spintronics. *Annual Review of Condensed Matter Physics*, 1:71, 2010.

[2] C. Chappert, A. Fert, and F. Nguyen Van Dau. The emergence of spin electronics in data storage. *Nature Materials*, 6:813, 2007.

[3] S. A. Wolf, D. D. Awschalom, R. A. Buhrman, J. M. Daughton, S von Molnár, M. L. Roukes, A. Y. Chtchelkanova, and D. M. Treger. Spintronics: a spin-based electronics vision for the future. *Science (New York, N.Y.)*, 294:1488, 2001.

[4] N. F. Mott. Electrons in transition metals. *Advances in Physics*, 13:325, 1964.

[5] A. Fert and I. A. Campbell. Two-Current Conduction in Nickel. *Physical Review Letters*, 21:1190, 1968.

[6] A. Fert and I. A. Campbell. Electrical resistivity of ferromagnetic nickel and iron based alloys. *Journal of Physics F: Metal Physics*, 6:849, 1976.

[7] M. Johnson and R. H. Silsbee. Interfacial Charge-Spin Coupling: Injection and Detection of Spin Magnetization in Metals. *Physical Review Letters*, 55:1790, 1985.

[8] M. N. Baibich, J. M. Broto, A. Fert, F. Nguyen Van Dau, and F. Petroff. Giant Magnetoresistance of (001)Fe/(001)Cr Magnetic Superlattices. *Physical Review Letters*, 61:2472, 1988.

[9] G. Binasch, P. Grünberg, F. Saurenbach, and W. Zinn. Enhanced magnetoresistance in layered magnetic structures with antiferromagnetic interlayer exchange. *Physical Review B*, 39:4828, 1989.

[10] P. van Son, H. van Kempen, and P. Wyder. Boundary Resistance of the Ferromagnetic-Nonferromagnetic Metal Interface. *Physical Review Letters*, 58:2271, 1987.

[11] T. Valet and A. Fert. Theory of the perpendicular magnetoresistance in magnetic multilayers. *Physical Review B*, 48:7099, 1993.

[12] B. Dieny, V. S. Speriosu, S. S. P. Parkin, B. A. Gurney, D. R. Wilhoit, and D. Mauri. Giant magnetoresistive in soft ferromagnetic multilayers. *Physical Review B*, 43:1297, 1991.

[13] B. Dieny, B. A. Gurney, S. E. Lambert, D. Mauri, S. S. P. Parkin, V. S. Speriosu, and D. R. Wilhoit. Magnetoresistive sensor based on the spin valve effect, 1993. US Patent 5,206,590.

[14] M. Julliere. Tunneling between ferromagnetic films. *Physics Letters A*, 54:225, 1975.

[15] J. S. Moodera, L. R. Kinder, T. M. Wong, and R. Meservey. Large Magnetoresistance at Room Temperature in Ferromagnetic Thin Film Tunnel Junctions. *Physical Review Letters*, 74:3273, 1995.

[16] W. H. Butler, X.-G. Zhang, T. C. Schulthess, and J. M. MacLaren. Spin-dependent tunneling conductance of Fe | MgO | Fe sandwiches. *Physical Review B*, 63:054416, 2001.

[17] J. Mathon and A. Umerski. Theory of tunneling magnetoresistance of an epitaxial Fe/MgO/Fe(001) junction. *Physical Review B*, 63:220403, 2001.

[18] S. S. P. Parkin, C. Kaiser, A. Panchula, P. M. Rice, B. Hughes, M. Samant, and S.-H. Yang. Giant tunnelling magnetoresistance at room temperature with MgO (100) tunnel barriers. *Nature Materials*, 3:862, 2004.

[19] S. Yuasa, T. Nagahama, A. Fukushima, Y. Suzuki, and K. Ando. Giant room-temperature magnetoresistance in single-crystal Fe/MgO/Fe magnetic tunnel junctions. *Nature Materials*, 3:868, 2004.

[20] J. C. Slonczewski. Current-driven excitation of magnetic multilayers. *Journal of Magnetism and Magnetic Materials*, 159:L1–L7, 1996.

[21] L. Berger. Emission of spin waves by a magnetic multilayer traversed by a current. *Physical Review B*, 54:9353, 1996.

[22] M. Tsoi, A. G. M. Jansen, J. Bass, W.-C. Chiang, M. Seck, V. Tsoi, and P. Wyder. Excitation of a Magnetic Multilayer by an Electric Current. *Physical Review Letters*, 80:4281, 1998.

[23] E. B. Myers, D. C. Ralph, J. A. Katine, R. N. Louie, and R. A. Buhrman. Current-Induced Switching of Domains in Magnetic Multilayer Devices. *Science*, 285:867, 1999.

[24] F. J. Albert, J. A. Katine, R. A. Buhrman, and D. C. Ralph. Spin-polarized current switching of a Co thin film nanomagnet. *Applied Physics Letters*, 77:3809, 2000.

[25] M. Stiles and A. Zangwill. Anatomy of spin-transfer torque. *Physical Review B*, 66:014407, 2002.

[26] A. Brataas, A. D. Kent, and H. Ohno. Current-induced torques in magnetic materials. *Nature Materials*, 11:372, 2012.

[27] S. S. P. Parkin, M. Hayashi, and L. Thomas. Magnetic domain-wall racetrack memory. *Science (New York, N.Y.)*, 320:190, 2008.

[28] L. Liu, C. F. Pai, Y. Li, H. W. Tseng, D. C. Ralph, and R. A. Buhrman. Spin-torque switching with the giant spin Hall effect of tantalum. *Science (New York, N.Y.)*, 336:555, 2012.

[29] K. Garello, I. M. Miron, C. O. Avci, F. Freimuth, Y. Mokrousov, S. Blügel, S. Auffret, O. Boulle, G. Gaudin, and P. Gambardella. Symmetry and magnitude of spin-orbit torques in ferromagnetic heterostructures. *Nature Nanotechnology*, 8:587, 2013.

[30] I. M. Miron, G. Gaudin, S. Auffret, B. Rodmacq, A. Schuhl, S. Pizzini, J. Vogel, and P. Gambardella. Current-driven spin torque induced by the Rashba effect in a ferromagnetic metal layer. *Nature Materials*, 9:230, 2010.

[31] I. M. Miron, K. Garello, G. Gaudin, P.-J. Zermatten, M. V. Costache, S. Auffret, S. Bandiera, B. Rodmacq, A. Schuhl, and P. Gambardella. Perpendicular switching of a single ferromagnetic layer induced by in-plane current injection. *Nature*, 476:189, 2011.

[32] T. Kimura, Y. Otani, and J. Hamrle. Switching Magnetization of a Nanoscale Ferromagnetic Particle Using Nonlocal Spin Injection. *Physical Review Letters*, 96:037201, 2006.

[33] A. van den Brink, S. Cosemans, S. Cornelissen, M. Manfrini, A. Vaysset, W. Van Roy, T. Min, H. J. M. Swagten, and B. Koopmans. Spin-Hall-assisted magnetic random access memory. *Applied Physics Letters*, 104:012403, 2014.

[34] J. E. Hirsch. Spin Hall Effect. *Physical Review Letters*, 83:1834, 1999.

[35] M. I. Dyakonov. Current-Induced Spin Orientation of Electrons in Semiconductors. *Physics Letters*, 35A:459, 1971.

[36] S. Zhang. Spin hall effect in the presence of spin diffusion. *Physical review letters*, 85:393, 2000.

[37] Y. K. Kato, R. C. Myers, A. C. Gossard, and D. D. Awschalom. Observation of the spin Hall effect in semiconductors. *Science (New York, N.Y.)*, 306:1910, 2004.

[38] J. Wunderlich, B. Kaestner, J. Sinova, and T. Jungwirth. Experimental Observation of the Spin-Hall Effect in a Two-Dimensional Spin-Orbit Coupled Semiconductor System. *Physical Review Letters*, 94:047204, 2005.

[39] E. M. Hankiewicz, J. Li, T. Jungwirth, Q. Niu, S.-Q. Shen, and J. Sinova. Charge Hall effect driven by spin-dependent chemical potential gradients and Onsager relations in mesoscopic systems. *Physical Review B*, 72:155305, 2005.

[40] S. O. Valenzuela and M. Tinkham. Direct electronic measurement of the spin Hall effect. *Nature*, 442:176, 2006.

[41] Y. Tserkovnyak, A. Brataas, and G. E. W. Bauer. Spin pumping and magnetization dynamics in metallic multilayers. *Physical Review B*, 66:224403, 2002.

[42] Y. Tserkovnyak, A. Brataas, and G. E. W. Bauer. Enhanced Gilbert Damping in Thin Ferromagnetic Films. *Physical Review Letters*, 88:117601, 2002.

[43] Y. Tserkovnyak, A. Brataas, and B. I. Halperin. Nonlocal magnetization dynamics in ferromagnetic heterostructures. *Reviews of Modern Physics*, 77:1375, 2005.

[44] S. Mizukami, Y. Ando, and T. Miyazaki. Ferromagnetic resonance linewidth for NM / 80NiFe / NM films (NM = Cu , Ta , Pd and Pt). *Journal of Magnetism and Magnetic Materials*, 230:1640, 2001.

[45] R. Urban, G. Woltersdorf, and B. Heinrich. Gilbert Damping in Single and Multilayer Ultrathin Films: Role of Interfaces in Nonlocal Spin Dynamics. *Physical Review Letters*, 87:217204, 2001.

[46] B. Heinrich, Y. Tserkovnyak, G. Woltersdorf, A. Brataas, R. Urban, and G. E. W. Bauer. Dynamic Exchange Coupling in Magnetic Bilayers. *Physical Review Letters*, 90:187601, 2003.

[47] E. Saitoh, M. Ueda, H. Miyajima, and G. Tatara. Conversion of spin current into charge current at room temperature: Inverse spin-Hall effect. *Applied Physics Letters*, 88:182509, 2006.

[48] H. Y. Inoue, K. Harii, K. Ando, K. Sasage, and E. Saitoh. Detection of pure inverse spin-Hall effect induced by spin pumping at various excitation. *Journal of Applied Physics*, 102:083915, 2007.

[49] O. Mosendz, J. E. Pearson, F. Y. Fradin, G. E. W. Bauer, S. D. Bader, and A. Hoffmann. Quantifying Spin Hall Angles from Spin Pumping: Experiments and Theory. *Physical Review Letters*, 104:046601, 2010.

[50] O. Mosendz, V. Vlaminck, J. E. Pearson, F. Y. Fradin, G. E. W. Bauer, S. D. Bader, and A. Hoffmann. Detection and quantification of inverse spin Hall effect from spin pumping in permalloy/normal metal bilayers. *Physical Review B*, 82:214403, 2010.

[51] A. Azevedo, L. Vilela-Leão, R. Rodríguez-Suárez, A. Lacerda Santos, and S. Rezende. Spin pumping and anisotropic magnetoresistance voltages in magnetic bilayers: Theory and experiment. *Physical Review B*, 83:144402, 2011.

[52] Z. Feng, J. Hu, L. Sun, B. You, D. Wu, J. Du, W. Zhang, A. Hu, Y. Yang, D. M. Tang, B. S. Zhang, and H. F. Ding. Spin Hall angle quantification from spin pumping and microwave photoresistance. *Physical Review B*, 85:214423, 2012.

[53] M. Obstbaum, M. Härtinger, H. G. Bauer, T. Meier, F. Swientek, C. H. Back, and G. Woltersdorf. Inverse spin Hall effect in Ni81Fe19/normal-metal bilayers. *Physical Review B*, 89:060407, 2014.

[54] L. Liu, R. A. Buhrmann, and D. C. Ralph. Review and Analysis of Measurements of the Spin Hall Effect in Platinum. *eprint arXiv:*, 1111.3702, 2012.

[55] Y. S. Gui, S. Holland, N. Mecking, and C. M. Hu. Resonances in Ferromagnetic Gratings Detected by Microwave Photoconductivity. *Physical Review Letters*, 95:056807, 2005.

[56] Y. S. Gui, N. Mecking, X. Zhou, G. Williams, and C.-M. Hu. Realization of a Room-Temperature Spin Dynamo: The Spin Rectification Effect. *Physical Review Letters*, 98:107602, 2007.

[57] Y. S. Gui, N. Mecking, and C.-M. Hu. Quantized Spin Excitations in a Ferromagnetic Microstrip from Microwave Photovoltage Measurements. *Physical Review Letters*, 98:217603, 2007.

[58] Y. S. Gui, N. Mecking, A. Wirthmann, L. H. Bai, and C.-M. Hu. Electrical detection of the ferromagnetic resonance: Spin-rectification versus bolometric effect. *Applied Physics Letters*, 91:082503, 2007.

[59] N. Mecking, Y. Gui, and C.-M. Hu. Microwave photovoltage and photoresistance effects in ferromagnetic microstrips. *Physical Review B*, 76:224430, 2007.

[60] T. J. Silva, C. S. Lee, T. M. Crawford, and C. T. Rogers. Inductive measurement of ultrafast magnetization dynamics in thin-film Permalloy. *Journal of Applied Physics*, 85:7849, 1999.

[61] S. S. Kalarickal, P. Krivosik, M. Wu, C. E. Patton, M. L. Schneider, P. Kabos, T. J. Silva, and J. P. Nibarger. Ferromagnetic resonance linewidth in metallic thin films: Comparison of measurement methods. *Journal of Applied Physics*, 99:093909, 2006.

[62] M. Weiler, J. M. Shaw, H. T. Nembach, and T. J. Silva. Phase-Sensitive Detection of Spin Pumping via the ac Inverse Spin Hall Effect. *Physical Review Letters*, 113:157204, 2014.

[63] H. Jiao and G. E. W. Bauer. Spin Backflow and ac Voltage Generation by Spin Pumping and the Inverse Spin Hall Effect. *Physical Review Letters*, 110:217602, 2013.

[64] D. Wei, M. Obstbaum, M. Ribow, C. H. Back, and G. Woltersdorf. Spin Hall voltages from a.c. and d.c. spin currents. *Nature Communications*, 5:3768, 2014.

[65] S. Zhang. Probing spin currents in semiconductors. *Journal of Applied Physics*, 89:7564, 2001.

[66] K. Ando, S. Takahashi, K. Harii, K. Sasage, J. Ieda, S. Maekawa, and E. Saitoh. Electric Manipulation of Spin Relaxation Using the Spin Hall Effect. *Physical Review Letters*, 101:036601, 2008.

[67] D. Ködderitzsch, S. Lowitzer, J. B. Staunton, and H. Ebert. Electronic and transport properties of disordered transition-metal alloys. *physica status solidi (b)*, 248:2248, 2011.

[68] D. Wei, M. Obstbaum, M. Ribow, C. H. Back, and G. Woltersdorf. Spin Hall voltages from a.c. and d.c. spin currents Supplementary. *Nature Communications*, 5:1–12, 2014.

[69] N. F. Mott. The Scattering of Fast Electrons by Atomic Nuclei. *Proceedings of the Royal Society A: Mathematical, Physical and Engineering Sciences*, 124:425, 1929.

[70] P. A. M. Dirac. The Quantum Theory of the Electron. *Proceedings of the Royal Society A: Mathematical, Physical and Engineering Sciences*, 117:610, 1928.

[71] S. Souma, A. Takayama, K. Sugawara, T. Sato, and T. Takahashi. Ultrahigh-resolution spin-resolved photoemission spectrometer with a mini Mott detector. *The Review of scientific instruments*, 81:095101, 2010.

[72] R. Karplus and J. Luttinger. Hall Effect in Ferromagnetics. *Physical Review*, 95:1154, 1954.

[73] N. Nagaosa, J. Sinova, S. Onoda, A. H. MacDonald, and N. P. Ong. Anomalous Hall effect. *Reviews of Modern Physics*, 82:1539, 2010.

[74] M. Dyakonov. Magnetoresistance due to Edge Spin Accumulation. *Physical Review Letters*, 99:126601, 2007.

[75] L. Berger. Side-Jump Mechanism for the Hall Effect of Ferromagnets. *Physical Review B*, 2:4559, 1970.

[76] J. Smit. The spontaneous hall effect in ferromagnetics I. *Physica*, 21:877, 1955.

[77] J. Sinova, D. Culcer, Q. Niu, N. Sinitsyn, T. Jungwirth, and A. MacDonald. Universal Intrinsic Spin Hall Effect. *Physical Review Letters*, 92:126603, 2004.

[78] J. Fabian, A. Matos-Abiague, C. Ertler, P. Stano, and I. Zutic. Semiconductor Spintronics. *acta physica slovaca*, 57:565, 2007.

[79] J. Smit. Magnetoresistance of ferromagnetic metals and alloys at low temperatures. *Physica*, 17:612, 1951.

[80] S. Datta. *Electronic Transport in Mesoscopic systems*. Oxford University Press, 1997.

[81] L. Berger. Influence of spin-orbit interaction on the transport processes in ferromagnetic nickel alloys, in the presence of a degeneracy of the 3d band. *Physica*, 30:1141, 1964.

[82] M. V. Berry. Quantal Phase Factors Accompanying Adiabatic Changes. *Proceedings of the Royal Society A: Mathematical, Physical and Engineering Sciences*, 392:45, 1984.

[83] D. Xiao, M.-C. Chang, and Q. Niu. Berry phase effects on electronic properties. *Reviews of Modern Physics*, 82:1959, 2010.

[84] A. Hoffmann. Spin Hall Effects in Metals. *IEEE Transactions on Magnetics*, 49:5172, 2013.

[85] J. Sinova, S. O. Valenzuela, J. Wunderlich, C. H. Back, and T. Jungwirth. Spin Hall effect. *eprint arXiv:*, 1411.3249, 2014.

[86] E. M. Pugh. Hall Effect and the Magnetic Properties of Some Ferromagnetic Materials. *Physical Review*, 36:1503, 1930.

[87] I. Zutic, J. Fabian, and S. D. Sarma. Spintronics : Fundamentals and applications. *Reviews of Modern Physics*, 76:323, 2004.

[88] M. I. Dyakonov. Spin Hall Effect. *eprint arXiv:*, 1210.3200, 2012.

[89] W. Nolting. *Grundkurs Theoretische Physik 1*. Springer, 2006.

[90] P. Zhang and Q. Niu. Charge-Hall effect driven by spin force: reciprocal of the spin-Hall effect. *eprint arXiv:*, page 4, 2004.

[91] J. Bass and W. P. Pratt. Spin-Diffusion Lengths in Metals and Alloys, and Spin-Flipping at Metal/Metal Interfaces: an Experimentalist's Critical Review. *Journal of Physics: Condensed Matter*, 19:183201, 2006.

[92] E. Hankiewicz, L. W. Molenkamp, T. Jungwirth, and J. Sinova. Manifestation of the spin Hall effect through charge-transport in the mesoscopic regime. *Physical Review B*, 70:241301, 2004.

[93] C. Brüne, A. Roth, E. G. Novik, M. König, H. Buhmann, E. M. Hankiewicz, W. Hanke, J. Sinova, and L. W. Molenkamp. Evidence for the ballistic intrinsic spin Hall effect in HgTe nanostructures. *Nature Physics*, 6:448, 2010.

[94] F. J. Jedema, A. T. Filip, and B. J. van Wees. Electrical spin injection and accumulation at room temperature in an all-metal mesoscopic spin valve. *Nature*, 410:345, 2001.

[95] T. Kimura and Y. Otani. Large Spin Accumulation in a Permalloy-Silver Lateral Spin Valve. *Physical Review Letters*, 99:196604, 2007.

[96] T. Kimura, Y. Otani, T. Sato, S. Takahashi, and S. Maekawa. Room-Temperature Reversible Spin Hall Effect. *Physical Review Letters*, 98:156601, 2007.

[97] T. Seki, Y. Hasegawa, S. Mitani, S. Takahashi, H. Imamura, S. Maekawa, J. Nitta, and K. Takanashi. Giant spin Hall effect in perpendicularly spin-polarized FePt/Au devices. *Nature Materials*, 7:125, 2008.

[98] T. Kimura, T. Sato, and Y. Otani. Temperature Evolution of Spin Relaxation in a NiFe/Cu Lateral Spin Valve. *Physical Review Letters*, 100:066602, 2008.

[99] S. Mizukami, Y. Ando, and T. Miyazaki. Effect of spin diffusion on Gilbert damping for a very thin permalloy layer in Cu/permalloy/Cu/Pt films. *Physical Review B*, 66:104413, 2002.

[100] L. Liu, T. Moriyama, D. C. Ralph, and R. A. Buhrman. Spin-Torque Ferromagnetic Resonance Induced by the Spin Hall Effect. *Physical Review Letters*, 106:036601, 2011.

[101] A. A. Tulapurkar, Y. Suzuki, A. Fukushima, H. Kubota, H. Maehara, K. Tsunekawa, D. D. Djayaprawira, N. Watanabe, and S. Yuasa. Spin-torque diode effect in magnetic tunnel junctions. *Nature*, 438:339, 2005.

[102] H. Kubota, A. Fukushima, K. Yakushiji, T. Nagahama, S. Yuasa, K. Ando, H. Maehara, Y. Nagamine, K. Tsunekawa, D. D. Djayaprawira, N. Watanabe, and Y. Suzuki. Quantitative measurement of voltage dependence of spin-transfer torque in MgO-based magnetic tunnel junctions. *Nature Physics*, 4:37, 2007.

[103] J. Sankey, P. Braganca, A. Garcia, I. Krivorotov, R. A. Buhrman, and D. C. Ralph. Spin-Transfer-Driven Ferromagnetic Resonance of Individual Nanomagnets. *Physical Review Letters*, 96:227601, 2006.

[104] C. F. Pai, L. Liu, Y. Li, H. W. Tseng, D. C. Ralph, and R. A. Buhrman. Spin transfer torque devices utilizing the giant spin Hall effect of tungsten. *Applied Physics Letters*, 101:122404, 2012.

[105] C. Hahn, G. de Loubens, O. Klein, M. Viret, V. V. Naletov, and J. Ben Youssef. Comparative measurements of inverse spin Hall effects and magnetoresistance in YIG/Pt and YIG/Ta. *Physical Review B*, 87:174417, 2013.

[106] K. Ando, Y. Kajiwara, S. Takahashi, S. Maekawa, K. Takemoto, M. Takatsu, and E. Saitoh. Angular dependence of inverse spin–Hall effect induced by spin pumping investigated in a Ni81Fe19/Pt thin film. *Physical Review B*, 78:014413, 2008.

[107] K. Ando, T. Yoshino, and E. Saitoh. Optimum condition for spin-current generation from magnetization precession in thin film systems. *Applied Physics Letters*, 94:152509, 2009.

[108] V. Vlaminck, J. E. Pearson, S. D. Bader, and A. Hoffmann. Dependence of spin-pumping spin Hall effect measurements on layer thicknesses and stacking order. *Physical Review B*, 88:064414, 2013.

[109] J.-C. Rojas-Sánchez, N. Reyren, P. Laczkowski, W. Savero, J.-P. Attané, C. Deranlot, M. Jamet, J.-M. George, L. Vila, and H. Jaffrès. Spin Pumping and Inverse Spin Hall Effect in Platinum: The Essential Role of Spin-Memory Loss at Metallic Interfaces. *Physical Review Letters*, 112:106602, 2014.

[110] H. Jiao and G. E. W. Bauer. Supplementary Information to " Spin-Backflow and AC Voltage Generation by Spin Pumping and Inverse Spin Hall Effect ". *Physical Review Letters, Supplementary*, pages 1–7, 2013.

[111] J. M. D. Coey. *Magnetism and Magnetic Materials*. Cambridge University Press, 2009.

[112] E. Lifshitz L. D. Landau. On the theory of the dispersion of magne- tic permeability in ferromagnetic bodies. *Physik. Z. Sowjetunion*, 8:101–114, 1935.

[113] T. L. Gilbert. A Lagrangian formulation of the gyromagnetic equation of the magnetic field. *Physical Review*, 100:1243–1244, 1955.

[114] B. Heinrich. *Ultrathin magnetic structures II, edited by B. Heinrich, J.A.C. Bland*. (Springer), 1994.

[115] G. A. Melkov A. G. Gurevich. *Magnetization Oscillations and Waves*. CRC Press, 1996.

[116] Z. Celinski, K. B. Urquhart, and B. Heinrich. Using ferromagnetic resonance to measure the magnetic moments of ultrathin films. *Journal of Magnetism and Magnetic Materials*, 166:6, 1997.

[117] D. L. Mills and S. M. Rezende. *Spin Dynamics in Confined Magnetic Structures II, edited by B. Hillebrands and K. Ounadjela.* Springer, Topics in Applied Physics, 2003.

[118] L. Kouwenhoven, A. Johnson, N. van der Vaart, C. Harmans, and C. Foxon. Quantized current in a quantum-dot turnstile using oscillating tunnel barriers. *Physical Review Letters*, 67:1626, 1991.

[119] H. Pothier, P. Lafarge, C. Urbina, D. Esteve, and M. H. Devoret. Single-Electron Pump Based on Charging Effects. *Europhysics Letters (EPL)*, 17:249, 1992.

[120] M. Switkes. An Adiabatic Quantum Electron Pump. *Science*, 283:1905, 1999.

[121] P. W. Brouwer. Scattering approach to parametric pumping. *Physical Review B*, 58:135, 1998.

[122] M. Büttiker, Y. Imry, R. Landauer, and S. Pinhas. Generalized many-channel conductance formula with application to small rings. *Physical Review B*, 31:6207, 1985.

[123] M. Büttiker. Four-Terminal Phase-Coherent Conductance. *Physical Review Letters*, 57:1761, 1986.

[124] A. Brataas, Y. V. Nazarov, and G. E. W. Bauer. Finite-element theory of transport in ferromagnet-normal metal systems. *Physical review letters*, 84:2481, 2000.

[125] A. Brataas, Y. V. Nazarov, and G. E. W. Bauer. Spin-transport in multi-terminal normal metal-ferromagnet systems with non-collinear magnetizations. *The European Physical Journal B*, 22:99, 2001.

[126] A. Brataas, G. E. W. Bauer, and P. Kelly. Non-collinear magnetoelectronics. *Physics Reports*, 427:157, 2006.

[127] S. Blundell. *Magnetism in Condensed Matter.* Oxford University Press, 2001.

[128] D. J. Griffiths. *Introduction to quantum mechanics.* Pearson Prentice Hall, 2005.

[129] J. R. Macdonald. Ferromagnetic Resonance and the Internal Field in Ferromagnetic Materials. *Proceedings of the Physical Society. Section A*, 64:968, 1951.

[130] B. Heinrich and J. F. Cochran. Ultrathin metallic magnetic films: magnetic anisotropies and exchange interactions. *Advances in Physics*, 42:523, 1993.

[131] G. Woltersdorf. *Spin pumping and two-magnon scattering in magnetic multilayers.* PhD thesis, Simon Fraser University, 2004.

[132] B. A. Kalinikos and A. N. Slavin. Theory of dipole-exchange spin wave spectrum for ferromagnetic films with mixed exchange boundary conditions. *Journal of Physics C: Solid State Physics*, 19:7013, 1986.

[133] S. O. Demokritov and B. Hillebrands. *Spin Dynamics in Confined Magnetic Structures I, edited by B. Hillebrands and K. Ounadjela.* Springer, Topics in Applied Physics, 2002.

[134] M. Vopsaroiu, G. V. Fernandez, M. J. Thwaites, J. Anguita, P. J. Grundy, and K. O'Grady. Deposition of polycrystalline thin films with controlled grain size. *Journal of Physics D: Applied Physics*, 38:490, 2005.

[135] M. Härtinger. Magnetische eigenschaften neuer ferromagnetischer materialien. Diploma thesis, Universität Regensburg, 2011.

[136] J. H. E. Griffiths. Anomalous High-frequency Resistance of Ferromagnetic Metals. *Nature*, 158:670, 1946.

[137] C. Kittel. Interpretation of Anomalous Larmor Frequencies in Ferromagnetic Resonance Experiment. *Physical Review*, 71:270, 1947.

[138] C. Kittel. Physical Theory of Ferromagnetic Domains. *Reviews of Modern Physics*, 21:541, 1949.

[139] B. Heinrich, K. Urquhart, A. Arrott, J. Cochran, K. Myrtle, and S. Purcell. Ferromagnetic-resonance study of ultrathin bcc Fe(100) films grown epitaxially on fcc Ag(100) substrates. *Physical Review Letters*, 59:1756, 1987.

[140] B. Heinrich, S. T. Purcell, J. R. Dutcher, K. B. Urquhart, J. F. Cochran, and A. S. Arrott. Structural and magnetic properties of ultrathin Ni/Fe bilayers grown epitaxially on Ag(001). *Physical Review B*, 38:12879, 1988.

[141] B. Heinrich, J. F. Cochran, A. S. Arrott, S. T. Purcell, K. B. Urquhart, J. R. Dutcher, and W. F. Egelhoff. Development of magnetic anisotropies in ultrathin epitaxial films of Fe(001) and Ni(001). *Applied Physics A Solids and Surfaces*, 49:473, 1989.

[142] B. Heinrich, J. F. Cochran, M. Kowalewski, J. Kirschner, Z. Celinski, A. S. Arrott, and K. Myrtle. Magnetic anisotropies and exchange coupling in ultrathin fcc Co(001) structures. *Physical Review B*, 44:9348, 1991.

[143] J. Jorzick, S. O. Demokritov, C. Mathieu, B. Hillebrands, B. Bartenlian, C. Chappert, F. Rousseaux, and A. N. Slavin. Brillouin light scattering from quantized spin waves in micron-size magnetic wires. *Physical Review B*, 60:15194, 1999.

[144] M. Zwierzycki, Y. Tserkovnyak, P. Kelly, A. Brataas, and G. E. W. Bauer. First-principles study of magnetization relaxation enhancement and spin transfer in thin magnetic films. *Physical Review B*, 71:064420, 2005.

[145] M. Büttiker, A. Prêtre, and H. Thomas. Dynamic conductance and the scattering matrix of small conductors. *Physical Review Letters*, 70:4114, 1993.

[146] M. Büttiker, H. Thomas, and A. Pretre. Current partition in multiprobe conductors in the presence of slowly oscillating external potentials. *Zeitschrift für Physik B*, 137:133, 1994.

[147] R. Meservey and P. Tedrow. Surface Relaxation Times of Conduction-Electron Spins in Superconductors and Normal Metals. *Physical Review Letters*, 41:805, 1978.

[148] E. Šimánek and B. Heinrich. Gilbert damping in magnetic multilayers. *Physical Review B*, 67:144418, 2003.

[149] E. Šimánek. Gilbert damping in ferromagnetic films due to adjacent normal-metal layers. *Physical Review B*, 68:224403, 2003.

[150] Y. Niimi, Y. Kawanishi, D. H. Wei, C. Deranlot, H. X. Yang, M. Chshiev, T. Valet, a. Fert, and Y. Otani. Giant Spin Hall Effect Induced by Skew Scattering from Bismuth Impurities inside Thin Film CuBi Alloys. *Physical Review Letters*, 109:156602, 2012.

[151] B. Gu, I. Sugai, T. Ziman, G. Y. Guo, N. Nagaosa, T. Seki, K. Takanashi, and S. Maekawa. Surface-Assisted Spin Hall Effect in Au Films with Pt Impurities. *Physical Review Letters*, 105:216401, 2010.

[152] B. Kardasz, O. Mosendz, B. Heinrich, Z. Liu, and M. Freeman. Spin current studies in Fe Ag, Au Fe by ferromagnetic resonance and time-resolved magneto-optics. *Journal of Applied Physics*, 103:07C509, 2008.

[153] O. Mosendz, G. Woltersdorf, B. Kardasz, B. Heinrich, and C. H. Back. Magnetization dynamics in the presence of pure spin currents in magnetic single and double layers in spin ballistic and diffusive regimes. *Physical Review B*, 79:224412, 2009.

[154] B. Kardasz and B. Heinrich. Ferromagnetic resonance studies of accumulation and diffusion of spin momentum density in Fe/Ag/Fe/GaAs(001) and Ag/Fe/GaAs(001) structures. *Physical Review B*, 81:094409, 2010.

[155] D. M. Pozar. *Microwave engineering*. John Wiley and Sons, Inc., 1997.

[156] K. Petermann and C. A. Bunge. *Hochfrequenztechnik 1*. Technische Universität Berlin, 2012. Vorlesungsskript.

[157] B. C. Wadell. *Transmission Line Design Handbook*. Artech House, Inc., 1991.

[158] M. Weiler, H. T. Nembach, J. M. Shaw, and T. J. Silva. Comment on Detection of Microwave Spin Pumping Using the Inverse Spin Hall Effect. *eprint arXiv:*, 1401.6407, 2014.

[159] C. Hahn, G. de Loubens, M. Viret, O. Klein, V. V. Naletov, and J. Ben Youssef. Detection of Microwave Spin Pumping Using the Inverse Spin Hall Effect. *Physical Review Letters*, 111:217204, 2013.

[160] G. Woltersdorf, O. Mosendz, B. Heinrich, and C. H. Back. Magnetization Dynamics due to Pure Spin Currents in Magnetic Double Layers. *Physical Review Letters*, 99:246603, 2007.

[161] C. Bayer et al. *Spin Dynamics in Confined Magnetic Structures III, edited by B. Hillebrands and A. Thiaville*. Springer, Topics in Applied Physics, 2006.

[162] H. Kurt, R. Loloee, K. Eid, W. P. Pratt, and J. Bass. Spin-memory loss at 4.2 K in sputtered Pd and Pt and at Pd/Cu and Pt/Cu interfaces. *Applied Physics Letters*, 81:4787, 2002.

[163] F. D. Czeschka, L. Dreher, M. S. Brandt, M. Weiler, M. Althammer, I.-M. Imort, G. Reiss, a. Thomas, W. Schoch, W. Limmer, H. Huebl, R. Gross, and S. T. B. Goennenwein. Scaling Behavior of the Spin Pumping Effect in Ferromagnet-Platinum Bilayers. *Physical Review Letters*, 107:046601, 2011.

[164] L. Vila, T. Kimura, and Y. Otani. Evolution of the Spin Hall Effect in Pt Nanowires: Size and Temperature Effects. *Physical Review Letters*, 99:226604, 2007.

[165] M. Gradhand, D. V. Fedorov, P. Zahn, and I. Mertig. Extrinsic Spin Hall Effect from First Principles. *Physical Review Letters*, 104:186403, 2010.

[166] T. Seki, I. Sugai, Y. Hasegawa, S. Mitani, and K. Takanashi. Spin Hall effect and Nernst effect in FePt/Au multi-terminal devices with different Au thicknesses. *Solid State Communications*, 150:496, 2010.

[167] A. Bastin, C. Lewiner, O. Betbeder-matibet, and P. Nozieres. Quantum oscillations of the hall effect of a fermion gas with random impurity scattering. *Journal of Physics and Chemistry of Solids*, 32:1811, 1971.

[168] H. Ebert, D. Ködderitzsch, and J. Minár. Calculating condensed matter properties using the KKR-Green's function method—recent developments and applications. *Reports on Progress in Physics*, 74:096501, 2011.

[169] T. Hupfauer, A. Matos-Abiague, M. Gmitra, F. Schiller, J. Loher, D. Bougeard, C. H. Back, J. Fabian, and D. Weiss. Emergence of spin-orbit fields in magnetotransport of quasi-two-dimensional iron on gallium arsenide. *Nature Communications*, 6:7374, 2015.

[170] D. Fang, H. Kurebayashi, J. Wunderlich, K. Výborný, L. P. Zârbo, R. P. Campion, A. Casiraghi, B. L. Gallagher, T. Jungwirth, and A. J. Ferguson. Spin-orbit-driven ferromagnetic resonance. *Nature Nanotechnology*, 6:413, 2011.

[171] H. Kurebayashi, J. Sinova, D. Fang, A. C. Irvine, T. D. Skinner, J. Wunderlich, V. Novák, R. P. Campion, B. L. Gallagher, E.K. Vehstedt, L. P. Zârbo, K. Výborný, A. J. Ferguson, and T. Jungwirth. An antidamping spin-orbit torque originating from the Berry curvature. *Nature Nanotechnology*, 9:211, 2014.

[172] C. Ciccarelli, K. M. D. Hals, A. Irvine, V. Novak, Y. Tserkovnyak, H. Kurebayashi, A. Brataas, and A. Ferguson. Magnonic charge pumping via spin-orbit coupling. *Nature Nanotechnology*, 10:50, 2015.

[173] T. Nan, S. Emori, C. T. Boone, X. Wang, T. M. Oxholm, J. G. Jones, B. M. Howe, G. J. Brown, N. X. Sun, and A. Samples. Comparison of spin-orbit torques and spin pumping across NiFe / Pt and NiFe / Cu / Pt interfaces. *Physical Review B*, 91:214416, 2015.

[174] F. Freimuth, S. Blügel, and Y. Mokrousov. Direct and inverse spin-orbit torques. *Physical Review B*, 92:064415, 2015.

Acknowledgment

I have been given the chance to wright my PhD-thesis in a great scientific and social environment. In the past four years I have learned many things from different people and have experienced many fruitful cooperations. I especially want to thank the following people:

- Prof. Christian Back for giving me the opportunity to wright my PhD-thesis under his supervision in the interesting field combining magnetization dynamics and spintronics. I have benefited immensely from the open-door culture concerning questions and problems he exemplifies at his chair of physics. I appreciate a lot the trust he set in me on different occasions.

- Prof. Georg Woltersdorf in whose work group I started my experimental efforts concerning the PhD thesis. As one of the world-wide experts in magnetization dynamics he was the one to introduce me to this very exiting field. I gratefully remember many discussions with him about measurement instrumentation, sample fabrication, presentation of data and writing styles for publications.

- Prof. Dieter Weiss for giving me access to clean room facilities which were very important for sample fabrication. Furthermore I appreciate his interest in my work and the continuous promotion of knowledge transfer in discussions and regular workshops.

- Kristina Chadova, Diemo Ködderitzsch and Prof. Hubert Ebert for first-principles calculations of spin Hall effects in AuPt-alloys. In the course of the scientific cooperation I benefited a lot from the discussions of both theoretical and experimental issues concerning spin-dependent scattering.

- Dahai Wei for the fruitful cooperation in terms of ac-ISHE.

- Hans Bauer for his support concerning the electromagnetic simulations and field calculations presented in my work. Thank you for giving me an insight in clear and effective programming. I also gratefully acknowledge the comprehensive discussions about the theoretical aspects of my work and corresponding proofreading.

- Markus Härtinger for giving me access to his field-sweep algorithm implemented in LabView. He constantly shared his profound knowledge in programming, measurement instrumentation and ferromagnetic resonance with me. I enjoyed a lot the time when we shared the same office. I especially acknowledge the FMR measurements he conducted for me.

- Martin Decker for the many discussions we had and still have about the inverse spin Hall effect, magnetization dynamics, ferromagnetic resonance and the reciprocity of his and my experimental approach. I especially enjoyed the times when discussing these issues on our office blackboard. In this respect I also want to thank Tobias Weindler who regularly joined with his profound knowledge in the discussion sessions.

- Martin Buchner for the illustrative discussions about spin injection apart from spin pumping.

- Helmut Körner for SQUID measurements and maintenance of the evaporation chamber.

- The secretaries of the chair of Prof. Back, Sylvia Hrdina, Magdalena Pfleger and Claudia Zange as well as of the chair of Prof. Weiss, Claudia Rahm and Elke Haushalter for their administrative support. I furthermore enjoyed a lot the discussions apart from physics, which I had especially with Sylvia Hrdina and Claudia Zange in occasional coffee breaks.

- Markus Hollnberger and Dieter Schierl for their support concerning mechanical engineering of experimental setups and yellow room management.

- All bachelor and master students who cooperated with me on the topic of magnetization dynamics, spin pumping and ISHE in the course of their theses.

- My office colleague Matthias Kronseder for the rewarding discussions about general aspects of magnetism and proofreading of the experimental results part of the present thesis.

- Stefan Günther for the support in terms of formating the LaTeX-file of my thesis.

Furthermore, I gratefully acknowledge the financial support from the Sonderforschungsbereich 689 “Spinphänomene in reduzierten Dimensionen”.
I want to thank all members of Prof. Back’s chair for the pleasant time during the last four years not only in the lab and in discussions. I will never forget the many occasions when enjoying barbecues together, watching soccer, going on excursions and having cheerful times in the coffee breaks.
Finally I want to thank my family for the constant support and especially my wife Eli for her loving patience and encouragement during my PhD-thesis.